BIOANALYTICAL ASSESSMENT OF CONTAMINANT COCKTAILS IN MARINE CETACEANS USING SPECIES-SPECIFIC CELL LINES

XINTONG LIU

PhD

The Hong Kong Polytechnic University

2026

The Hong Kong Polytechnic University

Department of Civil and Environmental Engineering

Bioanalytical Assessment of Contaminant Cocktails in Marine Cetaceans Using Species-specific Cell Lines

Xintong Liu

A thesis submitted in partial fulfilment of the requirements for the degree of Doctor of Philosophy

December 2025

CERTIFICATE OF ORIGINALITY

I hereby declare that this thesis is my own work and that, to the best of my knowledge and belief, it reproduces no material previously published or written, nor material that has been accepted for the award of any other degree or diploma, except where due acknowledgement has been made in the text.

_____ (Signed)

Xintong Liu
_____ (Name of student)

Abstract

The global marine environment increasingly acts as a sink for a complex array of chemical contaminants, originating from both intensified anthropogenic activities and naturally occurring biological processes. In subtropical coastal ecosystems, such as the waters surrounding Hong Kong adjacent, this pollution manifests as a chemical cocktail comprising legacy persistent organic pollutants (POPs), contaminants of emerging concerns (CECs) and pharmaceuticals and personal care products (PPCPs) originated from industrial discharges, and prevalent marine algal toxins produced by harmful algal blooms (HABs). Resident cetaceans, the Indo-Pacific humpback dolphin (*Sousa chinensis*) and the Indo-Pacific finless porpoise (*Neophocaena phocaenoides*), act as sentinel species for this ecosystem since their high trophic level, long lifespan, and extensive use of coastal habitats expose them to health risks from these complex mixtures. However, traditional ecotoxicological driven primary by *in vitro* single-chemical testing, cannot resolve the mixture effects of environmental contaminants, identify toxic drivers and link external environmental concentrations to biologically relevant internal doses. Furthermore, standard targeted screening analysis captures only a fraction of the chemical universe, leaving the majority of toxicity compounds in environmental mixtures unidentified. To address these critical knowledge gaps, this thesis establishes an integrated, mechanism-informed framework that combines the development of species-specific *in vitro* cell models, non-target screening (NTS) coupled with machine learning (ML), and physiologically based toxicokinetic (PBTK) modeling to provide a comprehensive risk assessment of seawater contaminant cocktails for Hong Kong's cetaceans.

The research methodology involved the collection of 72 surface seawater samples from Hong Kong coastal waters across wet and dry seasons. To overcome the ethical

and logistical constraints associated with studying endangered marine mammals, primary and immortalized fibroblast cell lines were successfully established from the skin of the humpback dolphin (CWDT), while cell lines from the finless porpoise (FPT) donated by Shantou University. These cell lines provided a biologically relevant platform for measuring cytotoxicity, intracellular reactive oxygen species (ROS) induction, and DNA damage caused by seawater extracts and 38 individual target contaminants. The study further conducted a five-compartment PBTK model to simulate the absorption, distribution, and elimination of contaminants, facilitating quantitative *in vitro* to *in vivo* extrapolation (QIVIVE) to predict internal tissue concentrations and refine risk assessments based on freely dissolved concentrations. Additionally, this study integrated a high-resolution Orbitrap mass spectrometry for non-target screening (NTS) and a random forest machine-learning model to train on experimental toxicity data to prioritize potential toxicants from tens of thousands of unknown chemical features. The *in vitro* bioassays revealed that seawater extracts elicited cytotoxicity and oxidative stress in both cetacean cell lines, with species-specific sensitivities. Specifically, the mean toxic units (TU) required to induce cytotoxicity and reactive oxygen species (ROS) generation were 0.0058 and 0.0269 in FPT, and 0.02 and 0.031 in CWDT. A pivotal finding of this research was the disproportionate role of natural toxins in driving observed toxicity. Algal toxins, specifically pectenotoxin-2 (PTX-2), okadaic acid (OA), and gymnodimine (GYM), were identified as the dominant drivers even at low detected concentration (Mean: 8.38 $\times 10^{-13}$ M, 6.88 $\times 10^{-13}$ M, and 5.33 $\times 10^{-13}$ M, respectively), far exceeding the toxicity contribution of anthropogenic pollutants. PTX-2 as extraordinarily toxic potent and explained majority of the cytotoxicity caused by known chemicals in mixture modeling. While PTX-2 drove cytotoxicity, other toxins like OA and GYM were the primary contributors to oxidative stress. Interestingly, anthropogenic chemicals such as per- and

polyfluoroalkyl substances (PFAS) and ultraviolet (UV) filters, while less cytotoxic, contributed measurably to ROS induction, suggesting they pose a risk of oxidative injury and skin barrier disruption rather than acute lethality. Despite characterizing a broad suite of target compounds, the study confirmed a significant iceberg effect, where the majority of cytotoxicity and ROS induction observed in seawater extracts remained unexplained by targeted chemicals, highlighting the presence of unidentified toxic drivers. The application of the PBTK model provided a critical shift in risk perspective from external exposure to internal dose. The simulations revealed that skin and blubber serve as major reservoirs for semi-lipophilic pollutants, with contaminants like phenanthrene and octocrylene accumulating substantially in the skin due to slow clearance and lipophilicity. A divergence was observed between *in vitro* potency and *in vivo* accumulation. High toxic potency algal toxins showed low skin accumulation due to rapid hepatic clearance, whereas anthropogenic contaminants persisted in tissues. Consequently, when risk was assessed using external seawater concentrations, the mixture appeared to pose low risk. However, utilizing PBTK-derived internal skin concentrations dramatically increased risk estimates, with the internal risk for cytotoxicity and DNA damage approaching the threshold of concern. Notably, algal toxin still emerged as a critical internal risk driver, as pharmacokinetic factors amplified its contribution to internal cytotoxicity risk to in the skin compartment.

To elucidate the unexplained toxicity observed in the bioassays, an integrated NTA and ML workflow successfully prioritized potential toxicity candidates from tens of thousands of unknown chemical features. The analysis revealed that the toxicological landscape is defined by endpoint-specific signatures, with the random forest (RF) models demonstrating a performance gradient where cytotoxicity prediction achieved the highest accuracy (80.0%). Specifically, the framework identified high-potency

candidates including resiniferatoxin (a natural neurotoxin), clarithromycin (a macrolide antibiotic), and a cinnamoyl-iridoid glycoside pro-toxicant. These findings point to a complex source profile where domestic wastewater markers and natural toxins constitute a persistent chemical background. Mechanistically, the ultrapotent receptor-binding of resiniferatoxin and the potential DNA interaction of organoheterocyclics align well with the observed toxicological endpoints. This discovery highlights that the hidden toxicity stems from a small subset of high-potency drivers within a stable wastewater-plastic complex, necessitating a multi-endpoint approach to fully deconstruct coastal chemical risks.

In conclusion, this thesis presents the first comprehensive, mechanism-based framework for assessing the dermal health risks of chemical mixtures to Hong Kong's resident cetaceans. The findings challenge the traditional regulatory focus on anthropogenic contaminants by demonstrating that natural algal toxins are primary drivers of acute toxicity, even in the absence of visible algal blooms. Simultaneously, widespread anthropogenic contaminants contribute to oxidative stress and accumulate significantly in cetacean skin. The integration of PBTK modeling underscores that external water monitoring drastically underestimates toxicological risk, as contaminants appearing safe at environmental levels can reach hazardous internal concentrations. Furthermore, the discovery of pharmaceutical residues and natural toxins via machine learning highlights the urgent need to expand monitoring programs to include these unknown pollutants. By elucidating the drivers of mixture toxicity, this research provides a scientific foundation for holistic monitoring strategies and internal dose-based frameworks, which are essential for the effective conservation of vulnerable Indo-Pacific cetacean populations.

Publication list

(1) **Liu, X.**; Liang, B.; Yao, S.; Xiong, A.; Zhang, X.; Sun, Y.; Zhang, L.; Li, C.; Ruan, Y.; Yan, M.; Ho, Y.-W.; Fang, J. K. H.; Wang, B.; Leusch, F. D. L.; Schlenk, D.; Liu, W.; Leung, K. M. Y.; Jin, L. N. Dissecting the Role of Natural Toxins and Anthropogenic Contaminants in Mixture Effects of Seawater Chemical Cocktails on Cetacean Skin Fibroblasts. ***Environ. Sci. Technol.*** 2025, 59 (28), 14203–14213. https://doi.org/10.1021/acs.est.4c14481.

(2) Han, Y.; Yu, J.; **Liu, X.**; Zhang, F.; Huang, X.; Lu, Y.; Zhang, W.; Zimmerman, R.; Rudich, Y.; Li, Q.; Chen, J.; Chen, Y.; Jin, L. N. Generation of More Potent Components at Higher Temperatures Offsets Toxicity Reduction despite Reduced Mass Emissions during Biomass Burning. ***Environ. Sci. Technol.*** 2025, 59 (36), 19244–19256. https://doi.org/10.1021/acs.est.5c05710.

(3) Zhang, L.; Xiong, A.; Li, C.; **Liu, X.**; Zhang, X.; Gong, S.; Yan, M.; Qin, X.; Liu, Y.; Hu, Z.; Fang, J. K.-H.; Duan, H.; Liu, H.; Chan, L. L.; Jin, L. N. Ecological Pattern of Microalgal Communities and Associated Risks in Coastal Ecosystems. ***ISME Commun.*** 2025, 5 (1). https://doi.org/10.1093/ismeco/ycaf109.

(4) Yu, J.; Chen, T.; Han, Y.; **Liu, X.**; Su, J.; Leung, P. H. M.; Kelly, F.; Ho, K.; Qu, G.; Jin, L. N. Disproportionately Higher Contribution of Endotoxin to PM2.5 Bioactivity than Its Mass Share Highlights the Need to Identify Low-Concentration, High-Potency Components. ***Environ. Sci. Technol.*** 2025, 59 (38). https://doi.org/10.1021/acs.est.5c07255.

Acknowledgements

I would like to express my deepest gratitude to my chief supervisor, Professor Jin Ling, Nathanael, for his guidance and mentorship throughout the past four years. Under his supervision, I learned how to identify meaningful scientific questions, design rigorous approaches to address them, and develop the persistence needed to complete complex research. Beyond academics, he helped me build the confidence to confront challenges in life with a steady mindset and the belief that, although each stage may be difficult, it is always possible to move forward and overcome.

I am also sincerely grateful to my co-supervisor, Professor Fang James, for his continuous support and thoughtful care in many subtle yet important ways. His encouragement and practical advice have made my cross-departmental learning and research activities far smoother and more effective, and I truly appreciate his steady presence throughout my doctoral journey.

My heartfelt thanks go to Professor Kenneth Mei Yee Leung and Professor Wenhua Liu for their careful guidance and valuable input during my PhD. I am also grateful to Professor Frederic Leusch and Professor Daniel Schlenk, every discussion with them regarding my research brought new insights and broadened my scientific perspective. I would like to thank Professor Li Li, who has always been exceptionally generous in responding to my questions with patience and clarity. I am thankful to Professor Bei Wang for kindly providing laboratory access at a critical stage of my experiments, which enabled me to complete key work smoothly. I also wish to acknowledge Professor Meng Yan and Professor Yuefei Ruan for offering comprehensive technical support that strengthened my training and progress in research.

I would like to thank Dr. Bo Liang and Dr. Yajing Sun. At the early stage of my PhD, when everything was unfamiliar, they devoted tremendous time and effort to teaching me essential experimental skills and sharing their knowledge without reservation. I am grateful to Dr. Yuen-Wa Ho for providing valuable sampling opportunities. My appreciation also goes to Dr. Qi Wang, Dr. Pui Kin So, and Chenyin Wang, who taught me many important procedures and practical skills in chemical analysis.

I am deeply thankful to my groupmates and colleagues. In particular, I would like to thank Dr. Li Zhang, Dr. Changchao Li, and Dr. Xiaohua Zhang, you were the first close friends I met at the beginning of my PhD journey, and your encouragement remains one of my most treasured memories. I also sincerely thank Siyu Yao, Anqi Xiong, Xin Li, Yong Han, Tian Chen, Junrong Su, Jinyan Yu, Hulong Yi, Qisheng Li, Ball Ching, Marco Shing Hei Yuen, Yanghui Chen, and Zixin Li for their assistance during field sampling campaigns and laboratory work over these four years.

I am profoundly grateful to my family for their unwavering support. With you as my solid foundation, I have been able not only to celebrate success, but also to face setbacks with courage and resilience. I am especially thankful to my husband, Dr. Yifan Jiang, for his patience, understanding, and companionship throughout these years as my best friend. I also thank my father, Mr. Jiang Liu, for his unconditional love and constant encouragement. Most importantly, I thank my mother, Ms. Wen Wang. The philosophy book Sophie's World, which you gave me on my twelfth birthday, was the beginning of my curiosity about the nature of the world. It was my first glimpse of a vast world waiting to be explored and it was also the first time I wished that I could one day get a PhD. Thank you, Mum, for your wholehearted and unwavering trust. At the age of twenty-eight, I feel I am finally receiving the gift you gave me when I was twelve.

Finally, I gratefully acknowledge the financial support that made this research

possible: the State Key Laboratory of Marine Pollution (SKLMP) Seed Collaborative Fund (SKLMP/SCRF/0030); the Hong Kong Branch of Southern Marine Science and Engineering Guangdong Laboratory (Guangzhou) (SMSEGL20SC02); the Hong Kong Offshore LNG Terminal Project Marine Conservation Enhancement Fund (MCEF20030); the Presidential Young Scholar Scheme (P0040336); the Research Centre for Nature-based Urban Infrastructure Solutions (P0053045) of The Hong Kong Polytechnic University; and the Co-funding Mechanism on Joint Laboratories with the Chinese Academy of Sciences sponsored by the Research Grants Council of the Hong Kong (JLFS/E-502/24).

Table of contents

List of figures

List of tables

List of abbreviations

Abbreviation	Full term / Definition
4-MBC	4-methylbenzylidene camphor
6:2 Cl-PFESA	6:2 Cl-polyfluorinated ether sulfonic acid
8-OHdG	8-hydroxy-2'-deoxyguanosine
8:2 Cl-PFESA	8:2 Cl-polyfluorinated ether sulfonic acid
ADI	Average daily input
AE	Assimilation efficiency
AMOX	Amoxicillin
ANA	Acenaphthylene
AUC	Area under the curve
AZA1	Azaspiracid-1
AZA2	Azaspiracid-2
BDE-209	Bis(pentabromophenyl) ether
BEQ	Bioanalytical equivalent concentration
BP-3	Benzophenone-3
BP-4	Benzophenone-4
BSA	Bovine serum albumin
BW	Body weight
CA	Concentration addition
CEC	Contaminants of emerging concerns
CLA	Clarithromycin
CPFX	Ciprofloxacin
CTC	Chlortetracycline hydrochloride
CTX	Cefotaxime
CWDT	Chinese white dolphin transfected skin fibroblast cell
DBE	Double bond equivalent
DBT	Dibutyltin
DC	Daily consumption
DCFHDA	2’ 7’-dichlorofluorescein diacetate
DDT	Dchlorodiphenyltrichloroethane
DEET	N, N-diethyl-m-toluamide
DMEM	Dulbecco's Modified Eagle Medium
DOX	Doxycycline-d3 hyclate

Abbreviation	Full term / Definition
DTX-1	Dinophysistoxin-1
DTX-2	Dinophysistoxin-2
EAR	Exposure activity ratios
$EC_{IR1.5}$	Effect concentration induced 1.5-fld induction ratio
EDA	Effect-directed analysis
EHMC	Ethylhexyl methoxycinnamate
EHS	Ethylhexyl salicylate
ELISA	Enzyme-linked immunosorbent assay
ESI	Electrospray ionization
ETM	Erythromycin
FBS	Fetal bovine serum
FPT	Finless porpoise transfected skin fibroblast cell
G418	Geneticin
GFP	Green fluorescent protein
GYM	and gymnodimine
HAB	Harmful algal blooms
HBA	Hydrogen-bond acceptors
HBD	Hydrogen-bond donors
HMS	Homosalate
HRMS	Advances in high-resolution mass spectrometry
IA	Independent action
IC_{10}	10% inhibition concentration
IPQ	Index of prediction quality
iPSCs	Induced pluripotent stem cells
LAS	4-dodecylbenzenesulfonic acid
LC_{50}	50% lethal concentration
MAE	Mean absolute error
MIE	Molecular initiating event
ML	Machine learning
MW	Molecular weight
NAP	Naphthalene
NFL	Norfloxacin
NOEC	No observed effect concentration
NTS	Non-target screening
OA	okadaic acid
OC	Octocrylene
ODPABA	Octyl dimethyl-p-aminobenzoic acid

Abbreviation	Full term / Definition
OFL	Ofloxacin
OPFR	Organophosphate flame retardants
PAH	Polycyclic aromatic hydrocarbon
PBDE	Polybrominated diphenyl ethers
PBTK	Physiologically based toxiccokinetic
PBS	Phosphate-buffered saline
PCB	Polychlorinated biphenyls
PEG	Polyethylene glycol
PFAS	Per- and polyfluoroalkyl substances
PFBA	Perfluorobutanoic acid
PFBS	Perfluorobutanesulfonic acid
PFOA	Perfluorooctanoic acid
PFOS	Perfluorooctane sulfonate
PHE	Phenanthrene
POPs	Persistent organic pollutants
PPCPs	Pharmaceuticals and personal care products
PPG	Polypropylene glycol
PRE	Pearl River Estuary
PTX-2	Pectenotoxin-2
QIVIVE	Quantitative in vitro to in vivo extrapolation
REF	Relative enrichment factor
RF	Random forest
RFE	Recursive feature elimination
RFP	Red fluorescent protein
RMSE	Root mean square error
ROS	Reactive oxygen species
ROX	Roxithromycin
RTX	namely resiniferatoxin
RT	Retention time
SMX	Sulfamethoxazole
SPE	Solid phase extraction
SUL	Sulfadiazine
SV40	Simian vacuolating virus 40
TBEP	Tris(2-butoxyethyl) phosphate
TU	Toxic unit
UHPLC	Ultra-high performance liquid chromatography
UV	Ultraviolet

Abbreviation	Full term / Definition
YTX	Yessotoxin

1. Introduction

1.1. Background

The global ocean acts as a sink for a wide range of toxic contaminants originating from both anthropogenic and natural sources (Dai et al., 2023; Zhang et al., 2024). Rapid industrialization, coastal urban expansion, and intensified human activities have introduced thousands of synthetic chemicals into marine environments (Escher et al., 2020). Many of these substances resist degradation, exhibit long environmental lifetimes, and bioaccumulate across trophic levels. In parallel, naturally derived bioactive compounds such as marine biotoxins produced during harmful algal blooms (HABs) have become increasingly prevalent, driven by climate change, eutrophication, and ocean warming (Global Harmful Algal Bloom Status Reporting, 2021). These anthropogenic contaminants and natural toxins create complex chemical mixtures in seawater.

Subtropical marine ecosystems, such as the waters surrounding Hong Kong adjacent to the Pearl River Estuary (PRE), exemplify this challenge. Like many other coastal regions, much of Hong Kong's seawater has been influenced by coastal development, anthropogenic pollution from the PRE **(H. Liu et al., 2024; W.-X. Wang & Rainbow, 2020)**, and locally triggered HABs events (Ho, 2022). These combined pressures generate seawater mixtures that contain both anthropogenic pollutants and naturally occurring toxins, posing risks for marine organisms inhabiting these ecosystems.

Marine mammals, particularly cetaceans, are among the most vulnerable species

to such contamination. As long-lived, high-trophic-level predators, cetaceans accumulate numerous contaminants through both dietary intake and direct environmental exposure (Moore, 2008). Their extensive use of coastal habitats, coupled with their physiological sensitivity, has led to their recognition as sentinel species that reflect marine ecosystems health. In Hong Kong waters, two vulnerable and iconic marine mammals (Jefferson et al., 2002; Karczmarski et al., 2016; Ramu et al., 2005): the Indo-Pacific finless porpoise (*Neophocaena phocaenoides*) and the Indo-Pacific humpback dolphin (*Sousa chinensis*) (Figure 1), occupy overlapping regions characterized by substantial anthropogenic pressure and frequent HAB events. These species provide a unique opportunity to investigate how complex seawater mixtures pose health risks to porpoises and dolphins. However, elucidating the toxic potential of seawater contaminant mixtures and identifying the drivers of mixture toxicity are hindered by ethical and logistical challenges in cetacean ecotoxicological research.

In recent years, *in vitro* approaches have emerged as valuable alternatives for assessing toxicity in marine toxicology using cetacean cell lines. A number of environmental pollutants have demonstrated varying toxic potency in cetacean cells. Nevertheless, most studies have focused on the individual toxicity of selected chemicals of concern. While dietary intake is a well-studied pathway of contaminant exposure for cetaceans, the skin serves as the primary defensive barrier through its direct contact with seawater (Menon et al., 2022). Given that the condition of cetacean skin often reflects the overall health status of these mammals, marine pollution has been identified as a significant factor that compromises its natural barrier function (Hart et al., 2012; Y. Ho et al., 2023). Consequently, a key scientific question remains unresolved: to what extent can the chemicals currently monitored or individually tested explain the observed biological effects of impacted seawater on dermal health-related endpoints in cetaceans?

Addressing this question is essential for determining from the contribution of compounds not typically included in environmental assessments, including both overlooked known chemicals and unknown contaminants.

Progress in mixture research is further limited by reliance on targeted analytical screening, which detects only a small subset of compounds present in the environment. Advances in high-resolution mass spectrometry (HRMS) have enabled nontarget screening (NTS) to reveal previously unrecognized contaminants (Hollender et al., 2019). Integrating automated computational workflows with machine-learning-based toxicity prediction and high-throughput experimental confirmation offers a path to prioritize toxicologically relevant features within complex environmental samples.

While chemical identification and prioritization are essential, they alone cannot establish toxicological relevance in living organisms. Understanding the potential health impacts of seawater contaminants requires linking external concentrations to internal biological exposure. The physicochemical properties of contaminants, together with species-specific absorption, distribution, metabolism, and elimination processes, determine the internal dose that ultimately drives toxicity (Weijs et al., 2012). Quantifying this internal dose is essential for evaluating health risks and for determining whether contaminants present in seawater reach levels that correspond to *vitro* toxicity thresholds. Despite its importance, integrating external exposure, internal tissue concentrations, and in vitro effect data remains in its infancy for high-trophic marine mammals. To date, no study has applied quantitative *in vitro* to *in vivo* extrapolation (QIVIVE) to assess risks in threatened cetacean species.

These gaps highlight the need for a more comprehensive framework that integrates mixture toxicity measurements, chemical prioritization, and internal-dose modeling.

Addressing these knowledge gaps is essential for improving ecological risk assessment and for supporting conservation efforts aimed at protecting vulnerable marine mammals in rapidly changing coastal environments.

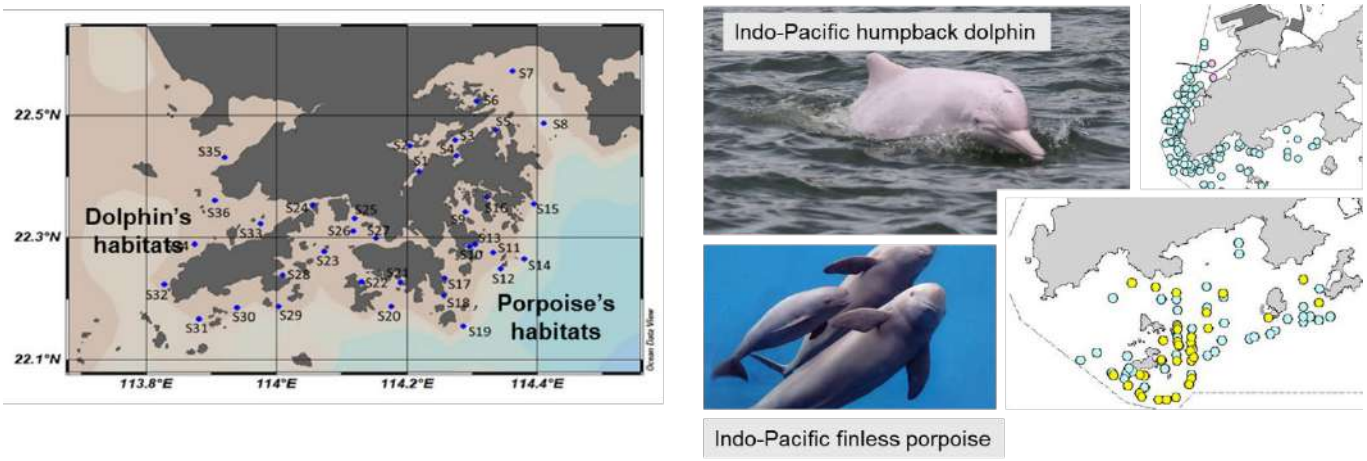

Figure 1. 1 Habitats and observation sites of Indo-Pacific humpback dolphin and finless porpoise in Hong Kong coastal waters.

1.2. Research Objectives

The overarching goal of this thesis is to develop an integrated, mechanism-informed framework for evaluating the risks posed by complex seawater contaminant mixtures to coastal cetaceans inhabiting Hong Kong waters. Building on the gaps identified in above, this research aims to overcome the limitations of traditional single-chemical and targeted monitoring approaches by combining species-specific in vitro assays, non-target chemical analysis with machine learning–based prioritization, and QIVIVE.

Objective 1: Establish cetacean-specific skin fibroblast cell lines and identify key toxic components in Hong Kong seawater that affect marine mammal health.

This objective focuses on developing and characterizing skin fibroblast cell lines

derived from the Indo-Pacific humpback dolphin and the Indo-Pacific finless porpoise. These cell models provide a species-relevant platform for evaluating the toxicological impacts of local seawater samples and for identifying major chemical drivers of toxicity within Hong Kong's coastal environment.

Objective 2: Develop a physiologically informed toxicokinetic model for cetaceans to evaluate whether environmentally detected chemical concentrations can reach harmful levels observed *in vitro*, thereby refining ecological risk assessment.

This objective establishes a cetacean-specific toxicokinetic modelling framework to link external seawater exposure with predicted internal tissue concentrations. The model assesses whether environmental levels of detected chemicals could yield *in vivo* doses comparable to *in vitro* effect thresholds and provides an stronger basis for risk characterization in coastal cetacean populations.

Objective 3: Efficiently identify and prioritize all toxicologically relevant compounds present in Hong Kong seawater using non-target screening and machine-learning approaches.

By integrating HRMS–based non-target analysis with machine learning-driven toxicity prediction workflows, this objective aims to comprehensively screen seawater samples and pinpoint compounds capable of eliciting toxic effects in the two cetacean species. The prioritized list of candidate toxicants supports subsequent mechanistic analyses and improves the interpretation of mixture toxicity.

1.3. Organization

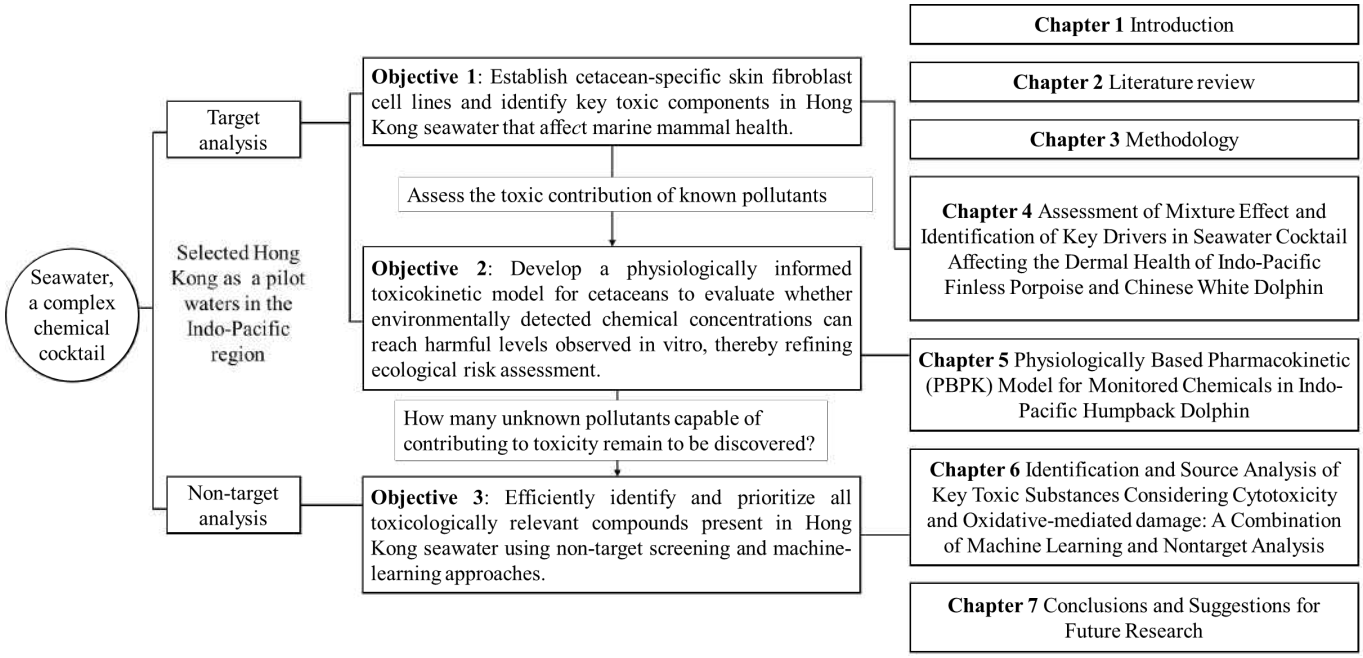

Figure 1. 2 A flowchart of the objectives and structures of the thesis

This thesis comprises seven chapters. The present chapter provides the background information on the global marine chemical mixtrues and its impact on marine cetaceans, particularly for the Indo-Pacific humpback dolphins and finless porpoises in Hong Kong waters. It clarifies the critical gaps in assessing the health risks of complex contaminant mixtures and the limitations of traditional monitoring, while stating the primary objectives of this PhD project. Chapter 2 gives a holistic review of current work regarding marine chemical pollution, the development of species-specific cell models, and the recent advances in bioanalytical tools and non-target screening integrated with machine learning for toxicity prediction. Subsequently, Chapter 3 presents experimental methodology and modeling frameworks, including the establishment and characterization of cetacean-specific skin fibroblast cell lines, sampling protocols for seawater extracts, and the technical procedures for model development.

The following three chapters describe and discuss the acquired results. Specifically, Chapter 4 targets the bioanalytical assessment of seawater mixtures and identifies the key toxicity drivers. With a shift to internal exposure and risk translation, Chapter 5 discusses the development of a PBTK model for the Indo-Pacific humpback dolphin to bridge the gap between external environmental concentrations and internal biologically effective doses. As an extension of the previous chapters and to further explore unknown stressors, Chapter 6 integrates NTS with ML to prioritize toxic features and identify potential chemical candicates, such as those related to sewage discharges and plastic additives, in the Hong Kong marine environment. Finally, Chapter 7 summarizes the major conclusions and contributions of the current project, addresses its limitations, and provides recommendations for future studies.

2. Literature Review

2.1. Marine Chemical Pollution and Its Implications for Marine Mammals' Health

2.1.1. Global context of marine contamination

Marine ecosystems worldwide are undergoing continuous affected by a broad spectrum of chemical contaminants. The contamination of the global marine environment by anthropogenic chemicals has evolved from a series of localized industrial incidents into a pervasive issue that fundamentally alters biogeochemical cycles and threatens marine biodiversity (Halpern et al., 2008; Persson et al., 2022; Schwarzenbach et al., 2006). Historically, the scientific and regulatory focus was circumscribed to legacy persistent organic pollutants (POPs), a group of halogenated compounds including polychlorinated biphenyls (PCBs) and organochlorine pesticides like dichlorodiphenyltrichloroethane (DDT). These contaminants become ubiquitous in the mid-20 century due to their resistance to environmental degradation. Despite the implementation of global treaties such as the Stockholm Convention, which successfully limited the primary production of these POPs, they remain biologically available in marine ecosystems. Consequently, legacy POPs continue to pose chronic risks to marine life, particularly in apex predators, such as marine mammals, where they biomagnify to hazardous concentrations (Desforges et al., 2018; Dietz et al., 2019).

However, the contemporary toxicological landscape has shifted dramatically with the proliferation of the Anthropocene chemical cocktail, a dynamic and rapidly expanding mixture of synthetic substances (Escher et al., 2020). This new era of

pollution is defined by contaminants of emerging concern (CECs), which include per- and polyfluoroalkyl substances (PFAS), organophosphate flame retardants (OPFRs), pharmaceuticals and personal care products (PPCPs), and diverse plasticizers. Unlike the legacy POPs, which are almost exclusively lipophilic and accumulate in fatty tissues, many CECs possess amphiphilic or hydrophilic properties (Sauvé & Desrosiers, 2014). This physicochemical diversity alters their environmental fate, transport mechanisms, and biological uptake pathways. For instance, while PCBs accumulate in sediments and blubber (Guo et al., 2021), PFAS are more intended to combine with protein in organisms and pharmaceutical residues are often highly mobile in the water column, exposing aquatic organisms through direct contact and respiration as well as diet (Ng & Hungerbühler, 2014; Reemtsma et al., 2016). The continuous introduction of these novel entities into the marine environment outpaces the traditional ability to assess their individual risks, and presents an even greater challenge regarding mixture toxicity (Persson et al., 2022).

At the same time, global climate change is increasing the prevalence and intensity of marine natural toxin production, particularly algal toxins produced by harmful algal blooms (HABs) (Bejarano et al., 2008). Lipophilic algal toxins can infiltrate marine food webs during bloom events (Dolah et al., 2003). Characterized by high chemical stability and significant bioaccumulation potential, these toxins frequently co-occur with anthropogenic contaminants.

Although the marine environment contains a complex and diverse array of contaminants, marine organisms are continuously exposed to complex mixture of bioactive compounds. These substances, even when present at trace concentrations, can perturb biological pathway at levels below lethality threshold (Desforges et al., 2016;

Göbölös et al., 2024). As anthropogenic and natural substances continue to rise globally, understanding the interactions within these complex mixtures and their long-term physiological implications for marine organisms has become one of the most pressing priorities in marine ecotoxicology.

2.1.2. Coastal vulnerability in the Indo-Pacific region

Although marine contamination is a global issue, the Indo-pacific region, and specifically Hong Kong, is one of the most affected due to its coastal populations and rapid economic expansion. The western coastal waters of Hong Kong are adjacent to the Pearl River Estuary (PRE) and is subject to a continuous influx of terrestrial pollutants originating from one of the most urbanized and industrialized regions (W.-X. Wang & Rainbow, 2020). Numerous studies have reported the legacy and energy POPs in surface waters and sediments of Hong Kong and PRE. Despite improvements in water management, these contaminants persist in complex forms that resist removal during conventional treatment processes.

This chemical burden on the marine environment is further exacerbated by eutrophic conditions. Enhanced anthropogenic inputs of nitrogen and phosphorus, derived from agricultural runoff, have accelerated nutrient enrichment in Hong Kong costal waters, leading to a significant increase in the frequency and intensity of HABs. These blooms transcend routine primary production events as they are often dominated by toxigenic species, like dinoflagellates and diatoms, which introduce produce potent toxins into the marine ecosystem (Hong Kong Red Tide Database). The co-occurrence of anthropogenic pollutants and natural toxins creates a multi-stressor environment of complexity. This mixture is likely to drive significant adverse health outcomes for marine ecosystem and organisms.

2.1.3. Cetaceans as sentinels of marine ecosystem health

Within the coastal waters of Hong Kong, two resident cetacean species act as critical indicators of marine environment: the Indo-Pacific humpback dolphin (*Sousa chinensis*) and the Indo-Pacific finless porpoise (*Neophocaena phocaenoides*). As long-lived, apex predators with high metabolic rates and substantial lipid stores, these cetaceans effectively integrate pollutant exposures over vast spatial and temporal scales (Hazen et al., 2024). Unlike lower-trophic organisms that may reflect only recent or localized contamination, cetaceans accumulate pollutants over decades, providing a comprehensive historical record of the ecosystem's chemical burden. Their mammalian physiology also makes them biologically relevant models for understanding potential risks of contaminants to marine ecosystem (Fossi et al., 2020). The population of the Ino-Pacific humpback dolphin in the Hong Kong coastal area is one of particular concern due to its strict fidelity to habitats. These dolphins inhabit shallow, nearshore waters that overlap almost entirely with zones of intense anthropogenic activity, including shipping lanes, dredging operations, and industrial discharge points (Jefferson et al., 2023). This habitat overlap ensures chronic, high-level exposure to the full spectrum of estuarine pollutants from PRE. Study analyzed blubber samples from stranded dolphins have revealed that the PRE population carries some of the highest recorded burdens of DDTs and other organochlorines in the world (Wei et al., 2025). These persistent pollutants not only impose prolonged oxidative stress on humpback dolphins but are also transferred to their calves, leading to high calf mortality rates and posing a serious threat to the long-term survival of the population (Parsons, 1998). Similarly, the Indo-Pacific finless porpoise, while preferring the more saline waters of the southern and eastern coastal water of Hong Kong, exhibits alarming levels of contamination. For example, tissues from stranded finless porpoises frequently contain high concentration of PFAS, halogenated flame retardants and organotins, suggesting

that these animals are living near the limits of their physiological tolerance.

Despite their value as sentinel species, dolphins and porpoise pose significant challenges for traditional ecotoxicological study (Bossart, 2011). Ethical, legal, and logistical constraints limit access to living tissues, experimental exposures are infeasible, and reliance on stranded individuals introduces uncertainty regarding cause of death and exposure history (Ochiai et al., 2020). These limitations have historically impeded mechanistic understanding of how contaminant mixtures affect cetacean health. While chemical monitoring provides valuable exposure data, it cannot reveal whether detected contaminants reach biologically relevant concentrations in specific tissues, nor can it identify mixture components driving observed toxic endpoints.

2.1.4. Species-specific cetacean cell models: a novel tool in marine toxicology

The development of cetacean-specific *in vitro* models represents a transformative advance in marine toxicology, directly addressing the ethical and logistical barriers that prohibit experimentation on living marine mammals (Ochiai et al., 2020). Over the past decade, researchers have successfully established immortalized fibroblast cell lines from the skin of cetaceans. These cell lines are derived from fresh tissue samples, typically obtained from stranded animals or non-lethal biopsies, and are immortalized to allow for continuous culture (Bjørneset et al., 2023; Hosen et al., 2023; Li et al., 2022; Otero-Sabio et al., 2022; Yajing et al., 2018). These cells retain the species-specific genetic background, karyotype, and basal metabolic characteristics of the donor animal, providing a biologically relevant platform for mechanistic toxicity testing.

2.2. Mixture Toxicity and Mechanistic Bioanalytical Advances

2.2.1. Evolution from single-compound toxicology to mixture understanding

The traditional paradigm of environmental toxicology has been dominated by evaluating the toxicity of individual chemicals in isolation. Substances identified as priority contaminants due to their persistence bioaccumulative potential, or known toxicity have become the basis of regulatory standards worldwide. Their safety thresholds are normally derived from dose-response curves specific to each attention contaminant (Backhaus & Faust, 2012). However, the limitations of this approach have become increasingly evident. In the realistic marine environment, cetaceans are not exposed to chemicals one at a time but are continuously immersed in complex chemical mixtures of anthropogenic pollutants and natural toxins (Escher et al., 2020). The complexity of chemical mixture renders individual chemical regulatory frameworks inadequate for assessing ecological outcomes. The simultaneous presence of tens of thousands of chemicals, even when each is present below its individual no observed effect concentration (NOEC), can elicit significant cumulative toxicity (Silva et al., 2002). Consequently, the field of ecotoxicology has undergone a necessary paradigm shift, moving from describing single-compound effects to modeling the joint action of chemical mixtures.

Historically, mixture modeling has been classed into two theoretical concepts: concentration addition (CA) and independent action (IA). CA assumes that chemicals in a mixture act via a similar mechanism of action, such as multiple estrogenic compounds binding to the same receptor. Under this model, the effects of individual components are additive. Conversely, IA applies to mixtures where components act on

different biological targets; here, the overall effect is calculated based on the probabilities of independent events (Escher et al., 2020). For decades, a central challenge in risk assessment was determining which model to apply to environmental mixtures of unknown composition. In a study involving over 200 designed mixtures, they demonstrated that the mathematical predictions of the full CA model and the full IA model converge and become statistically indistinguishable at effects below 10%. It provided a solid scientific justification for using CA model as a good approximations model for water quality assessment. This theoretical unification was crucial because it validated the assumption that the toxicity of complex mixtures could be assessed by summing the biological potencies of their components, laying the groundwork for toxic unit (TU) summation for quantifying and dissecting complex mixtures of contaminants in environments samples **(Jin et al., 2015b)**.

2.2.2. Emergence of bioanalytical methods for environmental mixture assessment

The purpose of studying the mixture toxicity of pollutants in seawater is to address a key question: to what extent can the observed effects in a water sample be explained by the known and detected chemical?

The integration of bioassays with chemical analysis has given rise to effect-directed analysis (EDA), a powerful investigative framework for identifying the specific drivers of toxicity in complex environmental samples (Hong et al., 2023). The EDA workflow typically begins with the biological testing of a whole environmental extract (e.g., organic extract of seawater). If toxicity is detected, the sample undergoes sequential fractionation based on physicochemical properties like polarity or molecular weight. These fractions are then re-tested to pinpoint which ones contain the toxic

activity. This iterative process of fractionation and bio-testing reduces the complexity of the mixture, the active components from the non-toxic background matrix will be isolated target (Escher et al., 2023). Finally, advanced analytical chemistry techniques are applied to active fractions to identify the key compounds.

This methodological development in the concept of iceberg (mixture) modeling, a mass-balance approach designed to quantify the known and unknown fraction of toxicity in a water, sediment or tissue sample (Xia et al., 2017). For non-specific endpoints like cytotoxicity or oxidative stress, TU summation is advocated. Unlike specific effects driven by high-potency ligands, non-specific toxicity is often driven by the total molar burden of all organic chemicals accumulating in biological membranes, known as baseline toxicity (Tang et al., 2013). Since there is no single specific reference compound for non-specific toxicity, the effect is best quantified as TUs, defined as the reciprocal of the effect concentration. For specific toxicity endpoints, such as estrogenicity or herbicide activity, the aggregate biological effect is expressed as a bioanalytical equivalent concentration (BEQ). This metric allows for a direct comparison between the biological response measured in a bioassay and the response predicted from targeted chemical analysis (Escher et al., 2018). Empirical applications of this model have consistently revealed that while targeted analysis can often explain a significant portion of specific effects (like estrogenicity), it explains only a minute fraction of non-specific toxicity and oxidative stress (Escher et al., 2013; Neale et al., 2015). This iceberg (mixture) modeling characterized the hazard present in the environments and provided a tool for advanced water quality management.

2.3. Linking External Exposure to Biological Relevance

2.3.1. Bridging exposure and effect through toxicokinetic

While chemical monitoring and bioassay-based toxicity testing provide valuable insights into contaminant occurrence and biological effects, they do not on their own reveal whether environmental levels of pollutants translate into meaningful internal exposures in marine mammals. The toxicological significance of a chemical depends not only on its concentration in seawater but also on the degree to which it is absorbed, distributed, metabolized, and ultimately accumulated within target tissues. For long-lived marine mammals such as cetaceans, evaluating internal exposure is particularly challenging due to the complexity of their physiology, their unique lipid-rich tissues, and the absence of controlled exposure data. Understanding these processes is essential for quantitative *in vitro* to *in vivo* extrapolation (QIVIVE), a computational framework designed to bridge the gap between environmental mixtures and realistic internal doses (Yoon et al., 2015). QIVIVE aims to calculate the external exposure level that would result in an internal tissue concentration equivalent to the bioactive concentration observed in vitro.

Central to QIVIVE is the use of physiologically based pharmacokinetic (PBTK) modeling. A PBTK model is a mathematical representation of an animal's anatomy and physiology, conceptualizing the body as a network of interconnected compartments (Krishnan & Peyret, 2009). These models are parameterized with species-specific physiological data, such as organ volumes, blood flow rates, and tissue lipid content, as well as chemical-specific data like partition coefficients and metabolic clearance rates. By simulating the movement of chemicals through this system, PBTK models allow for

reverse dosimetry, means back calculating the external exposure required to achieve a specific internal burden (Dogruer et al., 2021). This approach provides a mechanistic basis for risk assessment, moving beyond simple correlations between environmental levels and tissue residues.

Yet despite their utility, PBTK-QIVIVE frameworks for marine mammals remain rare, with most existing models developed for a few species and focused on a limited set of lipophilic legacy pollutants (Hickie et al., 1999; Weijs et al., 2010, 2013). The absence of models tailored to Indo-Pacific humpback dolphin, which experience chronically elevated exposure to complex contaminant mixtures, represents a substantial knowledge gap. Furthermore, integrating PBTK predictions with bioassay-derived toxicity endpoints has rarely been attempted in cetacean research, leaving the real-world implications of observed in vitro effects largely unresolved.

2.3.2. Relevance to cetacean dermal exposure

While dietary intake via biomagnification has long been considered the primary route of contaminant exposure for marine mammals, recent research necessitates a re-evaluation of the role of the skin. Cetacean's skin contains abundant lipids and structural proteins that may facilitate the uptake of certain contaminants (Menon et al., 2022). Moreover, cetaceans live in seawater and in direct contact with contaminants, their skin serves as the first line of defense for health. While legacy POPs are highly hydrophobic and partition strongly to sediment and food, many emerging contaminants, such as shorter-chain PFAS and certain flame retardants, exhibit moderate water solubility (Bargagli & Rota, 2024). This physicochemical property may facilitate their partitioning from the water phase into the lipid-rich epidermis. Furthermore, some anthropogenic chemicals can disrupt the skin's barrier function, effectively increase

physiological stress of cetaceans and open portals for infection by pathogens (Bressem et al., 2009; Takeshita et al., 2017). Therefore, ignoring the dermal route in exposure models may lead to a significant underestimation of the total chemical burden and health risk, particularly for animals inhabiting heavily polluted, shallow estuarine waters where surface contact with slick-associated contaminants is frequent. Bridging this gap is critical for interpreting mixture of toxicity results and for determining the ecological relevance of dissolved contaminants in coastal waters.

2.4. Integrating Non-target Screening and Machine Learning for Predictive Toxicity Identification

2.4.1. Non-target screening application in marine environment

The limitations of traditional targeted analysis are becoming increasingly apparent as the chemical complexity in marine environment. Targeted monitoring programs are designed to quantify the predefined list of known pollutants (Sobus et al., 2018). However, target analysis may ignore thousands of unknown chemicals which lack reference standards, structural annotation, or toxicological characterization. These unknown chemicals often contribute significantly to the mixture's overall toxicity. Transformation products, for instance, can sometimes be more persistent and toxic than the parent compound, yet they are rarely included in monitoring lists (Escher & Fenner, 2011). To address this issue, environmental chemistry is shifting towards non-target screening (NTS) using high-resolution mass spectrometry (HRMS). NTS techniques, such as Orbitrap mass spectrometry, acquire data across a broad mass range without pre-selection, generating a comprehensive digital archive of the sample's chemical composition. This approach reveals tens of thousands of features (molecular ions defined by mass and retention time) in a single seawater sample, providing a holistic

fingerprint of the chemical environment (Vosough et al., 2024). However, a large volume of features generated by NTS makes manual identification and toxicological assessment impossible, necessitating automated and intelligent data processing workflows.

2.4.2. The rise of machine learning in environmental toxicology

To navigate the massive datasets generated by NTS, machine learning (ML) and computational toxicology have emerged as indispensable tools. By leveraging large databases of chemical structures, physicochemical properties, and experimentally determined toxicological outcomes, ML models can infer potential bioactivity from structural fingerprints or predicted molecular descriptors. Early implementations using random forests or support vector machines established proof-of-concept approaches, demonstrating that statistical models trained on curated datasets could predict cytotoxicity, oxidative stress induction, or receptor activity with reasonable accuracy (Svetnik et al., 2003).

Recent advances in computational methods, such as deep neural networks (Mayr et al., 2016) and graph-based learning (Yang et al., 2019), further extend predictive capabilities to molecules with complex functional groups or atypical scaffolds, which commonly appear in environmental samples. These models learn from chemical structure–activity relationships in a high-dimensional feature space, enabling prediction of toxicological endpoints even for chemicals lacking close analogs in available datasets. As a result, ML approaches can ascribe provisional toxicological significance to non-target features, ranking them according to predicted hazard and highlighting those most likely to contribute to observed bioactivity (Arturi & Hollender, 2023a).

In marine systems, where chemical diversity is exceptionally high and toxicity

data for marine organisms are scarce, ML offers a practical solution for bridging the gap between chemical detection and biological interpretation. Importantly, ML models can be calibrated or validated against empirical toxicity data derived from species-specific cell assays. This capacity is particularly relevant for cetaceans, whose unique physiology and cellular characteristics diverge from conventional human or rodent models. By incorporating cetacean-specific toxicity benchmarks into ML workflows, predictions become more aligned with the biological responses of these species, facilitating more accurate identification of potentially harmful contaminants.

2.4.3. Integrating NTS and ML for toxicity driver identification

The integration of NTS and ML forms a comprehensive framework that transforms large-scale chemical profiling into biologically meaningful insights (Hong et al., 2023). NTS serves as the discovery engine, revealing the totality of detectable chemical features present in seawater. ML then acts as the interpretive layer, predicting which of these features are likely to elicit biological effects (Luo et al., 2024). When combined with empirical toxicity datasets generated from cetacean cell assays, these predictions infer connections between specific chemical signatures and observed toxic responses.

A central strength of this integrated approach lies in its ability to interrogate mixture effects without requiring structural identification of every detected feature. By ranking detected compounds according to predicted potency, a subset of high-priority candidates can be selected through narrowing the search space. These prioritized features can then be subject to manual or automated MS/MS fragmentation, computational formula generation, or spectral matching to refine structural hypotheses (Zweigle et al., 2025). In many cases, this process reveals that potent toxicity originates not from well-known pollutants but from previously unrecognized compounds or

transformation products that escape traditional monitoring efforts.

2.5. Summary and Outlook

This chapter constructs a review of the western Indo-Pacific region, especially Hong Kong as an ecosystem under siege, where resident cetaceans navigate a multi-stressor environment of exceptional complexity. The traditional toxicological paradigm, focused on the monitoring of legacy POPs and dietary exposure, is increasingly insufficient to capture the true risks posed by dynamic chemical cocktails. The convergence of massive industrial output, complex estuarine hydrodynamics, and eutrophication-driven algal blooms creates a scenario where Indo-Pacific humpback dolphin and finless porpoise are exposed to a synergistic barrage of neurotoxins, endocrine disruptors, and immunotoxicants.

The establishment of species-specific *in vitro* models has provided a critical methodological breakthrough, allowing for the mechanistic evaluation of these mixtures without the ethical constraints of *in vivo* testing. These models have revealed that the skin is not merely a barrier but a significant target organ and potential route of exposure, challenging the exclusive focus on biomagnification. Furthermore, the integration of high-resolution non-target screening with machine learning algorithms is transforming our ability to identify the unknown chemical pollution.

The integrated paradigm becomes particularly powerful when combined with toxicokinetic modeling. Candidate toxicity drivers identified through NTS-ML can be evaluated within cetacean-specific PBTK frameworks to assess whether their environmental concentrations are sufficient to reach biologically active levels in target tissues. This creates a unified exposure–hazard–effect approach that connects chemical occurrence, predicted toxicity, empirical cellular responses, and realistic internal doses.

In coastal environments like Hong Kong, where pollutants of diverse origins co-exist with algal toxins, this framework offers an unprecedented means of deciphering which contaminants are most likely to affect the health of resident cetacean populations.

3. Methodology

3.1. Collection of Seawater Samples and Preparation of Seawater Extracts

3.1.1. Sample collection

A total of 72 surface seawater samples were collected from Hong Kong coastal waters during two seasons: the wet season (August 2022) and the dry season (February 2023) (**Figure 3.** 1). At each sampling site, 500 mL of surface seawater was collected. The samples were stored in a 4 °C ice box, transported to the laboratory, kept in 4 °C cold storage, and processed within 24 h of collection. Sampling locations included mariculture zones, sewage outfalls, beaches, container terminals, freshwater inflows, and marine reserves. Detailed information about the sampling sites is provided in **Table 3. 1.**

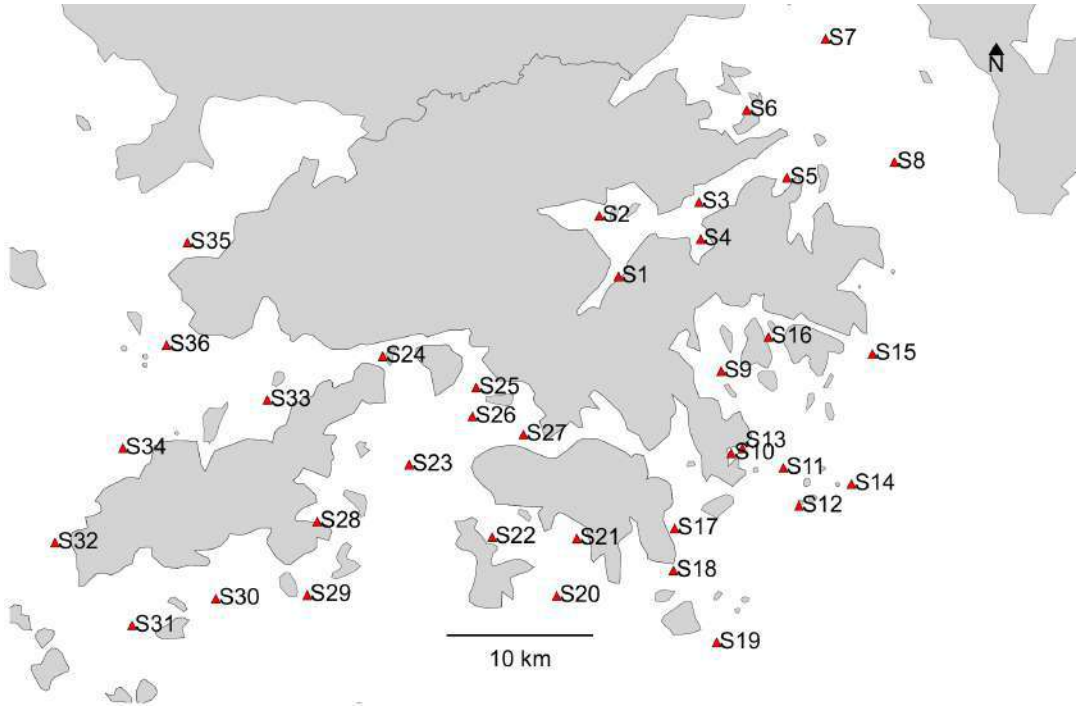

Figure 3. 1 Sampling sites during 2022 and 2023

Table 3. 1 Detailed information about the sampling sites

Site ID	Longitude (E)	Latitude (N)	Description
S1	114°13'6"	22°24'31"	
S2	114°12'18"	22°27'2"	Harbour
S3	114°16'27"	22°27'36"	
S4	114°16'31"	22°26'4"	Mariculture
S5	114°20'6"	22°28'37"	Marine reserve
S6	114°18'25"	22°31'25"	Mariculture
S7	114°21'42"	22°34'23"	
S8	114°24'34"	22°29'16"	
S9	114°17'22"	22°20'35"	
S10	114°17'47"	22°17'10"	Beach
S11	114°19'57"	22°16'34"	
S12	114°20'36"	22°14'59"	
S13	114°18'15"	22°17'22"	
S14	114°22'47"	22°15'54"	
S15	114°23'39"	22°21'18"	
S16	114°19'20"	22°22'0"	Mariculture
S17	114°15'26"	22°14'3"	Beach
S18	114°15'23"	22°12'18"	
S19	114°17'11"	22°9'19"	

Site ID	Longitude (E)	Latitude (N)	Description
S20	114°10'32"	22°11'15"	
S21	114°11'22"	22°13'38"	
S22	114°7'51"	22°13'41"	Mariculture
S23	114°4'24"	22°16'42"	
S24	114°3'18"	22°21'12"	Mariculture
S25	114°7'11"	22°19'54"	Container terminal
S26	114°7'2"	22°18'42"	Sewage treatment
S27	114°9'9"	22°17'57"	Harbour
S28	114°0'35"	22°14'20"	Mariculture
S29	114°0'10"	22°11'17"	
S30	113°56'22"	22°11'8"	
S31	113°52'53"	22°10'1"	
S32	113°49'41"	22°13'27"	
S33	113°58'30"	22°19'23"	
S34	113°52'30"	22°17'23"	
S35	113°55'11"	22°25'55"	Bay
S36	113°54'19"	22°21'40"	

3.1.2. Extraction

All seawater samples were filtered using glass microfiber filter (0.7 μm, Whatman). To capture a high level of bioactivity and a wide range of chemicals in water sample **(Zhou et al., 2024)**, the water samples were enriched with solid phase extraction (SPE) by Oasis HLB cartridges (200 mg sorbent, 6 mL, Waters, Medford, MA) stacked on top of a Supelclean coconut charcoal SPE tube (6 mL, 2 g, Sigma-Aldrich). The cartridges were preconditioned with 4 mL of ammonium hydroxide/methanol (3:1000, v:v) (Sigma-Aldrich, USA), 4 mL of methanol (Sigma-Aldrich, USA), and 4 mL of ultrapure MilliQ water sequentially. Then, 500 mL of sample was loaded onto each cartridge. Samples were loaded at a flow rate of 1 mL/min. Ultrapure water was included as a field blank. The cartridges were then rinsed with 4 mL of methanol/water (15:85, v:v) and dried by centrifuging at 3500 rpm for 2 minutes. After drying, the cartridges were eluted three times with 3 mL of ammonium hydroxide/methanol

(3:1000, v:v). The sample extracts were evaporated to dryness under a gentle nitrogen flow at a temperature of 40°C and immediately resuspended in 1 mL of Dulbecco's Modified Eagle Medium (DMEM). The relative enrichment factor (REF) was 500, which measured how much a sample needed to be enriched (REF > 1) or diluted (REF < 1) to achieve a given effect in the toxicity experiments

3.2. Establishment of Species-Specific Cetacean Fibroblast Skin Cell Lines and Cell Culture Conditions

3.2.1. Indo-Pacific finless porpoise fibroblast cell lines

The immortalized finless porpoise fibroblast cell line, named FPT was obtained through a collaboration between Shantou University. This cell line derived from skin samples of a finless porpoise founded stranded in Shantou, Guangdong province, mainland China.

3.2.2. Indo-Pacific humpback dolphin fibroblast cell lines

(1) Skin tissue collection

A small skin tissue sample of the Chinese white dolphin was collected at the back of an adult individual by biopsying in Zhanjiang city of mainland China. The skin tissue fragment was placed immediately into the centrifuge containing High Glucose Dulbecco’s modified Eagle’s medium (H-G DMEM), 10 % fetal bovine serum (FBS) and 1% antibiotics (penicillin (10000 U/mL) and streptomycin (10000 ug/mL)) and transported to laboratory at 4℃ within 2 h.

(2) Dermal processing

The skin tissue was washed twice with 70% alcohol and phosphate buffer saline (PBS, pH-7.2) in the 10 cm^2 culture dishes. During dissection of skin layers, epidermis, dermis, and blubber were separated. Then dermis specimens were cut into 1-3 mm^3 pieces using sterilized scalpel blades and tweezers in a culture dish. Approximately 3-4 fragments of skin tissue were distributed in each well of 6-well culture plate (Corning). Plates attached with skin fragments were inverted gently into a CO_2 incubator for at least 20 minutes until pieces were attaching tightly to the bottom of plate.

(3) Primary culture to sub-culture

After cell monolayer formation, the cells in 6-well plates were rinsed twice with PBS and detached by 0.25% trypsin-EDTA (Gibco). Suspended cells were counted by cytometer and an appropriate concentration of the seeding was transferred into new 25 cm2 flask, when confluency was observed at 80%-90% every 6-7 days. The primary cells culture was named CWD-pri.

(4) Cell immortalization

Transfection was carried out using Lipofectamine 3000 (Invitrogen) following the manufacturer's protocol. Three plasmids were introduced into Indo-Pacific humpback dolphin skin cell cultures. The pSV40LT-Puro plasmid encodes the Simian vacuolating virus 40 (SV40) large T antigen and a puromycin-resistance cassette. In addition, pCGFP and pCDsRed drive cytoplasmic expression of green fluorescent protein (GFP) and red fluorescent protein (RFP), respectively. For selection of stable clones expressing SV40 large T antigen, puromycin (Sigma; 1 μg/mL) was added to the complete medium 2 days post-transfection. After another 2 d later, the dead cells were removed, and the surviving cells were reseeded at 10^5 cells/ dish in complete medium

containing 1 μg/ml of puromycin for clonal growth.

For lentiviral infection, HEK293T cells were co-transfected with the transfer and packaging plasmids pSicoR, pMLg/pRRE, pRSV-REV, and pMD2. G. Viral particles were subsequently harvested, concentrated by ultracentrifugation, and used to infect CWD-pri cells. GFP expressions were examined using an inverted fluorescence microscope. To assess infection efficiency, 72 h post-infection, cells from three wells of a six-well plate were washed with PBS and trypsinized to generate a single-cell suspension. GFP-positive cells and total cells were then counted with a hemocytometer under an inverted fluorescence microscope. The resulting immortalized cell lines were designated CWDT.

3.2.3. Cell culture conditions

For primary cells, the formulations of growth medium were showed in **Table 3. 2**. In general, the culture medium comprised of (v:v) DMEM and Ham's F12 for passage-1 and 2. However, passage-3 and onwards the growth medium (40:60) of DMEM and Ham's F12 was supplemented respectively with 10% fetal bovine serum (FBS), 0.1mM nonessential amino acids, 2 mM/L glutamine, and antibiotics (100 U/ml penicillin, 100 μg/ml streptomycin). Moreover, in the first and second passages of the primary cell culture, 20% fetal bovine serum (FBS) is added to the medium. In the third and fourth passages, the serum concentration is reduced to 15% and eventually decreased to 10%. The attached tissue fragments/ cells were supplemented with 2 ml medium, which was replaced (1/3rd) every 48 h gently. The plates were incubated at 37 °C with 5% CO2 standard mammalian culture condition and cell growth was monitored at 12–24 h intervals by an inverted microscope.

For both cell lines, all cell lines cultured in the same complete medium (**Table 3.**

2). Culture medium consists of 45% high-glucose DMEM, 45% DMEM/F12, 10% FBS, 1.5% L-glutamine, 0.4% 200 μg m/L Geneticin, 1% essential amino acids, and 1% non-essential amino acids. The cell lines were maintained in an incubator under standard conditions at 37°C in a humidified atmosphere containing 5% CO_2.

Table 3. 2 Cell culture medium formulation of primary cell and cell line

Regents	Primary cell	Cell line
	500 mL (mL)	500 mL (mL)
Keratinocyte SFM	50	
H-G DMEM	150	225
F12/DMEM	150	225
FBS	100	50
L-Glutamine (200 mM)	15	7.5
Penicillin-Streptomycin (10,000 U/mL)	25	
MEM Amino Acids Solution (50X) and MEM Non-Essential Amino Acids Solution (100X)	5.5	2.5
Fibroblast growth factor	250 ug	
G418 antibiotic		0.8
Note: Final concentration of G418 = 200 μg/mL		

3.3.*In Vitro* Bioassays

3.3.1. Preparation for test compounds

Prior to the bioassays, test compounds were dissolved or reconstituted in methanol to prepare stock solutions, which were then serially diluted into 8 to 12 concentrations. The final concentration of methanol in the exposure medium was maintained at a maximum of 1% (*v*:*v*), and vehicle control was included in all bioassays to ensure that cytotoxicity, ROS and DNA damage were not compromised by the solvent. To assess the solubility limits of hydrophobic chemicals in the assay medium, it is important to consider the major phases relevant to chemical sorption: water, proteins, and lipids. The

concentration of a chemical in an *in vitro* bioassay medium (C_{medium}) can be estimated using equation 1. This estimation incorporates the aqueous concentration (C_w).The bovine serum albumin- and liposome-water partition coefficients (K_{BSAw} and K_{lipw}). The concentrations of proteins ($m_{protein}/V_{FBS}$) and lipids (m_{lip}/V_{FBS}) in the supplement fetal bovine serum (FBS), and the volume ratio of FBS and medium (V_{FBS}/V_{medium}).

Except for algal toxins, the highest test concentrations for all other compounds in the cell viability assays were determined using the C_{medium} calculated from Equation 1. Due to the high toxicity of algal toxins and the limited quantity and low stock concentrations of their standards, these compounds could not be tested at the same maximum concentrations. K_{BSAw} and K_{lipw} can be predicted by Equation 2 and 3, and $m_{protein}/V_{FBS}$ and m_{lip}/V_{FBS} were used based on literature data **(Jin et al., 2015a)**. Kow values were collected from literatures or predicted by EPI Suit^{TM} 4.11.

$$C_{medium}(M)=\frac{n_w(mol)+n_{protein}(mol)+n_{lip}(mol)}{V_{medium}(L)}$$

$$=C_w(M)+\frac{C_{potein}\left(\frac{mol}{kg}\right)\frac{m_{protein}\ (kg)}{V_{FBS}\ (L)}V_{FBS}\ (L)+C_{lip}\left(\frac{mol}{kg}\right)\frac{m_{lip}(kg)}{V_{FBS}(L)}V_{FBS}\ (L)}{V_{medium}\ (L)} \quad (1)$$

$$=C_w\left[1+\left(K_{BSAw}\frac{m_{protein}}{V_{FBS}}+K_{lipw}\frac{m_{lip}}{V_{FBS}}\right)\frac{V_{FBS}}{V_{medium}}\right]$$

$$\log K_{BSAw} = 0.71 \times \log K_{ow} + 0.42 \quad (2)$$

$$\log K_{lipw} = 1.01 \times \log K_{ow} + 0.12 \quad (3)$$

3.3.2. Cytotoxicity assay

Test compounds were dissolved or reconstituted in methanol to prepare stock solutions, which were then serially half-diluted into 8 to 12 concentrations based on the

calculated Cmedium. The 3-(4,5-Dimethylthiazol-2-yl)-5-(3-carboxymethoxyphenyl)-2-(4-sulfophenyl)-2H-tetrazolium (MTS) colorimetric assay was used to assess cell viability. Cells were seeded at a density of 5×10^4 cells/mL in 96-well plates and allowed to grow to confluence for 24 hours. After removing the medium, the cells were exposed to 100 µL of each individual chemical or seawater extract in medium. Following 24 hours of exposure, the medium was removed, and 100 µL of phenol red-free DMEM containing 20 µL of MTS solution was added to the cells. After 2 hours of incubation at 37°C, the absorbance was measured using an automated microplate reader at 490 nm.

3.3.3. Intracellular ROS assay

Intracellular ROS generation induced by seawater extracts was determined using a 2',7'-dichlorofluorescein diacetate (DCFHDA) assay, following the protocol provided in the ROS assay kit manual. Briefly, cells were seeded at a density of 2×10^5 cells m/L in black 96-well plates and allowed to grow to confluence for 24 hours. After removing the medium, the cells were washed with 100 µL per well of buffer (provided by the kit). The buffer was then removed, and the cells were stained by adding 100 µL per well of a 20 µM DCFHDA solution. The cells were incubated with the DCFHDA solution for 45 minutes at 37 °C in the dark. Following this, 100 µL per well of buffer containing 10% FBS and seawater extracts at a highest REF of 250 were added. After 24 hours of exposure, fluorescence intensity was measured using an automated microplate reader at excitation/emission wavelengths of 485/535 nm. ROS production was expressed as the induction ratio (IR), calculated as the fluorescence signal of the sample relative to the control after 24 hours.

3.3.4. DNA oxidative damage

DNA oxidative damage was quantified by measuring 8-hydroxy-2'-deoxyguanosine (8-OHdG) in culture supernatants using a competitive ELISA kit (DNA Damage Competitive ELISA Kit, Thermo Fisher Scientific, EIADNAD), following the manufacturer's instructions. The concentration of 8-OHdG was quantified in the culture supernatant rather than the intracellular fraction. This approach was adopted because 8-OHdG, once excised from the DNA by repair mechanisms, is transported out of the cell and remains stable in the extracellular environment. After chemical exposure, cell culture media were collected and centrifuged at 1,000 × g for 20 min at 4°C to remove debris, and the clarified supernatants were stored at −80°C until analysis. Prior to the assay, all samples were gently thawed and diluted four-fold with the kit-provided Assay Buffer to ensure readings fell within the quantifiable range. All reagents were equilibrated to room temperature before use. Standards (0–8000 pg/mL) were prepared by reconstituting the 8-OHdG standard and performing serial two-fold dilutions. For each assay, 50 µL of standard or diluted sample was added to each well, followed immediately by 25 µL of 8-OHdG conjugate and antibody. Plates were incubated for 2 hours at room temperature with shaking, washed four times, incubated with 100 µL TMB Substrate to each well for 30 min at room temperature without shaking, then stopped with 50 µL stop solution. Absorbance at 450 nm was recorded within 10 min. Sample concentrations were determined using a four-parameter logistic standard curve and multiplied by the dilution factor to obtain final 8-OHdG levels.

3.3.5. Toxic potency calculation

Cell viability was expressed as the ratio of absorbance in treatment groups relative to controls within the same plate. Concentration-effect curves from cell viability assays were fitted using a non-linear regression model of the best-fit logarithmically

transformed concentration with GraphPad Prism 10 (GraphPad Software, USA). The effect concentration at which 10% of the exposed cells exhibit a notable effect from samples ($IC_{10,\ sample}$) and each chemical ($IC_{10,\ i}$). ROS and 8-OHdG production were quantified as the induction ratio (IR) of the treatment groups relative to the control within the same plate (equation 4). A fitted linear concentration-effect curve with an interception of 1 and a fitted slope (equation 5) was used to estimate the $EC_{IR1.5}$ (equation 6). $EC_{IR1.5}$ defined as the concentration producing a 1.5-fold in ROS signal or 8-OHdG formation from samples ($EC_{IR1.5,\ sample}$) and each individual contaminant ($EC_{IR1.5,\ i}$).

$$IR = \frac{fluorescence_{sample}}{fluorescence_{control}} \quad (4)$$

$$IR = 1 + slope \times concentration \quad (5)$$

$$EC_{IR1.5} = \frac{0.5}{slope} \quad (6)$$

3.4. Chemical Analysis

3.4.1. Target analysis

Detailed physicochemical characteristics of the target compounds are provided in **Table 3.** 3. The selection of the 38 target chemicals was guided by the following steps. First, priority chemical classes were identified by referring to the routine marine water quality monitoring program established by the Hong Kong Environmental Protection Department. Second, a literature review covering the past 20 years of environmental monitoring data in Hong Kong was performed (K. K. Y. Ho et al., 2016; Huang et al., 2015; J. Liu et al., 2022; Tsui et al., 2019; Q. Wang et al., 2019). For each identified chemical type, the top ten compounds exhibiting the highest reported environmental concentrations were prioritized for analysis. Individual solutions of each analyte were

prepared in pure methanol. The analysis of the studied chemicals followed previously established procedures with slight modifications11,14–16. Separation and quantification of target chemicals in sample extracts were performed using an ExionLC UHPLC system (Sciex, Foster City, CA, USA), equipped with an ACQUITY UPLC BEH C18 Column (2.1 mm × 50 mm, particle size: 1.7 µm, Waters, Medford, MA, USA). The column was maintained at 40°C. A gradient mobile phase of ammonia in Milli-Q water (solvent A, pH = 11) and ammonia in acetonitrile/Milli-Q water (90:10, solvent B, pH = 11) was used. At a flow rate of 0.5 mL min-1, the gradient condition (starting with 5% solvent B) increased to 45% at 3.5 minutes, followed by a linear increase to 55% at 6.5 minutes, and finally to 100% at 7.5 minutes. After holding at 100% for 1 minute, the gradient was returned to its original condition at 9.5 minutes and held for 2 minutes. The total run time was 11.5 minutes. For each sample, 10 µL was injected, and sample illumination in the autosampler was turned off during analysis. A Sciex 6500+ Liquid Chromatography/Electrospray Ionization - 6500+ QTRAP mass spectrometer (Sciex, Foster City, CA, USA) equipped with an ESI interface was used for MS analysis. Instrumental data were acquired and processed using Analyst 1.6.3 software (Sciex, Foster City, CA, USA). For each target compound, two product ions from the precursor ions were monitored for qualitative analysis, with the more intense ion used for quantification. Along with retention times, the precursor ion and the two product ions were used to ensure accurate peak identification.

Table 3. 3 Details of each studied chemical.

No.	Category	CAS number	Chemicals	Abbreviation	$logK_{ow}$	MW (g mol^{-1})
1	PAHs	91-20-3	Naphthalene	NAP	3.3	128.17
2		208-96-8	Acenaphthylene	ANA	3.93	152.19
3		85-01-8	Phenanthrene	PHE	4.46	178.23
4	PFAS	83329-89-9	8:2 Cl-polyfluorinated ether sulfonic acid	8:2 Cl-PFESA	6.58	670.69

No.	Category	CAS number	Chemicals	Abbreviation	$logK_{ow}$	MW (g mol^{-1})
5		73606-19-6	6:2 Cl-polyfluorinated ether sulfonic acid	6:2 Cl-PFESA	5.42	570.67
6		1763-23-1	Perfluorooctanesulfonic acid	PFOS	4.49	500.13
7		375-73-5	Perfluorobutanesulfonic acid	PFBS	1.82	300.1
8		335-67-1	Perfluorooctanoic acid	PFOA	4.81	414.07
9		2706-90-3	Perfluoropentanoic acid	PFPeA	1.98	264.05
10		375-22-4	Perfluorobutanoic acid	PFBA	1.43	214.04
11		21245-02-3	Octyl dimethyl-p-aminobenzoic acid	ODPABA	5.77	277.4
12		36861-47-9	4-methylbenzylidene camphor	4-MBC	5.47	254.4
13		5466-77-3	Ethylhexyl methoxycinnamate	EHMC	5.8	290.4
14	UV filters	6197-30-4	Octocrylene	OC	6.88	361.5
15		131-57-7	Benzophenone-3	BP-3	3.79	228.24
16		118-60-5	Ethylhexyl salicylate	EHS	5.97	250.33
17		4065-45-6	Benzophenone-4	BP-4	0.89	308.31
18		118-56-9	Homosalate	HMS	6.16	262.34
19		78111-17-8	Okadaic acid	OA	5.05	805
20		81720-10-7	Dinophysistoxin-1	DTX-1	6.88	819
21		139933-46-3	Dinophysistoxin-2	DTX-2	5.61	805
22	Algal	112514-54-2	Yessotoxin	YTX	9.66	1143.4
23	toxins	214899-21-5	Azaspiracid-1	AZA1	7.54	842.1
24		265996-92-7	Azaspiracid-2	AZA2	8.18	856.1
25		97564-91-5	Pectenotoxin-2	PTX-2	6.47	857
26		173792-58-0	Gymnodimine	GYM	6.64	507.7
27		85721-33-1	Ciprofloxacin	CPFX	0.28	331.34
28		70458-96-7	Norfloxacin	NFL	0.46	319.33
29		82419-36-1	Ofloxacin	OFL	-0.39	361.4
30		63527-52-6	Cefotaxime	CTX	0.64	455.5
31		26787-78-0	Amoxicillin (>90%)	AMOX	0.87	365.4
32	Antibiotics	24390-14-5	Doxycycline-d3 Hyclate	DOX	-1.4	444.4
33		64-72-2	Chlortetracycline hydrochloride	CTC	-0.326	515.3
34		68-35-9	Sulfadiazine	SUL	-0.09	250.28
35		723-46-6610	Sulfamethoxazole	SMX	0.89	253.28
36		114-07-8	Erythromycin	ETM	3.06	733.9
37		81103-11-9	Clarithromycin	CLA	3.16	748
38		80214-83-1	Roxithromycin	ROX	2.75	837

3.4.2. Non-target screening

Chromatographic separation was conducted on an ACQUITY UHPLC BEH C18 analytical column (2.1 × 100 mm, 1.7-μm particle size, Waters Corporation, Milford, MA). A binary gradient elution was applied at a flow rate of 0.3 mL min-1, with mobile phase A of 0.1% formic acid in water and mobile phase B of 0.1% formic acid in acetonitrile. A gradient elution was performed as follows: 0–3 min, 30%–60% mobile phase B; 3–8 min, 60%–99% mobile phase B; 8–12 min, held at 99% mobile phase B; 12–12.1 min, 98%–30% mobile phase B; and held at 30% mobile phase B for 3 min. The total run time was 15 min. The injection volume was 3 μL. The Orbitrap IQ-X mass spectrometer was equipped with an electrospray ionization (ESI) source. Mass spectra of all samples were acquired in ESI (–) and (+) modes in the mass range between m/z 40 and 1200 with a resolving power of 120,000 for MS and a resolving power of 30,000 for data-dependent MS/MS mode. The elemental compositions of the ions were determined with the Compounds Discoverer software v3.3 using a mass tolerance of $\pm$ 10 ppm. A threshold intensity value of 1×10^5 arbitrary was applied to all measurements. The molecular formulas were presented as CcHhOoNnSs, where c, h, o, n, s was the number of carbons, hydrogen, oxygen, nitrogen, and sulfur atoms, respectively. The formulas were calculated with $c \leq 50$, $h \leq 200$, $o \leq 50$, $n \leq 7$ and $s \leq 4$. To eliminate the chemically unreasonable formulas, the identified formulas were constrained by setting $0.3 \leq H/C \leq 3.0$, $0.0 \leq O/C \leq 3.0$, $0.0 \leq N/C \leq 1.3$, and $0.0 \leq S/C \leq 0.8$. The resulting neutral formulas with a non-integer or negative double bond equivalent (DBE) or elemental composition which disobey the nitrogen rule for even electron ions were also removed. The DBE value was calculated as $(2c + 2 - h + n)/2$. The compounds in samples were compared to those in blanks, and only compounds with a sample-to-blank abundance ratio larger than 10 were retained for further data analysis. The collected MS (Mass Spectrometry) and MS/MS (Tandem Mass Spectrometry) spectra were submitted to the Compound Discoverer software

(v3.3, Thermo Fisher Scientific) for further compound identification with various databases, including mzCloud, ChemSpider, MassBank, and NIST, to infer potential chemical structures. A manual selection process filtered out compounds with spectral match confidence exceeding 85%. Compounds were then categorized based on functional groups to compile a list of potential chemical structure information. Then compounds with available data were deleted for machine learning analysis.

3.5. Machine Learning

3.5.1. Preparation of the Training Dataset

The curated toxicity dataset, containing IC_{10} (cytotoxicity) and $EC_{IR1.5}$ (ROS induction and DNA damage) measured in CWDT, was used as the training dataset. Each compound was annotated with structural descriptors derived from the SMILES column, including molecular weight (MW), LogKow, TPSA, hydrogen-bond donors (HBD), hydrogen-bond acceptors (HBA), rotatable bond count, aromatic ring count, and formal charge, all computed using RDKit (v2023.09). To ensure compatibility with Orbitrap non-target descriptors, analytical features analogous to non-target measurements were also included: precursor mass-to-charge ratio, chromatographic retention time (RT), ionization mode, and precursor adduct information (Adduct).

Measured IC_{10} and $EC_{IR1.5}$ values were converted to molar concentrations and transformed into continuous regression targets using equation 7:

$$\text{Label} = -\log_{10} IC_{10} \text{ or } EC_{IR1.5} \quad (7)$$

Entries flagged as censored (CensorFlag = ">") were excluded from model fitting. The complete dataset therefore consisted of harmonized structural and analytical descriptors alongside transformed toxicity labels, forming the feature matrix used for model development.

3.5.2. Model Training and Cross-Validation

Random forest (RF) models were implemented in Python using the scikit-learn library (v1.4.0). Separate models were constructed for cytotoxicity, ROS induction, and DNA damage. To validate the predictive ability of the models and minimize overfitting, a five-fold cross-validation (CV) strategy was applied.

For each fold, the dataset was randomly partitioned into a training set (80%) and test set (20%). To ensure all samples belonging to the same compound, compounds were identified through InChIKey and assigned to the same fold to avoid information leakage. This process was repeated five times so that each sample appeared in the test set exactly once and, in the training, set at least once. After model construction for each fold, the predicted toxicity values were compared with the experimentally measured labels to evaluate generalization performance.

Model optimization followed standard RF procedures. The number of variables randomly sampled at each split (analogous to mtry) was tuned through grid search, while the number of trees (ntree) was selected based on the convergence of the out-of-bag error estimate. Model accuracy was evaluated using the root mean square error (RMSE), mean absolute error (MAE), and coefficient of determination (R^2).

3.5.3. Pre-Processing and Feature Extraction of Orbitrap Non-Target Data

Non-target chemical features were processed using Thermo Compound Discoverer. Each feature included precursor mass-to-charge ratio, RT, theoretical molecular formula, calculated MW, and precursor ion information.

Signal intensity fields (Area (Max.), Peak Rating: S#raw, Area: S#raw) were used to derive abundance-normalized metrics, blank-to-sample intensity ratios, and detection

frequency across samples. Missing continuous variables were imputed using median values, and missing categorical variables were assigned an “Unknown” category.

3.5.4. Prediction, Feature Ranking, and Model Interpretation

The optimized RF models were applied to the pre-processed non-target dataset to generate predicted toxicity values for each detected feature. Variable importance was quantified using permutation-based importance measures, calculated as the increase in mean squared error (IncMSE) when the values of a given feature were randomly shuffled. To further prioritize suspect toxicants, recursive feature elimination (RFE) was applied to identify the minimal subset of descriptors capable of maintaining predictive performance.

High-scoring non-target features were subsequently inspected through MS^2 fragmentation patterns, 80% spectral library matching (e.g., mzCloud), Schymanski level assignment, abundance characteristics, and environmental distribution to identify probable toxicants in the seawater chemical mixture.

3.6. Development of Physiologically Based Toxicokinetic (PBTK) model of Chinese White Dolphin

3.6.1. Model development

The refined PBTK model of monitored chemicals, consisting of five compartments, including blood, skin, blubber, liver and kidney, is displayed in **Figure 3.** 2. The following differential equations describe chemical balance across the five compartments.

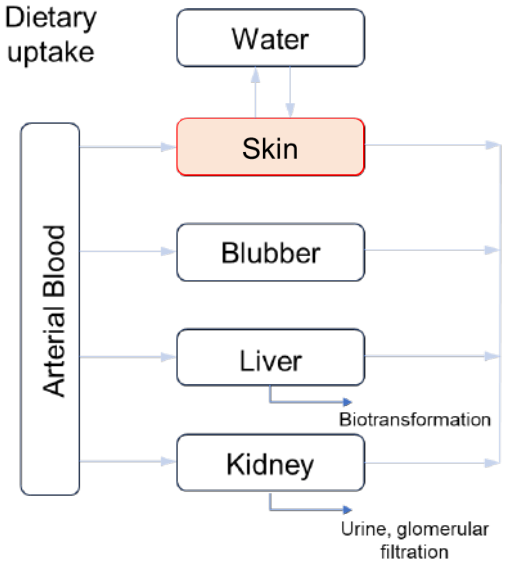

Figure 3. 2 Schematic representation of the refined physiologically based toxicokinetic (PBTK) model developed for monitored chemicals.

$$\frac{dC_{blood}}{dt}=\frac{1}{V_{blood}}\left[Q_{bsk}\left(\frac{C_{sk}}{P_{skb}}-C_{blood}\right)+Q_{fat}\left(\frac{C_{fat}}{P_{fab}}-C_{blood}\right)+Q_{liver}\left(\frac{C_{liver}}{P_{liver}}-C_{blood}\right)+Q_{kidney}\left(\frac{C_{kidney}}{P_{kidney}}-C_{blood}\right)\right] - \frac{Q_{gfr}(1-\phi)f_{ub,plasma}}{V_{blood}}C_{blood}+\frac{ADI}{V_{blood}} \quad (8)$$

$$\frac{dC_{sk}}{dt}=\frac{Q_{bsk}}{V_{sk}}\left(C_{blood}-\frac{C_{sk}}{P_{skb}}\right)+\frac{K_pA_{ex}}{C_fV_{sk}}\left(C_{water}-\frac{C_{sk}}{P_{skw}}\right) \quad (9)$$

$$\frac{dC_{fat}}{dt}=\frac{Q_{fat}}{V_{fat}}\left(C_{blood}-\frac{C_{fat}}{P_{fab}}\right) \quad (10)$$

$$\frac{dC_{liver}}{dt}=\frac{Q_{liver}}{V_{liver}}\left(C_{blood}-\frac{C_{liver}}{P_{liver}}\right)-\frac{CL_{liver}}{V_{liver}}C_{liver} \quad (11)$$

$$\frac{dC_{kidney}}{dt}=\frac{Q_{kidney}}{V_{kidney}}\left(C_{blood}-\frac{C_{kidney}}{P_{kidney}}\right) \quad (12)$$

The symbols and parameters appearing in equations 8–12 represent physiological properties, transport processes, and chemical-specific characteristics governing the distribution and elimination of contaminants in the five-compartment PBTK model.

C_{blood}, C_{sk}, C_{fat}, C_{liver}, and C_{kidney} denote the chemical concentrations (mg/L) in arterial blood, skin, blubber (fat), liver, and kidney, respectively. V_{blood}, V_{sk}, V_{fat}, V_{liver}, and V_{kidney} are the physiological volumes (L) of the corresponding compartments. Q_{bsk}, Q_{fat}, Q_{liver}, and Q_{kidney} represent the volumetric blood flow rates (L/h) from arterial blood into the skin, blubber, liver, and kidney compartments. Exchange between the skin and blubber compartments is described by Q_{skf} (L/h), which reflects combined perfusion- and diffusion-driven mass transfer across the dermal–subcutaneous interface.

Partitioning of chemicals between blood and individual tissues is governed by tissue: blood partition coefficients, including P_{skb} (skin–blood), P_{fat} (fat–blood), P_{liver} (liver–blood), and P_{kidney} (kidney–blood). These coefficients account for compound-specific solubility in lipids, proteins, phospholipids, and water, and determine the equilibrium distribution of chemicals across physiological compartments. Dermal exchange with ambient seawater is represented by P_{skw} (skin–water partition coefficient), in conjunction with the permeability coefficient K_p (cm h^{-1}), exposed surface area A_{ex} (cm^2), and unit conversion factor $C_f = 1000\ cm^3\ L^{-1}$. C_{water} denotes the concentration of the chemical in seawater (mg/L) that drives dermal uptake.

Metabolic and renal elimination are incorporated explicitly into the model. Hepatic biotransformation is parameterized using the intrinsic hepatic clearance CL_{liver} (L/h), derived from in vitro or QSAR-predicted intrinsic clearance data. Renal filtration is described by the glomerular filtration rate Q_{gfr} (L/h), the unbound fraction of chemical in plasma $f_{ub,plasma}$, and the tubular reabsorption fraction φ. Together, these parameters determine the fraction of filtered chemical that is excreted from the kidney versus reabsorbed back into systemic circulation. For scenarios involving continuous external exposure, the term ADI/V_{blood} represents an absorbed dose input (mg/h/L)

added directly into the arterial blood pool.

Together, these physiological and chemical-specific parameters establish a mechanistic framework that characterizes uptake, systemic distribution, metabolic transformation, dermal exchange, and renal clearance of contaminants in the skin-focused PBTK model developed for the Indo-Pacific humpback dolphin. The uptake of all monitored chemicals in an adult Chinese white dolphin occurs mainly through food intake. The main food sources are fish and some crustaceans. For diet, the average daily input (ADI) express in ng chemicals per day, was calculated by the following equation 13:

$$ADI = DC \times C_{diet} \times AE \quad (13)$$

$DC = 0.12 \times BW^{0.80}$ (kg/day) is the daily consumption (g/day), it depends on the body weight. In this study, an adult Chinese white dolphin's weight was regarded as 200 kg. C_{diet} is the concentration of each monitored chemicals in the diet. All input data were obtained from published studies conducted in the South China Sea (including Hong Kong). The concentrations of all chemicals were measured in fish species except for DBT, which was quantified in Rock shell. Detailed information is summarized in **Table 3.** 4. AE is assimilation efficiency. All AE of 90% of the total amount of each chemical ingested is used for the actual uptake (Weijs et al., 2010).

Table 3. 4 Summary of chemical concentrations accumulated in food used for PBTK model parameterization. All data were obtained from published studies conducted in the South China Sea (including Hong Kong), LOD: limit of detection.

Compounds	Concentration (ng/g)	Species
PFBA	13.41	Fish
PFPeA	2.13	Fish
PFOA	0.231	Fish

Compounds	Concentration (ng/g)	Species
PFBS	0.02	Fish
ODPABA	< LOD	Fish
EHMC	< LOD	Fish
OC	16.9	Fish
BP-3	3.9	Fish
BDE-209	0.875	Fish
Ace	1.81	Fish
Phe	23.59	Fish
Nap	< LOD	Fish
4-MBC	8.40	Fish
HMS		No reported
EHS		No reported
BP-4		No reported
PTX-2	0.012	Fish
OA	0.360	Fish
DTX-1	0.033	Fish
GYM	0.016	Fish
PFOS	5.58	Fish
6:2 Cl-PFESA	< LOD	Not detected in
8:2 Cl-PFESA	< LOD	Not detected in
DBT	5.8	Rock shell

3.6.2. Parameters

(1) Partitions between tissue and blood ($P_{tissue:blood}$)

The partition coefficients of individual chemical for tissues (skin, blubber, liver and kidney) were calculated as the following equation 14:

$$P_{tissue:blood}=\frac{K_{lipid\text{-}water}\times Fl_t+K_{protein\text{-}water}\times Fp_t+K_{phospholipid\text{-}water}\times Fm_t+Fw_t}{K_{lipid\text{-}water}\times Fl_b+K_{protein\text{-}water}\times Fp_b+K_{phospholipid\text{-}water}\times Fm_b+Fw_b} \quad (14)$$

$\boldsymbol{K}_{lipid–water}$, $\boldsymbol{K}_{protein–water}$, and $\boldsymbol{K}_{phospholipid–water}$ denote the lipid–water, protein–

water, and phospholipid–water partition coefficients, which describe the compound's affinity for neutral lipids, structural proteins, and phospholipid membranes, respectively. The terms $\boldsymbol{F_{l,t}}$, $\boldsymbol{F_{p,t}}$, $\boldsymbol{F_{m,t}}$, and $\boldsymbol{F_{w,t}}$ are the fractional volumes of neutral lipids, proteins, phospholipids, and water in the tissue, whereas $\boldsymbol{F_{l,b}}$, $\boldsymbol{F_{p,b}}$, $\boldsymbol{F_{m,b}}$, and $\boldsymbol{F_{w,b}}$ represent the corresponding fractions in blood.

For PFAS, these partition values were obtained from experimentally measured values reported in the literature **(Allendorf et al., 2019; Chen et al., 2025; Droge, 2019)**. Partitioning into proteins and phospholipids can be correlated with octanol-water partition coefficients. Therefore, for other chemicals estimated using the following empirical equations 15–17:

$$\log K_{\text{phospholipid-water}} = 1.01 \times \log \text{Dow} + 0.12 \quad (15)$$

$$\log K_{\text{protein-water}} = 0.73 \times \log D_{ow} - 0.39 \quad (16)$$

$$K_{\text{lipid-water}} = D_{ow} \quad (17)$$

D_{ow} is the octanol-water distribution ratio of each chemical, predicted by OPERA 2.9 model.

(2) Partitions between skin and water (P_{skw})

Due to lake of experimental data, we assume that the skin of Chinese white dolphin is similar to human skin and there for contains a stratum corneum. The P_{skw} was estimated using relating the stratum corneum/water partition coefficient 16:

$$P_{\text{skin:water}} = K_{\text{lipid-water}} \times Fl_s + K_{\text{protein-water}} \times Fp_s + K_{\text{phospholipid-water}} \times Fm_s + Fw_s \quad (18)$$

(3) Permeability coefficient (K_p)

For neutral hydrophobic organic chemicals, we predicted them by EPIWEB. For neutral hydrophilic chemicals (equations 19–22), Berge (2010) “SKINPERM” (cm/h) model.

$$\mathrm{Log}K_p=\log\left[\frac{1}{\frac{1}{K_{LIP}+K_{POL}+\frac{1}{K_{AQ}}}}\right] \tag{19}$$

$$\mathrm{Log}K_{LIP}=-2.69+0.981\cdot\mathrm{log}Kow-0.0079MW \tag{20}$$

$$K_{POL}=\frac{0.0552}{MW^{1.38}} \tag{21}$$

$$K_{AO}=\frac{1121}{MW^{1.96}} \tag{22}$$

KPOL is the permeation coefficient of the protein fraction of stratum corneum. KAQ is the permeation coefficient of watery dermal layer. KLIP is the permeation coefficient of the lipid medium. MW is the molecular weight (g/mol) of each chemical.

(4) Tissue blood flow rate

The blood flow through the tissues were represented by the cardiac output and given in **Table 3.** 5. Then the cardiac output of marine mammals was treated as a function of body weight using empirical formulas (equation 23–24).

$$Q_{cardiac}=0.1017BW^{0.9988} \tag{23}$$

$$Q_{tissue}=Q_{cardiac}\times T_i \tag{24}$$

(5) Tisue Volume

Volume was calculated by mass and density of tissues (equation 25–30).

Compartment mass was calculated through body weight. Because no empirical measurements of cetacean skin density exist, the skin volume could not be derived from mass. Instead, it was estimated using the reported skin thickness (4 mm) and body surface area (28000 cm^2) ratio from cetacean anatomical studies. Compartment parameters dependent on the body was given in **Table 3.** 5.

$$M_{blubber}\ (g) = 18.41 \times BW^{0.607} \quad (25)$$

$$M_{brain}\ (g) = 49.20 \times BW^{0.211} \quad 26)$$

$$M_{liver}\ (g) = 0.060 \times BW^{0.932} \quad (27)$$

$$M_{kidney}\ (g) = 0.002 \times BW^{1.137} \quad (28)$$

$$M_{blood}\ (g) = 0.143 \times BW \quad (29)$$

$$\text{Volume (L)} = \frac{M_{tissue}}{\rho} \quad (30)$$

Table 3. 5 Parameters used for PBTK model calibration of adult Chinese white dolphin.

Parameter	Value
Body weight (BW), kg	200
Fractional blood flow (%)	
To blubber	5%
To liver	25%
To kidney	19%
To skin	51%
Cardiac output (Qc, L/hr)	
Q_c (total cardiac output)	20.2
$Q_{blubber}$	1.01
Q_{liver}	5.05
Q_{kidney}	3.84
Q_{skin}	10.3
Density (ρ, g/L)	

Blubber	920
Liver	1040
Kidney	1050
Blood	1068
Skin	—

(6) Liver clearance

Liver clearance was calculated by the following equation 31:

$$CL_{liver}=\frac{\ln 2}{t_{1/2}}\times[(V_{liver}\times P_{liver:blood})+V_{blood}] \quad (31)$$

$t_{1/2}$ refers to the elimination of half-life of the contaminant (h). The half-life values for all chemicals were obtained from the literature, as shown in **Table 3.** 6.

Table 3. 6 Elimination half-lives ($t_{1/2}$, h) of monitored contaminants used in the PBTK model.

Compounds	$t_{1/2}$ **(h)**	**Compounds**	$t_{1/2}$ **(h)**
PFBA	55.2	4-MBC	15.0
PFPeA	12.0	HMS	46.9
PFOA	2.39E+04	EHS	8.00
PFBS	1032	BP-4	19.0
ODPABA	360	PTX-2	69.6
EHMC	0.80	OA	127
OC	43.9	DTX-1	139
BP-3	19.0	GYM	33.2
BDE-209	21.6	PFOS	4.12E+04
ACE	14.0	6:2 Cl-PFESA	429240
PHE	7.70	8:2 Cl-PFESA	134028
NAP	4.00	DBT	72.0

Renal reabsorption efficiency (φ) (equation 32).

$$\varphi=(1-\frac{0.06}{Q_{gfr}})\times\frac{Papp_{caco2}^{2.7}}{(34.4\times10^{6})^{2.7}+Papp_{caco2}^{2.7}} \quad (32)$$

$Papp_{caco2}$ values are predicted by OPERA 2.9 model.

3.6.3. Sensitivity analysis

Sensitivity analysis was performed to identify the model parameters that exert the greatest influence on the predicted outcomes. Each input parameter was varied by +5% and –5% from its original value while all other parameters were held constant, and the PBTK model was rerun for each perturbed value (equation 33). The effect of parameter variation on model predictions was quantified using equation, based on changes in the area under the blood concentration–time curve (AUC). Blood was selected as the evaluation compartment because it serves as the central circulating medium linking all model compartments; therefore, any change in contaminant concentration in a specific tissue is ultimately reflected in the blood.

$$S_c=\left(\frac{AUC_5}{AUC_{orig}}-1\right) \quad (33)$$

where S_c represents the sensitivity coefficient (%); $AUC_{orig}$is the area under the blood concentration–time curve obtained using the original parameter value; and AUC_5 is the area obtained when the parameter is increased or decreased by 5%. According to the WHO/IPCS (2010) guidance, $|S_c|\geq0.5$ indicates high sensitivity, $0.2\leq|S_c|<0.5$ indicates medium sensitivity, and $0.1\leq|S_c|<0.2$ indicates low sensitivity.

3.7. Mixture-Toxicity Modeling and Risk Assessment

3.7.1. Derivation of the freely dissolved concentration in cells

The mass balance of a chemical spiked into a cell-based assay is governed by its equilibrium distribution among (1) the aqueous phase, (2) FBS-derived lipid and protein, and (3) intracellular constituents. The total mass of chemical added to the system can therefore be expressed as equation 34:

$$M_{total}=M_w+M_{FBS}+M_{cell} \quad (34)$$

where M_w, M_{FBS}, and M_{cell}denote the masses in the aqueous medium, the FBS components, and the cells, respectively (ng).

The mass in the aqueous phase is given by equation 35:

$$M_w=C_w V_{w,in+out} \quad (35)$$

where $C_w$is the freely dissolved concentration in water (ng/L), and $V_{w,in+out}$ is the combined extracellular and intracellular water volume (L).

Chemical associated with FBS consists of lipid-bound and protein-bound fractions. The measured mass in FBS can be written as equation 36:

$$M_{FBS}=C_{FBS-lip}M_{FBS-lip}+C_{FBS-p}M_{FBS-p} \quad (36)$$

where $M_{FBS-lip}$and $M_{FBS-p}$are the lipid and protein masses in FBS (kg), and $C_{FBS-lip}$and C_{FBS-p}(ng kg^{-1}) are the chemical concentrations in these phases.

Assuming equilibrium partitioning between water and FBS components (equation 37–38):

$$C_{FBS-lip}=K_{lipw}C_w \quad (37)$$

$$C_{FBS\text{-}p}=K_{pw}C_w \tag{38}$$

where K_{lipw} and K_{pw} (L/kg) are the lipid–water and protein–water partition coefficients.

Substituting equation 37–38 into equation 36 yields:

$$M_{FBS}=C_w\left(K_{lipw}M_{FBS\text{-}lip}+K_{pw}M_{FBS\text{-}p}\right) \tag{39}$$

The chemical mass in cells is composed of intracellular water, cellular lipid, and cellular protein (equation 38):

$$M_{cell}=C_wV_{w,incell}+C_{cell\text{-}lip}M_{lip,cell}+C_{cell\text{-}p}M_{p,cell} \tag{40}$$

Assuming identical partitioning behavior within cells (equation 41–42):

$$C_{cell\text{-}lip}=K_{lipw}C_w \tag{41}$$

$$C_{cell\text{-}p}=K_{pw}C_w \tag{42}$$

Substituting equation 41–42 into equation 40:

$$M_{cell}=C_w\left(V_{w,incell}+K_{lipw}M_{lip,cell}+K_{pw}M_{p,cell}\right) \tag{43}$$

Combining equations in the mass balance relationship, and grouping terms yields:

$$M_{total}=C_w\left[V_{w,in+out}+K_{lipw}\left(M_{FBS\text{-}lip}+M_{lip,cell}\right)+K_{pw}\left(M_{FBS\text{-}p}+M_{p,cell}\right)\right] \tag{44}$$

When exposure was administered as a nominal IC_{10} or $EC_{IR1.5}$ (mol/L), the total mass added per well was calculated as (equation 45):

$$M_{total}=IC_{10}\text{ or }EC_{IR1.5}\times V_{total}\times MW\times 10^9 \tag{45}$$

where MW is the molecular weight (g mol^{-1}), and 10^9 converts g to ng.

3.7.2. Mixture -Toxicity Modeling

We used cell viability, ROS induction and 8-OHdG induction as end points to quantify the contribution of the monitored contaminants to the overall effects of seawater extracts on porpoise and dolphin cells via mixture-toxicity modeling. For both baseline cytotoxicity, ROS formation and DNA damage, the applicability of the CA model, where the summed toxic unit (TU) of each individual component approximates the TU of these components mixed together, has been extensively validated in mammalian cell models. To ensure robustness, we selected cytotoxicity to test the validity of the CA model again. The accuracy of the mixture-toxicity modeling predictions was evaluated by comparing the estimated mixture effects with experimentally observed outcomes.

Firstly, we tested the validity of the assumption that the sum of the effects of each individual studied chemical on cell viability approximates the combined effect of these toxicant mixtures, using the CA model. Using the CA model, we predicted the concentration-effect for cell viability based on the realistic mixture effects of all monitored toxicants at the percent concentration composition (p_i) determined in the sample, as calculated using equation 46. An index of prediction quality (IPQ) was used to assess the deviation between the predicted and observed mixture effects. An IPQ of 0 perfect agreement between the model prediction and experimental observation. A positive IPQ signifies that the CA-predicted IC10 ($IC_{10,CA}$) is higher than the experimental IC_{10} ($IC_{10,exp}$), whereas a negative IPQ indicates the opposite (as defined in equations 47 and 48. If the IPQ falls within the range of -1 to +1, good agreement is considered to have been achieved between the experimental determination and the model prediction. This implies that the joint effects of the targeted chemicals align with the predictions of the CA model.

$$IC_{10,\,CA} = \frac{1}{\sum_{i=1}^{n} \frac{pi}{IC_{10,i}}} \quad (46)$$

$$\text{If } IC_{10,\,CA} > IC_{10,\,exp}, \text{ then IPQ} = \frac{EC_{10,CA}}{EC_{10,exp}} - 1 \quad (47)$$

$$\text{If } IC_{10,\,CA} < IC_{10,\,exp}, \text{ then IPQ} = 1 - \frac{EC_{10,CA}}{EC_{10,exp}} \quad (48)$$

The combined toxicity of a seawater extract was expressed as the toxic unit (TU_{sample}), calculated as the reciprocal of $IC_{10,\,sample}$ or $EC_{IR1.5,\,sample}$ (equation 49). The concentration (C_i) and $IC_{10,\,i}$ or $EC_{IR1.5,\,i}$ of individual compounds, were used to calculate the mixture effects of identified contaminants based on the CA model (equation 50). Finally, we assessed the quantitative contribution of the identified contaminant individually and in mixtures to the cytotoxicity and oxidative stress response of each seawater sample (equation 51).

$$TU_{sample} = \frac{1}{IC_{10,\,sample} \text{ or } EC_{IR1.5,\,sample}} \quad (49)$$

$$TU_{chem} = \sum_{i=1}^{n} \frac{C_i}{IC_{10,\,i} \text{ or } EC_{IR1.5,i}} \quad (50)$$

$$\text{Percent contribution} = \frac{TU_{chem}}{TU_{sample}} \times 100\% \quad (51)$$

3.7.3. Risk Assessment

Exposure activity ratio (EAR) analysis was used for *in vitro* risk assessment for individual chemicals and their mixtures. EAR was determined by dividing C_i by $IC_{10,i}$ or $EC_{IR1.5,\,i}$ for each compound (equation 52). Risk classification was based on ranking criteria, where EAR = 1×10^{-3} was considered the threshold for potential environmental effects of a chemical or mixture.

$$EAR = \frac{C_i}{IC_{10,\,i} \text{ or } EC_{IR1.5,\,i}} \quad (52)$$

4. Assessment of Mixture Effect and Identification of Key Drivers in Seawater Cocktail Affecting the Dermal Health of Indo-Pacific Finless Porpoise and Chinese White Dolphin

The dermal exposure of marine mammals to complex seawater chemical mixtures represents a critical yet understudied dimension of coastal ecosystem health. In Hong Kong and the broader Indo-Pacific region, the co-occurrence of naturally derived algal toxins and diverse anthropogenic contaminants has raised increasing concern regarding their combined impacts on sensitive apex species such as the Indo-Pacific humpback dolphin, also named Chinese White Dolphin (*Sousa chinensis*) and the Indo-Pacific finless porpoise (*Neophocaena asiaeorientalis*). Building upon comprehensive chemical measurements and *in vitro* toxicological assays, this chapter investigates the cytotoxic and oxidative stress responses induced by seawater extracts collected across key cetacean habitats. By integrating concentration–response profiling, concentration addition-based mixture toxicity modelling, and region-specific comparisons, this chapter aims to elucidate (1) the relative contributions of natural toxins versus anthropogenic pollutants to observed cellular effects, (2) the extent to which targeted analytes explain the overall toxicity of environmental mixtures, and 3) the dominant risk drivers shaping dermal hazard landscapes for porpoise and dolphins.

4.1. Cytotoxicity and Key Drivers of Seawater Chemical Mixtures in Cetacean Skin Cells

The seawater extracts from Hong Kong cetacean habitats elicited measurable cytotoxicity on CWDT and FPT cell lines. However, the two cell types exhibited species-specific sensitivity differences (**Figure 4.**1). The CWDT cells were more sensitive overall, with an average sample toxic unit for cytotoxicity ($TU_{sample,\ cytotoxicity}$) of 0.02 (range 0.0015–0.10) compared to 0.0058 (range 0.0009–0.018) in FPT cells (Appendix I). In other words, on average the dolphin fibroblasts experienced about four-fold higher toxic burden from the same seawater samples. Cytotoxic effects also varied spatially across the 36 sampled sites, underscoring heterogeneous pollution exposure. **Figure 4.1** illustrates the distribution of cytotoxic potency in each sample across Hong Kong for both cell lines. Notably, certain clusters of sites (e.g. around the Pearl River estuary and urban bays) showed elevated $TU_{sample,\ cytotoxicity}$. This spatial variability in cytotoxicity aligns with localized contaminant inputs, motivating an analysis of the chemical drivers behind these patterns.

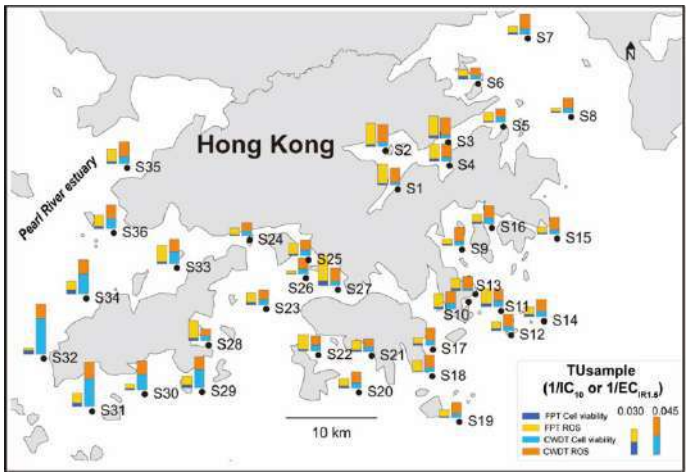

Figure 4.1 The toxic unit of each seawater sample (TU_{sample}) collected from Hong Kong's coastal waters, which induced cytotoxicity and ROS formation in the cells of Indo-Pacific finless porpoise and humpback dolphin.

To pinpoint the responsible chemicals, we screened 38 prevalent seawater contaminants (including natural algal toxins and various anthropogenic pollutants) individually for cytotoxicity. Sixteen of these chemicals were found cytotoxic (active) in at least one of the two cetacean cell lines. Species-specific differences were again evident in the *in vitro* assays of individual compound toxicity. In the bioassays, FPT and CWDT cells were seeded at identical initial densities, and no significant differences in cell density were observed after 24 or 48 hours of culture. Both cell lines were treated in exactly the same manner when exposed to seawater extracts and individual chemicals. Under these identical experimental conditions, FPT exhibited different sensitivities from CWDT in cytotoxicity to the tested chemicals, showing particularly higher sensitivity to compounds with stronger cytotoxic effects **Figure 4.** 2. Despite species-specific sensitivities, the four algal toxins (PTX-2, OA, DTX-1, and GYM) showed much higher toxic potency than any of the anthropogenic contaminants tested. As shown in **Figure 4. 3 (a)**, the algal toxins had high toxic potency in cetacean skin fibroblast cells, whereas active anthropogenic chemicals (antibiotics, UV filters, PFASs, and PAHs) required higher effective concentration to achieve similar effects. For example, PTX-2 was extraordinarily potent, with IC_{10} value of 6.1×10^{-10} M in FPT and 9.5×10^{-8} M in CWDT. This makes PTX-2 roughly 4–6 orders of magnitude more cytotoxic than other tested anthropogenic chemicals. Other algal toxins (DTX-1, OA, GYM) also consistently out-ranked the man-made chemicals in cytotoxic strength for both species (**Figure 4. 3 (a)**), underscoring that naturally produced toxins cannot be ignored in seawater.

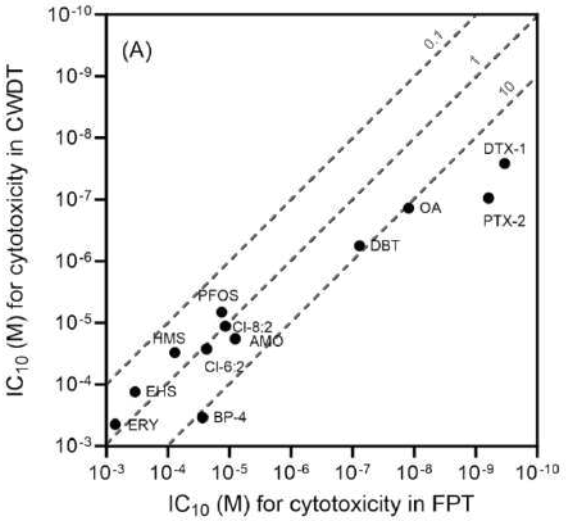

Figure 4. 2 Species sensitivity comparison of contaminant toxic potency between CWDT and FPT for (a) cytotoxicity.

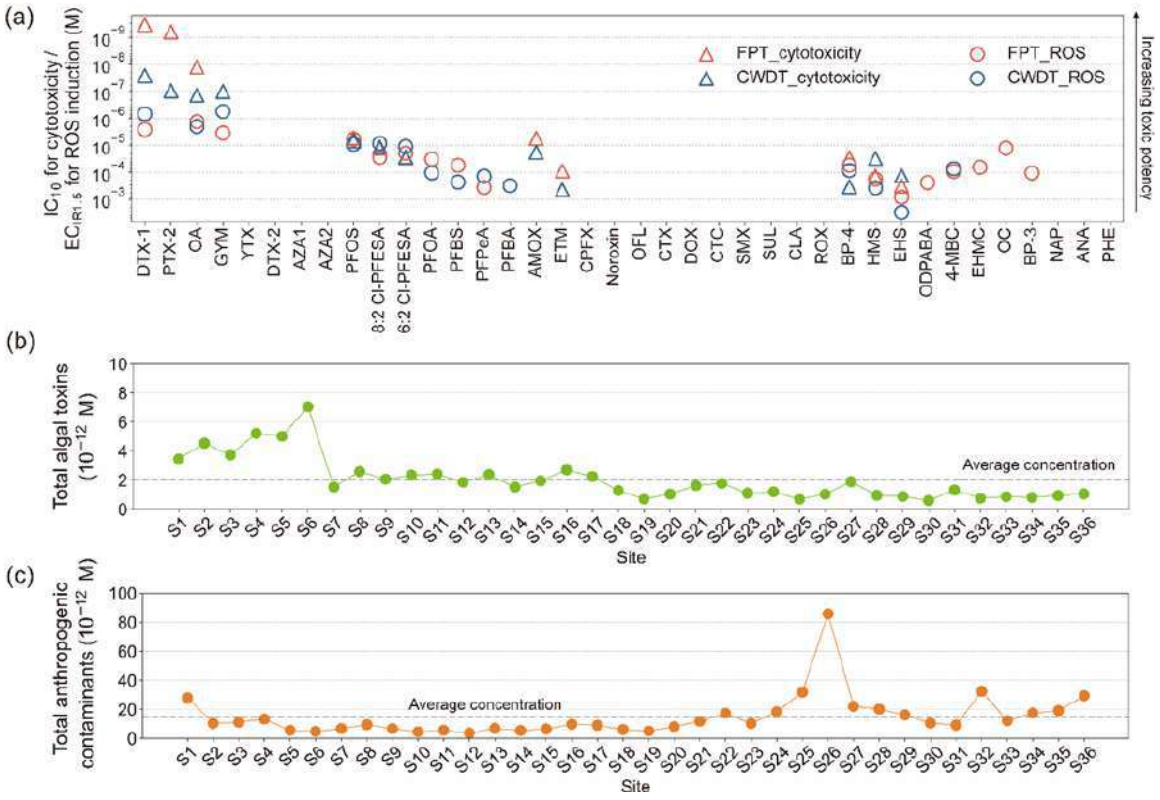

Figure 4. 3 (a) The inhibitory concentration causing 10% decline in cell viability (IC_{10}; triangles) and the effect concentration resulting in 1.5-fold induction of ROS ($EC_{IR1.5}$; circles) for each tested compound in the cells of Indo-Pacific finless porpoise (FPT; red) and humpback dolphin (CWDT; blue). Total concentration of (b) studied algal toxins and (c) anthropogenic contaminants ordered by sampling site ID.

Before quantifying the contribution of each compound, we verified whether the combined chemical cocktails behave according to concentration addition (CA), the typical toxic mixture model assumption. Prior studies indicate that complex pollutant mixtures often act additively on biological endpoints in mammalian cells (Escher et al., 2020). We created synthetic mixtures of all cytotoxic chemicals at the ratios detected in select water samples (**Table 4. 1**) and compared the observed mixture toxicity to CA model predictions (Appendix I). The experimental mixture dose–response closely matched the predicted additive response in both cell lines, with IPQ values around –0.54 (FPT) and –0.13 (CWDT) (within the ±1 range denoting good agreement). These findings demonstrate that both natural and anthropogenic toxicants in the mixtures exert their effects on cetacean cells in a manner consistent with the principle of concentration addition. This result provides a basis for quantitatively resolving how individual chemical components contribute to the cytotoxicity elicited by seawater extracts.

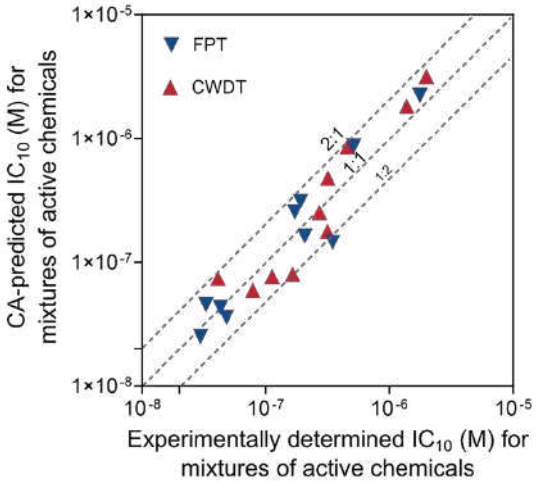

Figure 4. 4 Comparison of the concentration addition (CA)-predicted versus experimentally determined inhibition concentrations of mixtures of cytotoxicity-active chemicals, combined at the concentration ratios found in each corresponding seawater sample, that caused 10% decline in cell viability in FPT (blue) and CWDT (red). The dashed lines represent the IPQ value.

Table 4. 1 Molar fraction (pi, %) of each chemical determined in the corresponding sample and used in the mixture experiments for validating the concentration-addition model (full chemical names provided in **Table 3. 3**)

Sample ID	Season	PTX-2	OA	GYM	DTX-1	PFOS	6:2 Cl-PFESA	8:2 Cl-PFESA	EHS	BP-4	HMS	AMOX	ETM
S1	Wet	6.1%	5.2%	2.2%	0.0%	8.2%	0.1%	0.0%	4.9%	52.2%	1.1%	5.6%	14.6%
S9	Wet	27.3%	12.4%	13.9%	0.0%	3.3%	0.1%	0.1%	38.4%	2.3%	2.3%	0.0%	0.0%
S17	Wet	9.1%	3.3%	10.5%	0.0%	1.3%	0.0%	0.0%	0.0%	35.3%	0.0%	18.3%	22.1%
S26	Wet	0.5%	0.3%	0.1%	0.0%	0.1%	0.1%	0.0%	0.0%	83.8%	0.0%	2.0%	13.1%
S35	Wet	3.2%	2.7%	0.5%	0.0%	23.6%	0.9%	0.0%	0.0%	69.1%	0.0%	0.0%	0.0%
S1	Dry	1.2%	5.3%	9.8%	0.1%	1.2%	0.0%	0.0%	0.0%	69.9%	0.0%	3.8%	8.7%
S9	Dry	19.2%	19.9%	2.9%	2.0%	0.7%	0.0%	0.0%	0.0%	55.3%	0.0%	0.0%	0.0%
S17	Dry	19.6%	10.3%	2.9%	2.0%	0.7%	0.1%	0.0%	0.0%	36.1%	0.0%	11.4%	16.9%
S26	Dry	0.8%	1.3%	1.1%	0.0%	0.5%	0.0%	0.0%	0.0%	72.3%	0.0%	5.4%	18.6%
S35	Dry	8.9%	25.6%	0.6%	2.0%	11.1%	0.1%	0.0%	0.0%	14.7%	0.0%	37.1%	0.0%

Having validated the mixture concept in our system, we next dissected the proportional contributions of each chemical to the seawater mixture's cytotoxicity. Despite its low concentration (only 3% of the total molar concentration of measured chemicals in the extracts), PTX-2 emerged as the individual largest contributor to cytotoxicity. TU-based contribution analysis revealed that PTX-2 alone accounted for 92% of the cytotoxic effect of all studied chemicals in FPT, and 45% in CWDT. This disproportionate impact of PTX-2 highlights the outsized risk posed by natural bloom toxins even when present at lower concentrations. By comparison, the remaining chemicals each contributed only marginally. However, even when the contributions of all 38 measured chemicals are summed, the explained mixture effect remains modest, accounting for only about 34% of the observed cytotoxicity induced by the seawater extracts in FPT (**Figure 4. 5 (a)**). In other words, roughly one-third of the cytotoxic effect in FPT was attributable to these targeted compounds, while the remaining 66% of toxicity was due to other unidentified contaminants. The CWDT showed a similar pattern that a significant fraction of cytotoxicity (more than 99%) remained unexplained by the targeted chemicals (**Figure 4. 5 (b)**). These findings indicate that the catalog of common contaminants represents just the "tip of the iceberg" in terms of dermal toxicity. There are likely many other bioactive compounds in seawater (e.g. unmonitored algal metabolites or emerging pollutants) contributing to skin cell death that were not captured in our targeted analysis. The dominance of PTX-2 was unexpected, and it points to the need to look beyond routine anthropogenic chemicals when assessing environmental risks.

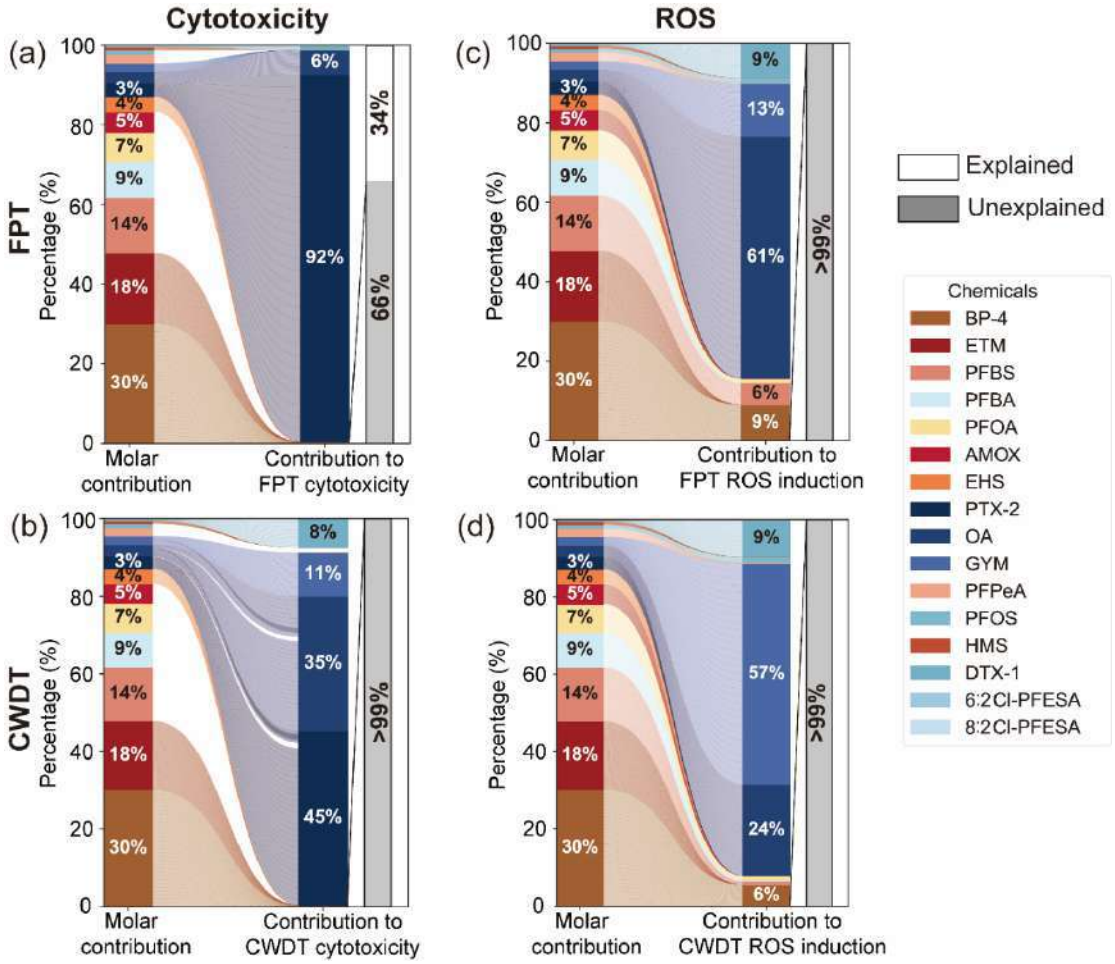

Figure 4. 5 The molar fraction of each chemical in all studied chemicals versus its contribution to the mixture effects of all studied chemicals and of seawater extracts on cytotoxicity in skin fibroblast cells of (a) Indo-Pacific finless porpoise (FPT) and (b) Indo-Pacific humpback dolphin (CWDT) and on ROS induction in (c) FPT and (d) CWDT.

It is noteworthy that PTX-2 was the only chemical in our panel that exceeded a screening-level risk threshold of 10^{-3} via dermal exposure (**Figure 4. 6**). In FPT cells, PTX-2's ambient concentration produced an EAR slightly above 1×10^{-3}, indicating a potential risk for skin effects. Prior research suggests that when environmental contaminants yield EAR values on the order of 10^{-3} or higher in dermal systems, they can contribute to skin disorders in mammals (Anderson & Meade, 2014; Gao et al., 2024; Pradhan et al., 2022). While PTX-2 stood out, the combined EAR considering all known chemicals in the seawater mixtures was even greater up to10^{-2} (for cytotoxicity

in some samples). This cumulative risk metric, though an approximation, underscores that the cocktail of contaminants (both measured and unmeasured) could plausibly pose a significant hazard to cetacean skin health. Notably, no HABs events were recorded in Hong Kong during our sampling periods (Hong Kong Red Tide Database). Yet algal toxins were consistently detected in all samples across both the wet summer and dry winter seasons, indicating that these compounds persist in the marine environment throughout the year, likely through chronic low-level production or transport from surrounding regions, rather than occurring only during acute HAB episodes. Algal toxins can adsorb detritus or be carried by currents, enabling them to persist beyond the immediate bloom location or timeframe. This finding advocates for incorporating key algal toxins into routine water quality surveillance throughout the year, not just during visible red tides.

Our results also align with broader cetacean toxicology data, reinforcing the importance of natural toxins. We compiled cytotoxicity data (e.g. EC_{50} values) from the literature for 28 chemicals tested on skin fibroblasts of seven other cetacean species (ranging from dolphins, porpoises and whales) and compared them to our findings. In this comparison (**Figure 4. 7**), algal toxin compounds similarly ranked among the most potent skin toxicants, far more toxic than many anthropogenic chemicals tested. This cross-species perspective confirms that natural marine toxins can significantly impair skin cell viability, and their impact should not be overlooked. In practical terms, management of marine mammal health needs to pay attention not only to industrial pollutants but also to biogenic toxins from phytoplankton. Ultimately, commonly monitored pollutants explain only a fraction of the observed cytotoxic effects in seawater, indicating that ecotoxicologists must broaden the scope of chemical analysis. Unidentified contaminants, possibly novel algal metabolites, degradation products, or

less studied anthropogenies, are likely contributing to the remaining cytotoxicity. Unraveling this unexplained fraction of mixture toxicity will be critical for fully protecting marine wildlife health.

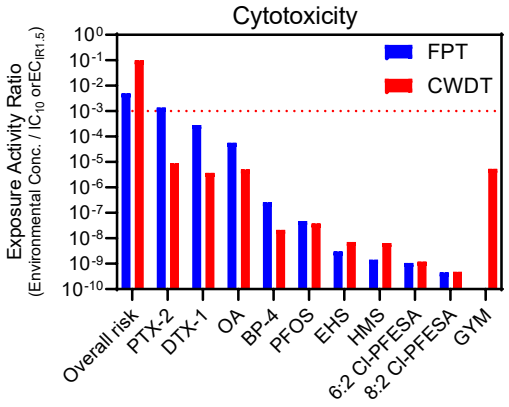

Figure 4. 6 Exposure-activity ratio (EAR) of each chemical active in inducing cytotoxicity in CWDT and FPT. EAR is calculated as the ratio of the detected concentration of a chemical to its IC_{10} for cytotoxicity. The red dashed line represents the risk threshold of 10^{-3}.

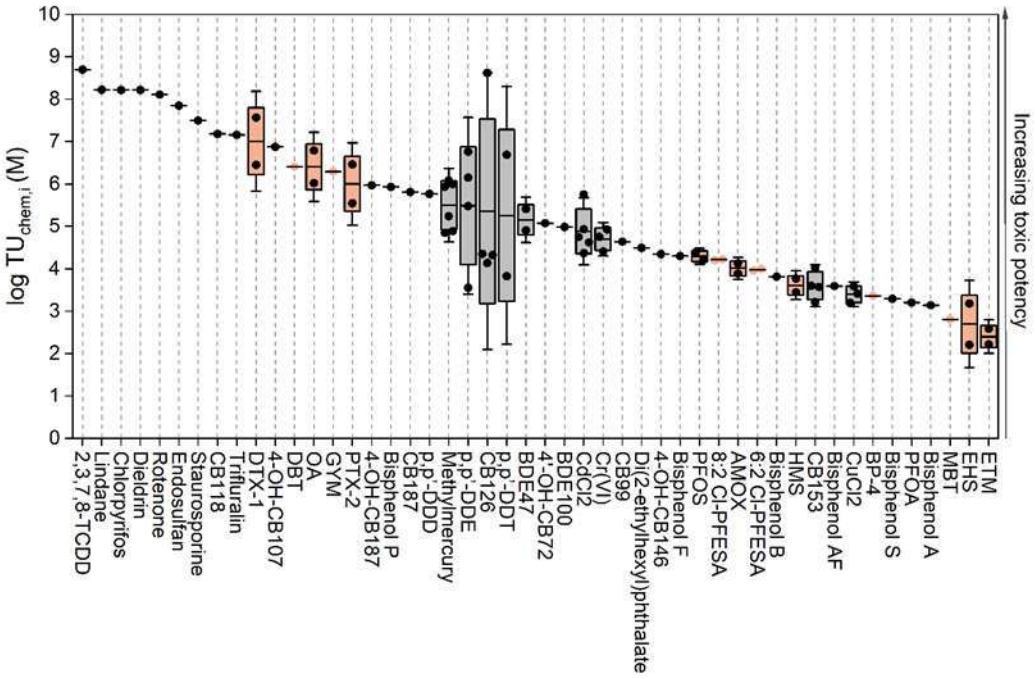

Figure 4. 7 Toxic unit of active pollutants on fibroblast cells of the Indo-Pacific humpback dolphin (*Sousa chinensis*), finless porpoise (*Neophocaena asiaeorientalis*), pantropical spotted dolphin (*Stenella attenuata*), pygmy killer whale (*Feresa attenuata*),

humpback whale (*Megaptera novaeangliae*), Burrunan dolphin (*Tursiops australis*), and common bottlenose dolphin (*Tursiops truncatus*) ((Bjørneset et al., 2023; "Cell Cycle Alterations Due to Perfluoroalkyl Substances PFOS, PFOA, PFBS, PFBA and the New PFAS C6O4 on Bottlenose Dolphin (Tursiops Truncatus) Skin Cell," 2022; Frenzilli et al., 2014; Hung et al., 2006; Li et al., 2022; Ochiai et al., 2020; W. Sun et al., 2024; X. Sun et al., 2023; Yu et al., 2018, 2019)). Orange bars represent results from this study, while grey bars represent results from literature.

4.2. Oxidative Stress Response and Drivers of ROS Induction

In addition to cell viability, we examined intracellular reactive oxygen species (ROS) generation in the two cetacean cell lines as an indicator of oxidative stress. Interestingly, the seawater extracts induced ROS at lower concentrations and to a greater relative extent than they caused cytotoxicity. For every sampling site, the toxic unit for ROS ($TU_{sample, ROS}$) was consistently higher than the corresponding $TUs_{ample, cytotoxicity}$ in both FPT and CWDT cells (**Figure 4.1**). This means that comparatively small doses of the mixtures could trigger a significant oxidative stress response before notable cell death occurred. Oxidative stress is a more sensitive and earlier indicator of cellular injury from seawater contaminants than acute cytotoxicity. This finding aligns with the notion that many pollutants initiate cellular damage via ROS generation, leading to inflammation or functional impairment even if cells have not yet died. The elevated ROS burden observed (often several-fold above cytotoxic TU) implied that the skin of wild cetaceans may be experiencing chronic oxidative pressure from environmental mixtures, which can erode skin barrier function over time.

We estimated the exposure–activity ratios for the ROS endpoint as well. The combined mixture of EAR for ROS induction in our samples reached up to 2×10^{-3}. When considered alongside the EAR for cytotoxicity, these values provide screening-level evidence of dermal health risk to coastal cetaceans. Although EAR thresholds are

not definitive predictors of pathology, our results suggest that the chemical mixtures in Hong Kong waters have the potential to cause oxidative stress in cetacean skin at environmental exposure levels.

Spatial patterns in ROS induction reflected the distribution of certain contaminants. Sites with the highest levels of algal toxins (e.g. sites S1–S4 in semi-enclosed bays) tended to show above-average ROS responses in both cell lines (**Figure 4. 3 (b)**). Meanwhile, sites S25–S36, which had the greatest loads of anthropogenic contaminants (near urban/industrial inputs), also elicited high ROS formation (**Figure 4. 3 (c)**). These observations suggest that both natural toxins and anthropogenic chemicals in the mixture contributed to oxidative stress on both FPT and CWDT cells. We therefore quantitatively parsed the mixture components driving ROS in each species, similar to the cytotoxicity analysis.

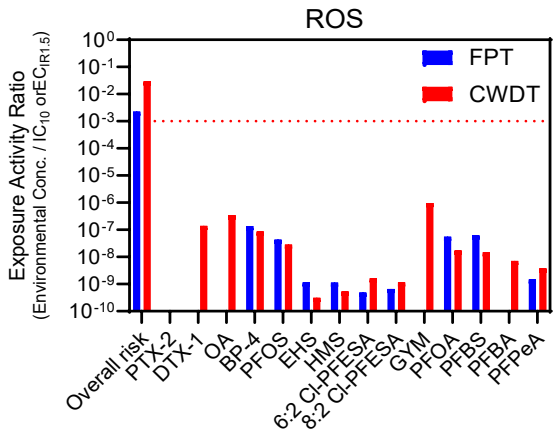

Figure 4. 8 Exposure-activity ratio (EAR) of each chemical active in inducing intracellular reactive oxygen species (ROS) formation in CWDT and FPT. EAR is calculated as the ratio of the detected concentration of a chemical to its $EC_{IR1.5}$ (for ROS). The red dashed line represents the risk threshold of 10^{-3}.

Notably, PTX-2, despite its extreme cytotoxicity, did not induce any significant ROS in either FPT or CWDT cells (**Figure 4. 5 (c)** and **(d)**). This indicates PTX-2's mode of action leads to cell death through other pathways (e.g. disrupting actin

cytoskeleton **(**Espiña & Rubiolo**2008)** or protein phosphatases **(**Butler et al., 2012**)**, as pectenotoxins are known to do) rather than causing oxidative damage. In contrast, the other algal toxins, such as DTX-2, OA and GYM, were all active in triggering ROS formation, and they exhibited relatively high ROS-inducing potencies in both cell lines (**Figure 4. 5 (c)** and **(d)**). **Figure 4. 3 (a)** illustrated that these algal toxins had low $EC_{IR1.5}$ values (concentrations causing a 1.5-fold ROS increase), generally far lower than the ROS thresholds of most tested anthropogenic chemicals. Much like in the cytotoxicity endpoint, the algal toxins emerged as principal contributors to ROS effects in the mixtures. Although they constituted <10% of the total molar composition of known chemicals, the four studied algal toxins collectively accounted for about 83% of the explained ROS induction in FPT and 90% in CWDT.

Interestingly, there were species-specific differences in ROS sensitivity also evident in both FPT and CWDT (**Figure 4. 9**). OA was roughly equipped in both cell lines ($EC_{IR1.5}$ on the order of 1.3 to 2×10^{-6} M). However, DTX-1 and GYM were about an order of magnitude more potent in the CWDT than in the FPT. DTX-1's $EC_{IR1.5}$ was 6.8×10^{-7} M in CWDT versus 2.6×10^{-6} M in FPT, and GYM's was 5.5×10^{-7} M in CWDT versus 3.5×10^{-6} M in FPT (**Figure 4. 3 (a)**). These potencies shifted mean that, at equivalent environmental concentrations, DTX-1 and GYM pose a greater oxidative threat to CWDT than FPT. Consequently, the main ROS-driving toxin differed by species: in FPT, OA which was similarly effective in both cell types and present at significant levels, emerged as the top contributor (67% of the total mixture ROS effect attributable to known chemicals) (**Figure 4. 5 (c)**). In CWDT, the more GYM took the lead, accounting for 57% of the known mixture ROS effect (**Figure 4. 5 (d)**).

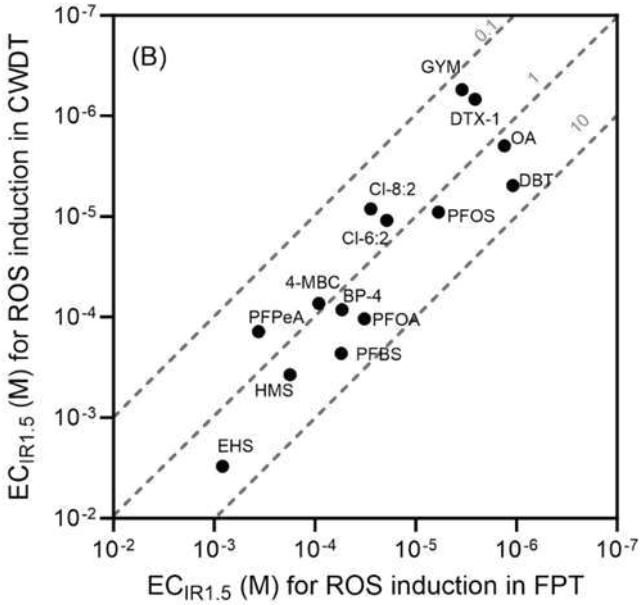

Figure 4. 9 Species sensitivity comparison of contaminant toxic potency between CWDT and FPT for intracellular ROS formation.

Although algal toxins overwhelmingly drove ROS generation into our known mixture, the contributions of certain anthropogenic chemicals were non-negligible, particularly compared to their minimal role in cytotoxicity. In the endpoint, several PFASs notably contributed a few percent each to the total ROS induced by the mixture. In FPT, the PFAS class cumulatively contributed 8% of the explained ROS effect, and 4% in CWDT cells (**Figure 4. 5 (c)** and **(d)**). The most influential were PFOS, PFOA, and PFBS, which individually accounted for roughly 1–6% of the ROS activity in one or both cell lines. This represents a significant jump from the cytotoxicity scenario, where no PFAS exceeded 1% contribution. The reason lies in their greater relative potency for ROS induction, the $EC_{IR1.5}$ values of these PFASs were lower than their IC_{10} values (**Figure 4. 3 (a)**).

The fact that PFAS exposure caused ROS generation at effect concentrations is consistent with mechanistic studies in skin models. Many PFAS are known to disrupt

skin barrier function by inducing oxidative damage and lipid peroxidation in cells (Mousavi et al., 2021). For instance, *in vitro* experiments have shown that exposing human keratinocytes to 5×10^{-5}M PFOA for 24 h lead to a significant rise in free radical levels and membrane disruption (Peropadre et al., 2018). Likewise, exposing bottlenose dolphin (*Tursiops truncatus*) skin cells to 2.6×10^{-5} M PFOS altered the expression of genes involved in oxidative stress responses (Mollenhauer et al., 2009). These examples mirrored our observations and underscored that PFAS induced ROS is an early warning sign of cellular injury. In the wild, cetacean skin is continuously bathed in seawater; even at low pollutant concentrations, a chronic oxidative assault could occur. Over time, such sustained ROS stress may lead to inflammation, impaired healing, opportunistic infections, and a higher incidence of skin lesions in marine mammals. It is noteworthy that our study provides the first quantitative evidence of PFAS contributions to oxidative stress in any cetacean tissue. This finding expands the concern about PFAS beyond systemic and developmental toxicity to include dermal health risks.

Despite accounting for the contributions of dozens of chemicals, we found that the vast majority of the ROS response (>99%) remained unexplained by the analyzed compounds (**Figure 4. 5 (c)** and **(d)**). This gap is even larger than for cytotoxicity, indicating that ROS induction is likely driven by a host of unknown or unmeasured chemicals with pro-oxidant activity. Addressing this shortfall is a major challenge, it requires moving beyond targeted chemical analysis to identify “hidden” drivers in the mixture. We are pursuing an integrated strategy to tackle this: using high-resolution mass spectrometry (HRMS) (Cheng et al., 2024) and non-target analysis to detect suspect peaks in the seawater extracts and then applying *in silico* prioritization to focus on those likely to be toxic (Arturi & Hollender, 2023b).

4.3. Regional Mixture Toxicity Risks in Indo-Pacific Coastal Waters

Beyond Hong Kong, many Indo-Pacific coastal habitats host the Indo-Pacific finless porpoise and humpback dolphin and face parallel pollution challenges. We extended our analysis to evaluate mixture toxicity in other regions by leveraging reported contaminant concentrations from the literature. Using 20 years of data for coastal waters in the western Indo-Pacific (including the Bohai Sea, Yellow Sea, East China Sea, and South China Sea), we compiled average seawater levels for the same suite of chemicals (**Table 4. 2**). Combining these concentrations with our experimentally determined effect potencies (IC_{10} and $EC_{IR1.5}$ values for FPT and CWDT), we calculated the predicted TU_{chem} contributed by known contaminants in each region. The results suggest that coastal waters in China's seas could exert even higher dermal toxic pressure on these marine mammals than the levels observed around Hong Kong. For cytotoxicity, the combined TUs of the studied chemicals were roughly 14 times higher in the Yellow Sea, 7 times higher in the East China Sea, 4 times higher in the South China Sea, and 1.2 times higher in the Bohai Sea, compared to our Hong Kong reference, for both species (**Figure 4. 10**).

Importantly, the drivers of mixture toxicity in each region were again dominated by algal bloom toxins, according to our model. In the Yellow Sea and East China Sea, which occasionally experience dense dinoflagellate blooms, DTX-1 emerged as a primary cytotoxic toxin for the CWDT. On average, DTX-1 was predicted to contribute 47% (range: 4-87%) of the cytotoxic effect in CWDT in the Yellow and East China Seas. This is notable because DTX-1's absolute concentrations in those regions were

not the highest (compared to other pollutants), but its high potency made it a major risk driver. For FPT, PTX-2 remained a dominant contributor in most regions with contributing average 61% to cytotoxicity. In the Bohai Sea, OA was predicted to be the top cytotoxic contributor for both species' cells. These patterns mirror our Hong Kong findings in that Dinophysis-produced toxins (PTX-2, OA, DTX-1) are consistently implicated. All three of those toxins originate from *Dinophysis* algae (He et al., 2022), which have caused lipophilic toxin contamination in many Asian coastal waters. The heavy contribution of DTX-1 in particular corroborates our earlier conclusion, as overall mixture toxicity increases, potent algal toxins like DTX-1 likely take on an even larger share of the toxicity burden. This suggests that management of dolphin and porpoise habitats in East Asia cannot ignore algal toxins when assessing risks, even though they are natural chemicals.

For ROS induction, a similar dominance of natural toxins was evident. In the FPT, OA was the major contributor to ROS induction in most regions, accounting for an average of 94% of the known mixture ROS effect in Bohai Sea, 88% in Yellow Sea and 67% in East China Sea. Meanwhile, in CWDT, GYM drove ROS responses, especially in areas like the East China Sea and South China Sea. This is consistent with our Hong Kong observations where GYM was the top ROS contributor in CWDT. Thus, depending on species and region, either OA or GYM (or occasionally DTX-1) would be the toxin of greatest concern for oxidative stress.

Notably, the South China Sea scenario for FPT showed a particularly high ROS potential due to a combination of algal toxins and UV filter pollutants. Results indicated that at sites in the South China Sea, the co-occurrence of sunscreen chemicals (like BP-4, a common UV filter) with algal toxins produced the highest ROS induction in FPT

cells among all regional comparisons. In Hong Kong, a similar observation that BP-4 had minimal effect on cell viability but significantly enhanced ROS generation in CWDT. These findings suggest that certain anthropogenic contaminants, while not outright lethal to cells, can impose oxidative stress that potentially undermines skin health. The enhanced oxidative pressure from contaminant mixtures may impose a long-term threat to cetacean skin health.

Overall, the Indo-Pacific regional extrapolation reinforces the broad relevance of our Hong Kong findings. Algal toxins likely play a significant role in baseline dermal toxicity risk across many coastal habitats, yet they are seldom included in routine monitoring outside of HABs events. Countries around the Indian Ocean and Southeast Asia have reported numerous HAB incidents (Furuya et al., 2018; Soon Eong & Sulit, 2017; Tholkapiyan et al., 2014; Yñiguez et al., 2021), but systematic measurements of algal toxin residues in the water or in marine mammals are limited. The absence of data does not equate to absence of risk. Our results imply that undetected algal toxins could be insidiously contributing to chronic health effects in those ecosystems.

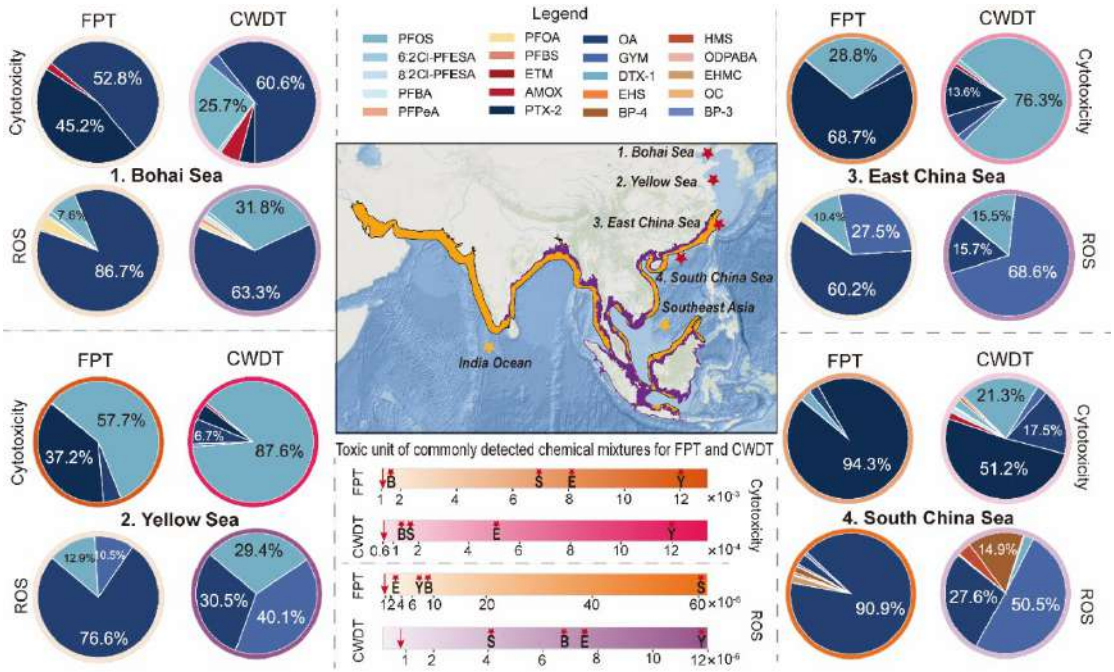

Figure 4. 10 Regional comparison of mixture effect potency of monitored organic contaminants in the habitat waters of Indo-Pacific finless porpoise and humpback dolphin. The orange and purple ribbons on the map indicate the global habitat ranges of finless porpoise and humpback dolphin, respectively. Background rings indicate toxic unit, per the colour legend at the bottom of the figure. The darker the colour, the higher the toxic potency compared to this study. Conversely, the lighter the colour, the lower the toxic potency. The red arrows in colour gradations indicate the toxicity of mixture chemicals in Hong Kong surface seawater (this study), while the stars with letters indicate the four different regions represented in this figure: ★B (Bohai Sea), ★Y (Yellow Sea), ★E (East China Sea) and ★S (South China Sea).

Table 4. 2 Average concentrations (M) of studied chemicals in the Indo-Pacific regions.

Compound	Hong Kong waters (This study)	East China sea	Bohai	South China Sea	Yellow Sea	India Ocean	Pacific Ocean
PFOS	1.46E-13	7.02E-14	2.00E-13	4.48E-14	n.a.	1.26E-12	2.58E-13
6:2 Cl-PFESA	5.38E-15	n.a.	4.38E-14	1.66E-14	n.a.	2.78E-14	n.a.
8:2 Cl-PFESA	4.86E-15	n.a.	8.20E-15	3.62E-14	n.a.	2.64E-14	n.a.
PFBA	2.21E-13	n.a.	5.24E-11	5.01E-13	n.a.	n.a.	n.a.
PFBS	3.42E-12	9.50E-13	2.86E-12	2.86E-13	n.a.	n.a.	n.a.
PFOA	1.80E-12	1.29E-12	2.12E-10	2.60E-13	n.a.	n.a.	n.a.
PFPeA	5.32E-13	n.a.	2.86E-11	1.68E-13	n.a.	n.a.	n.a.
ETM	2.94E-12	3.31E-11	7.90E-13	1.07E-11	1.23E-13	n.a.	n.a.
AMOX	1.05E-12	8.37E-11	1.46E-10	4.68E-11	1.50E-10	n.a.	n.a.
PTX-2	6.76E-13	3.56E-12	3.62E-13	4.30E-12	2.70E-12	n.a.	n.a.
OA	4.78E-13	2.41E-12	8.34E-12	2.39E-12	6.94E-12	n.a.	n.a.
GYM	2.66E-13	2.92E-12	1.43E-12	1.21E-12	2.52E-12	n.a.	n.a.
DTX-1	6.58E-14	8.18E-13	n.a.	7.33E-14	2.30E-12	n.a.	n.a.
EHS	7.57E-13	n.a.	n.a.	5.09E-11	n.a.	n.a.	2.72E-09
BP-4	3.44E-12	n.a.	n.a.	5.48E-11	n.a.	n.a.	n.a.
HMS	1.73E-13	n.a.	n.a.	6.17E-11	n.a.	n.a.	9.61E-10

4.4. Implications

From a conservation management perspective, our findings call for a more holistic approach. Traditionally, efforts focus on anthropogenic pollutants in endangered marine mammals. We show that natural toxins can rival or exceed anthropogenic contaminants in certain impact metrics, highlighting a dual threat. Both toxin types must be considered in risk assessments for marine megafauna. For the Indo-Pacific humpback dolphins and finless porpoises, they are already under pressure from habitat loss and fisheries, but deteriorating water quality adds another layer of threat. Actionable recommendations include expanding HAB toxin monitoring programs year-round (not just when visible blooms occur) and integrating such data into wildlife health surveillance. In the Hong Kong marine environment, dinoflagellates produce PTX-2, DTX-1, OA and GYM, are often present year-round, suggesting a chronic rather than purely episodic exposure. To establish a definitive causal link between HABs and cetacean health, future monitoring must transition to a 'source-to-effect' framework. This involves comparative sampling across both HAB and non-HAB periods, integrated with analysis of toxin profiles in the tissues of stranded individuals. By correlating the seasonal peaks of environmental toxins with the pathological data from stranding records, we can move beyond bioanalytical screening to a more rigorous attribution of health threats, ultimately identifying the specific environmental windows that pose the greatest risk to local population of dolphin and porpoise.

Early warning of algal toxin surges could enable management interventions (like temporary area closures) to reduce exposure of cetacean during peak risk times.

Additionally, species-specific research is vital. We observed meaningful

differences between the two cetacean species' cellular responses. To improve ecological relevance, establishing cell lines from local populations. For example, using East Asian finless porpoise (*Neophocaena asiaeorientalis sunameri*) fibroblasts for the Yellow Sea and Bohai Sea region (Cheznowski, 2015), it would allow more accurate toxicity thresholds for those particular animals. We recommend developing a cetacean cell line bank representing various populations, which could be a powerful tool for environmental risk assessment and pollutant screening in the future.

Finally, translating *in vitro* findings to real-world risk requires bridging the gap between exposure and dose. Our use of EAR and TU provides a conservative screening-level risk estimate, but it assumes direct exposure equivalence. In reality, chemical uptake into skin and distribution in the body will modulate risk. Thus, a promising next step is to construct PBTK models for these species. By iterating between model predictions and biological measurements, we can refine the risk assessment from a screening toward a more quantitative, mechanism-based evaluation. This study provides new insights into how complex seawater chemical cocktails affect cetacean skin cells, revealing that a few potent algal toxins largely drive the observed cytotoxic and oxidative stress effects (at least among known chemicals). However, a considerable fraction of toxicity remains unexplained, pointing to the need for advanced analytical techniques and broader contaminant inventories. For example, automated computational pipelines can filter complex HRMS data for features correlating with bioactivity. In parallel, machine learning models trained on known chemical structures and toxicological data to predict which of the detected unknowns might have high toxic potency. Such innovative analytics, combining non-target screening with AI-driven toxicity prediction, will accelerate the discovery of the "missing" toxicants contributing to mixture effect

This study advocates a more comprehensive and balanced management strategy. Ultimately, preserving the health of these sentinel marine mammals in an era of complex environmental change.

4.5. Summary

In summary, this chapter quantitatively dissected the dermal toxic potential of complex seawater chemical mixtures on Indo-Pacific humpback dolphin and finless porpoise skin fibroblasts, using Hong Kong coastal waters as a model system and extending the analysis to broader Indo-Pacific habitats. By combining species-specific *in vitro* bioassays with mixture-toxicity modeling, we demonstrated that a small subset of highly potent algal toxins, including PTX-2, OA, DTX-1, and GYM, acts as dominant drivers of both cytotoxicity and ROS induction, despite representing only a minor fraction of the total molar concentration of monitored chemicals. PTX-2 emerged as a disproportionate contributor to baseline cytotoxicity, whereas OA and GYM largely governed oxidative stress responses, with clear species-specific differences between humpback dolphin and finless porpoise cell lines. These results highlight that natural marine biotoxins can contribute substantially to the dermal risk landscape for coastal cetaceans, even in the absence of overt HAB events, and therefore warrant inclusion in routine monitoring and risk assessment frameworks.

At the same time, anthropogenic contaminants, especially PFASs and selected organic UV filters, were shown to make non-negligible contributions to ROS-inducing mixture effects and to impose chronic oxidative pressure at environmentally realistic levels. The consistent finding that TUs for ROS exceeded those for cytotoxicity underscores oxidative stress as a more sensitive and earlier-onset endpoint for assessing mixture impacts on cetacean skin. However, a considerable proportion of both cytotoxic

and ROS responses to seawater extracts remained unexplained by the monitored chemical set, indicating that unresolved contaminants and uncharacterized natural products still constitute a “hidden” component of the toxic burden. Regionally, application of the toxic-unit and EAR framework to literature concentration data revealed that coastal seas in the western Indo-Pacific can exhibit substantially higher predicted dermal risk than Hong Kong waters, with algal toxins again emerging as key mixture drivers.

Collectively, these findings establish a mechanistic and quantitative basis for identifying priority toxicants across different dermal endpoints, while emphasizing the need for a balanced consideration of both natural and anthropogenic chemicals in mixture risk assessment for sentinel marine mammals. They also provide a critical empirical foundation for the subsequent chapters of this thesis, which aim to (1) employ non-target screening and machine-learning approaches to identify currently unresolved toxicity drivers within complex environmental mixtures, and (2) link *in vitro* effect concentrations to internal tissue burdens via physiologically based toxicokinetic modeling.

5. Physiologically Based Toxicokinetic (PBTK) Model for Monitored Chemicals in Indo-Pacific Humpback Dolphin

Building upon the *in vitro* findings from Chapter 4 that highlighted the cellular toxicity of chemical mixtures in Hong Kong seawater, this chapter employs a physiologically based toxicokinetic (PBTK) modeling approach to bridge external exposure concentrations and internal dosimetry in Indo-Pacific humpback dolphins (*Sousa chinensis)* as a case model. Given the ecological importance and sentinel role of these cetaceans and considering their prolonged dermal and dietary exposure to coastal contaminants, an integrated PBTK-QIVIVE (quantitative *in vitro*-to-*in vivo* extrapolation) framework was developed. This chapter aims to (1) predict steady-state tissue concentrations of monitored pollutants in dolphins under environmental exposure scenarios, (2) assess the relationship between internal accumulation and toxicological potency, and (3) characterize both external and internal health risks, with an emphasis on chemical-specific drivers and mixture dermal hazards.

5.1. PBTK Model Development

A five-compartment PBTK model was constructed to simulate the absorption, distribution, and retention of monitored contaminants in the Indo-Pacific humpback dolphin. The model accounts for both dermal absorption through seawater and dietary uptake, which are two principal exposure pathways for marine mammals. Physiological

parameters were species-specific, and compound-specific parameters incorporated physicochemical properties such as $\log_{Kow}$, molecular weight, and clearance rates. The modeled compartments included blood, liver, kidney, skin, and blubber.

5.2. Tissue Distribution and Accumulation Patterns

The seawater concentrations and dietary bioaccumulation levels of monitored chemicals were incorporated into the species-specific PBTK model for the Indo-Pacific humpback dolphin. The resulting steady-state concentrations in blood, blubber, skin, liver, and kidney tissues are summarized in **Table 5. 2**, and the corresponding concentration–time trajectories are illustrated in Appendix II. Across all chemicals, an initial phase of rapid uptake followed by a progressive deceleration as internal concentrations approached steady state. At equilibrium, skin and blubber persistently showed the highest burdens among all compartments, highlighting their physiological roles not only as structural or insulating tissues but also as long-term reservoirs for semi-lipophilic and protein-affinitive contaminants.

Among the pollutants, phenanthrene (PHE) displayed the highest concentration in skin tissue (4.94×10^{-5} g/L), followed by the UV filter OC (4.09×10^{-5} g/L) (**Table 5. 2**). These compounds, despite lacking observable cytotoxicity, ROS induction or DNA damage *in vitro*, accumulated substantially in skin, their persistent accumulation raises concern. Field data from 2012–2017 confirmed that PHE was the most enriched polycyclic aromatic hydrocarbon (PAH) in stranded Indo-Pacific humpback dolphins in the Pearl River Estuary (Gui et al., 2018), aligning with our model predictions and supporting its accuracy. A strong correlation ($R^2 = 0.94$) was observed between simulated steady-state skin concentrations and dietary intake levels of these compounds (**Figure 5. 1**), particularly for PHE, which showed both the highest dietary intake and

skin burden. Although PHE and OC demonstrated no toxic response under tested concentration, their high accumulation raises concern for potential chronic or indirect effects. Literature indicates that chronic exposure to environmentally realistic concentrations of PHE impair immune responses in primate renal cells (Ruan et al., 2021), while OC has shown hepatic accumulation and maternal-fetal transfer in marine mammals (Gago-Ferrero et al., 2013). These findings suggest that there is the possibility of alternative toxicological pathways in cetaceans that extend beyond direct toxic effects and potential long-term health risks that may not be evident through acute toxic assays alone.

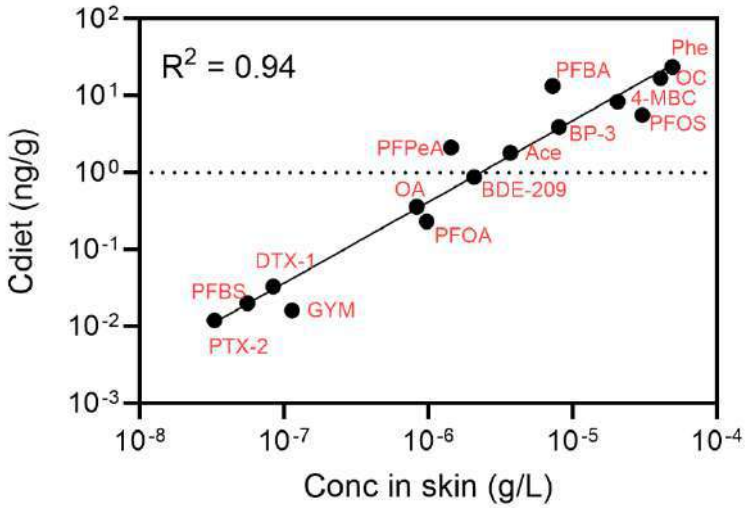

Figure 5. 1 Correlation between simulated steady-state concentrations of contaminants in CWDT and their respective dietary intake levels. R^2 represents the coefficient of determination.

Conversely, compounds such as PFOS and DBT, which exhibited high toxic potency *in vitro*, also accumulated at significant levels in skin (3.06×10^{-5} g/L and 1.05×10^{-5} g/L, respectively,**Table 5. 2**). In contrast, algal toxins, despite their high toxic potency, showed low skin accumulation. This inverse trend was attributed to rapid hepatic clearance rates (**Table 5. 1**), particularly for hydrophilic or protein-bound toxins

like PTX-2 (2.44 L/h) and DTX-1 (1.22 L/h). By contrast, poorly metabolized compounds, such as long-chain perfluoroalkyl substances (0.0002-0.0008 L/h), accumulated extensively due to their slow systemic clearance.

Table 5. 1 Predicted hepatic clearance rates (CLliver, L/h) for the studied contaminants in the Indo-Pacific humpback dolphin (Sousa chinensis).

Compound	CL_{liver} (L/h)	Compound	CL_{liver} (L/h)
PFBA	0.61910	4-MBC	11.08256
PFPeA	3.94128	HMS	3.60150
PFOA	0.00424	EHS	21.03604
PFBS	0.07947	BP-4	2.18407
ODPABA	0.46540	PTX-2	2.43922
EHMC	209.57848	OA	1.28894
OC	3.88736	DTX-1	1.22597
BP-3	8.01908	GYM	5.12556
BDE-209	7.98398	PFOS	0.00272
Ace	11.00992	6:2 Cl-PFESA	0.00023
Phe	20.72776	8:2 Cl-PFESA	0.00083
Nap	36.14341		

Table 5. 2 Predicted steady-state concentrations (g/L) of monitored contaminants in five key tissues of Indo-Pacific humpback dolphins (*Sousa chinensis*) simulated using a five-compartment PBTK model. Tissues include blood, skin, blubber, liver, and kidney.

Compound	C_{blood}	C_{skin}	$C_{blubber}$	C_{liver}	C_{kidney}
PFBA	8.72E-07	7.29E-06	2.62E-06	2.52E-06	4.39E-06
PFPeA	8.99E-08	1.44E-06	5.05E-07	9.97E-08	8.35E-07
PFOA	2.07E-08	9.76E-07	3.39E-07	4.82E-07	5.55E-07
PFBS	1.50E-09	5.60E-08	1.88E-08	2.13E-08	3.09E-08
ODPABA	0.00E+00	0.00E+00	0.00E+00	0.00E+00	0.00E+00
EHMC	0.00E+00	0.00E+00	0.00E+00	0.00E+00	0.00E+00
OC	7.04E-07	4.09E-05	4.60E-05	8.88E-07	3.30E-05
BP-3	1.64E-07	8.10E-06	9.18E-06	1.02E-07	6.71E-06

Compound	C_{blood}	C_{skin}	$C_{blubber}$	C_{liver}	C_{kidney}
BDE-209	3.50E-08	2.08E-06	2.31E-06	2.18E-08	1.67E-06
Ace	7.39E-08	3.71E-06	4.20E-06	3.35E-08	3.06E-06
Phe	9.36E-07	4.94E-05	5.59E-05	2.27E-07	4.05E-05
Nap	0.00E+00	0.00E+00	0.00E+00	0.00E+00	0.00E+00
4-MBC	3.69E-07	2.06E-05	2.33E-05	1.66E-07	1.68E-05
HMS	3.48E-10	3.35E-08	2.24E-08	4.72E-10	1.61E-08
EHS	5.29E-10	5.10E-08	3.40E-08	1.26E-10	2.44E-08
BP-4	4.94E-13	5.86E-12	3.73E-12	8.44E-13	3.32E-12
PTX-2	5.72E-10	3.31E-08	3.71E-08	1.13E-09	2.67E-08
OA	1.51E-08	8.34E-07	9.34E-07	5.40E-08	6.74E-07
DTX-1	1.41E-09	8.41E-08	9.22E-08	5.31E-09	6.62E-08
GYM	1.43E-09	1.14E-07	9.31E-08	1.38E-09	6.69E-08
PFOS	5.55E-07	3.06E-05	1.02E-05	1.46E-05	1.68E-05
6:2 Cl-PFESA	4.79E-14	2.90E-12	7.46E-13	1.08E-12	1.22E-12
8:2 Cl-PFESA	2.75E-13	1.96E-11	5.02E-12	7.25E-12	8.22E-12

For amphiphilic and semi-lipophilic pollutants with strong affinity for lipid- and protein-rich tissues, skin accumulation was primarily governed by partitioning-driven mechanisms. Additionally, a trophic-amplification effect was evident that chemical concentrations in the diet were positively correlated with steady-state skin concentrations, consistent with the well-documented biomagnification patterns of PFAS, PAHs, and structurally related organic pollutants in apex marine mammals. Collectively, these mechanisms explain why different pollutant classes occupy distinct regions of the skin concentration landscape and underscore the chemical-specific nature of dermal toxicokinetics. The findings highlight the importance of integrating PBTK modeling with mixture-oriented toxicity assays and machine-learning-based chemical identification to more accurately assess contaminant risks in cetaceans inhabiting complex coastal ecosystems.

5.3. Internal Toxicity Assessment through QIVIVE Approach

To assess potential health impacts from exposure to commonly monitored environmental contaminants, QIVIVE was performed using the predicted steady-state concentrations in CWDT. Since the effective concentrations ($EC_{IR1.5}$ or IC_{10}) obtained from *in vitro* bioassays are nominal concentrations, they do not fully reflect the bioavailable fraction that interacts with cells. A portion of the compounds become bound to lipids and proteins on the cell membrane during cellular uptake. Only the unbound fraction of a chemical can diffuse across cell membranes to exert toxicity, making $EC_{IR1.5,\ free}$ or $IC_{10,free}$ a more biologically meaningful metric for extrapolation. Using partition coefficients, nominal *in vitro* effect concentrations for cytotoxicity, ROS induction, and DNA damage on CWDT were corrected to yield freely dissolved effective concentration values.

The adjusted data revealed similar toxicity trends for most chemicals, like PFAS compounds when compared to nominal concentrations (**Figure 5. 2** and **Table 5. 3**). However, notable discrepancies emerged for certain compounds, particularly four high toxic algal toxins, including DTX-1, PTX-2, GYM and OA. For example, DTX-1 displayed $EC_{IR1.5,\ free}$ and $IC_{10,free}$ that were approximately two orders of magnitude lower than $EC_{IR1.5}$ and IC_{10} across all three toxicity endpoints. Similar patterns were observed for PTX-2 and GYM, whose C_{free} values were 30 to 50 times lower than their respective nominal values. The least variation was observed for OA, where freely dissolved effective concentration was approximately two-fold lower across endpoints. These adjustments suggest that algal toxins possess exceptionally high intrinsic potency, as even minimal unbound concentrations can elicit cellular responses. In contrast, UV

filters such as HMS and EHS, which showed low nominal toxicity, exhibited significant increases in potency after correction, even exceeding the toxicity of compounds that appeared more potent under nominal conditions. For instance, HMS had a ROS induction nominal $EC_{IR1.5}$ of 3.04×10^{-3} M, higher than PFBS, PFPeA, and PFOA, yet its $EC_{IR1.5,\ free}$ surpassed these PFAS compounds by nearly one order of magnitude.

The comparison between *in vitro* potency and *in vivo* accumulation highlights divergent risk pathways. PFAS compounds accumulated relatively high concentrations in CWDT and showed moderate cytotoxic and oxidative activity, suggesting potential chronic risks through bioaccumulation. Conversely, algal toxins demonstrated extreme potency *in vitro* but low tissue accumulation, reflecting a risk profile shaped by rapid metabolism. Correcting for freely dissolved effective concentration enables a more accurate interpretation of toxicological risk in relation to internal exposure, providing critical input for the subsequent EAR-based risk assessment.

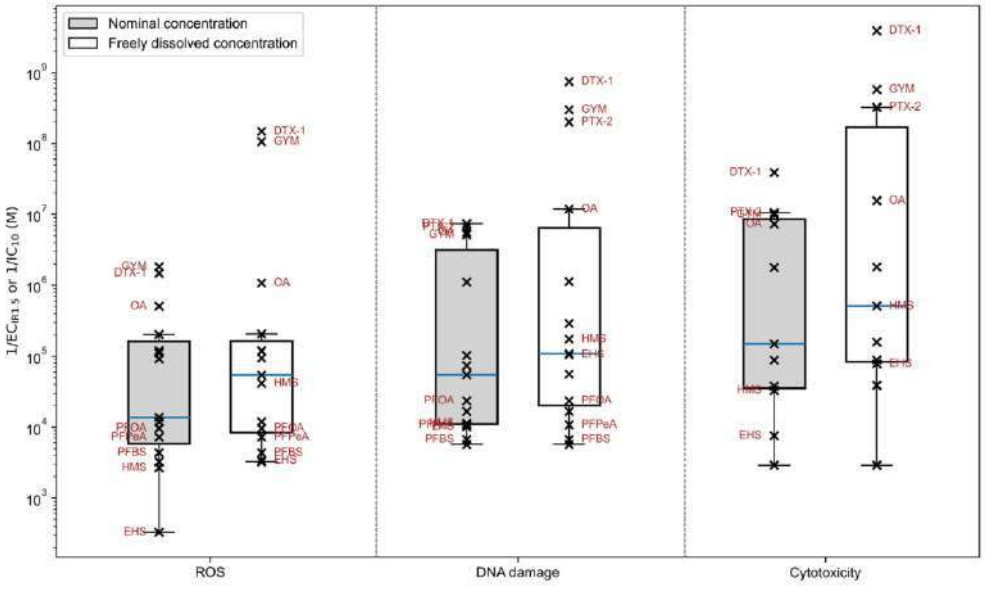

Figure 5. 2 Comparison between nominal and freely dissolved effect concentrations across chemical classes in *in vitro* toxicity assays.

Table 5. 3 Nominal concentration and predicted freely dissolved concentration of each studied chemicals.

	Nominal concentration ($EC_{IR1.5}$/ IC_{10}, M)			Freely dissolved concentration ($EC_{IR1.5, free}$/ $IC_{10, free}$, M)		
Compound	**ROS**	**DNA damage**	**Cytotoxicity**	**ROS**	**DNA damage**	**Cytotoxicity**
PFBA	3.08E-04	1.76E-04	inactive	3.08E-04	1.76E-04	inactive
PFPeA	1.39E-04	9.33E-05	inactive	1.39E-04	9.33E-05	inactive
PFOA	1.04E-04	4.27E-05	inactive	1.04E-04	4.27E-05	inactive
PFBS	2.29E-04	1.50E-04	inactive	2.29E-04	1.50E-04	inactive
4-MBC	7.28E-05	1.36E-05	inactive	1.84E-05	3.44E-06	inactive
HMS	3.73E-04	8.88E-05	3.04E-05	2.41E-05	5.74E-06	1.96E-06
EHS	3.04E-03	9.81E-05	1.32E-04	2.94E-04	9.48E-06	1.28E-05
BP-4	8.45E-05	inactive	3.44E-04	8.45E-05	inactive	3.44E-04
PTX-2	inactive	1.53E-07	9.45E-08	inactive	4.99E-09	3.09E-09
OA	1.98E-06	1.80E-07	1.37E-07	9.31E-07	8.45E-08	6.43E-08
DTX-1	6.78E-07	1.35E-07	2.58E-08	6.76E-09	1.34E-09	2.57E-10
GYM	5.47E-07	1.93E-07	1.00E-07	9.42E-09	3.33E-09	1.73E-09
PFOS	9.00E-06	9.74E-06	6.72E-06	8.46E-06	9.16E-06	6.32E-06
6:2 Cl-PFESA	8.37E-06	5.99E-05	1.13E-05	8.35E-06	5.97E-05	1.13E-05
8:2 Cl-PFESA	1.09E-05	1.82E-05	2.64E-05	1.06E-05	1.78E-05	2.58E-05

5.4. External and Internal Risk Assessment

To contrast environmental exposure with biologically effective dose, we conducted both external and internal risk assessments. The external risk (EAR_{water}) was calculated as the ratio between measured seawater concentrations and nominal effect concentrations, while the internal risk (EAR_{skin}) was derived as the ratio between modeled skin concentrations and freely dissolved effective concentrations.

As presented in **Figure 5. 3** and **Table 5. 3**, mixture-level of EAR_{water} values across three endpoints (ROS induction, DNA damage, and cytotoxicity) were 1.62×10^{-6}, 1.29×10^{-5}, and 2.30×10^{-5}, respectively. These values fell several orders of magnitude below the potential risk threshold of concern (10^{-3}), indicating the monitored chemical cocktail in Hong Kong coastal waters would be likely to elicit low perceived risk in cetacean skin cells if evaluated solely on the basis of seawater concentrations. When internal risks (EAR_{skin}) were computed for the same mixture and endpoints, the mixture-level of risks increased substantially, reaching 5.02×10^{-2} for ROS induction, 1.95×10^{-1} for DNA damage, and 5.68×10^{-1} for cytotoxicity on CWDT. These values approach the internal risk benchmark of 1, indicating that the same chemical mixture that appears essentially harmless from an external perspective may pose a non-negligible risk once dermal accumulation and intracellular bioavailability are accounted for.

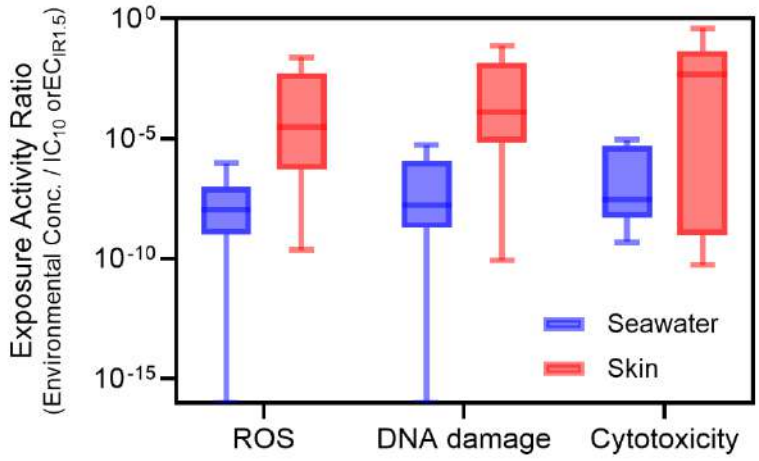

Figure 5. 3 Comparison of exposure activity ratios (EAR) based on environmental concentrations in seawater (blue) and modeled steady-state skin concentration (red) across three toxicological endpoints: ROS generation, DNA damage, and cytotoxicity.

Table 5. 4 External (EAR_{water}) and internal (EAR_{skin}) risk assessment in ROS, DNA damage and cytotoxicity on CWDT.

Compound	EAR_{water}			EAR_{skin}		
	ROS	DNA damage	Cytotoxicity	ROS	DNA damage	Cytotoxicity
PFBA	7.18E-09	1.26E-08		1.11E-04	1.94E-04	
PFPeA	3.83E-09	5.71E-09		3.91E-05	5.83E-05	
PFOA	1.72E-08	4.20E-08		2.27E-05	5.53E-05	
PFBS	1.49E-08	2.28E-08		8.17E-07	1.25E-06	
4-MBC	0.00E+00	0.00E+00		4.41E-03	2.36E-02	
HMS	5.33E-10	2.24E-09	6.54E-09	2.07E-06	8.70E-06	2.54E-05
EHS	3.13E-10	9.69E-09	7.18E-09	6.94E-07	2.15E-05	1.59E-05
BP-4	8.74E-08		2.15E-08	2.25E-10		5.53E-11
PTX-2		5.50E-06	8.87E-06		7.74E-03	1.25E-02
OA	3.48E-07	3.83E-06	5.04E-06	1.11E-03	1.23E-02	1.61E-02
DTX-1	1.41E-07	7.10E-07	3.71E-06	1.52E-02	7.64E-02	4.00E-01
GYM	9.74E-07	2.76E-06	5.31E-06	2.39E-02	6.76E-02	1.30E-01
PFOS	2.84E-08	2.62E-08	3.80E-08	7.23E-03	6.68E-03	9.68E-03
6:2 Cl-PFESA	1.62E-09	2.27E-10	1.20E-09	6.09E-10	8.51E-11	4.50E-10
8:2 Cl-PFESA	1.16E-09	6.95E-10	4.79E-10	2.74E-09	1.64E-09	1.13E-09
Mixture	1.62E-06	1.29E-05	2.30E-05	5.20E-02	1.95E-01	5.68E-01

Risk contributor analysis further revealed a shift in chemical drivers when transitioning from total EAR_{water} to EAR_{skin} (**Table 5. 4**). Decomposition of mixture EAR values by compound revealed that algal toxins consistently dominated the risk profiles across all three biological endpoints. However, the contributions of individual toxins changed substantially when moving from seawater-based to skin-based metrics (**Figure 5. 4**). The most striking example is DTX-1. In ROS induction, its proportional contribution increased from 8.7% in total external risks to 29% in total internal risks. Similarly, its role in DNA damage and cytotoxicity risk rose from 5.5% to 39%, and from 16% to 70%, respectively. In contrast, PTX-2 and OA showed marked declines in their proportional risk contributions within total internal risks for all three endpoints, both falling below 10% (**Figure 5. 4**). These patterns reflect how pharmacokinetic differences alter chemical-specific risk prominence, especially for compounds with high potency but low tissue retention.

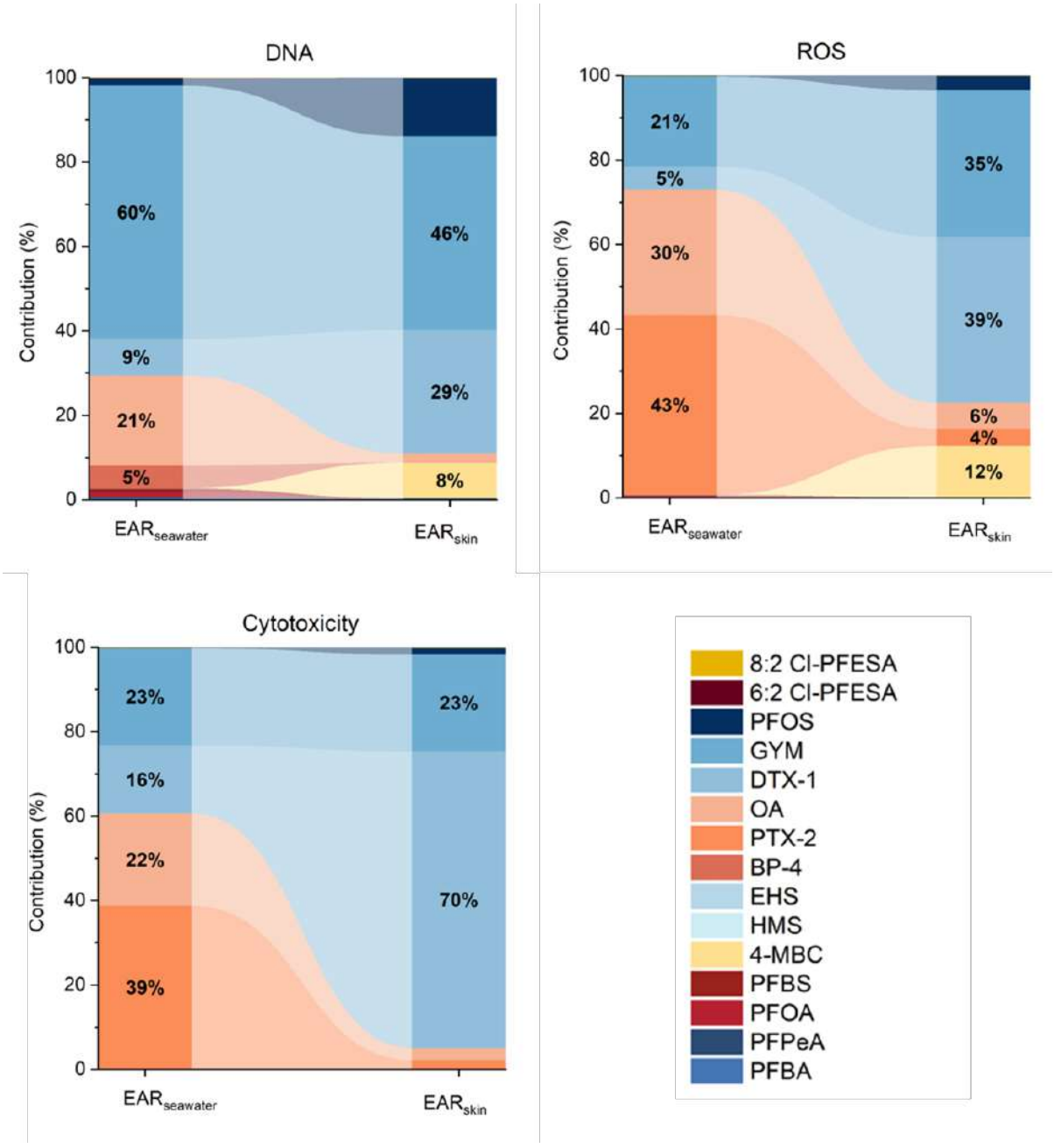

Figure 5. 4 Contribution of individual chemicals to total toxicological risk across (a) ROS induction, (b) DNA damage, and (c) cytotoxicity in external seawater concentrations (left panels) and internal skin concentrations (right panels).

Notably, PFOS and 4-MBC also demonstrated upward shifts in internal risk relevance. Risk contribution of PFOS to ROS induction on CWDT increased from 1.8% in total EAR_{water} to 14% in total EAR_{skin}. Similarly, 4-MBC, which was undetected in

seawater and thus absent from external risks, contributed 12% to DNA damage risk in total internal risks due to its presence in dietary intake. These increases were linked to physicochemical parameters, specifically high lipid–water ($K_{lip\text{-}water}$) and protein–water ($K_{protein\text{-}water}$) partition coefficients, which promote dermal accumulation and bioavailability. A Spearman correlation analysis (**Figure 5. 5**) confirmed that strong positive correlations between log EAR_{skin} for all three endpoints and the $K_{lip\text{-}water}$ and $K_{protein\text{-}water}$, as well as a strong negative correlation with log $EC_{IR1.5,\ free}/IC_{10,free}$ for the corresponding endpoint. Compounds with high EAR_{skin} contributions, such as PFOS, DTX-1, GYM, and 4-MBC, clustered in the upper right quadrant of the partitioning coefficient plot (**Figure 5. 6**). These relationships indicate that chemicals with higher lipophilicity and protein affinity tend to reach higher steady-state concentrations in skin, and that those with lower $EC_{IR1.5,\ free}/IC_{10,free}$ values exert stronger biological effects at a given internal dose. In other words, dermal internal risk is jointly governed by the ability of a compound to accumulate skin tissue and by its intrinsic cellular potency.

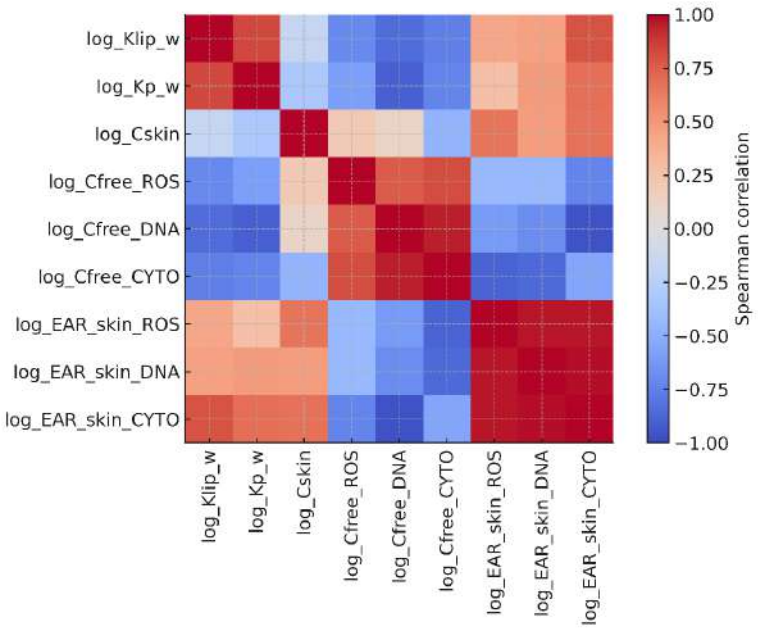

Figure 5. 5 Spearman correlation among parameters, concentrations and EAR.

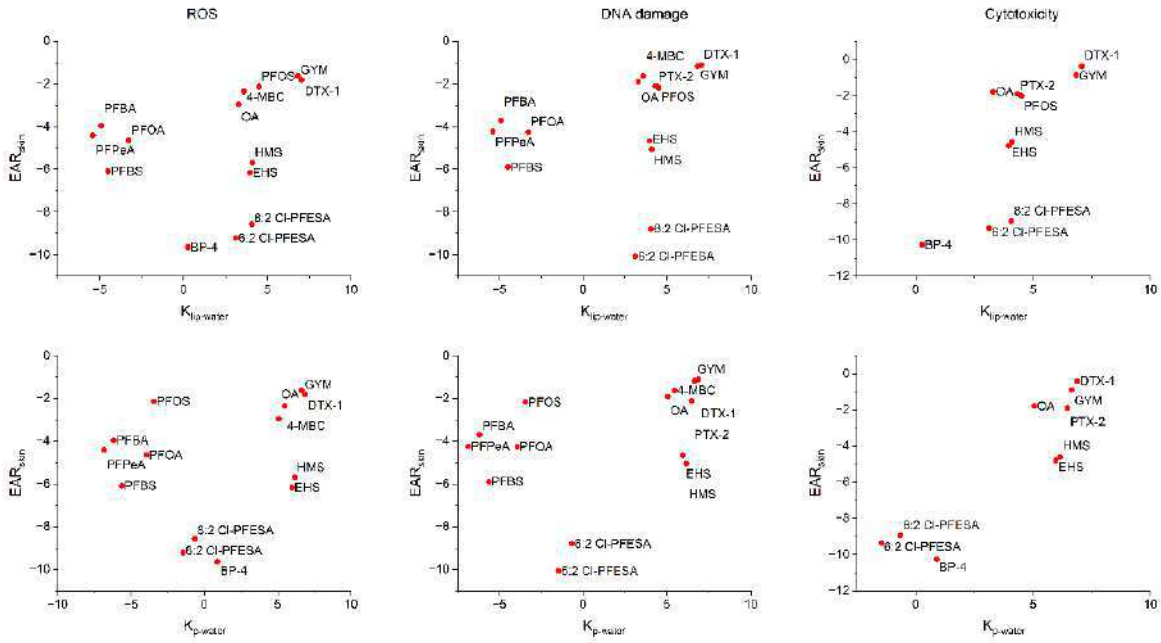

Figure 5. 6 Relationships between internal risk (EAR_{skin}) and physicochemical properties

Short-chain PFASs, despite their relatively high seawater concentrations, showed limited contribution to total internal risks for any endpoints due to low $K_{lip\text{-}water}$ and

$K_{protein\text{-}water}$. For instance, PFBA and PFBS demonstrated minimal internal risk, even though they are among the more prevalent PFASs in Hong Kong waters. This highlights the importance of tissue-specific accumulation over environmental abundance in defining risk. However, it is important to note that short-chain PFASs may target non-skin tissues of marine mammals. For example, PFBA can induce PPARα-mediated transcriptional activity in Baikal seal (*Pusa sibirica*) hepatocytes, and PPARα is primarily expressed in metabolically active organs such as liver and kidney rather than skin (Ishibashi et al., 2011). Historical data further indicate increasing PFBS levels in dolphin livers over the past two decades (Lam et al., 2016). These findings suggest that the primary toxicity targets of short-chain PFAS are likely located in internal organs rather than the dermis and the need to assess non-target effects in future research.

The comparison between external and internal risks demonstrates that internal dose modelling is indispensable for understanding the actual health risks posed by complex contaminant cocktails to Indo-Pacific humpback dolphins. By explicitly linking seawater exposure to tissue-level concentrations and cellular responses, the PBTK–QIVIVE framework used here provides a more biologically meaningful basis for prioritising chemicals of concern and for designing monitoring strategies that are aligned with the internal risk profiles of marine mammals.

5.5. Derivation of Concentration Risk Thresholds and Regional Risk Comparison

A reverse dosimetry approach was applied to derive minimum seawater concentrations of monitored chemicals that would elicit potential toxic risks in CWDT ($EAR_{skin}=1$). Based on PBTK model, predicted risk-inducing seawater concentrations

($C_{water,\ threshold}$) for various compounds spanned 10^{-12} to 10^{-4} M. This indicates that the minimum environmental concentrations of pollutants required to pose a risk to the most sensitive cellular endpoints in CWDT would be 10 to 10^9 times higher than the levels currently detected in Hong Kong waters. Since most of the anthropogenic contaminants studied are not hydrophilic and are subject to regulatory controls, their concentrations in Hong Kong seawater are far below the predicted risk thresholds.

Two algal toxins, DTX-1 and GYM, presented a different picture. Their predicted $C_{water,\ threshold}$ closely approached observed concentrations in Hong Kong seawater, differing by only 26.8-fold for DTX-1 and 11.2-fold for GYM. Considering that sampling did not coincide with HABs and these margins are relatively narrow. Therefore, seasonal or episodic HABs could elevate toxin levels sufficiently to breach dermal toxicity thresholds and may increase the vulnerability of dolphin skin, highlighting the need for continuous monitoring during bloom periods.

When the reverse dosimetry concentrations of monitored, chemicals were extended to other coastal regions of the western Indo-Pacific, notably higher ambient concentrations of certain contaminants were observed. In the Bohai Sea, East China Sea, and Yellow Sea, average concentrations of DTX-1 exceeded $C_{water,\ threshold}$ by 1.32-, 8.07-, and 8.11-fold, respectively (Compared with **Table 4. 2**). This implies up to 10 times of potential dermal toxicity risks for dolphin populations in those areas under DTX-1 exposure in seawater. GYM also approached toxic thresholds in the East China Sea, with an average concentration of 5.71×10^{-12} M compared to its predicted effect threshold of 5.98×10^{-12} M. Although direct dietary intake data for these regions were not modeled in PBTK simulations, it is reasonable to assume that higher seawater concentrations correspond to elevated trophic exposure levels, further amplifying

internal burdens. Therefore, the skin toxicity risks predicted for Indo-Pacific humpback dolphins in these regions may be underestimated.

The PBTK-QIVIVE framework enables not only retrospective health risk estimation but also prospective threshold setting for environmental monitoring. Identifying compounds that exert risk at low environmental concentrations, particularly highly potent algal toxins like DTX-1 and GYM, allows for proactive intervention strategies. These insights are especially critical for regions where monitoring capacity is limited, and where cetacean populations may face elevated contaminant exposure due to industrial or agricultural runoff.

5.6. Sensitivity Analysis of PBTK Model

Sensitivity analysis of the PBTK model identified three principal categories of influential parameters: exposure magnitude, chemical-specific distribution behavior, and organism-level physiological constraints. Dietary intake concentration (C_{diet}) consistently emerged as the most dominant determinant of internal dosimetry across all chemical classes. This reflects the fundamental role of exposure intensity in bounding the maximum achievable internal concentrations, regardless of downstream kinetic modulation (**Figure 5. 7**).

Additionally, parameter influence varied by chemical property. Concentration in seawater (C_{water}) exerted high sensitivity for more hydrophilic compounds and UV filters, underscoring the importance of dermal uptake for chemicals with low lipid affinity. Conversely, permeability coefficients (K_p) held greater sway (**Figure 5. 7**) for lipophilic substances, such as PAHs, whose systemic burdens were governed more by distributional behavior than initial concentration. These trends illustrate the divergent

drivers of accumulation based on physicochemical profiles: aqueous transport dominates for hydrophilic species, while lipid-associated partitioning controls hydrophobic compounds.

Physiological parameters, particularly hepatic blood flow (Q_{liver}), showed broad though moderate sensitivity across many compounds (**Figure 5. 7**). This indicates that metabolic clearance is limited by the liver's perfusion rate, which constrains the elimination of both rapidly and slowly metabolized substances. While Q_{liver} rarely represented the top-ranked parameter, it featured consistently in the sensitivity spectrum for compounds with hepatic clearance as their dominant elimination route.

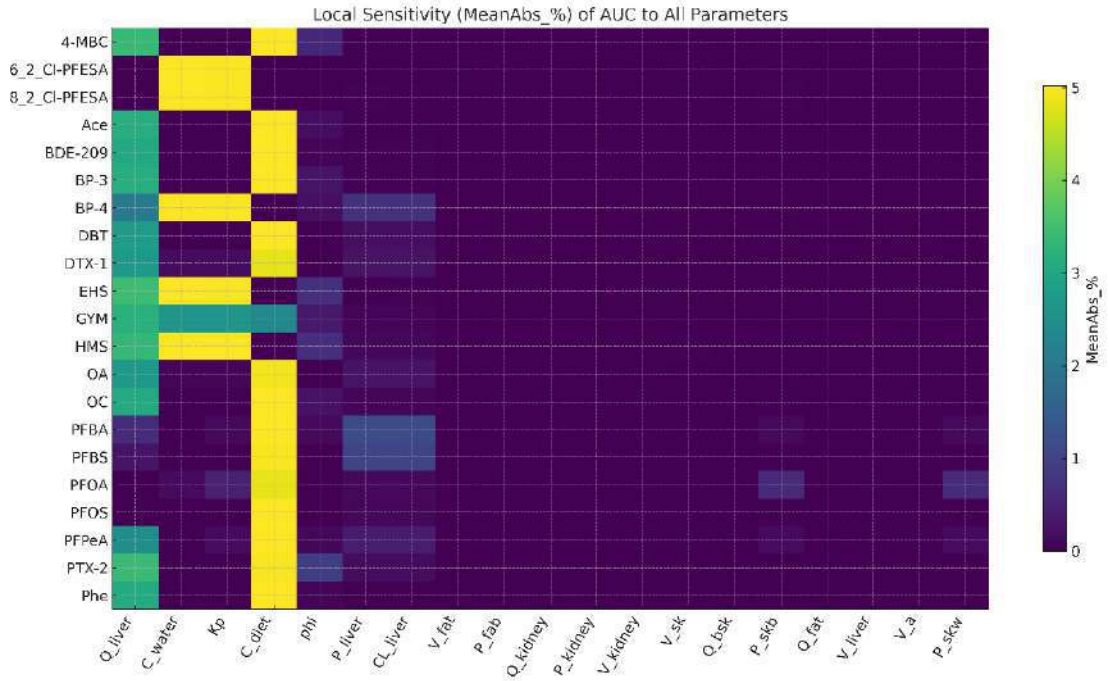

Figure 5. 7 Local sensitivity of all parameters in Indo-Pacific humpback dolphin PBTK model.

This triadic sensitivity structure which is defined by exposure level, compound-specific partitioning, and systemic clearance bottlenecks clarifies the determinants of internal chemical burden in marine mammals. Understanding which parameters contribute most to variability allows for targeted model refinement and more confident

interpretation of predictive uncertainty. Moreover, these insights inform future data collection priorities, suggesting where species-specific physiological measurements or chemical-specific kinetic constants would most improve model fidelity.

5.7. Implications

The PBTK-QIVIVE framework presented in this study offers a mechanistic and species-specific platform for evaluating internal contaminant risks in marine mammals. Yet, several areas for advancement remain critical to enhance its predictive power and ecological relevance. First, while the current model captures major physiological compartments, future iterations should incorporate additional organs such as the brain, gonads, and fetal compartments to reflect potential neurodevelopmental, reproductive, and transgenerational effects. These extensions are particularly relevant for contaminants with known endocrine-disrupting or neurotoxic profiles.

Since the skin fibroblasts of Indo-Pacific humpback dolphins cannot substitute for the toxicological responses of other organs, the integration of induced pluripotent stem cell (iPSC)-derived cell lines from dolphins represents a promising direction for refining in vitro toxicity extrapolation. Organoid-based systems reflecting liver, kidney, or neural tissues would improve QIVIVE resolution by allowing endpoint-specific toxicity estimates, thereby moving beyond the fibroblast model currently used. Such models would also enable the assessment of chemical impacts in tissues beyond the dermis, which is particularly important for hydrophilic and rapidly cleared compounds such as short-chain PFASs.

Cetaceans, as top predators, accumulate these toxins via the marine food web. To enhance the predictive power of the PBTK model, it is imperative to monitor the accumulation of contaminants across multiple trophic levels of the dolphins' prey.

Future iterations of the model will incorporate these food-web-derived concentrations into the dietary intake parameters (ADI). This refinement will allow for a more realistic simulation of biomagnification effects, ensuring that the model captures the cumulative risk posed by the 'cocktail' of toxins stored in their prey.

In this study, model uncertainty remains largely driven by variability in partition coefficients and metabolic clearance parameters. Thus, experimental determination of these compound-specific kinetic constants, especially for non-model species like cetaceans, should be prioritized in future work. Improved parameterization will enhance the reliability of internal dosimetry predictions, particularly for less-characterized pollutants or emerging contaminants.

In Chapter 4, we identified the presence of numerous unrecognized toxic pollutants in seawater, while in this chapter, we found that many affected but previously unidentified toxicological endpoints exist for marine mammals exposed to polluted environments. Machine learning approaches hold substantial potential to complement traditional toxicokinetic modeling. By training models on molecular descriptors and empirical toxicity datasets, predictive tools could be developed to flag chemicals with high dermal or systemic risk potential, even in the absence of *in vivo* data. These tools could also aid in high-throughput prioritization of unmonitored or newly detected environmental contaminants.

Finally, this study further underscores the importance of regionalized risk assessment. While current contaminant levels in Hong Kong waters appear below risk thresholds, reverse dosimetry projections reveal that nearby ecosystems such as the Bohai, East China, and Yellow Seas may exceed dermal toxicity thresholds for compounds like DTX-1. Continuous seasonal monitoring, particularly during HABs, is

essential to accurately capture episodic exposure peaks. Such region-specific data will allow PBTK-QIVIVE tools to support environmental threshold setting, early warning systems, and more targeted conservation policies for marine mammals.

Collectively, these advancements will enable more holistic and predictive assessments of chemical mixture risks in cetaceans, bridging laboratory-derived toxicological insights with ecological health protection.

5.8. Summary

This chapter presented a PBTK-QIVIVE framework to quantify internal exposure, assess chemical-specific dermal burdens, and predict in vivo toxicological risks for Indo-Pacific humpback dolphins. By integrating environmental concentration data, physiologically informed modeling, and in vitro potency metrics, this approach revealed substantial differences between external and internal risk estimations. Notably, chemicals such as DTX-1, GYM, PFOS, and 4-MBC emerged as key internal risk drivers, while highly prevalent short-chain PFASs showed low dermal accumulation and risk under current assumptions.

The results highlight the critical role of pharmacokinetics in shaping dermal hazard patterns. High-potency, fast-clearing algal toxins posed episodic but acute risks, particularly in bloom-prone regions, whereas slowly cleared lipophilic contaminants contributed to cumulative, chronic burdens. External concentrations alone were insufficient to capture these dynamics, underscoring the importance of internal dose modeling and freely dissolved effect concentration correction in ecological risk assessment.

Reverse dosimetry further allowed the derivation of minimum environmental

concentrations required to trigger risk-relevant skin responses. Comparisons with real-world data identified certain coastal hotspots, such as the East China Sea and Bohai Sea, where dolphin populations may face elevated exposure to toxins exceeding modeled effect thresholds.

Future efforts should expand PBTK model compartments, incorporate organ-specific cell types, and integrate emerging techniques such as iPSC and machine learning–based toxicity predictors. These advancements will improve mechanistic understanding, facilitate cross-species extrapolation, and enable proactive conservation measures for threatened marine mammals in dynamic pollutant landscapes.

6. Identification and Source Analysis of Key Toxic Substances Considering Cytotoxicity and Oxidative-mediated damage: A Combination of Machine Learning and Nontarget Analysis

Interpreting non-target chemical fingerprints is a major bottleneck in coastal environmental toxicology, where complex mixtures arise from overlapping anthropogenic and natural inputs. In subtropical waters influenced by Hong Kong coastal seawater, high-resolution mass spectrometry detects thousands of chemical features, yet only a small fraction can be confidently identified or causally linked to bioassay responses. This high-dimensional, low-annotation constraint limits targeted monitoring and motivates ML approaches that infer toxicity–chemistry relationships directly from feature space. Building on previous results of mixture toxicity and the chemical iceberg effect, this chapter develops a data-driven framework to connect non-target fingerprints with endpoint-specific toxicological outcomes relevant to cetacean habitats. Through this approach, this chapter aims to elucidate (1) the feasibility and limitations of RF-based toxicity prediction from non-target fingerprints, (2) the endpoint-specific chemical class signatures, and (3) the dominant high- and medium-toxicity drivers and source sectors in coastal waters.

6.1. Performance evaluation of random forest classifiers for toxicity prediction

To assess the feasibility of predicting toxicological outcomes based on non-target chemical fingerprints, random forest (RF) classification models were constructed for cytotoxicity, DNA damage, and ROS endpoints. The model performance was rigorously evaluated using k-fold cross-validation, accuracy and F1-macro scores to ensure reliability.

Among the three endpoints, the cytotoxicity model demonstrated the most robust predictive capability. It achieved an average accuracy of 80.0% and an F1-macro score of 0.796 across a 3-fold cross-validation (**Table 6. 1**). Although the cross-validation scores exhibited variance (ranging from 0.60 to 1.0), likely due to the limited sample size inherent in field-based toxicological studies, the high average F1-score indicates that the identified chemical features possess a strong, linear correlation with acute cell viability.

In contrast, the DNA damage model displayed moderate predictive power, yielding an average accuracy of 74.4% but a notably lower F1-macro score of 0.598 (**Table 6. 1**). The discrepancy between the high accuracy and the moderate F1 score points to challenges in class balancing, implying that while the model can identify the general trend of DNA damage, its sensitivity in distinguishing between specific toxicity levels (e.g., medium or high) is lower than that of the cytotoxicity model.

The ROS model showed the most limited performance, with an average accuracy of 64.6% and an F1-macro score of 0.467 (**Table 6. 1**). Due to sample constraints, only a 2-fold cross-validation was feasible, further indicating the data scarcity for this

endpoint. The low F1 score suggests that the chemical features detected by the current analytical window were insufficient to fully explain the variance in ROS generation. Consequently, the cytotoxicity and DNA damage model were selected as the primary tools for the subsequent feature importance analysis. The predicted results of the ROS model will be discussed in a supplementary.

Table 6. 1 Performance metrics of random forest (RF) classification models predicting cytotoxicity, DNA damage, and reactive oxygen species (ROS) generation based on non-target chemical fingerprints. Model performance was assessed using k-fold cross-validation, reporting both average classification accuracy and F1-macro scores.

Endpoints	Average accuracy	Average F1_macro	Cross-validation
Cytotoxicity	80.0%	0.796	3-fold
DNA damage	74.4%	0.598	3-fold
ROS	64.6%	0.467	2-fold

6.2. Profile analysis and distribution characteristics of predicted toxicity compounds

A comparative analysis of the chemical source profiles reveals a distinct decoupling between the structural diversity of detected compounds and their cumulative abundance across different toxicological endpoints. As illustrated in the cytotoxicity source analysis (**Figure 6. 1 (a)**), the profile is predominantly driven by benzenoids and lipids and lipid-like molecules. Benzenoids exhibited both the highest structural diversity (> 85 compounds) and the greatest cumulative peak area, suggesting that the bulk of cellular lethality is attributable to a wide array of abundant aromatic compounds. Furthermore, while lipids ranked second in both metrics, the presence of specific high-toxicity features within this class indicates that lipophilic components significantly contribute to cell death mechanisms. Conversely, the DNA damage profile (**Figure 6. 1 (b)**) presents a marked contrast in the behavior of organoheterocyclic

compounds. While this superclass displayed the highest structural diversity (> 105), a finding consistent with the known pharmacological propensity of heterocyclic moieties to interact with nucleic acids by intercalation, their relative abundance was notably low compared to benzenoids and lipids. This discrepancy implies that while the sample contains a vast array of distinct organoheterocyclic structures capable of interacting with DNA. In contrast, the abundance of induced DNA damage compounds is dominated in abundance by benzenoids, indicating that fewer, but highly abundant species within this class may be responsible for the majority of genotoxic stress. Additionally, the ROS generation profile (**Figure 6. 1 (c)**) was characterized by a unique dominance of organic oxygen compounds in terms of abundance, despite having only moderate diversity. Whereas the contribution from lipids is distributed across a wider variety of structural analogs susceptible to peroxidation.

Across all three toxicity endpoints, only a small fraction of compounds was identified as high toxicity compounds (8 for cytotoxicity, 8 for DNA damage and 0 for ROS) (**Figure 6. 2**). It suggests that cytotoxicity and DNA damage risk are driven by a very small subset of the detected chemical features. Hundreds of compounds were classified as medium toxicity (322 for cytotoxicity, 507 for DNA damage, and 397 for ROS) (**Figure 6. 2**). This distribution indicates that while the studied environment contains a complex mixture of bioactive compounds, the majority present a moderate rather than acute toxicological risk at environmental concentrations.

Comparing the wet and dry seasons reveals a high degree of temporal stability (**Figure 6. 2**). The overall structure of the Sankey flows remains consistent, with no drastic shifts in the proportional contributions of major chemical classes or the distribution of toxicity levels. For instance, while the contribution of lipids to DNA

damage appeared marginally more pronounced in the dry season, and the benzenoid contribution to cytotoxicity was visually robust in the wet season, these variations were subtle. The absence of any sudden emergence of high toxicity or the disappearance of major chemical streams confirms that the sources of toxicity are persistent and not subject to extreme seasonal fluctuations.

A Pareto analysis about three endpoints was conducted to quantify this concentration of chemical load. For cytotoxicity (**Figure 6. 3 (a)**), the top 10 most abundant compounds (representing about 2.8% of features) accounted for 64.6% of the total peak area. Similarly, for the DNA damage endpoint (**Figure 6. 3 (b)**), the top 10 compounds contributed 58.2% of the total abundance. The ROS endpoint showed the most extreme concentration, with the top 10 compounds explaining 72.1% of the total signal intensity (**Figure 6. 3 (c)**). In all cases, extending the analysis to the top 30 compounds (**Table 6. 2**) covered approximately 80% of the cumulative chemical load. Therefore, in the subsequent analysis of medium toxic compound sources, the focus is primarily on the top 30 compounds in terms of the peak area.

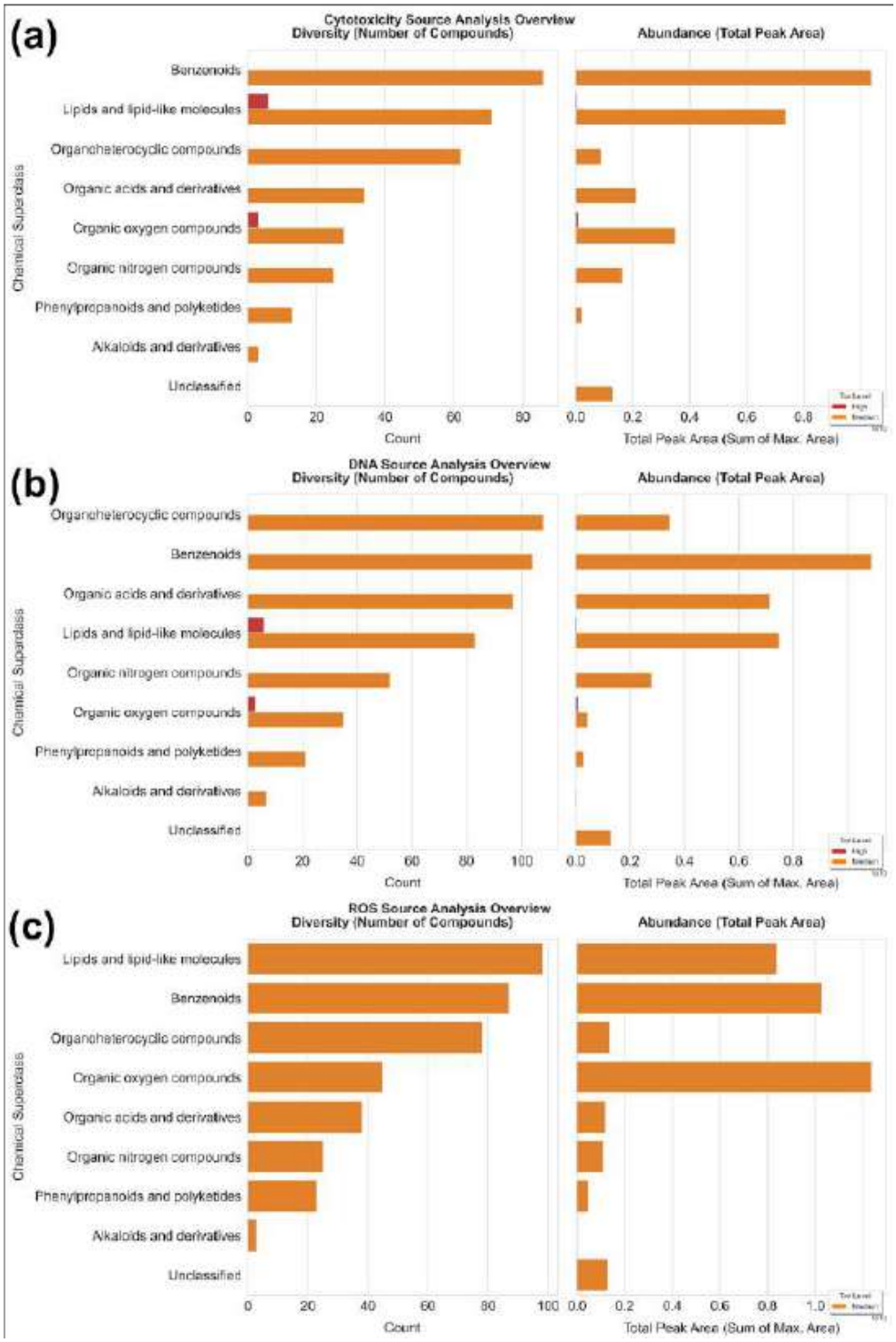

Figure 6. 1 Source class profiles of toxicologically active compounds across three biological endpoints: (a) cytotoxicity, (b) DNA damage, and (c) ROS induction.

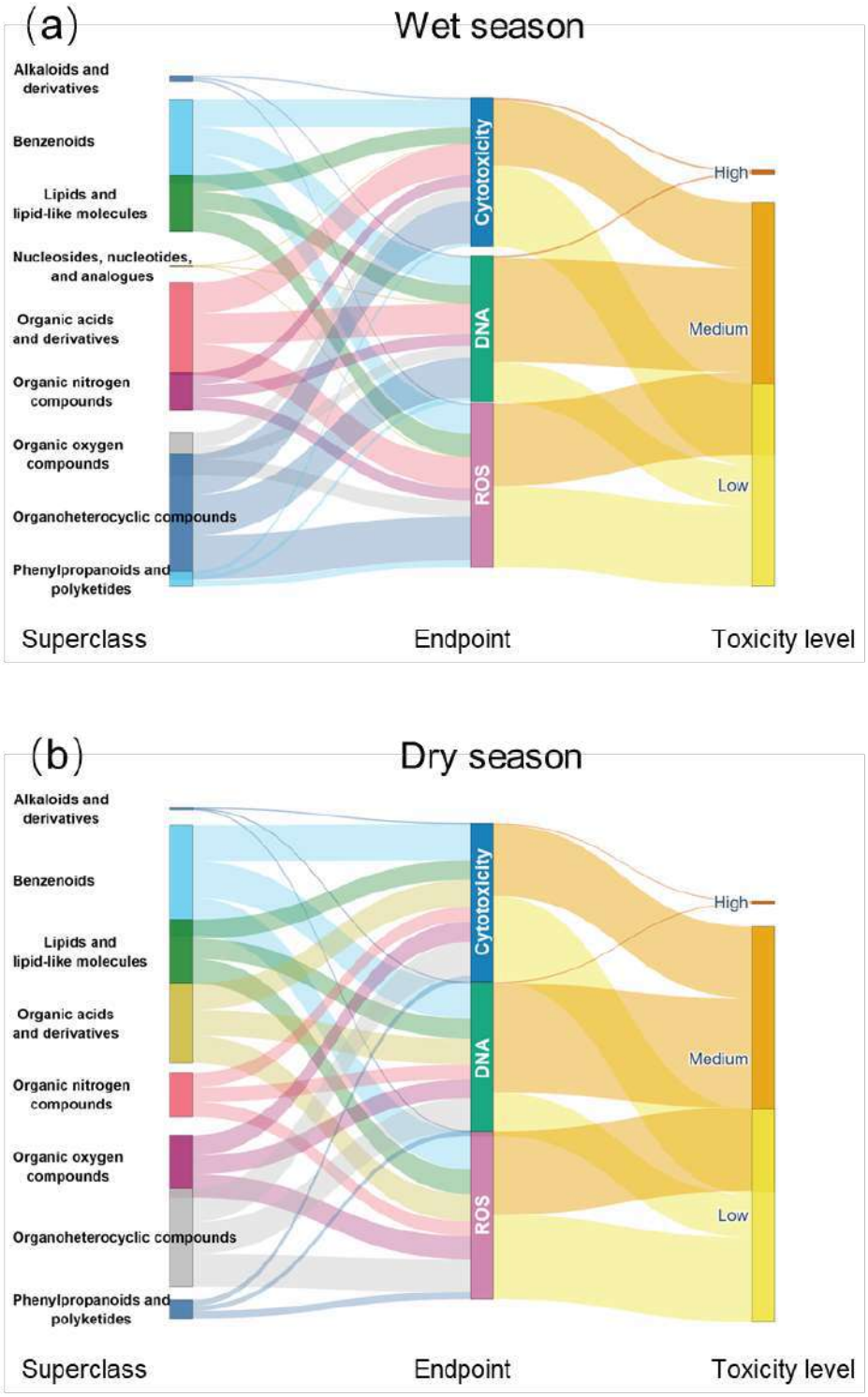

Figure 6. 2 The Sankey shift of the distribution of chemical superclass contributing to different toxicological endpoints and toxicity level during the (a) wet and (b) dry seasons.

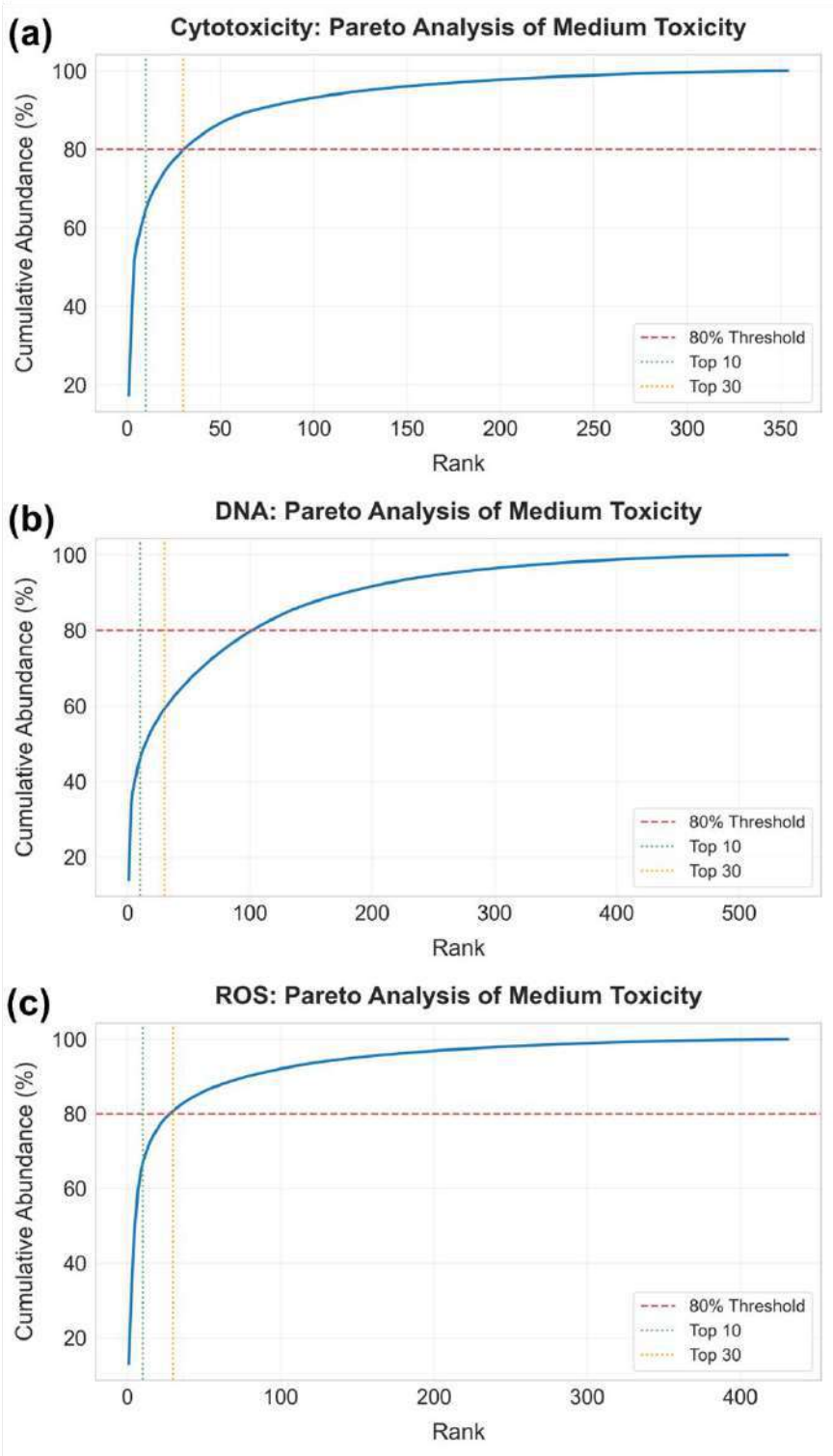

Figure 6. 3 Cumulative abundance (Pareto) analysis of medium-toxicity compounds across three toxicity endpoints: (a) Cytotoxicity, (b) DNA damage, and (c) ROS generation. The green and yellow dashed lines indicate the cumulative contribution of the top 10 and 30 ranked compounds, respectively, demonstrating that a small fraction of dominant features accounts for the majority (58%–72%) of the total chemical load.

6.3. Identification of predicted high toxicity compounds and source analysis

Although eight highly toxic compounds (**Table 6. 2**) were predicted in both the cytotoxicity and DNA damage endpoints, only three had mzCloud match scores exceeding 0.75, namely resiniferatoxin (RTX), clarithromycin, and a specific cinnamoyl-iridoid glycoside identified as lippianoside B. This indicates that the detection of these three compounds in the samples is the most reliable, and thus their sources are analyzed in detail.

RTX is a naturally occurring high-potency toxin with influence for aquatic vertebrates. Originating from the latex of *Euphorbia* species such as *Euphorbia resinifera*, RTX is classified as a lipid and lipid-like molecule. RTX with its homovanillic ring is a natural, high-potency ligand of the capsaicin receptor in a subpopulation of primary afferent sensory neurons involved in the transmission of pain (Mourtzoukou et al., 2008). It functions as an ultrapotent agonist of the TRPV1 channel. Therefore, RTX has been normally used as a treatment for chronic pain.

While this selective neuroablation is therapeutically exploited for intractable pain, systemic exposure to RTX carries severe toxicological risks. While mammalian toxicity is often defined by an oral LD_{50} of 148.1 mg/kg in rats (Material Safety Data Sheet for resiniferatoxin, 2009), aquatic vertebrates are far more susceptible due to direct absorption across gill membranes. Studies on related Euphorbia latex extracts have demonstrated lethal concentrations in catfish (*Heteropneustes fossilis*) as low as 1.3 μL/L over 96 hours (Kumar et al., 2010). Historically, the latex containing this compound has been utilized as a piscicide, a practice that highlights its extremely acute toxicity to fish (Kgosiemang et al., 2025).

In contrast to the natural source of RTX, clarithromycin is a semisynthetic macrolide antibiotic. Classified chemically within the phenylpropanoids and polyketides superclass, derived from erythromycin A through 6-O-methylation (Della-Negra et al., 2025). As a pharmaceutical and personal care product, clarithromycin is typically discharged into aquatic environments through wastewater treatment plants and maintained long-term exposure levels in surface waters to aquatic organisms. The acute toxicity assays for fish (*Oncorhynchus mykiss*) and invertebrates is low at environmentally relevant levels compared to RTX. Due to its ability to inhibit the 50S ribosomal subunit in bacteria, clarithromycin can also suppress protein binding within the chloroplasts of algae and cyanobacteria. Standard toxicity tests with the green alga *Pseudokirchneriella subcapitata* have established a 72-hour LC_{50} of approximately 6.9 μg/L, a toxic potency order of magnitude higher than that for vertebrates (Aderemi et al., 2018). This specific toxicity places primary production at risk, potentially destabilizing aquatic food webs from the bottom up.

The third compound analyzed is defined by the IUPAC designation (1S,4aS,7aS)-7-({[(2E)-3-phenylprop-2-enoyl]oxy}methyl)-1-{oxy}-1H,4aH,5H,7aH-cyclopenta[c]pyran-4-carboxylic acid. Structural deconstruction reveals this molecule to be an iridoid glycoside. From a structure-activity relationship perspective, this molecule serves as a pro-toxicant in aquatic environments. The intact glycoside is relatively polar and water-soluble, facilitating transport in the water column. However, its environmental hazard is predicated on two reactive pharmacophores: the α, β-unsaturated carbonyl of the cinnamoyl ester and the potentially reactive iridoid core (Wisetsai et al., 2022). In aquatic organisms, α, β-unsaturated carbonyls exhibit excess toxicity relative to their hydrophobicity because they can irreversibly alkylate nucleophilic sulfhydryl groups on enzymes and deplete cellular glutathione (Jackson et

al., 2017). Studies on related cinnamic acid esters have demonstrated significant larvicidal activity against aquatic invertebrates (e.g., *Aedes aegypti*), with LC_{50} values in the range of 48 μg/mL (Correia et al., 2022). Furthermore, metabolic or microbial hydrolysis of the glycosidic bond releases the aglycone, which can rearrange to form genipin (Sobolewska et al., 2025). Genipin is a potent protein cross-linking agent that has been shown to induce teratogenic effects in zebrafish embryos (Danio rerio), including pericardial edema, tail malformations, and hepatotoxicity, at concentrations as low as 50 μg/mL (Xia et al., 2021).

6.4. Identification of predicted medium toxicity compounds and source analysis

The source apportionment analysis of medium-toxicity compounds across all three endpoints (**Table 6. 2**). By cross-referencing the 30 most abundant compounds identified in each toxicity endpoint, a core set of nine ubiquitous pollutants was isolated, constituting the permanent chemical background of the receiving water body. This foundational assemblage is dominated by 4-dodecylbenzenesulfonic acid (LAS), erucamide, N,N-diethyl-m-toluamide (DEET), and tris(2-butoxyethyl) phosphate (TBEP). The extremely high abundance of LAS and DEET across all endpoints serves as definitive evidence of domestic wastewater discharge, directly linking the pollution load to high-density anthropogenic activities such as daily washing and personal care. Concurrently, the pervasive presence of erucamide, a slip agent, and TBEP, a flame retardant, indicates substantial and continuous inputs from microplastic leaching and urban surface runoff containing indoor dust.

The specific contaminant profiles for each endpoint elucidated the complexity of the mixture's toxicological mechanisms. The ROS induction was uniquely

characterized by a high load of hydrophilic polymers, particularly polyethylene glycol (PEG) and polypropylene glycol (PPG) series. Unlike abundance drivers of cytotoxicity or DNA damage, the primary contributors to ROS generation were not highly bioactive monomers but rather a complex matrix derived from personal care products, such as shampoos and toothpastes. This suggests that oxidative stress within seawater is not primarily induced by acute specific compounds, but rather by the cumulative osmotic stress and metabolic burden imposed by a high load of synthetic polymers.

In contrast, the DNA damage profile captured specific bioactive threats and industrial emission signals. Unique markers for DNA damage included caprolactam, a monomer used in nlon-6 production, pointing towards textile industry effluents or the degradation of environmental microplastic fibers. Furthermore, the detection of beta-blocker alprenolol and additives like betaine implies that specific pharmaceutical residues and agricultural or cosmetic additives are key contributors to DNA damage, potentially interfering with DNA replication or repair mechanisms (Maszkowska et al., 2014; Sanz-Serrano et al., 2021). Similarly, the cytotoxicity profile prioritized complex heterocyclic compounds and legacy plasticizers such as DEHP, indicating inputs from fine chemical manufacturing and toxic plastic additives that directly compromise cell viability (Al-Saleh et al., 2020). In summary, the water body of Hong Kong coastal water exhibits a complex mixed-source pollution profile where the fundamental chemical burden is driven by a domestic wastewater-plastic complex, creating a shared stress environment, while specific toxicological pathways are triggered by distinct sectors, underscoring the necessity of a multi-endpoint approach to fully deconstruct environmental chemical risks.

Table 6. 2 List of prioritized compounds classified as high and medium toxic componds across cytotoxicity, DNA damage, and ROS endpoints, based on RF integrated with NTS prediction.

Compounds	Superclass	Class	Peak area (Max.)	mzCloud best match	Toxicity level	Endpoints
(1S,4aS,7aS)-7-({[(2E)-3-phenylprop-2-enoyl]oxy}methyl)-1-{[(2S,3R,4S,5S,6R)-3,4,5-trihydroxy-6-(hydroxymethyl)oxan-2-yl]oxy}-1H,4aH,5H,7aH-cyclopenta[c]pyran-4-carboxylic acid	Lipids and lipid-like molecules	Prenol lipids	3.55E+07	93.6	High	Cytotoxicity; DNA damage
Resiniferatoxin	Lipids and lipid-like molecules	Prenol lipids	1.06E+07	84.7	High	Cytotoxicity; DNA damage
Clarithromycin	Organic oxygen compounds	Organooxygen compounds	8.18E+06	93.7	High	Cytotoxicity; DNA damage
3,3,5,5-Tetramethylpyrroline-N-	Organoheterocyclic compounds	Pyrrolidines	1.84E+08	93.9	Medium	DNA damage

Compounds	Superclass	Class	Peak area (Max.)	mzCloud best match	Toxicity level	Endpoints
oxide						
4-Dodecylbenzenesulfonic acid	Benzenoids	Benzene and substituted derivatives	3.13E+09	99.8	Medium	Cytotoxicity; DNA damage; ROS
5-(1,3-diphenyl-1H-pyrazol-4-yl)-7-(4-methylphenyl)-5H-[1,3]thiazolo[3,2-a]pyrimidin-3(2H)-one	Organoheterocyclic compounds	Benzodiazepines	1.39E+08	97.9	Medium	Cytotoxicity; ROS
Alprenolol	Benzenoids	Phenol ethers	1.95E+08	98.8	Medium	DNA damage
Bis(2-ethylhexyl) amine	Organic nitrogen compounds	Organonitrogen compounds	2.53E+08	88	Medium	Cytotoxicity; DNA damage; ROS
Bis(2-ethylhexyl) phthalate	Benzenoids	Benzene and substituted derivatives	1.35E+08	99.5	Medium	Cytotoxicity; ROS
Caprolactam	Organoheterocyclic	Lactams	2.76E+08	95.6	Medium	DNA damage

Compounds	Superclass	Class	Peak area (Max.)	mzCloud best match	Toxicity level	Endpoints
	compounds					
Citroflex A-4	Organic acids and derivatives	Carboxylic acids and derivatives	3.05E+08	99.2	Medium	Cytotoxicity; DNA damage; ROS
DEET	Benzenoids	Benzene and substituted derivatives	3.66E+09	99.4	Medium	Cytotoxicity; DNA damage; ROS
Erucamide	Lipids and lipid-like molecules	Fatty Acyls	4.75E+09	90	Medium	Cytotoxicity; DNA damage; ROS
Hexadecanamide	Lipids and lipid-like molecules	Fatty Acyls	1.47E+08	97.8	Medium	Cytotoxicity; DNA damage
Octadecanamine	Organic nitrogen compounds	Organonitrogen compounds	5.52E+08	99.7	Medium	Cytotoxicity; DNA damage
PEG n7	Organic oxygen compounds	Organooxygen compounds	1.67E+09	98.7	Medium	ROS
PEG n8	Organic oxygen	Organooxyg	1.79E+09	97.3	Medium	ROS

Compounds	Superclass	Class	Peak area (Max.)	mzCloud best match	Toxicity level	Endpoints
	compounds	en compounds				
PPG n4	Organic oxygen compounds	Organooxygen compounds	4.19E+09	99.3	Medium	ROS
PPG n5	Lipids and lipid-like molecules	Glycerolipids	9.31E+08	98.9	Medium	Cytotoxicity; DNA damage; ROS
PPG n6	Organic oxygen compounds	Organooxygen compounds	2.61E+09	98.8	Medium	Cytotoxicity; ROS
PPG n7	Lipids and lipid-like molecules	Fatty Acyls	1.03E+09	99.8	Medium	ROS
Stearamide	Organic acids and derivatives	Carboximidic acids and derivatives	4.61E+08	98.9	Medium	Cytotoxicity; DNA damage
Tributylamine	Organic nitrogen compounds	Organonitrogen compounds	2.30E+08	92.1	Medium	Cytotoxicity; DNA damage; ROS
Tris(2-butoxyethyl)	Organic acids and	Organic	1.72E+08	94.5	Medium	Cytotoxicity;

Compounds	Superclass	Class	Peak area (Max.)	mzCloud best match	Toxicity level	Endpoints
phosphate	derivatives	phosphoric acids and derivatives				DNA damage; ROS

6.5. Summary

Chapter 6 demonstrated that non-target chemical fingerprints can be operationalized into predictive and interpretive tools for mixture toxicity assessment by integrating random forest (RF) classification with chemical profile analysis and source apportionment. Model evaluation across three biological endpoints established a clear performance gradient. The cytotoxicity classifier showed the strongest predictive capability, achieving an average accuracy of 80.0% and an F1-macro score of 0.796 under 3-fold cross-validation, indicating that the detected chemical features captured a comparatively direct and consistent relationship with acute loss of cell viability, despite fold-to-fold variability attributable to the constrained sample size typical of field-derived datasets. The DNA damage model exhibited moderate performance, with an average accuracy of 74.4% but a lower F1-macro score of 0.598, implying that class imbalance and overlap among toxicity levels limited the model's ability to discriminate medium and high responses even when overall trend prediction was acceptable. The ROS model performed least well, with an average accuracy of 64.6% and an F1-macro score of 0.467, and its evaluation was further restricted to 2-fold cross-validation, collectively suggesting that the current analytical feature space was insufficient to explain ROS variability; therefore, subsequent interpretation prioritized the cytotoxicity and DNA damage models, while ROS predictions were retained as supplementary evidence.

Chemical profile analysis further revealed that toxicity was not simply proportional to the structural diversity or total abundance of detected compounds, but instead reflected endpoint-specific superclasses with distinct "diversity–abundance"

decoupling. Cytotoxicity was dominated by benzenoids and lipid-like molecules, where benzenoids combined the greatest diversity and cumulative signal, consistent with aromatic compounds constituting the bulk of lethal mixture burden. For DNA damage, organoheterocyclic compounds displayed the highest diversity yet relatively low abundance, supporting the inference that many structurally diverse heterocycles may contribute to genotoxic potential, while a smaller set of highly abundant benzenoids likely drives the majority of the measured DNA stress. ROS profiles were characterized by high abundance of organic oxygen compounds despite only moderate diversity, consistent with oxidative potential being driven by oxygenated matrices and broad susceptibility to downstream peroxidation processes rather than a few discrete, highly bioactive toxins.

Across endpoints, the toxicity distribution was highly skewed: only eight compounds were classified as highly toxic for cytotoxicity and DNA damage, and none for ROS, whereas hundreds of compounds fell into the medium-toxicity category, indicating that risk is concentrated in a small subset of features while most detected compounds impose moderate bioactivity at environmental levels. Seasonal comparison using Sankey-based source–toxicity flows showed strong temporal stability between wet and dry periods, with only subtle shifts and no evidence of abrupt emergence or disappearance of dominant toxicological streams, implying persistent sources rather than episodic seasonal drivers. Consistent with this concentration, Pareto analysis indicated that a small fraction of the most abundant features accounted for the majority of cumulative signal across endpoints, and the top 30 compounds captured approximately 80% of the chemical load, justifying a focused source interpretation on the most abundant candidates.

High-toxicity identification emphasized the importance of annotation confidence: among the eight predicted high-toxicity compounds in both cytotoxicity and DNA damage, only three achieved high mzCloud match scores (>0.85), namely resiniferatoxin, clarithromycin, and lippianoside B, and these were therefore prioritized for detailed source and hazard interpretation. Finally, medium-toxicity source apportionment converged on a core background assemblage shared across endpoints, dominated by markers of domestic wastewater discharge (e.g., LAS and DEET) alongside signals consistent with microplastic leaching and urban runoff (e.g., erucamide and TBEP). Endpoint-specific patterns further clarified mechanistic diversity: ROS-associated mixtures were enriched in hydrophilic polymer series (PEG/PPG), consistent with a cumulative "chemical soup" burden, while DNA damage and cytotoxicity profiles incorporated more specific industrial and legacy pollutant signatures (e.g., caprolactam, pharmaceuticals, and plasticizers). Collectively, Chapter 6 supports a multi-endpoint, machine-learning-enabled framework in which persistent mixed sources generate a shared background stress environment, while distinct chemical sectors preferentially activate specific toxicological pathways.

7. Conclusions and Suggestions for Future Research

This thesis establishes a comprehensive and mechanism-based bioanalytical framework to address the escalating challenges posed by complex chemical cocktails in the marine environment, with a particular focus on the Indo-Pacific humpback dolphin and finless porpoise as sentinel species. By integrating species-specific cell lines, high-resolution non-target analysis, machine learning algorithms, and PBTK-QIVIVE, this research advances the field of cetacean toxicology from descriptive assessments to predictive, dose-based risk evaluations.

A fundamental achievement of this study is the successful establishment and characterization of the species-specific skin fibroblast cell line for the Indo-Pacific humpback dolphin. Given the extreme ethical and logistical constraints associated with sampling endangered marine mammals, this immortalized cell platform provides a robust and biologically relevant surrogate for assessing toxicological assessment. Comparative analyses with the Indo-Pacific finless porpoise revealed significant interspecies differences in sensitivity to environmental contaminants. These findings underscore the critical necessity of using species-specific models rather than generic laboratory animal-based assays to avoid underestimating or miscalculating the actual risks faced by local cetacean populations.

One of the most significant discoveries of this research is the identification of naturally occurring algal toxins as the primary drivers of biological toxicity in the coastal waters of the Indo-Pacific. While anthropogenic contaminants such as PFAS,

UV filters, and pharmaceuticals were found to be ubiquitous in the marine environment, their acute toxic potencies were several orders of magnitude lower than those of natural toxins. Specifically, PTX-2, OA, and GYM were identified through targeted analysis and bioanalytical mixture modeling as the dominant contributors to cytotoxicity and oxidative stress. These finding challenges prevailing regulatory paradigms that focuses almost on industrial and agricultural chemicals, suggesting that the natural chemical background in warming oceans may pose a more immediate threat to the health of marine megafauna than previously recognized.

This thesis also presents the first PBTK-QIVIVE model developed for the Indo-Pacific humpback dolphin. By constructing a five-compartment model, the research successfully bridged the gap between external exposure concentrations and internal tissue doses. The internal risk assessment revealed that conventional water quality monitoring underestimates the actual hazard. The model revealed that pharmacokinetic factors, such as high protein binding and tissue-specific accumulation, amplify the internal risk of toxins like DTX-1 and GYM in the skin and blubber compartments. This modeling framework provides a more accurate, physiologically grounded perspective for ecological risk assessment, allowing for the calculation of biologically effective doses that traditional monitoring fails to capture.

To address the unexplained fraction of mixture effects, where targeted chemical analysis could only explain a small fraction of the observed biological effects, this study integrated NTS with RF machine learning algorithms. The implementation of NTS in this thesis aligns with pioneering international efforts, such as the European LIFE APEX project (Treu et al., 2022), which advocates for the systematic use of chemical monitoring data from apex predators to support chemical prioritization and risk

assessment. High-resolution NTS has proven highly effective in European marine ecosystems; for instance, a 30-year temporal trend study in the Baltic Sea successfully identified over 300 organic contaminants in harbor porpoises (Rebryk et al., 2022), while recent investigations in the North Sea used NTS to characterize complex patterns of legacy and emerging PFAS in dolphin bones (Salangad et al., 2025).

While these European studies underscore the persistent burden of anthropogenic pollutants in high-latitude waters, this research in Hong Kong reveals a unique toxicological landscape dominated by the interplay between natural algal toxins and anthropogenic chemicals. The machine learning model achieved high accuracy in predicting cytotoxicity and identified several high-potency candidates, including resiniferatoxin and certain pharmaceuticals like clarithromycin, which had been overlooked previously. The integration of NTS and ML demonstrates that the unknown toxic compounds in these waters may origin from a persistent matrix of wastewater- and plastic-associated compounds. Furthermore, while this research extracts most chemicals from seawater, the inorganic contaminants remain to be analyzed. Future studies should incorporate specialized extraction protocols for inorganic fractions alongside organic enrichment.

Collectively, these findings provide a holistic view of the chemical pressures facing cetaceans and offer a scientific basis for more targeted conservation and management strategies.

Building upon the methodologies and findings of this thesis, several promising directions for future research are proposed to further enhance the conservation of marine mammals and our understanding of marine chemical ecology. Primary direction involves the transition from traditional bioassays to an integrated approach combining

deep learning-based predictive approach with biological experimental validation. Our ongoing work implements an in-house deep representation learning framework to systematically resolve the toxicological contributions of unidentified chemical features in seawater samples. This framework employs a chemical foundation model pre-trained on extensive bioactivity data from cetacean fibroblasts and uses a Siamese meta-learning architecture to encode pairwise differences between compounds. Fine-tuned with species-specific bioassay data, the model will enable quantitative predictions of effect concentrations (e.g., EC_{10} for cytotoxicity and $EC_{IR1.5}$ for oxidative stress or DNA damage) for unidentified chemical features resolved by HRMS. This specific technical pipeline allows for a precise apportionment of biological risk to specific chemicals within the complex marine matrix, even in the absence of analytical standards.

The toxic effects of marine pollutants in marine mammals often begin with direct interactions with intracellular macromolecules such as proteins, DNA, and lipids. Among these, binding to specific proteins or interfering with their functions constitutes a critical molecular initiating event (MIE) that triggers downstream biological cascades. Current *in vitro* assays are limited to known endpoints and fail to capture large-scale molecular responses to the chemical diversity found in marine environments. The integration of chemical exposomics with molecular responses, a multi-diagnostic approach recently employed to evaluate the susceptibility of Mediterranean fin whales to complex anthropogenic contaminants exposure (Fossi et al., 2025). Therefore, future Hong Kong based monitoring programs should transition from conventional, endpoint-limited bioassays to a multi-dimensional, predictive framework that bridges the gap between chemical exposure and molecular health effects. This could be achieved by combing high-resolution NTS with transcriptomics to predict MIEs and adverse outcomes across multiple biological endpoints using advanced transformer-based deep

learning approach. By validating these predicted protein targets against the transcriptomic fingerprints, specifically the differentially expressed genes from cetacean cell exposures, critical biological pathways perturbed by contaminants such as xenobiotic metabolism and inflammatory signaling will be elucidated. This integrative strategy facilitates the high-throughput prediction of diverse endpoints, including endocrine disruption and neurotoxicity, providing a more comprehensive, physiologically grounded perspective for cetacean conservation.

Another critical frontier is the advancement of stem cell technology in marine toxicology. While the skin fibroblast cell lines established in this work are valuable, they represent only a single tissue type. Future research should focus on the conversion of humpback dolphin fibroblasts into iPSCs. These iPSCs could then be differentiated into various tissue-specific cells, such as hepatocytes for metabolic studies, neurons for neurotoxicity assessment, or renal cells for excretion studies. Developing these organ-on-a-chip or 3D organoid platforms would provide a more comprehensive system to evaluate systemic toxicity and the metabolic activation of pro-toxicants, which cannot be fully captured by 2D fibroblast cultures.

Finally, a primary focus for our future work involves adapting the current framework to assess ecotoxicological exposure for non-resident cetacean species with large migration patterns. To achieve this, the PBTK-QIVIVE model must transition from a steady-state assumption to a dynamic exposure model. For example, the ADI parameter needs to be adjusted from a constant value to a dynamic function based on contaminant monitoring data collected along specific migration routes. Furthermore, as migratory cetaceans inhabit diverse water bodies, the composition and ratios of accumulated contaminants vary significantly. Future research should utilize NTS to

analyze the chemical profiles within different layers of stratified blubber tissues. By incorporating these real-world tissue measurements, we can optimize the partition coefficients and refine the predictive accuracy of the PBTK model for species facing heterogeneous exposure across vast geographic scales. The continuous refinement and validation of these predictive PBTK models necessitate extensive global cooperation and the harmonization of regional monitoring data. To truly perfect the modeling framework, it is essential to obtain more detailed and stage-specific exposure parameters from diverse geographic hotspots. In the future, we propose to establish a global network for data exchange to link the toxicological findings in Hong Kong with international exposomics initiatives and large-scale monitoring projects like LIFE APEX, it will be the cornerstone for developing a truly holistic model. Such collaborative efforts are essential for obtaining comprehensive data required to improve model predictions and provide a scientific basis for the global management of pollutants and the protection of vulnerable cetacean species worldwide.

Integrating these improved methods into regional long-term monitoring programs will allow for the development of dynamic, proactive protection measures that can adapt to the evolving chemical landscape of the world's oceans. This integrated approach combining cutting-edge molecular biology, computational modeling, and environmental chemistry will be essential for ensuring the long-term survival of these iconic marine species.

8. References

Aderemi, A. O., Novais, S. C., Lemos, M. F. L., Alves, L. M., Hunter, C., & Pahl, O. (2018). Oxidative stress responses and cellular energy allocation changes in microalgae following exposure to widely used human antibiotics. *Aquatic Toxicology*, *203*, 130–139. https://doi.org/10.1016/j.aquatox.2018.08.008

Allendorf, F., Berger, U., Goss, K.-U., & Ulrich, N. (2019). Partition coefficients of four perfluoroalkyl acid alternatives between bovine serum albumin (BSA) and water in comparison to ten classical perfluoroalkyl acids. *Environmental Science: Processes & Impacts*, *21*(11), 1852–1863. https://doi.org/10.1039/c9em00290a

Al-Saleh, I., Elkhatib, R., Al-Rajoudi, T., Al-Qudaihi, G., Manogarannogaran, P., Eltabache, C., Alotaibi, A., Mummer, A. B., & Almugbel, S. (2020). Cytotoxic and genotoxic effects of e-liquids and their potential associations with nicotine, menthol and phthalate esters. *Chemosphere*, *249*, 126153. https://doi.org/10.1016/j.chemosphere.2020.126153

Anderson, S. E., & Meade, B. J. (2014). Potential health effects associated with dermal exposure to occupational chemicals. *Environmental Health*

Insights, *8*(Suppl 1), 51–62. https://doi.org/10.4137/EHI.S15258

Arturi, K., & Hollender, J. (2023a). Machine Learning-Based Hazard-Driven Prioritization of Features in Nontarget Screening of Environmental High-Resolution Mass Spectrometry Data. *Environmental Science & Technology*, *57*(46), 18067–18079. https://doi.org/10.1021/acs.est.3c00304

Arturi, K., & Hollender, J. (2023b). Machine Learning-Based Hazard-Driven Prioritization of Features in Nontarget Screening of Environmental High-Resolution Mass Spectrometry Data. *Environmental Science & Technology*, *57*(46), 18067–18079. https://doi.org/10.1021/acs.est.3c00304

Backhaus, T., & Faust, M. (2012). Predictive Environmental Risk Assessment of Chemical Mixtures: A Conceptual Framework. *Environmental Science & Technology*, *46*(5), 2564–2573. https://doi.org/10.1021/es2034125

Bargagli, R., & Rota, E. (2024). Mediterranean Marine Mammals: Possible Future Trends and Threats Due to Mercury Contamination and Interaction with Other Environmental Stressors. *Animals : An Open Access Journal from MDPI*, *14*(16), 2386. https://doi.org/10.3390/ani14162386

Bejarano, A. C., VanDola, F. M., Gulland, F. M., Rowles, T. K., & Schwacke, L. H. (2008). Production and Toxicity of the Marine Biotoxin Domoic Acid and Its Effects on Wildlife: A Review. *Human and Ecological Risk Assessment: An*

International Journal, *14*(3), 544–567. https://doi.org/10.1080/10807030802074220

Bjørneset, J., Blévin, P., Bjørnstad, P. M., Dalmo, R. A., Goksøyr, A., Harju, M., Limonta, G., Panti, C., Rikardsen, A. H., Sundaram, A. Y. M., Yadetie, F., & Routti, H. (2023). Establishment of killer whale (*Orcinus orca*) primary fibroblast cell cultures and their transcriptomic responses to pollutant exposure. *Environment International*, *174*, 107915. https://doi.org/10.1016/j.envint.2023.107915

Bossart, G. D. (2011). Marine Mammals as Sentinel Species for Oceans and Human Health. *Veterinary Pathology*, *48*(3), 676–690. https://doi.org/10.1177/0300985810388525

Bressem, M.-F. V., Waerebeek, K. V., Aznar, F. J., Raga, J. A., Jepson, P. D., Duignan, P., Deaville, R., Flach, L., Viddi, F., Baker, J. R., Beneditto, A. P. D., Echegaray, M., Genov, T., Reyes, J., Félix, F., Gaspar, R., Ramos, R., Peddemors, V., Sanino, G. P., & Siebert, U. (2009). Epidemiological pattern of tattoo skin disease: A potential general health indicator for cetaceans. *Diseases of Aquatic Organisms*, *85*, 225–237. https://doi.org/10.3354/dao02080

Butler, S. C., Miles, C. O., Karim, A., & Twiner, M. J. (2012). Inhibitory effects of pectenotoxins from marine algae on the polymerization of various actin

isoforms. *Toxicology in Vitro*, *26*(3), 493–499. https://doi.org/10.1016/j.tiv.2011.12.015

Cell cycle alterations due to perfluoroalkyl substances PFOS, PFOA, PFBS, PFBA and the new PFAS C6O4 on bottlenose dolphin (tursiops truncatus) skin cell. (2022). *Ecotoxicology and Environmental Safety*, *244*, 113980. https://doi.org/10.1016/j.ecoenv.2022.113980

Chen, R., Muensterman, D., Field, J., & Ng, C. (2025). Deriving membrane–water and protein–water partition coefficients from in vitro experiments for per- and polyfluoroalkyl substances (PFAS). *Environmental Science & Technology*, *59*(1), 82–91. https://doi.org/10.1021/acs.est.4c06734

Cheng, F., Escher, B. I., Li, H., König, M., Tong, Y., Huang, J., He, L., Wu, X., Lou, X., Wang, D., Wu, F., Pei, Y., Yu, Z., Brooks, B. W., Zeng, E. Y., & You, J. (2024). Deep Learning Bridged Bioactivity, Structure, and GC-HRMS-Readable Evidence to Decipher Nontarget Toxicants in Sediments. *Environmental Science & Technology*. https://doi.org/10.1021/acs.est.3c10814

Cheznowski, J. A. (2015). Distribution and overlap of five coastal indo-pacific cetacean species. *Journal of Aquaculture & Marine Biology*, *Volume 2*(Issue 4). https://doi.org/10.15406/jamb.2015.02.00034

Dai, Y., Yang, S., Zhao, D., Hu, C., Xu, W., Anderson, D. M., Li, Y., Song, X.-P., Boyce,

D. G., Gibson, L., Zheng, C., & Feng, L. (2023). Coastal phytoplankton blooms expand and intensify in the 21st century. *Nature*, *615*(7951), 280–284. https://doi.org/10.1038/s41586-023-05760-y

Della-Negra, O., Bastos, M. C., Bru-Adan, V., Santa-Catalina, G., Ait-Mouheb, N., Chiron, S., & Patureau, D. (2025). Temporal dynamics of the soil resistome and microbiome irrigated with treated wastewater containing clarithromycin. *Environmental Research*, *270*, 120954. https://doi.org/10.1016/j.envres.2025.120954

Desforges, J. P. W., Sonne, C., Levin, M., Siebert, U., De Guise, S., & Dietz, R. (2016). Immunotoxic effects of environmental pollutants in marine mammals. *Environment International*, *86*, 126–139. https://doi.org/10.1016/j.envint.2015.10.007

Desforges, J.-P., Hall, A., McConnell, B., Rosing-Asvid, A., Barber, J. L., Brownlow, A., De Guise, S., Eulaers, I., Jepson, P. D., Letcher, R. J., Levin, M., Ross, P. S., Samarra, F., Víkingson, G., Sonne, C., & Dietz, R. (2018). Predicting global killer whale population collapse from PCB pollution. *Science*, *361*(6409), 1373–1376. https://doi.org/10.1126/science.aat1953

Dietz, R., Letcher, R. J., Desforges, J.-P., Eulaers, I., Sonne, C., Wilson, S., Andersen-Ranberg, E., Basu, N., Barst, B. D., Bustnes, J. O., Bytingsvik, J.,

Ciesielski, T. M., Drevnick, P. E., Gabrielsen, G. W., Haarr, A., Hylland, K., Jenssen, B. M., Levin, M., McKinney, M. A., … Víkingsson, G. (2019). Current state of knowledge on biological effects from contaminants on arctic wildlife and fish. *Science of The Total Environment*, *696*, 133792. https://doi.org/10.1016/j.scitotenv.2019.133792

Dogruer, G., Kramer, N. I., Schaap, I. L., Hollert, H., Gaus, C., & van de Merwe, J. P. (2021). An integrative approach to define chemical exposure threshold limits for endangered sea turtles. *Journal of Hazardous Materials*, *420*, 126512. https://doi.org/10.1016/j.jhazmat.2021.126512

Dolah, F. M. V., Doucette, G. J., Gulland, F. M. D., Rowles, T. L., & Bossart, G. D. (2003). *Impacts of algal toxins on marine mammals*.

dos Santos Correia, P. R., de Carvalho, C. M., da Silva Cunha, C. R., da Silva, R. A. S., de Oliveira Lima, M., França, S. B., de Oliveira Barreto, E., Tonholo, J., & da Paz Lima, D. J. (2022). Synthesis of Esters Containing Cinnamoyl Motif with Potential Larvicide Action: A Computational, Ecotoxicity and in Vitro Cytotoxicity Assessments. *Chemistry & Biodiversity*, *19*(11), e202200256. https://doi.org/10.1002/cbdv.202200256

Droge, S. T. J. (2019). Membrane–water partition coefficients to aid risk assessment of perfluoroalkyl anions and alkyl sulfates. *Environmental*

Science & Technology, *53*(2), 760–770. https://doi.org/10.1021/acs.est.8b05052

Escher, B., Braun, G., & Zarfl, C. (2020). Exploring the Concepts of Concentration Addition and Independent Action Using a Linear Low-Effect Mixture Model. *Environmental Toxicology and Chemistry*, *39*(12), 2552–2559. https://doi.org/10.1002/etc.4868

Escher, B. I., Aït-Aïssa, S., Behnisch, P. A., Brack, W., Brion, F., Brouwer, A., Buchinger, S., Crawford, S. E., Du Pasquier, D., Hamers, T., Hettwer, K., Hilscherová, K., Hollert, H., Kase, R., Kienle, C., Tindall, A. J., Tuerk, J., van der Oost, R., Vermeirssen, E., & Neale, P. A. (2018). Effect-based trigger values for *in vitro* and *in vivo* bioassays performed on surface water extracts supporting the environmental quality standards (EQS) of the European Water Framework Directive. *Science of The Total Environment*, *628–629*, 748–765. https://doi.org/10.1016/j.scitotenv.2018.01.340

Escher, B. I., & Fenner, K. (2011). Recent Advances in Environmental Risk Assessment of Transformation Products. *Environmental Science & Technology*, *45*(9), 3835–3847. https://doi.org/10.1021/es1030799

Escher, B. I., Stapleton, H. M., & Schymanski, E. L. (2020). Tracking complex mixtures of chemicals in our changing environment. *Science*, *367*(6476),

388–392. https://doi.org/10.1126/science.aay6636

Escher, B. I., van Daele, C., Dutt, M., Tang, J. Y. M., & Altenburger, R. (2013). Most oxidative stress response in water samples comes from unknown chemicals: The need for effect-based water quality trigger values. *Environmental Science & Technology*, *47*(13), 7002–7011. https://doi.org/10.1021/es304793h

Espiña, B., & Rubiolo, J. A. (n.d.). *Marine toxins and the cytoskeleton: Pectenotoxins, unusual macrolides that disrupt actin*. Retrieved March 5, 2026, from https://febs.onlinelibrary.wiley.com/doi/epdf/10.1111/j.1742-4658.2008.06714.x

Fossi, M. C., Baini, M., & Simmonds, M. P. (2020). Cetaceans as Ocean Health Indicators of Marine Litter Impact at Global Scale. *Frontiers in Environmental Science*, *8*. https://doi.org/10.3389/fenvs.2020.586627

Fossi, M. C., Limonta, G., Baini, M., Urban R, J., Athanassiadis, I., Martin, J. W., Papazian, S., Rosso, M., & Panti, C. (2025). Fin Whale as a Sink of Legacy and Emerging Contaminants: First Integrated Chemical Exposomics and Gene Expression Analysis in Cetaceans. *Environmental Science & Technology*, *59*(23), 11477–11492. https://doi.org/10.1021/acs.est.5c00844

Frenzilli, G., Bernardeschi, M., Guidi, P., Scarcelli, V., Lucchesi, P., Marsili, L., Fossi, M. C., Brunelli, A., Pojana, G., Marcomini, A., & Nigro, M. (2014). Effects of in vitro exposure to titanium dioxide on DNA integrity of bottlenose dolphin (*Tursiops truncatus*) fibroblasts and leukocytes. *Marine Environmental Research, Large Marine Vertebrates as Sentinels of GES in the European MSFD*, *100*, 68–73. https://doi.org/10.1016/j.marenvres.2014.01.002

Furuya, K., Iwataki, M., Lim, P. T., Lu, S., Leaw, C.-P., Azanza, R. V., Kim, H.-G., & Fukuyo, Y. (2018). Overview of Harmful Algal Blooms in Asia. In P. M. Glibert, E. Berdalet, M. A. Burford, G. C. Pitcher, & M. Zhou (Eds.), *Global Ecology and Oceanography of Harmful Algal Blooms* (pp. 289–308). Springer International Publishing. https://doi.org/10.1007/978-3-319-70069-4_14

Gago-Ferrero, P., Alonso, M. B., Bertozzi, C. P., Marigo, J., Barbosa, L., Cremer, M., Secchi, E. R., Azevedo, A., Lailson-Brito Jr., J., Torres, J. P. M., Malm, O., Eljarrat, E., Díaz-Cruz, M. S., & Barceló, D. (2013). First Determination of UV Filters in Marine Mammals. Octocrylene Levels in Franciscana Dolphins. *Environmental Science & Technology*, *47*(11), 5619–5625. https://doi.org/10.1021/es400675y

Gao, X., Wang, H., Chen, K., Guo, Y., Zhou, J., & Xie, W. (2024). Toxicological and pharmacological activities, and potential medical applications, of marine

algal toxins. *International Journal of Molecular Sciences*, *25*(17), 9194. https://doi.org/10.3390/ijms25179194

Global harmful algal bloom status reporting. (2021). *Harmful Algae*, *102*, 101992. https://doi.org/10.1016/j.hal.2021.101992

Göbölös, B., Sebők, R. E., Szabó, G., Tóth, G., Szoboszlay, S., Kriszt, B., Kaszab, E., & Háhn, J. (2024). The Cocktail Effects on the Acute Cytotoxicity of Pesticides and Pharmaceuticals Frequently Detected in the Environment. *Toxics*, *12*(3), 189. https://doi.org/10.3390/toxics12030189

Gui, D., Zhang, L., Zhan, F., Liu, W., Yu, X., Chen, L., & Wu, Y. (2018). Levels and trends of polycyclic aromatic hydrocarbons in the Indo-Pacific humpback dolphins from the Pearl River Estuary (2012–2017). *Marine Pollution Bulletin*, *131*, 693–700. https://doi.org/10.1016/j.marpolbul.2018.04.058

Guo, L., Zhang, X., Luo, D., Yu, R.-Q., Xie, Q., & Wu, Y. (2021). Population-level effects of polychlorinated biphenyl (PCB) exposure on highly vulnerable Indo-Pacific humpback dolphins from their largest habitat. *Environmental Pollution*, *286*, 117544. https://doi.org/10.1016/j.envpol.2021.117544

Halpern, B. S., Walbridge, S., Selkoe, K. A., Kappel, C. V., Micheli, F., D'Agrosa, C., Bruno, J. F., Casey, K. S., Ebert, C., Fox, H. E., Fujita, R., Heinemann, D., Lenihan, H. S., Madin, E. M. P., Perry, M. T., Selig, E. R., Spalding, M.,

Steneck, R., & Watson, R. (2008). A Global Map of Human Impact on Marine Ecosystems. *Science*, *319*(5865), 948–952. https://doi.org/10.1126/science.1149345

Hart, L. B., Rotstein, D. S., Wells, R. S., Allen, J., Barleycorn, A., Balmer, B. C., Lane, S. M., Speakman, T., Zolman, E. S., Stolen, M., McFee, W., Goldstein, T., Rowles, T. K., & Schwacke, L. H. (2012). Skin lesions on common bottlenose dolphins (tursiops truncatus) from three sites in the northwest atlantic, USA. *PLOS ONE*, *7*(3), e33081. https://doi.org/10.1371/journal.pone.0033081

Hazen, E. L., Savoca, M. S., Clark-Wolf, T. J., Czapanskiy, M., Rabinowitz, P. M., & Abrahms, B. (2024). Ecosystem Sentinels as Early-Warning Indicators in the Anthropocene. *Annual Review of Environment and Resources*, *49*(Volume 49, 2024), 573–598. https://doi.org/10.1146/annurev-environ-111522-102317

He, X., Chen, J., Wang, J., Sun, X., Xin, M., Wang, B., & Liang, S. (2022). Spatial variation of lipophilic marine algal toxins and its relationship with physicochemical parameters in spring in laizhou bay, China. *Journal of Oceanology and Limnology*, *40*(6), 2242–2255. https://doi.org/10.1007/s00343-022-1426-5

Hickie, B. E., Mackay, D., & de Koning, J. (1999). Lifetime pharmacokinetic model for hydrophobic contaminants in marine mammals. *Environmental Toxicology and Chemistry*, *18*(11), 2622–2633. https://doi.org/10.1002/etc.5620181132

Ho, K. C. (2022). Overview of harmful algal blooms (red tides) in hong kong during 1975–2021. *Journal of Oceanology and Limnology*, *40*(6), 2094–2106. https://doi.org/10.1007/s00343-022-2205-z

Ho, K. K. Y., Zhou, G.-J., Xu, E. G. B., Wang, X., & Leung, K. M. Y. (2016). Long-Term Spatio-Temporal Trends of Organotin Contaminations in the Marine Environment of Hong Kong. *PLOS ONE*, *11*(5), e0155632. https://doi.org/10.1371/journal.pone.0155632

Ho, Y., Wu, P.-Y., Chou, L.-S., & Yang, W.-C. (2023). Skin Marks in Critically Endangered Taiwanese Humpback Dolphins (Sousa chinensis taiwanensis). *Animals*, *13*(4), Article 4. https://doi.org/10.3390/ani13040608

Hollender, J., van Bavel, B., Dulio, V., Farmen, E., Furtmann, K., Koschorreck, J., Kunkel, U., Krauss, M., Munthe, J., Schlabach, M., Slobodnik, J., Stroomberg, G., Ternes, T., Thomaidis, N. S., Togola, A., & Tornero, V. (2019). High resolution mass spectrometry-based non-target screening can

support regulatory environmental monitoring and chemicals management. *Environmental Sciences Europe*, *31*(1), 42. https://doi.org/10.1186/s12302-019-0225-x

Hong Kong Red Tide Database. (n.d.). Retrieved October 14, 2024, from https://redtide.afcd.gov.hk/urtin/#/maps?mode=1&lang=en

Hong, S., Lee, J., Cha, J., Gwak, J., & Khim, J. S. (2023). Effect-Directed Analysis Combined with Nontarget Screening to Identify Unmonitored Toxic Substances in the Environment. *Environmental Science & Technology*, *57*(48), 19148–19155. https://doi.org/10.1021/acs.est.3c05035

Hosen, M. H. A., Sykes, A. M., Wood, S. A., Leusch, F. D. L., Whitworth, D. J., & Bengtson Nash, S. M. (2023). Novel Use of Cell Profiling Technology to Visualize Mitochondrial Responses of Humpback Whale Fibroblasts to Chemical Exposure. *Environmental Science & Technology*, *57*(24), 8975–8982. https://doi.org/10.1021/acs.est.2c07159

Huang, S., He, S., Xu, H., Wu, P., Jiang, R., Zhu, F., Luan, T., & Ouyang, G. (2015). Monitoring of persistent organic pollutants in seawater of the Pearl River Estuary with rapid on-site active SPME sampling technique. *Environmental Pollution*, *200*, 149–158. https://doi.org/10.1016/j.envpol.2015.02.016

Hung, C. L. H., Xu, Y., Lam, J. C. W., Jefferson, T. A., Hung, S. K., Yeung, L. W. Y.,

Lam, M. H. W., O'Toole, D. K., & Lam, P. K. S. (2006). An assessment of the risks associated with polychlorinated biphenyls found in the stomach contents of stranded Indo-Pacific Humpback Dolphins (Sousa chinensis) and Finless Porpoises (Neophocaena phocaenoides) from Hong Kong waters. *Chemosphere*, *63*(5), 845–852. https://doi.org/10.1016/j.chemosphere.2005.07.059

I. Escher, B., J. Binnington, M., König, M., D. Lei, Y., & Wania, F. (2023). Mixture effect assessment applying in vitro bioassays to in-tissue silicone extracts of traditional foods prepared from beluga whale blubber. *Environmental Science: Processes & Impacts*, *25*(11), 1759–1770. https://doi.org/10.1039/D3EM00076A

Ishibashi, H., Kim, E.-Y., & Iwata, H. (2011). Transactivation Potencies of the Baikal Seal (Pusa sibirica) Peroxisome Proliferator-Activated Receptor α by Perfluoroalkyl Carboxylates and Sulfonates: Estimation of PFOA Induction Equivalency Factors. *Environmental Science & Technology*, *45*(7), 3123–3130. https://doi.org/10.1021/es103748s

Jackson, P. A., Widen, J. C., Harki, D. A., & Brummond, K. M. (2017). Covalent Modifiers: A Chemical Perspective on the Reactivity of α,β-Unsaturated Carbonyls with Thiols via Hetero-Michael Addition Reactions. *Journal of*

Medicinal Chemistry, *60*(3), 839–885. https://doi.org/10.1021/acs.jmedchem.6b00788

Jefferson, T. A., Becker, E. A., & Huang, S.-L. (2023). Influences of natural and anthropogenic habitat variables on Indo-Pacific humpback dolphins Sousa chinensis in Hong Kong. *Endangered Species Research*, *51*, 143–160. https://doi.org/10.3354/esr01249

Jefferson, T. A., Curry, B., & Kinoshita, R. (2002). Mortality and morbidity of hong kong finless porpoises, with emphasis on the role of environmental contaminants. *Raffles Bulletin of Zoology*, 161–171.

Jin, L., Gaus, C., & Escher, B. I. (2015a). Adaptive stress response pathways induced by environmental mixtures of bioaccumulative chemicals in dugongs. *Environmental Science & Technology*, *49*(11), 6963–6973. https://doi.org/10.1021/acs.est.5b00947

Jin, L., Gaus, C., & Escher, B. I. (2015b). Bioanalytical Approaches to Understanding Toxicological Implications of Mixtures of Persistent Organic Pollutants in Marine Wildlife. In *Comprehensive Analytical Chemistry* (Vol. 67, pp. 57–84). Elsevier. https://doi.org/10.1016/B978-0-444-63299-9.00002-8

Karczmarski, L., Huang, S.-L., Or, C. K. M., Gui, D., Chan, S. C. Y., Lin, W., Porter,

L., Wong, W.-H., Zheng, R., Ho, Y.-W., Chui, S. Y. S., Tiongson, A. J. C., Mo, Y., Chang, W.-L., Kwok, J. H. W., Tang, R. W. K., Lee, A. T. L., Yiu, S.-W., Keith, M., … Wu, Y. (2016). Chapter two - humpback dolphins in hong kong and the pearl river delta: Status, threats and conservation challenges. In T. A. Jefferson & B. E. Curry (Eds.), *Advances in Marine Biology* (Vol. 73, pp. 27–64). Academic Press. https://doi.org/10.1016/bs.amb.2015.09.003

Kgosiemang, I. K. R., Lefojane, R., Adegoke, A. M., Ogunyemi, O., Mashele, S. S., & Sekhoacha, M. P. (2025). Pharmacological Significance, Medicinal Use, and Toxicity of Extracted and Isolated Compounds from Euphorbia Species Found in Southern Africa: A Review. *Plants*, *14*(3), 469. https://doi.org/10.3390/plants14030469

Krishnan, K. (n.d.). *Quantitative modeling in toxicology*.

Krishnan, K., & Peyret, T. (2009). Physiologically based toxicokinetic (PBTK) modeling in ecotoxicology. In J. Devillers (Ed.), *Ecotoxicology Modeling* (pp. 145–175). Springer US. https://doi.org/10.1007/978-1-4419-0197-2_6

Kumar, A., Prasad, M., Mishra, D., Srivastav, S. K., & Srivastav, A. K. (2010). Toxicity of aqueous extract of *Euphorbia tirucalli* latex on catfish, *Heteropneustes fossilis*. *Ecotoxicology and Environmental Safety*, *73*(7), 1671–1673. https://doi.org/10.1016/j.ecoenv.2010.08.003

Lam, J. C. W., Lyu, J., Kwok, K. Y., & Lam, P. K. S. (2016). Perfluoroalkyl Substances (PFASs) in Marine Mammals from the South China Sea and Their Temporal Changes 2002–2014: Concern for Alternatives of PFOS? *Environmental Science & Technology*, *50*(13), 6728–6736. https://doi.org/10.1021/acs.est.5b06076

Li, T., Sun, Y., Zeng, Y., Sanganyado, E., Liang, B., & Liu, W. (2022). 6-OH-BDE-47 inhibited proliferation of skin fibroblasts from pygmy killer whale by inducing cell cycle arrest. *Science of The Total Environment*, *807*, 150561. https://doi.org/10.1016/j.scitotenv.2021.150561

Liu, H., Zhao, B., Jin, M., Wang, R., Ding, Z., Wang, X., Xu, W., Chen, Q., Tao, R., Fu, J., & Xie, D. (2024). Anthropogenic-induced ecological risks on marine ecosystems indicated by characterizing emerging pollutants in pearl river estuary, China. *Science of The Total Environment*, *926*, 172030. https://doi.org/10.1016/j.scitotenv.2024.172030

Liu, J., Deng, W.-J., Ying, G.-G., Tsang, E. P. K., & Hong, H.-C. (2022). Occurrence and distribution of antibiotics in surface water. *Ecotoxicology*, *31*(7), 1111–1119. https://doi.org/10.1007/s10646-022-02567-x

Luo, W., Chou, L., Cui, Q., Wei, S., Zhang, X., & Guo, J. (2024). High-efficiency effect-directed analysis (EDA) advancing toxicant identification in aquatic

environments: Latest progress and application status. *Environment International*, *190*, 108855. https://doi.org/10.1016/j.envint.2024.108855

Maszkowska, J., Stolte, S., Kumirska, J., Łukaszewicz, P., Mioduszewska, K., Puckowski, A., Caban, M., Wagil, M., Stepnowski, P., & Białk-Bielińska, A. (2014). Beta-blockers in the environment: Part II. Ecotoxicity study. *Science of The Total Environment*, *493*, 1122–1126. https://doi.org/10.1016/j.scitotenv.2014.06.039

Mayr, A., Klambauer, G., Unterthiner, T., & Hochreiter, S. (2016). DeepTox: Toxicity Prediction using Deep Learning. *Frontiers in Environmental Science*, *3*. https://doi.org/10.3389/fenvs.2015.00080

Menon, G. K., Elias, P. M., Wakefield, J. S., & Crumrine, D. (2022). Cetacean epidermal specialization: A review. *Anatomia, Histologia, Embryologia*, *51*(5), 563–575. https://doi.org/10.1111/ahe.12829

Mollenhauer, M. A. M., Carter, B. J., Peden-Adams, M. M., Bossart, G. D., & Fair, P. A. (2009). Gene expression changes in bottlenose dolphin, *tursiops truncatus*, skin cells following exposure to methylmercury (MeHg) or perfluorooctane sulfonate (PFOS). *Aquatic Toxicology*, *91*(1), 10–18. https://doi.org/10.1016/j.aquatox.2008.09.013

Moore, S. E. (2008). Marine mammals as ecosystem sentinels. *Journal of*

Mammalogy, *89*(3), 534–540. https://doi.org/10.1644/07-MAMM-S-312R1.1

Mourtzoukou, E. G., Iavazzo, C., & Falagas, M. E. (2008). Resiniferatoxin in the treatment of interstitial cystitis: A systematic review. *International Urogynecology Journal*, *19*(11), 1571–1576. https://doi.org/10.1007/s00192-008-0663-2

Mousavi, S. E., Delgado-Saborit, J. M., & Godderis, L. (2021). Exposure to per- and polyfluoroalkyl substances and premature skin aging. *Journal of Hazardous Materials*, *405*, 124256. https://doi.org/10.1016/j.jhazmat.2020.124256

Neale, P. A., Ait-Aissa, S., Brack, W., Creusot, N., Denison, M. S., Deutschmann, B., Hilscherová, K., Hollert, H., Krauss, M., Novák, J., Schulze, T., Seiler, T.-B., Serra, H., Shao, Y., & Escher, B. I. (2015). Linking in Vitro Effects and Detected Organic Micropollutants in Surface Water Using Mixture-Toxicity Modeling. *Environmental Science & Technology*, *49*(24), 14614–14624. https://doi.org/10.1021/acs.est.5b04083

Ng, C. A., & Hungerbühler, K. (2014). Bioaccumulation of Perfluorinated Alkyl Acids: Observations and Models. *Environmental Science & Technology*, *48*(9), 4637–4648. https://doi.org/10.1021/es404008g

Ochiai, M., Kurihara, N., Hirano, M., Nakata, A., & Iwata, H. (2020). In Vitro Cytotoxicity and Risk Assessments of Environmental Pollutants Using Fibroblasts of a Stranded Finless Porpoise (Neophocaena asiaeorientalis). *Environmental Science & Technology*, *54*(11), 6832–6841. https://doi.org/10.1021/acs.est.9b07471

Otero-Sabio, C., Giacomello, M., Centelleghe, C., Caicci, F., Bonato, M., Venerando, A., Graïc, J.-M., Mazzariol, S., Finos, L., Corain, L., & Peruffo, A. (2022). Cell cycle alterations due to perfluoroalkyl substances PFOS, PFOA, PFBS, PFBA and the new PFAS C6O4 on bottlenose dolphin (*Tursiops truncatus*) skin cell. *Ecotoxicology and Environmental Safety*, *244*, 113980. https://doi.org/10.1016/j.ecoenv.2022.113980

Parsons, E. C. M. (1998). Trace metal pollution in Hong Kong: Implications for the health of Hong Kong's Indo-Pacific hump-backed dolphins (*Sousa chinensis*). *Science of The Total Environment*, *214*(1), 175–184. https://doi.org/10.1016/S0048-9697(98)00063-1

Peropadre, A., Fernández Freire, P., & Hazen, M. J. (2018). A moderate exposure to perfluorooctanoic acid causes persistent DNA damage and senescence in human epidermal HaCaT keratinocytes. *Food and Chemical Toxicology*, *121*, 351–359. https://doi.org/10.1016/j.fct.2018.09.020

Persson, L., Carney Almroth, B. M., Collins, C. D., Cornell, S., de Wit, C. A., Diamond, M. L., Fantke, P., Hassellöv, M., MacLeod, M., Ryberg, M. W., Søgaard Jørgensen, P., Villarrubia-Gómez, P., Wang, Z., & Hauschild, M. Z. (2022). Outside the Safe Operating Space of the Planetary Boundary for Novel Entities. *Environmental Science & Technology*, *56*(3), 1510–1521. https://doi.org/10.1021/acs.est.1c04158

Pradhan, B., Kim, H., Abassi, S., & Ki, J.-S. (2022). Toxic Effects and Tumor Promotion Activity of Marine Phytoplankton Toxins: A Review. *Toxins*, *14*(6), Article 6. https://doi.org/10.3390/toxins14060397

Ramu, K., Kajiwara, N., Tanabe, S., Lam, P. K. S., & Jefferson, T. A. (2005). Polybrominated diphenyl ethers (PBDEs) and organochlorines in small cetaceans from hong kong waters: Levels, profiles and distribution. *Marine Pollution Bulletin, 4th International Conference on Marine Pollution and Ecotoxicology*, *51*(8), 669–676. https://doi.org/10.1016/j.marpolbul.2005.02.041

Rebryk, A., Gallampois, C., & Haglund, P. (2022). A time-trend guided non-target screening study of organic contaminants in Baltic Sea harbor porpoise (1988–2019), guillemot (1986–2019), and white-tailed sea eagle (1965–2017) using gas chromatography–high-resolution mass spectrometry.

Science of The Total Environment, *829*, 154620. https://doi.org/10.1016/j.scitotenv.2022.154620

Reemtsma, T., Berger, U., Arp, H. P. H., Gallard, H., Knepper, T. P., Neumann, M., Quintana, J. B., & Voogt, P. de. (2016). Mind the Gap: Persistent and Mobile Organic Compounds—Water Contaminants That Slip Through. *Environmental Science & Technology*, *50*(19), 10308–10315. https://doi.org/10.1021/acs.est.6b03338

Ruan, F., Wu, L., Yin, H., Fang, L., Tang, C., Huang, S., Fang, L., Zuo, Z., He, C., & Huang, J. (2021). Long-term exposure to environmental level of phenanthrene causes adaptive immune response and fibrosis in mouse kidneys. *Environmental Pollution*, *283*, 117028. https://doi.org/10.1016/j.envpol.2021.117028

Salangad, O., Cappelli, F., Simon, F., Galatius, A., Sonne, C., Poma, G., Møller, P. R., Dietz, R., & Covaci, A. (2025). Occurrence and patterns of legacy and emerging per- and polyfluoroalkyl substances (PFAS) in bones of white-beaked dolphin (*Lagenorhynchus albirostris*) using target, suspect, and non-target screening. *Environmental Research*, *283*, 122114. https://doi.org/10.1016/j.envres.2025.122114

Sanz-Serrano, J., Vettorazzi, A., Muruzabal, D., Azqueta, A., & López de Cerain, A.

(2021). In Vitro Genotoxicity Assessment of Functional Ingredients: Betaine, Choline, and Taurine. *Foods*, *10*(2), 339. https://doi.org/10.3390/foods10020339

Sauvé, S., & Desrosiers, M. (2014). A review of what is an emerging contaminant. *Chemistry Central Journal*, *8*(1), 15. https://doi.org/10.1186/1752-153X-8-15

Schwarzenbach, R. P., Escher, B. I., Fenner, K., Hofstetter, T. B., Johnson, C. A., von Gunten, U., & Wehrli, B. (2006). The Challenge of Micropollutants in Aquatic Systems. *Science*, *313*(5790), 1072–1077. https://doi.org/10.1126/science.1127291

Silva, E., Rajapakse, N., & Kortenkamp, A. (2002). Something from "Nothing" – Eight Weak Estrogenic Chemicals Combined at Concentrations below NOECs Produce Significant Mixture Effects. *Environmental Science & Technology*, *36*(8), 1751–1756. https://doi.org/10.1021/es0101227

Sobolewska, D., Galanty, A., Grabowska, K., Makowska-Wąs, J., Podolak, I., & Wróbel-Biedrawa, D. (2025). Genipin—Simple but Significant Bioactive Iridoid for Therapeutical Application and Beyond: A Review. *Life*, *15*(2), 159. https://doi.org/10.3390/life15020159

Sobus, J. R., Wambaugh, J. F., Isaacs, K. K., Williams, A. J., McEachran, A. D.,

Richard, A. M., Grulke, C. M., Ulrich, E. M., Rager, J. E., Strynar, M. J., & Newton, S. R. (2018). Integrating tools for non-targeted analysis research and chemical safety evaluations at the US EPA. *Journal of Exposure Science & Environmental Epidemiology*, *28*(5), 411–426. https://doi.org/10.1038/s41370-017-0012-y

Soon Eong, Y., & Sulit, V. T. (2017). Monitoring and identification of harmful algal blooms in Southeast Asia to support SDG 14.1. *Fish for the People*, *15*(1), 39–46.

Sun, W., Guo, Y., Sun, X., Liu, Z., Luo, D., Huang, N., Xu, Z., Wu, J., & Wu, Y. (2024). Alternatives Exert Higher Health Risks than Bisphenol A on Indo-Pacific Humpback Dolphins. *Environmental Science & Technology*, *58*(1), 63–74. https://doi.org/10.1021/acs.est.3c02977

Sun, X., Xie, Y., Zhang, X., Song, J., & Wu, Y. (2023). Estimation of Per- and Polyfluorinated Alkyl Substance Induction Equivalency Factors for Humpback Dolphins by Transactivation Potencies of Peroxisome Proliferator-Activated Receptors. *Environmental Science & Technology*, *57*(9), 3713–3721. https://doi.org/10.1021/acs.est.2c05044

Svetnik, V., Liaw, A., Tong, C., Culberson, J. C., Sheridan, R. P., & Feuston, B. P. (2003). Random Forest: A Classification and Regression Tool for

Compound Classification and QSAR Modeling. *Journal of Chemical Information and Computer Sciences*, *43*(6), 1947–1958. https://doi.org/10.1021/ci034160g

Takeshita, R., Sullivan, L., Smith, C., Collier, T., Hall, A., Brosnan, T., Rowles, T., & Schwacke, L. (2017). *The Deepwater Horizon oil spill marine mammal injury assessment*. https://doi.org/10.3354/esr00808

Tang, J. Y. M., McCarty, S., Glenn, E., Neale, P. A., Warne, M. St. J., & Escher, B. I. (2013). Mixture effects of organic micropollutants present in water: Towards the development of effect-based water quality trigger values for baseline toxicity. *Water Research*, *47*(10), 3300–3314. https://doi.org/10.1016/j.watres.2013.03.011

Tholkapiyan, M., Shanmugam, P., & Suresh, T. (2014). Monitoring of ocean surface algal blooms in coastal and oceanic waters around India. *Environmental Monitoring and Assessment*, *186*(7), 4129–4137. https://doi.org/10.1007/s10661-014-3685-x

Treu, G., Slobodnik, J., Alygizakis, N., Badry, A., Bunke, D., Cincinelli, A., Claßen, D., Dekker, R. W. R. J., Göckener, B., Gkotsis, G., Hanke, G., Duke, G., Jartun, M., Movalli, P., Nika, M.-C., Rüdel, H., Tarazona, J. V., Thomaidis, N. S., Tornero, V., … Dulio, V. (2022). Using environmental monitoring data from

apex predators for chemicals management: Towards better use of monitoring data from apex predators in support of prioritisation and risk assessment of chemicals in Europe. *Environmental Sciences Europe*, *34*(1), 82. https://doi.org/10.1186/s12302-022-00665-5

Tsui, M. M. P., Chen, L., He, T., Wang, Q., Hu, C., Lam, J. C. W., & Lam, P. K. S. (2019). Organic ultraviolet (UV) filters in the south China sea coastal region: Environmental occurrence, toxicological effects and risk assessment. *Ecotoxicology and Environmental Safety*, *181*, 26–33. https://doi.org/10.1016/j.ecoenv.2019.05.075

Vosough, M., Schmidt, T. C., & Renner, G. (2024). Non-target screening in water analysis: Recent trends of data evaluation, quality assurance, and their future perspectives. *Analytical and Bioanalytical Chemistry*, *416*(9), 2125–2136. https://doi.org/10.1007/s00216-024-05153-8

Wang, Q., Tsui, M. M. P., Ruan, Y., Lin, H., Zhao, Z., Ku, J. P. H., Sun, H., & Lam, P. K. S. (2019). Occurrence and distribution of per- and polyfluoroalkyl substances (PFASs) in the seawater and sediment of the south China sea coastal region. *Chemosphere*, *231*, 468–477. https://doi.org/10.1016/j.chemosphere.2019.05.162

Wang, W.-X., & Rainbow, P. S. (2020). Pollution in the Pearl River Estuary. In W.-X.

Wang & P. S. Rainbow (Eds.), *Environmental Pollution of the Pearl River Estuary, China: Status and Impact of Contaminants in a Rapidly Developing Region* (pp. 13–35). Springer. https://doi.org/10.1007/978-3-662-61834-9_3

Wei, K., Xu, Z., Sun, X., Zhang, X., Xie, Q., Luo, D., Yu, X., Liu, Z., Sun, W., Wang, N., & Wu, Y. (2025). In Vitro Cytotoxic Mechanism and Exposure Risk Assessments of Banned Organochlorine Pesticides in Indo-Pacific Humpback Dolphins. *Environmental Science & Technology*, *59*(21), 10145–10156. https://doi.org/10.1021/acs.est.4c13776

Weijs, L., Covaci, A., Yang, R. S. H., Das, K., & Blust, R. (2012). Computational toxicology: Physiologically based pharmacokinetic models (PBTK) for lifetime exposure and bioaccumulation of polybrominated diphenyl ethers (PBDEs) in marine mammals. *Environmental Pollution*, *163*, 134–141. https://doi.org/10.1016/j.envpol.2011.12.037

Weijs, L., Yang, R. S. H., Covaci, A., Das, K., & Blust, R. (2010). Physiologically based pharmacokinetic (PBTK) models for lifetime exposure to PCB 153 in male and female harbor porpoises (phocoena phocoena): Model development and evaluation. *Environmental Science & Technology*, *44*(18), 7023–7030. https://doi.org/10.1021/es101688h

Weijs, L., Yang, R. S. H., Das, K., Covaci, A., & Blust, R. (2013). Application of bayesian population physiologically based pharmacokinetic (PBTK) modeling and markov chain monte carlo simulations to pesticide kinetics studies in protected marine mammals: DDT, DDE, and DDD in harbor porpoises. *Environmental Science & Technology*, *47*(9), 4365–4374. https://doi.org/10.1021/es400386a

Wisetsai, A., Schevenels, F. T., Faksri, K., Tontapha, S., Amornkitbamrung, V., & Lekphrom, R. (2022). New iridoid glucosides from the roots of Rothmannia wittii (Craib) Bremek. *Natural Product Research*, *36*(7), 1716–1724. https://doi.org/10.1080/14786419.2020.1813133

Xia, P., Zhang, X., Zhang, H., Wang, P., Tian, M., & Yu, H. (2017). Benchmarking water quality from wastewater to drinking waters using reduced transcriptome of human cells. *Environmental Science & Technology*, *51*(16), 9318–9326. https://doi.org/10.1021/acs.est.7b02648

Xia, Z.-S., Hao, E.-W., Wei, Y., Hou, X.-T., Chen, Z., Wei, M., Du, Z.-C., & Deng, J.-G. (2021). Genipin induces developmental toxicity through oxidative stress and apoptosis in zebrafish. *Comparative Biochemistry and Physiology Part C: Toxicology & Pharmacology*, *241*, 108951. https://doi.org/10.1016/j.cbpc.2020.108951

Yajing, S., Rajput, I. R., Ying, H., Fei, Y., Sanganyado, E., Ping, L., Jingzhen, W., & Wenhua, L. (2018). Establishment and characterization of pygmy killer whale (feresa attenuata) dermal fibroblast cell line. *PLOS ONE*, *13*(3), e0195128. https://doi.org/10.1371/journal.pone.0195128

Yang, K., Swanson, K., Jin, W., Coley, C., Eiden, P., Gao, H., Guzman-Perez, A., Hopper, T., Kelley, B., Mathea, M., Palmer, A., Settels, V., Jaakkola, T., Jensen, K., & Barzilay, R. (2019). Analyzing Learned Molecular Representations for Property Prediction. *Journal of Chemical Information and Modeling*, *59*(8), 3370–3388. https://doi.org/10.1021/acs.jcim.9b00237

Yñiguez, A. T., Lim, P. T., Leaw, C.-P., Jipanin, S. J., Iwataki, M., Benico, G., & Azanza, R. V. (2021). Over 30 years of HABs in the Philippines and Malaysia: What have we learned? *Harmful Algae*, *102*, 101776. https://doi.org/10.1016/j.hal.2020.101776

Yoon, M., Blaauboer, B. J., & Clewell, H. J. (2015). Quantitative in vitro to in vivo extrapolation (QIVIVE): An essential element for in vitro-based risk assessment. *Toxicology, Quantitative in Vitro to in Vivo Extrapolation (QIVIVE): An Essential Element for in Vitro-Based Risk Assessment*, *332*, 1–3. https://doi.org/10.1016/j.tox.2015.02.002

Yu, X., Yu, R.-Q., Gui, D., Zhang, X., Zhan, F., Sun, X., & Wu, Y. (2018). Hexavalent chromium induces oxidative stress and mitochondria-mediated apoptosis in isolated skin fibroblasts of Indo-Pacific humpback dolphin. *Aquatic Toxicology*, *203*, 179–186. https://doi.org/10.1016/j.aquatox.2018.08.012

Yu, X., Yu, R.-Q., Zhang, X., Zhan, F., Sun, X., & Wu, Y. (2019). DDT exposure induces cell cycle arrest and apoptosis of skin fibroblasts from Indo-Pacific humpback dolphin via mitochondria dysfunction. *Aquatic Toxicology*, *213*, 105229. https://doi.org/10.1016/j.aquatox.2019.105229

Zhang, X., Li, L., Xie, Z., Ma, J., Li, Y.-F., Cai, M., Ren, N.-Q., Kallenborn, R., Zhang, Z.-F., Zhang, X., & C.G. Muir, D. (2024). Exploring global oceanic persistence and ecological effects of legacy persistent organic pollutants across five decades. *Science Advances*, *10*(39), eado5534. https://doi.org/10.1126/sciadv.ado5534

Zhou, J., Wang, S., He, X., Ren, H., & Zhang, X.-X. (2024). Comparative evaluation of SPE methods for biotoxicity assessment of water and wastewater: Linkage between chemical extracting efficiency and biotoxicity outcome. *Journal of Environmental Sciences*, *142*, 33–42. https://doi.org/10.1016/j.jes.2023.07.016

Zweigle, J., Tisler, S., Bevilacqua, M., Tomasi, G., Nielsen, N. J., Gawlitta, N.,

Lübeck, J. S., Smilde, A. K., & Christensen, J. H. (2025). Prioritization strategies for non-target screening in environmental samples by chromatography – High-resolution mass spectrometry: A tutorial. *Journal of Chromatography A*, *1751*, 465944. https://doi.org/10.1016/j.chroma.2025.465944

ten Berge, W. (2011). QSARs for skin permeation of chemicals.

Appendix I

Concentration-effect curves for cytotoxicity induced by seawater extracts in the Indo-Pacific finless porpoise cell line

Sites	Wet season	Dry season
1	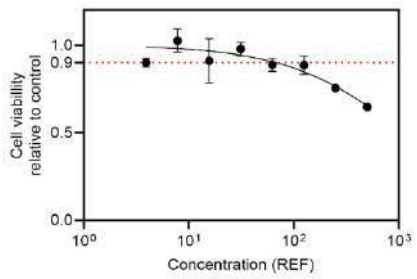	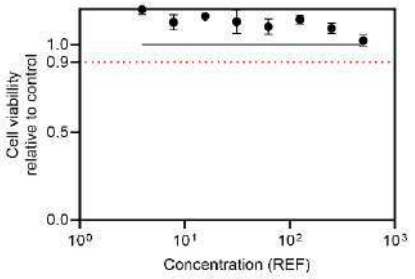
2	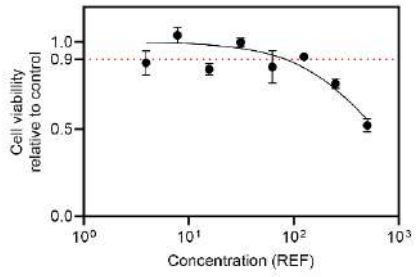	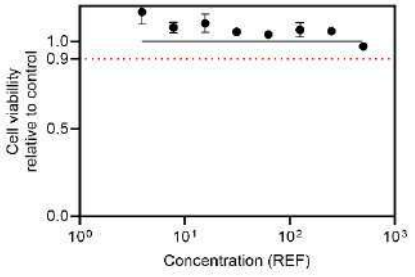
3	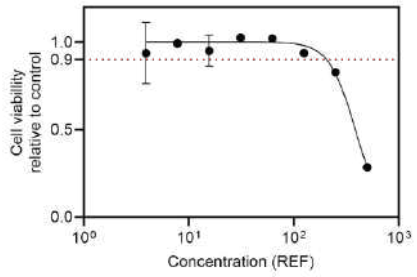	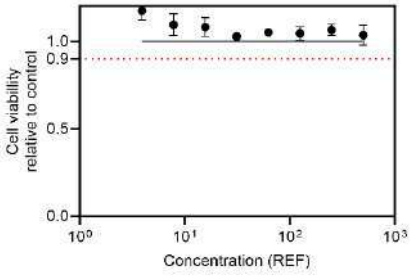
4	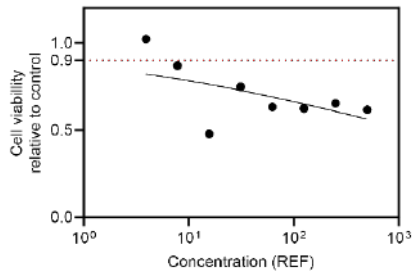	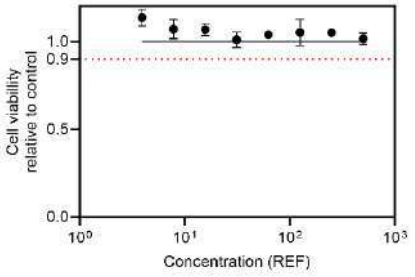

Sites	Wet season	Dry season
5	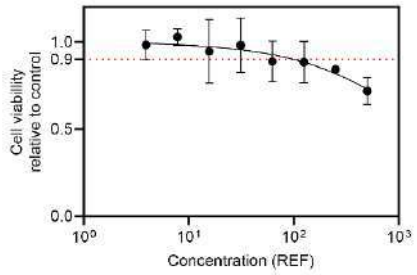	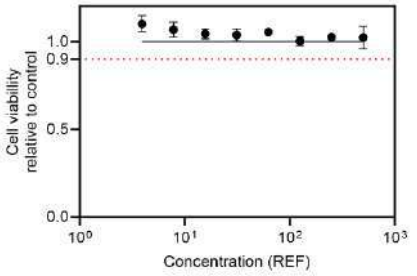
6	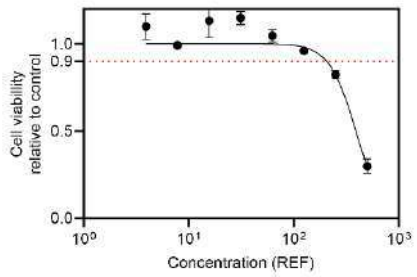	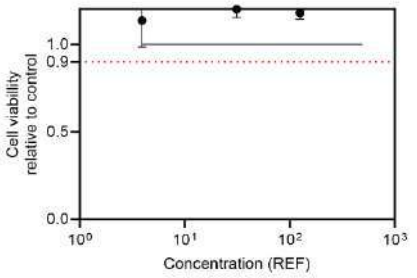
7	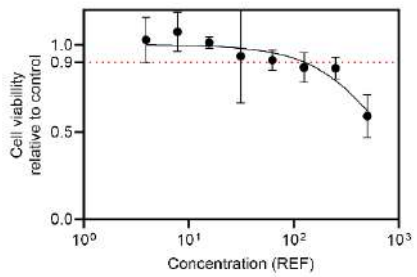	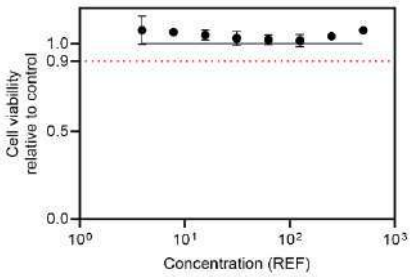
8	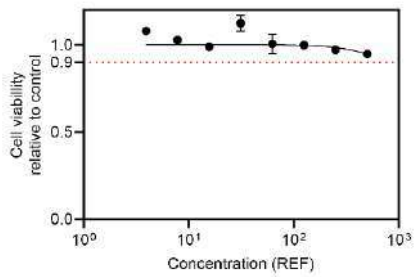	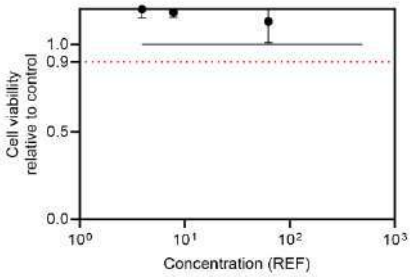
9	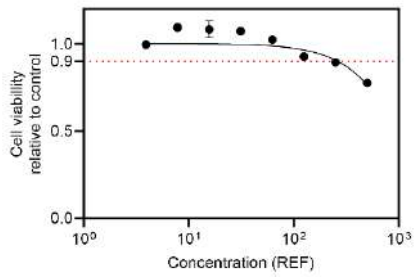	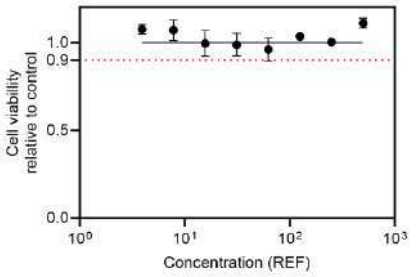

Sites	Wet season	Dry season
10	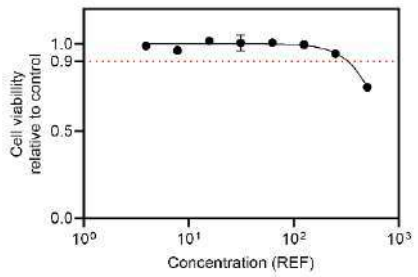	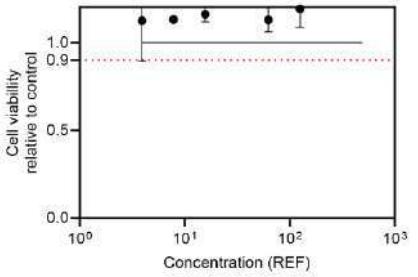
11	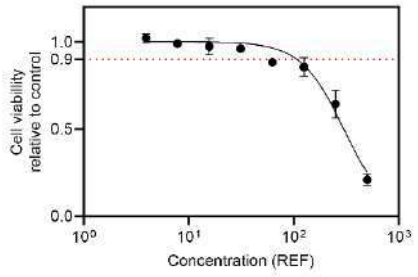	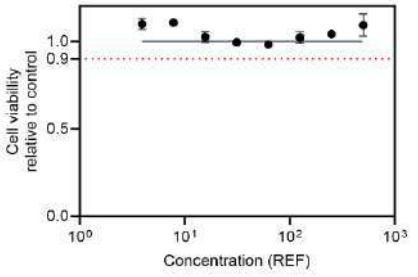
12	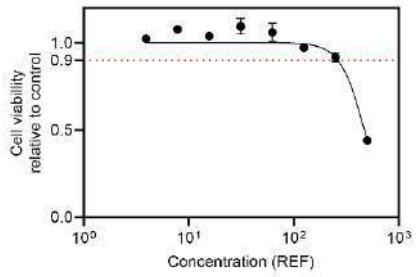	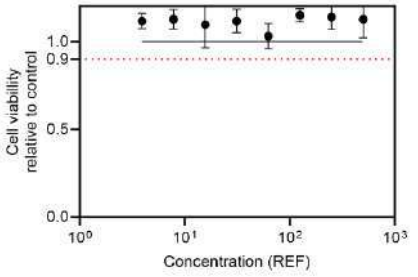
13	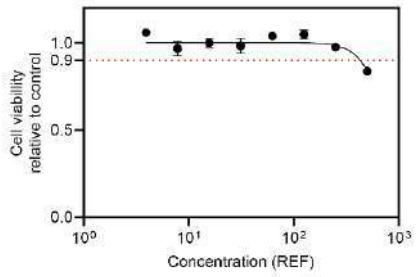	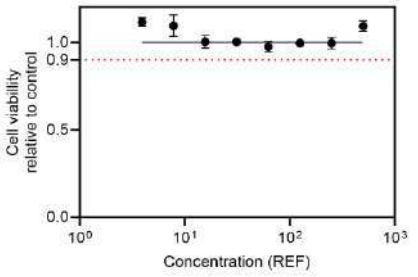
14	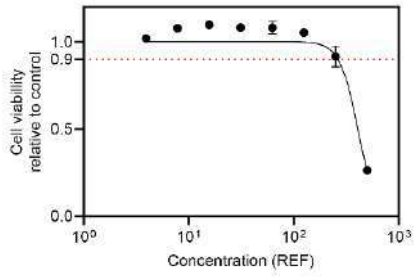	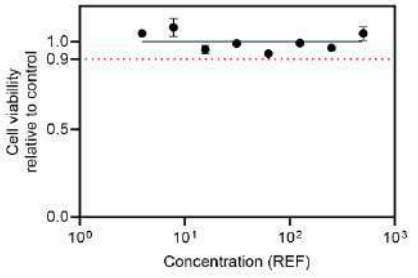

Sites	Wet season	Dry season
15	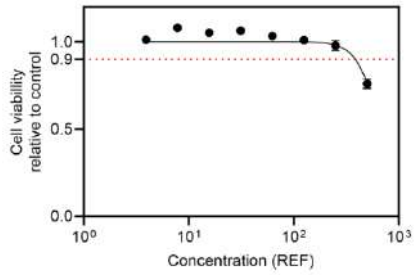	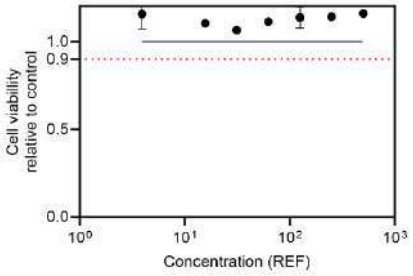
16	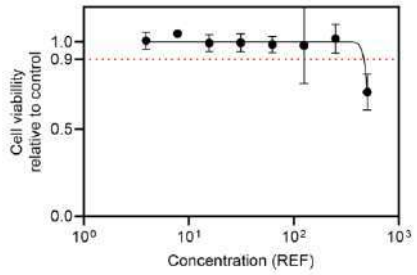	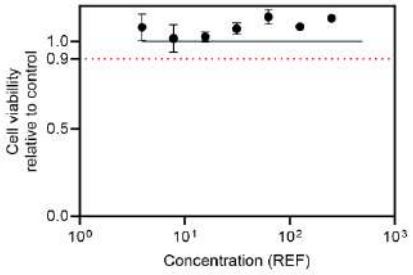
17	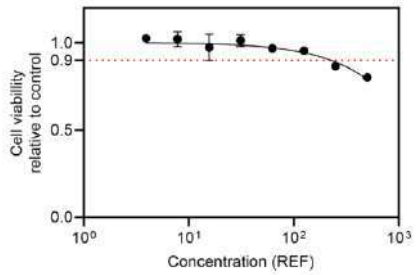	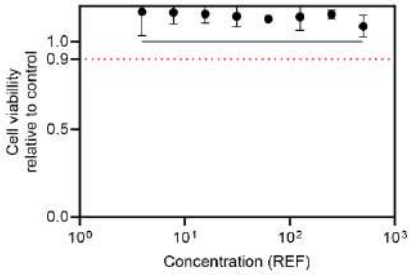
18	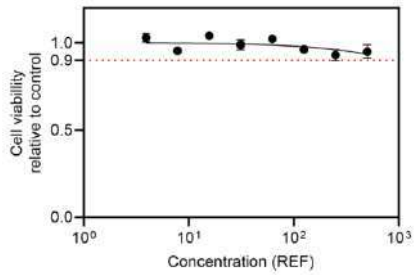	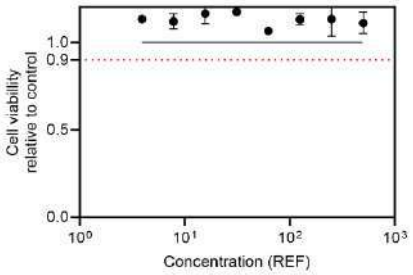
19	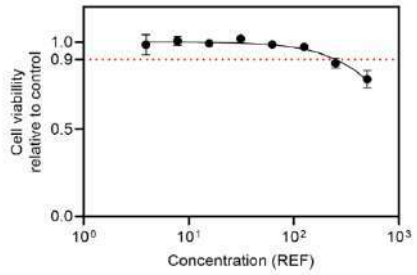	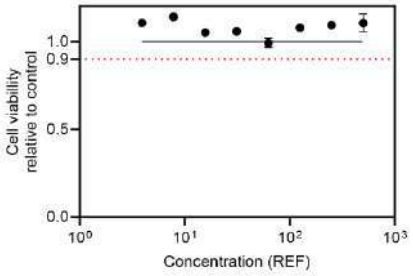

Sites	Wet season	Dry season
20	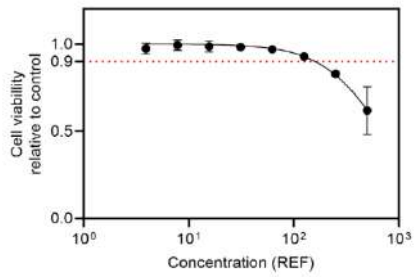	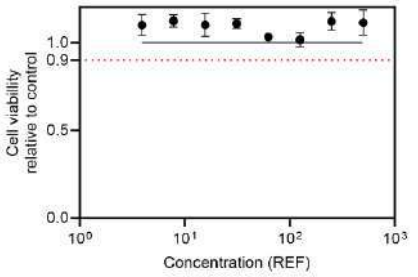
21	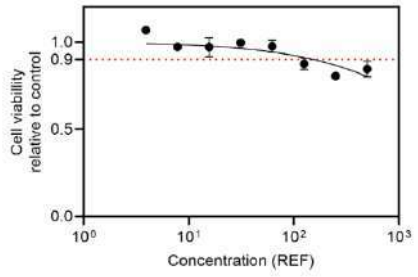	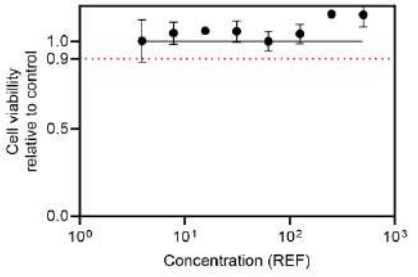
22	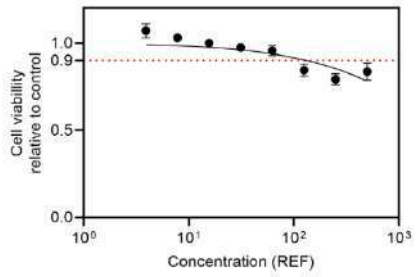	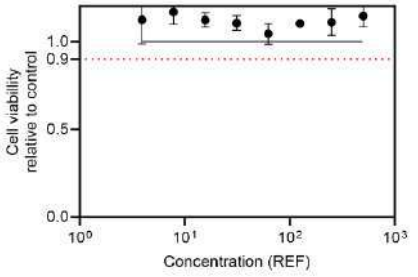
23	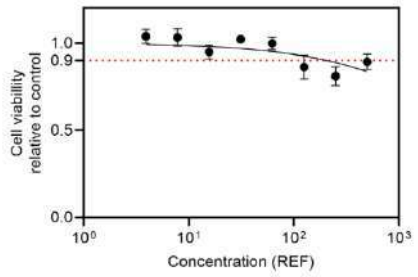	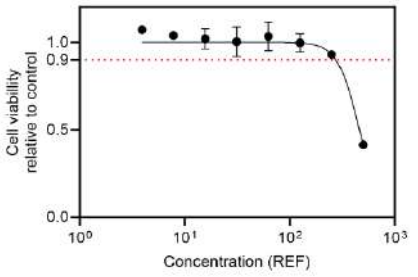
24	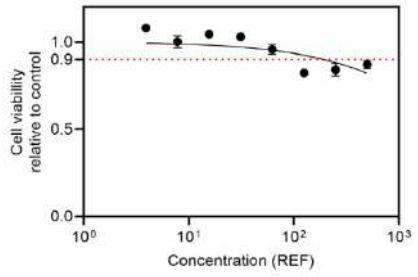	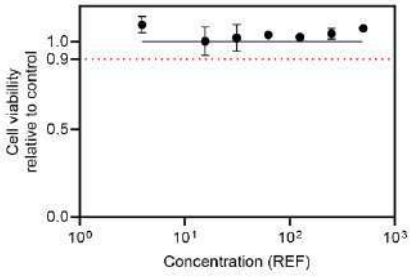

Sites	Wet season	Dry season
25	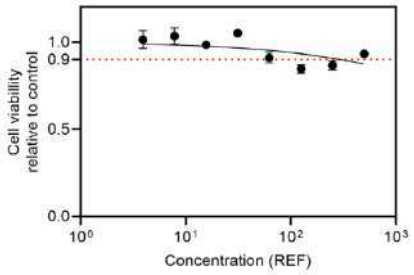	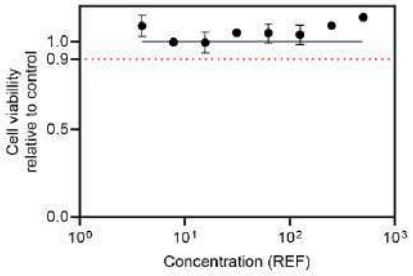
26	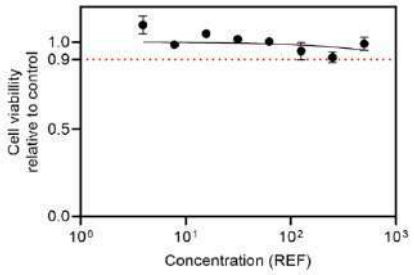	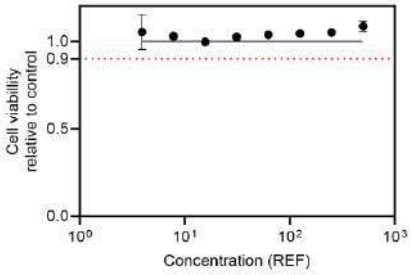
27	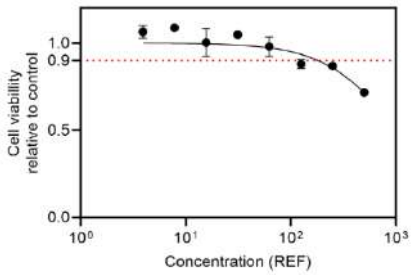	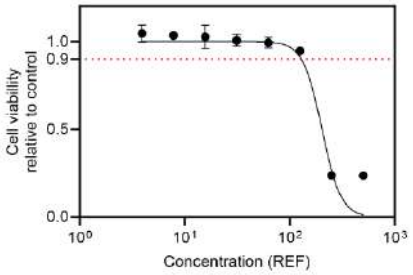
28	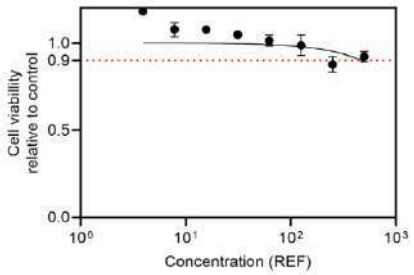	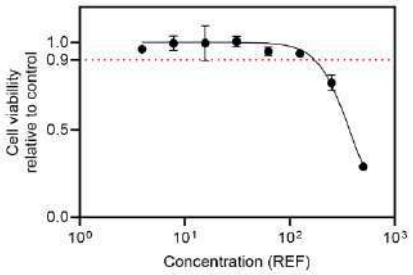
29	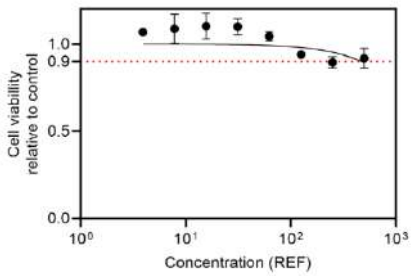	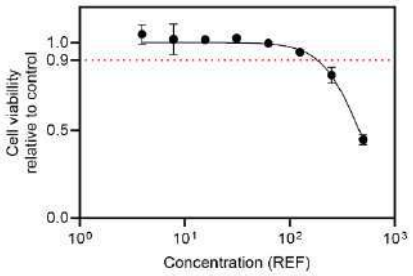

Sites	Wet season	Dry season
30	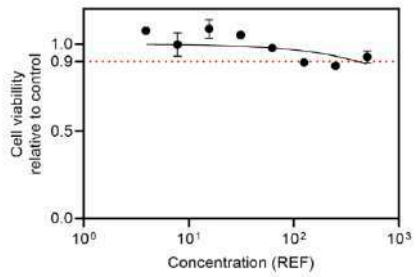	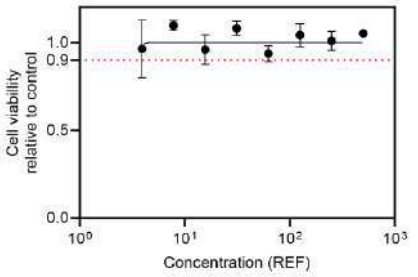
31	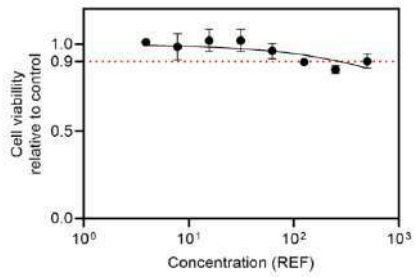	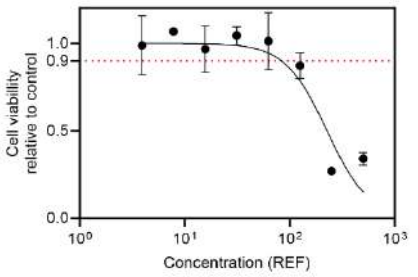
32	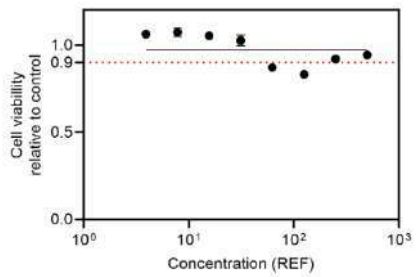	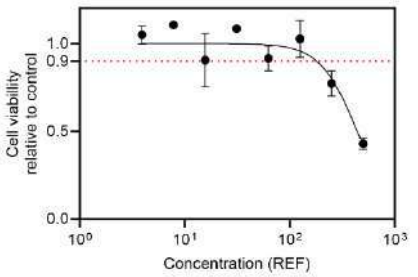
33	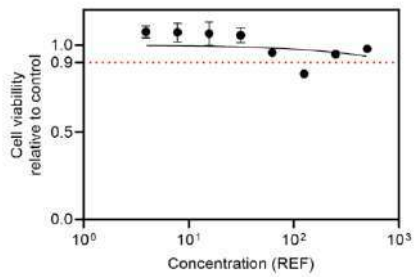	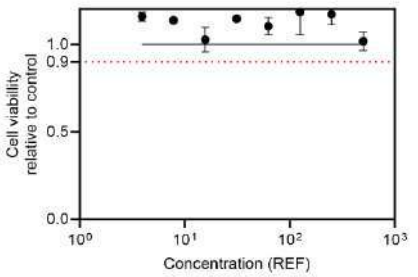
34	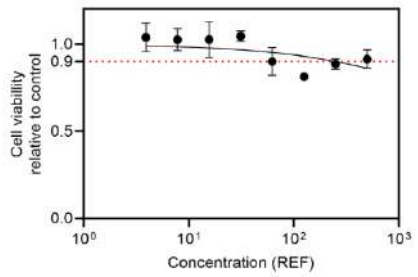	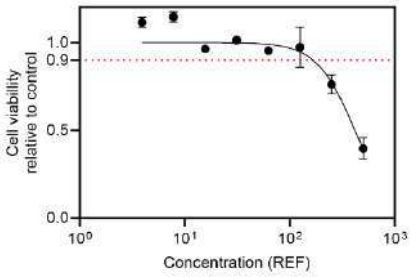

Sites	Wet season	Dry season
35	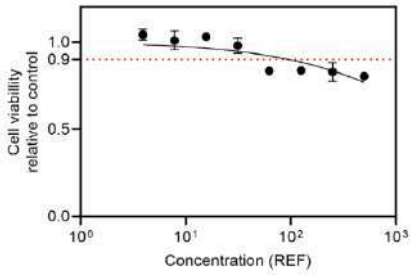	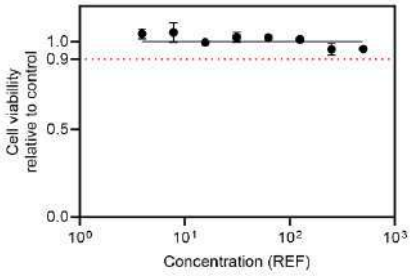
36	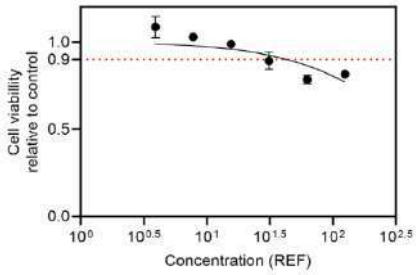	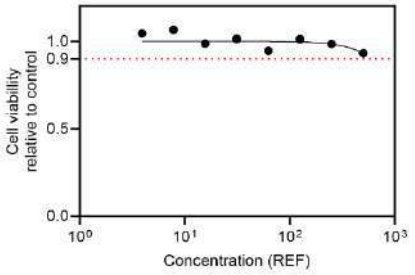

Concentration-effect curves for cytotoxicity induced by seawater extracts in the Indo-Pacific humpback dolphin cell line.

Sites	Wet season	Dry season
1	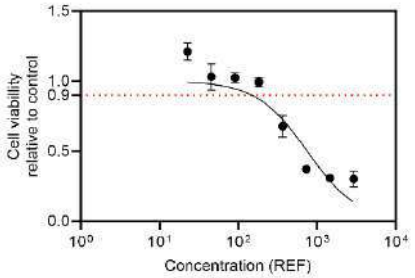	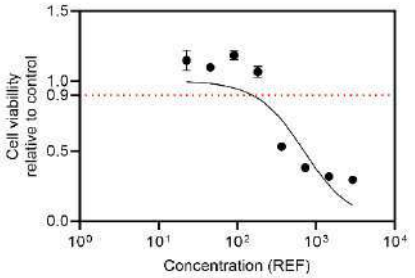
2	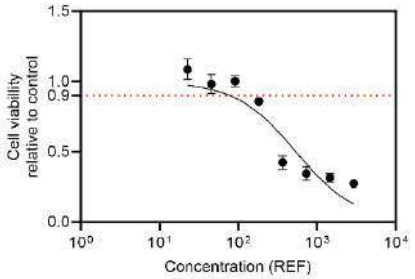	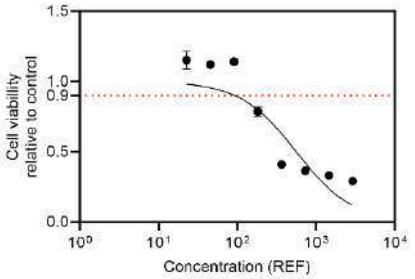

Sites	Wet season	Dry season
3	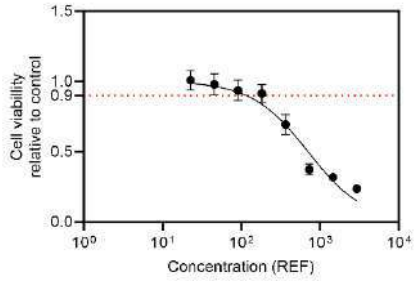	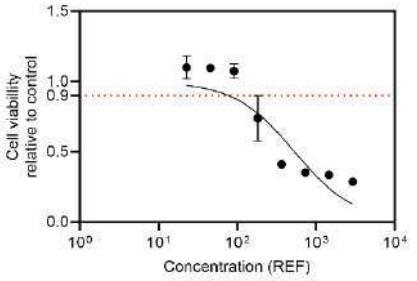
4	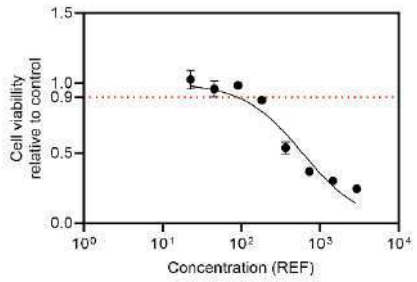	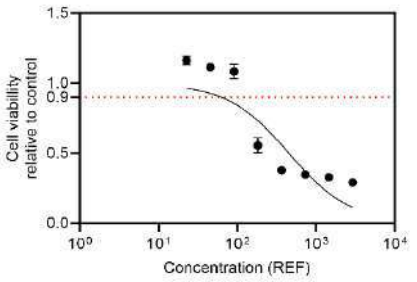
5	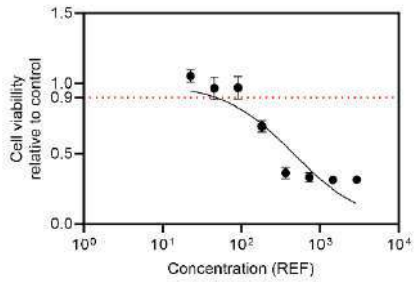	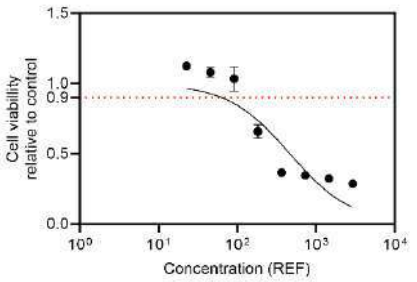
6	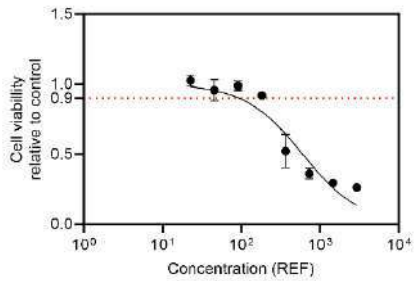	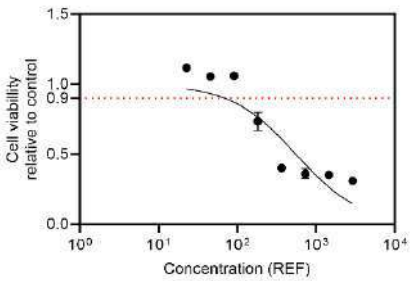
7	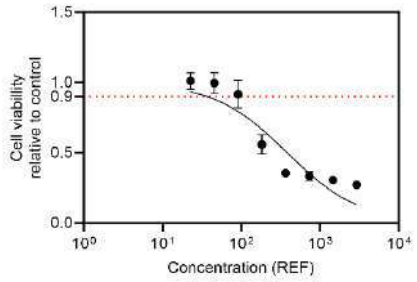	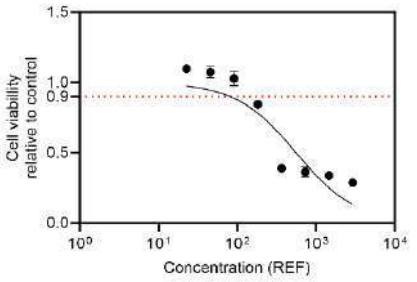

Sites	Wet season	Dry season
8	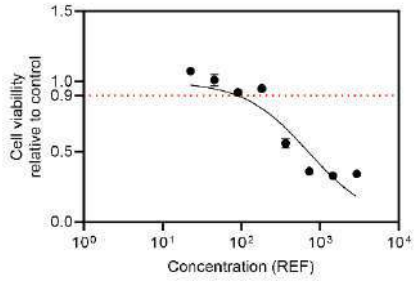	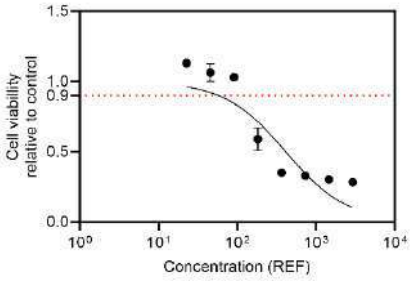
9	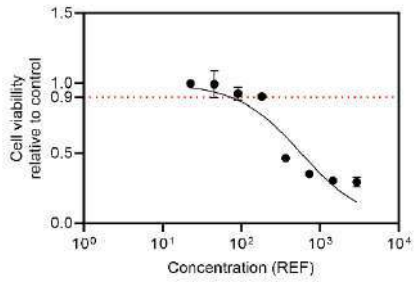	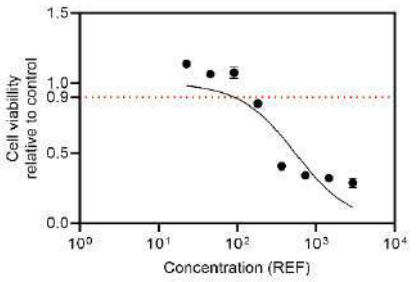
10	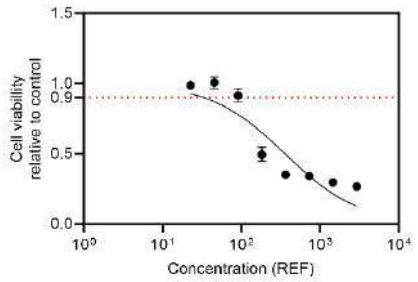	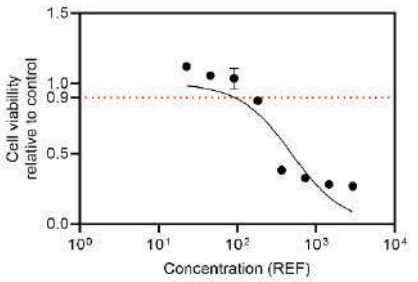
11	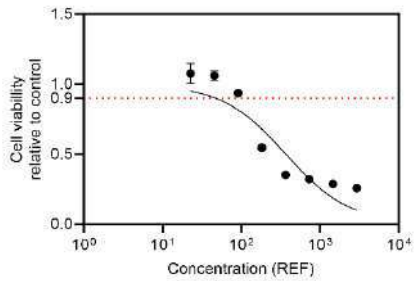	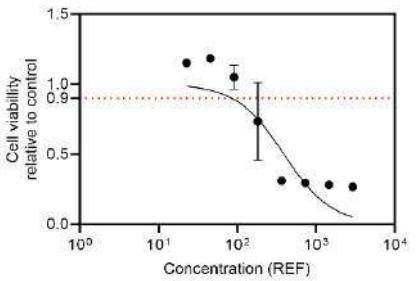
12	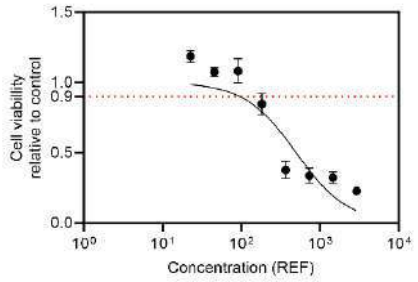	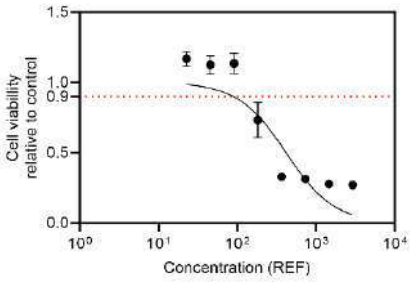

Sites	Wet season	Dry season
13	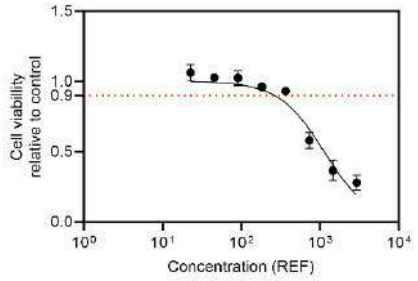	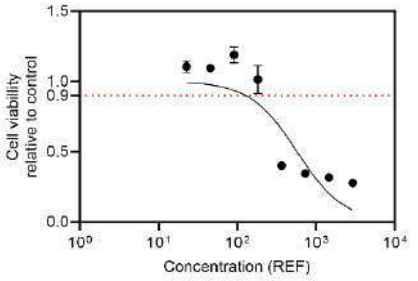
14	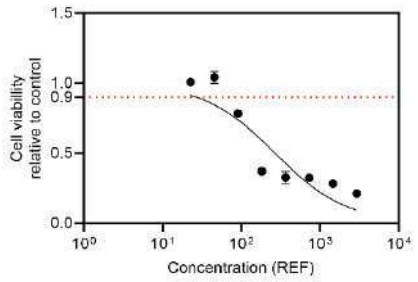	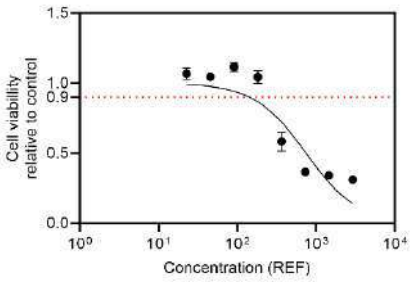
15	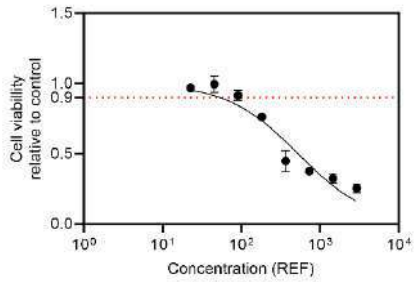	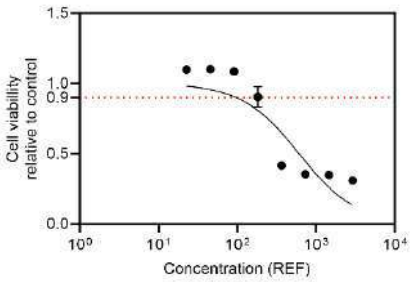
16	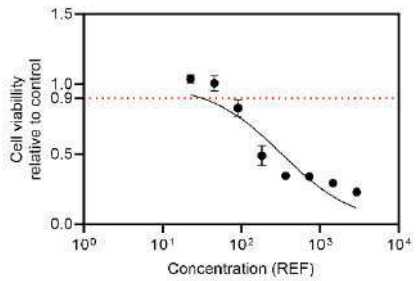	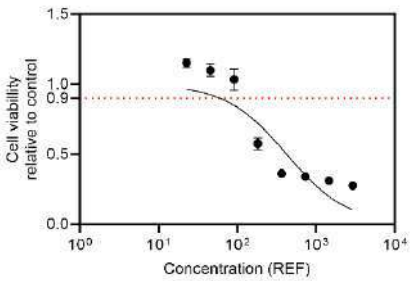
17	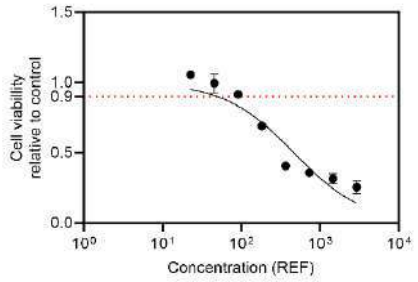	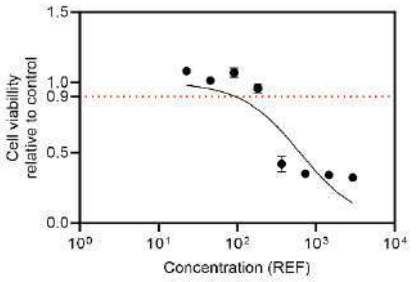

Sites	Wet season	Dry season
18	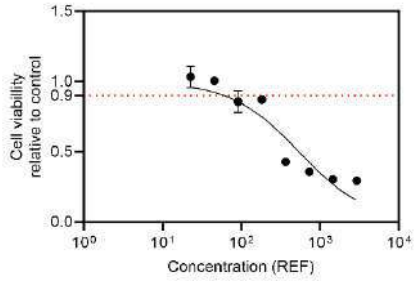	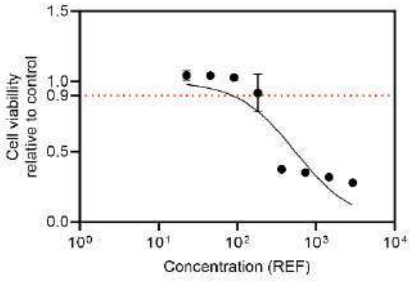
19	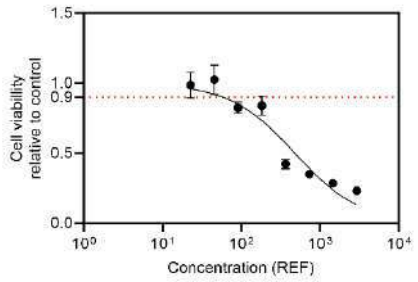	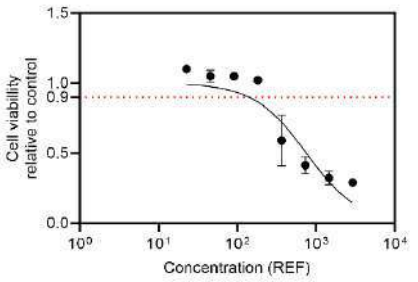
20	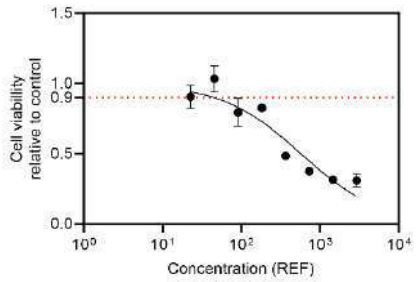	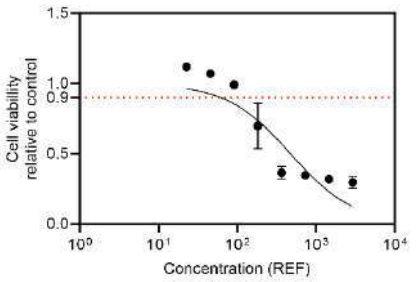
21	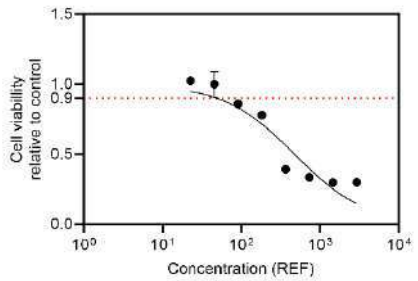	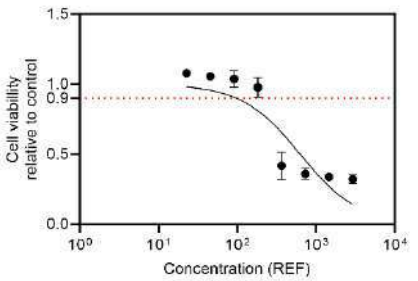
22	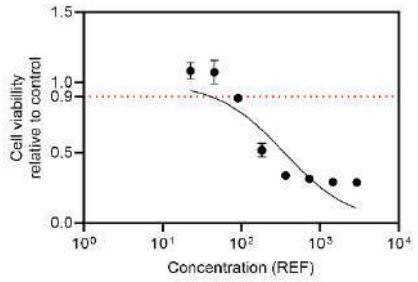	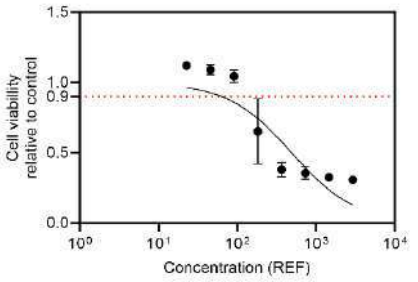

Sites	Wet season	Dry season
23	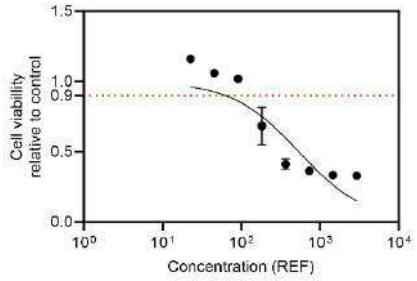	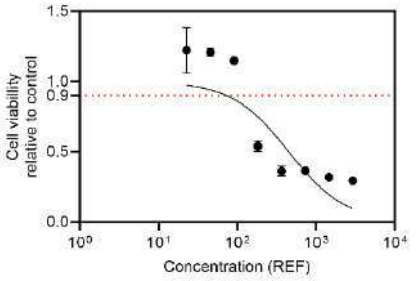
24	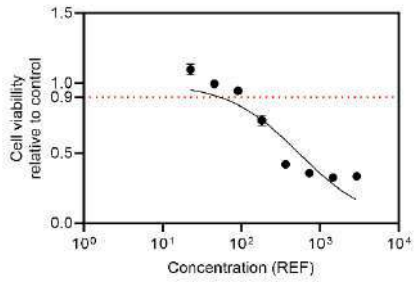	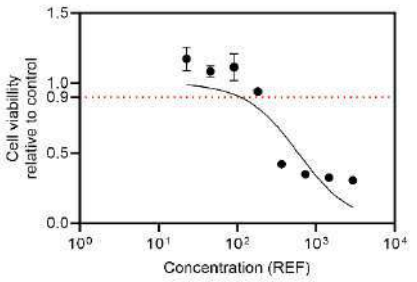
25	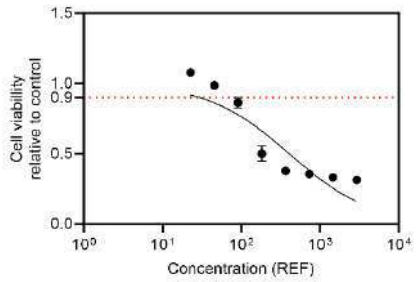	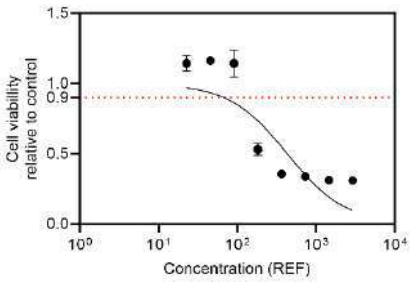
26	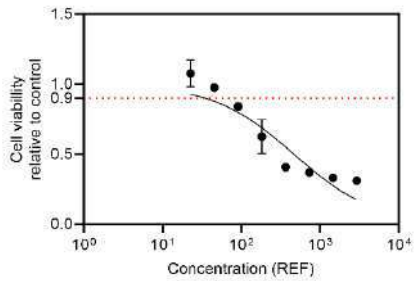	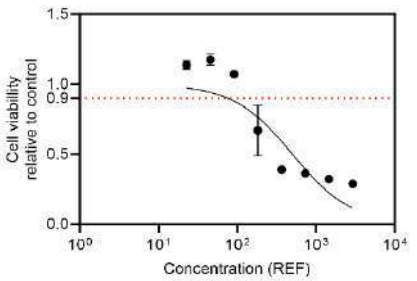
27	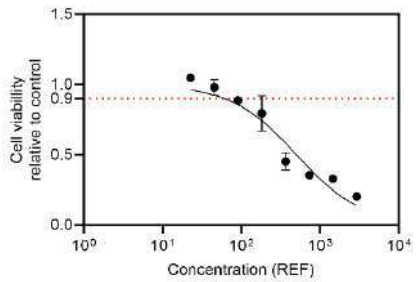	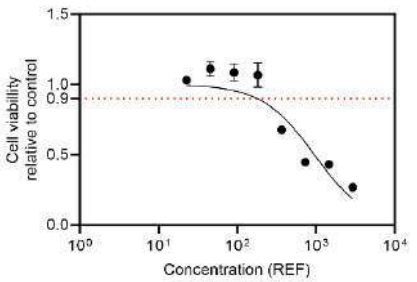

Sites	Wet season	Dry season
28	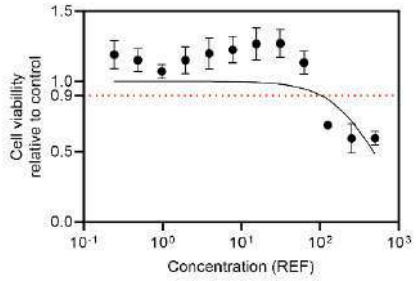	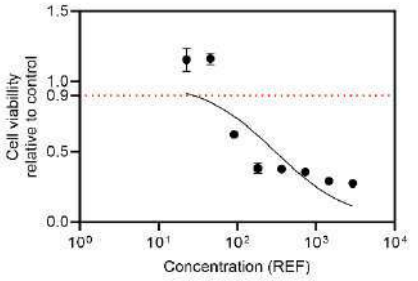
29	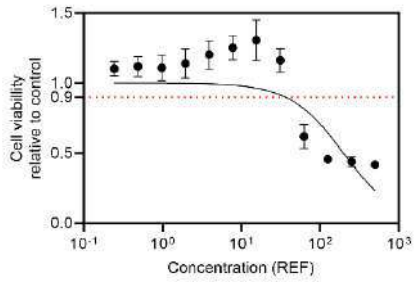	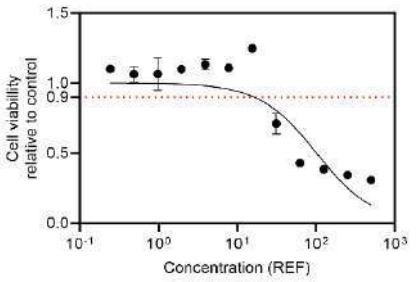
30	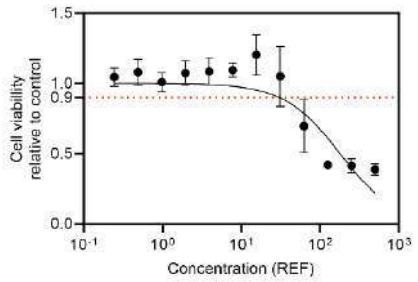	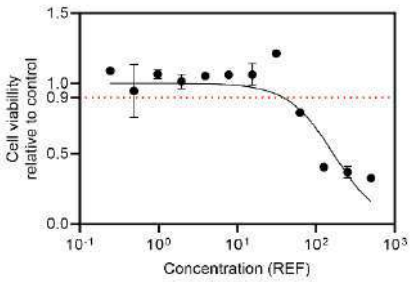
31	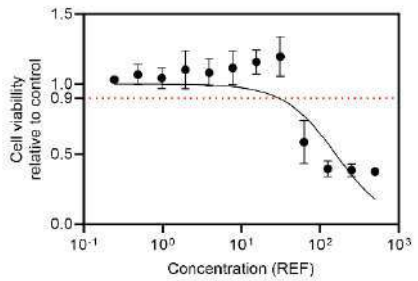	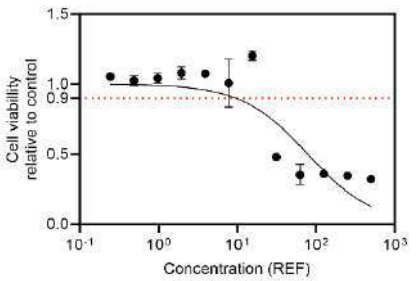
32	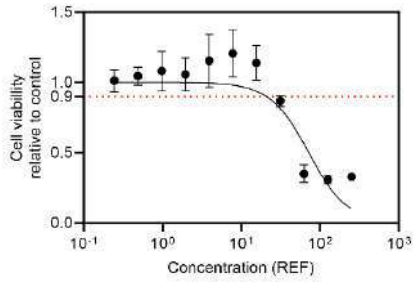	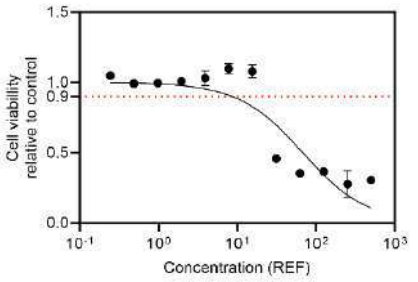

Sites	Wet season	Dry season
33	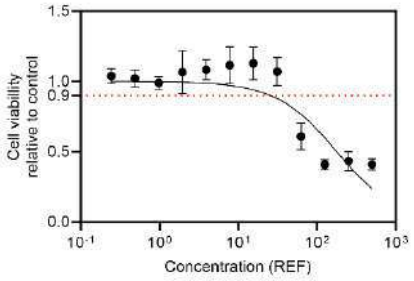	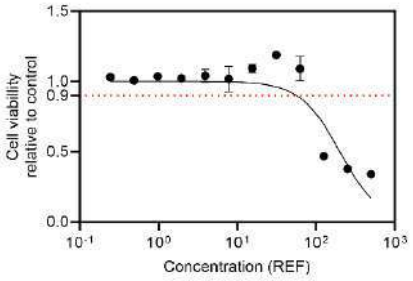
34	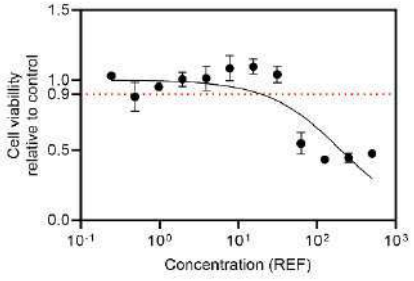	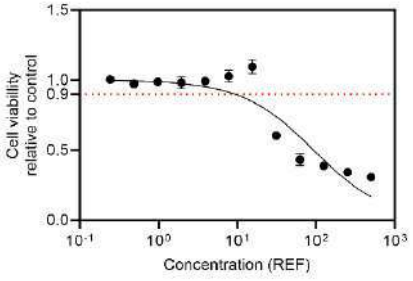
35	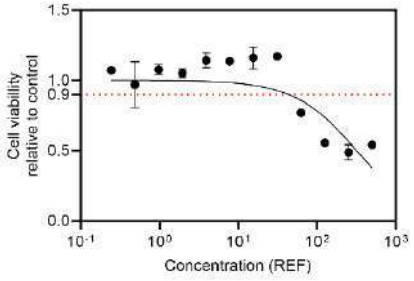	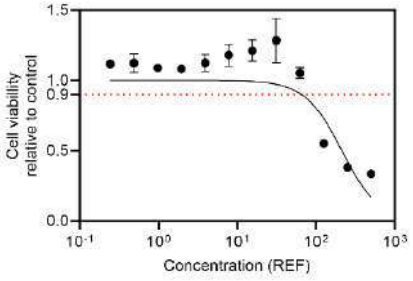
36	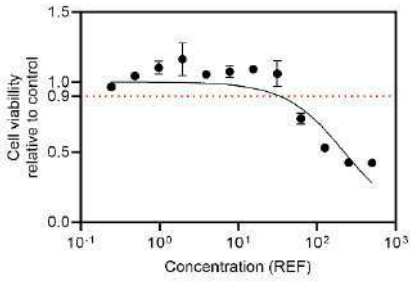	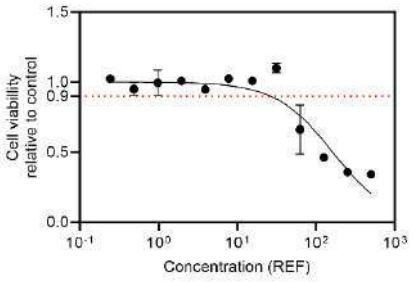

Concentration-effect curves of ROS induced by seawater extracts in the Indo-Pacific finless porpoise skin fibroblast cell line.

Sites	Wet season	Dry season

1	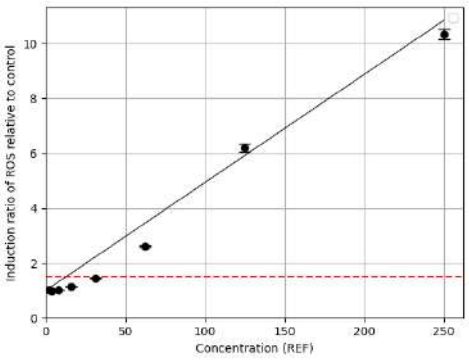 induction ratio of ROS relative to control Concentration (REF)	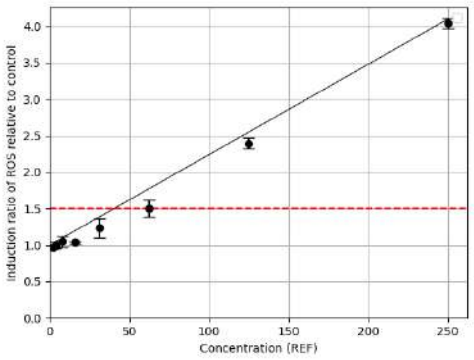 induction ratio of ROS relative to control Concentration (REF)
2	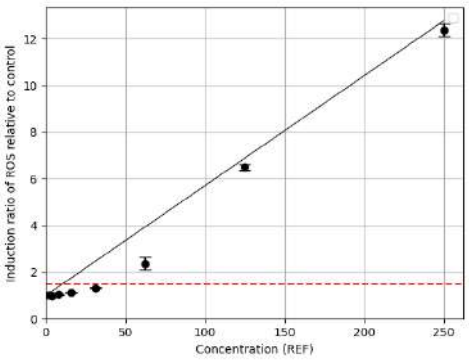 induction ratio of ROS relative to control Concentration (REF)	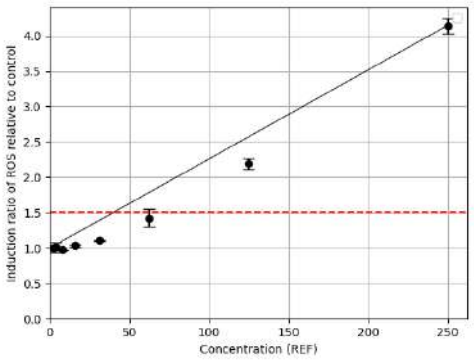 induction ratio of ROS relative to control Concentration (REF)
3	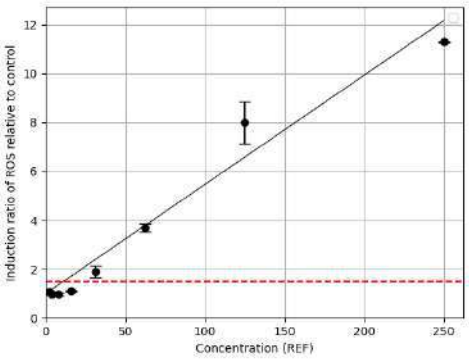 induction ratio of ROS relative to control Concentration (REF)	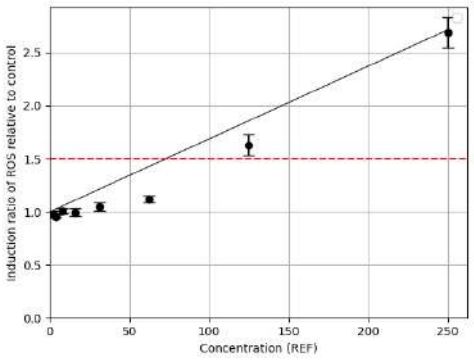 induction ratio of ROS relative to control Concentration (REF)
4	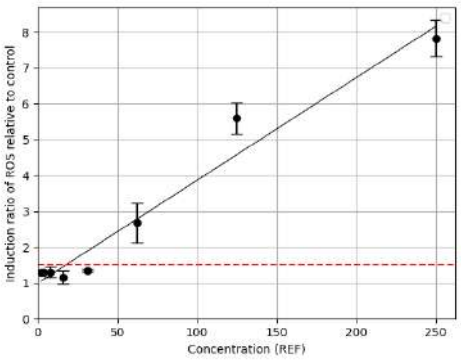 induction ratio of ROS relative to control Concentration (REF)	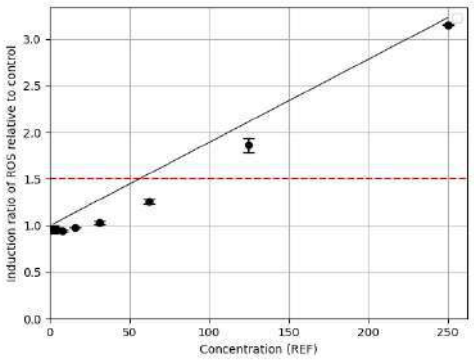 induction ratio of ROS relative to control Concentration (REF)

5	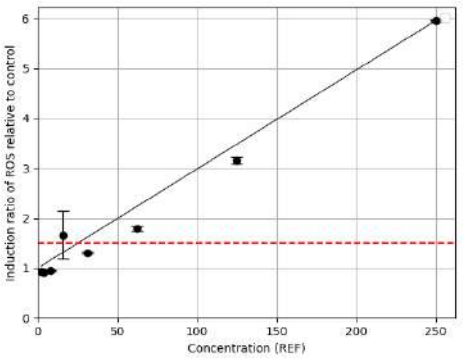 induction ratio of ROS relative to control Concentration (REF)	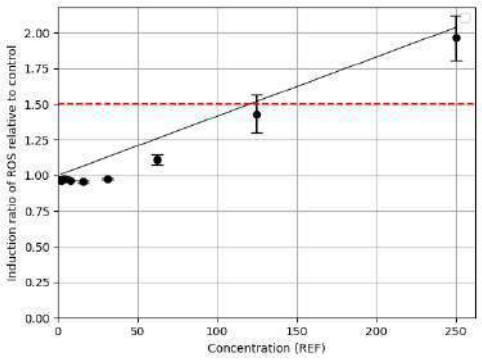 induction ratio of ROS relative to control Concentration (REF)
6	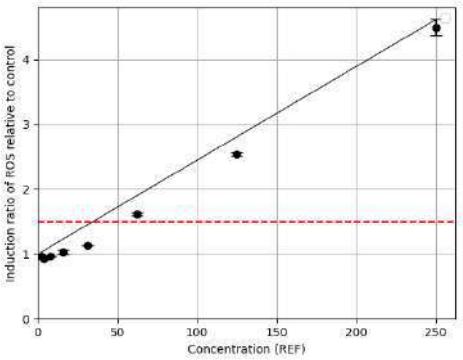 induction ratio of ROS relative to control Concentration (REF)	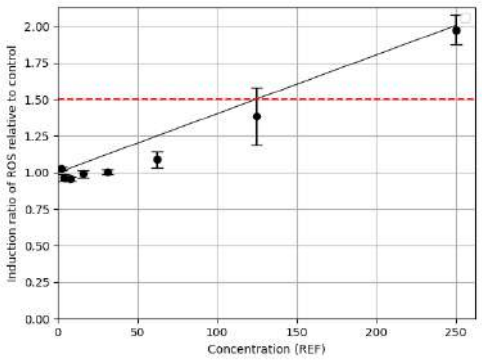 induction ratio of ROS relative to control Concentration (REF)
7	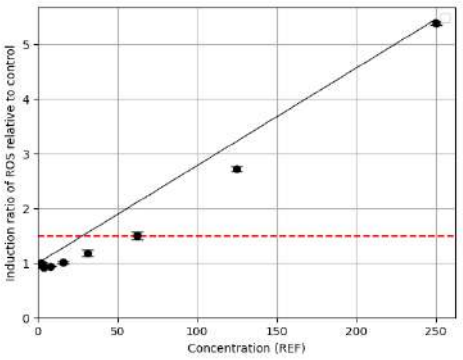 induction ratio of ROS relative to control Concentration (REF)	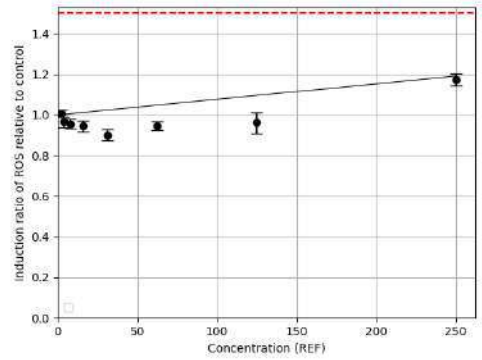 induction ratio of ROS relative to control Concentration (REF)
8	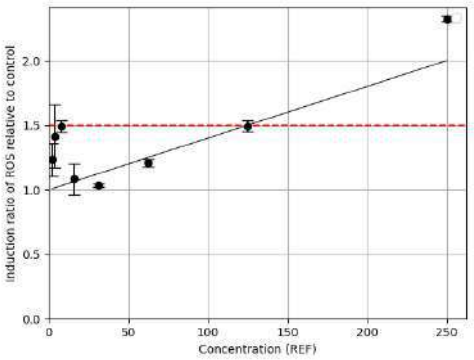 induction ratio of ROS relative to control Concentration (REF)	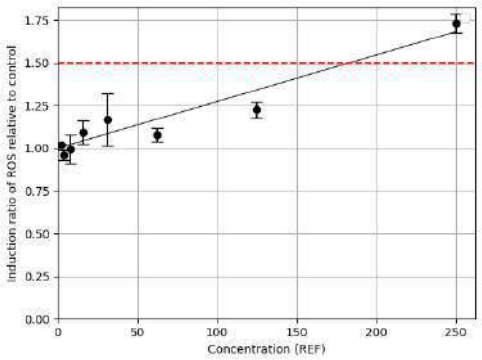 induction ratio of ROS relative to control Concentration (REF)

9	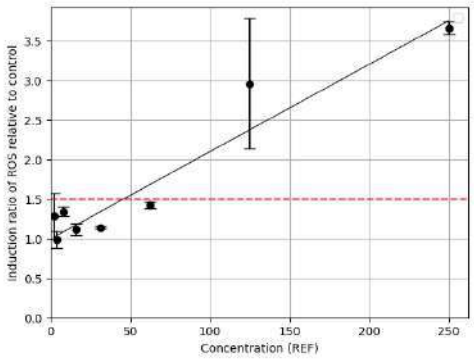 induction ratio of ROS relative to control Concentration (REF)	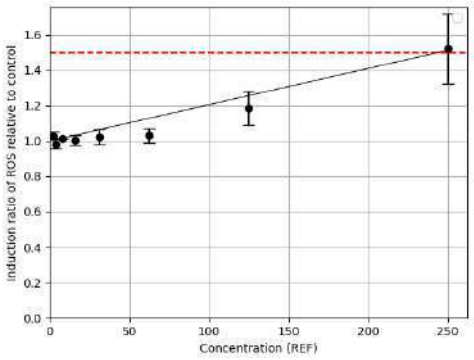 induction ratio of ROS relative to control Concentration (REF)
10	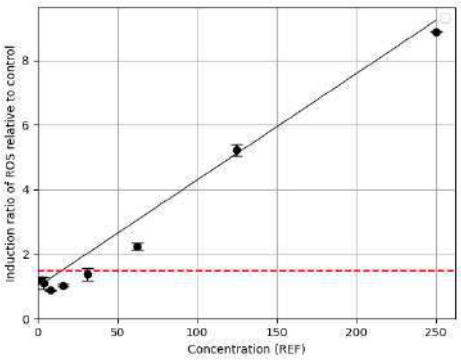 induction ratio of ROS relative to control Concentration (REF)	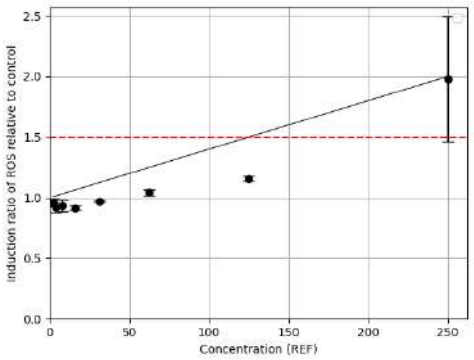 induction ratio of ROS relative to control Concentration (REF)
11	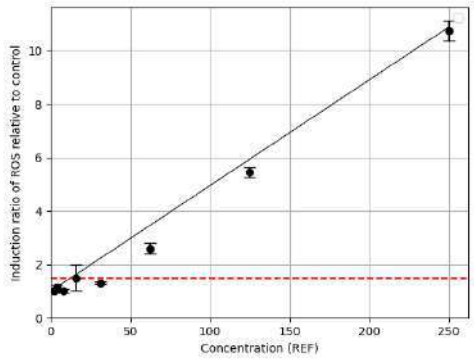 induction ratio of ROS relative to control Concentration (REF)	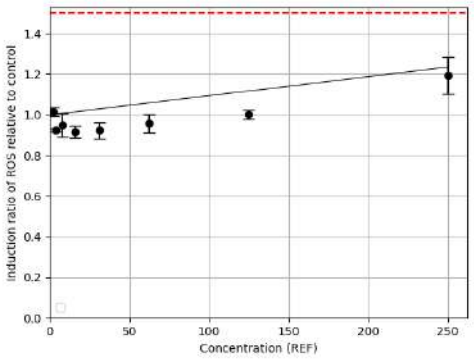 induction ratio of ROS relative to control Concentration (REF)
12	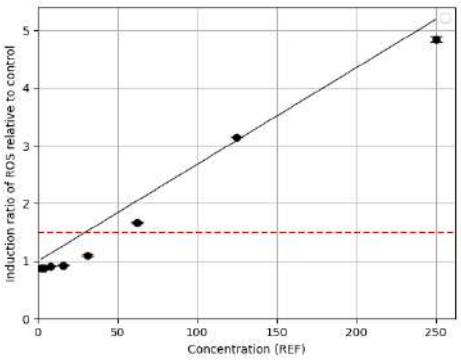 induction ratio of ROS relative to control Concentration (REF)	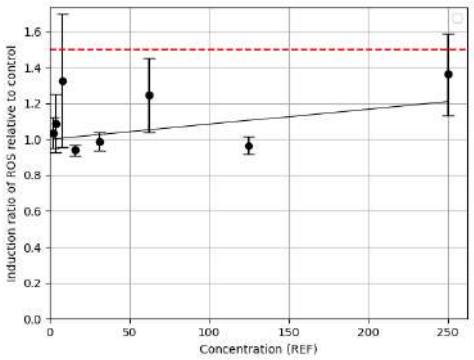 induction ratio of ROS relative to control Concentration (REF)

13	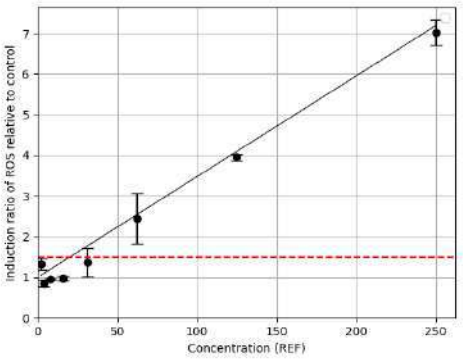 induction ratio of ROS relative to control Concentration (REF)	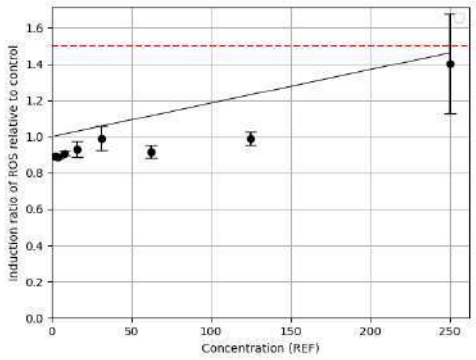 induction ratio of ROS relative to control Concentration (REF)
14	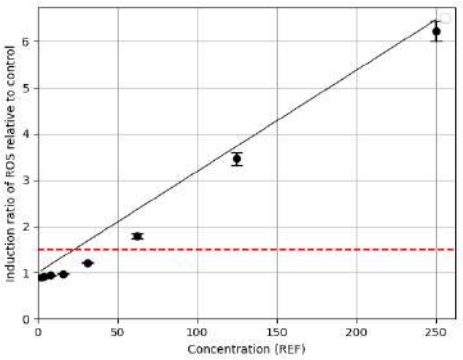 induction ratio of ROS relative to control Concentration (REF)	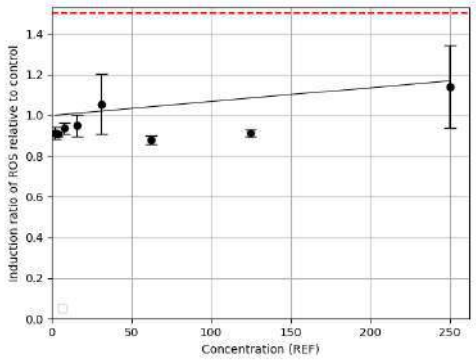 induction ratio of ROS relative to control Concentration (REF)
15	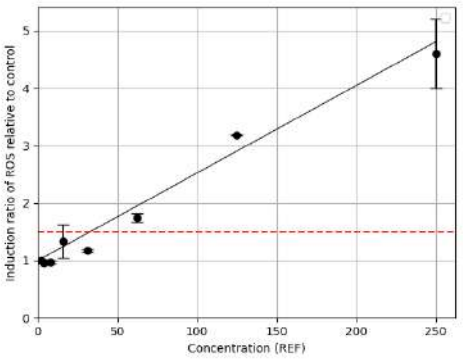 induction ratio of ROS relative to control Concentration (REF)	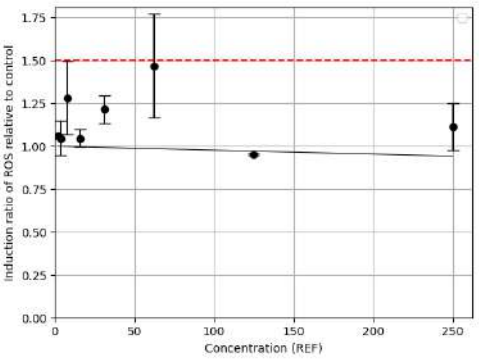 induction ratio of ROS relative to control Concentration (REF)
16	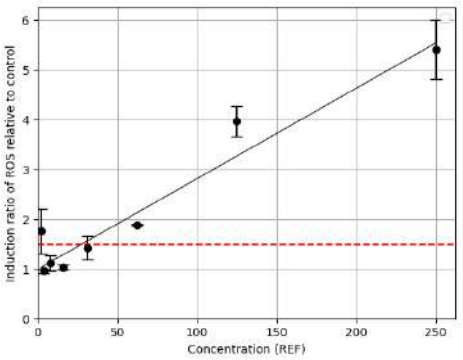 induction ratio of ROS relative to control Concentration (REF)	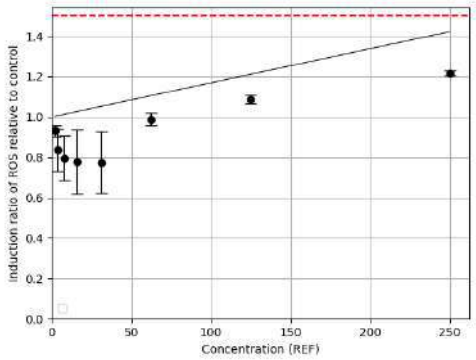 induction ratio of ROS relative to control Concentration (REF)

17	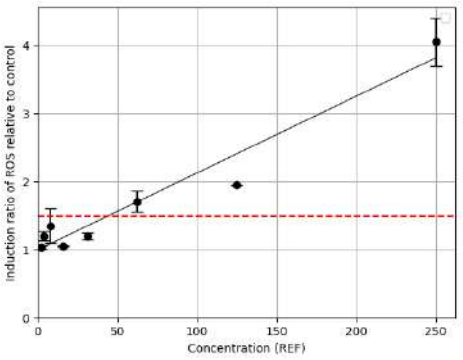 induction ratio of ROS relative to control Concentration (REF)	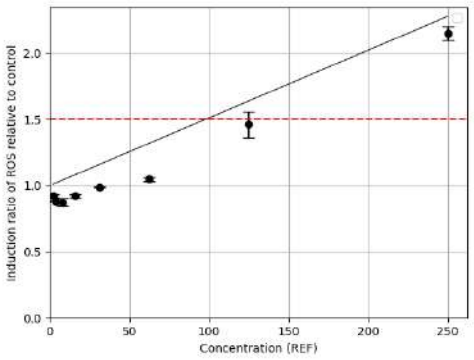 induction ratio of ROS relative to control Concentration (REF)
18	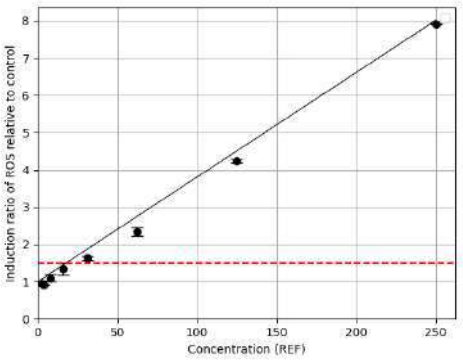 induction ratio of ROS relative to control Concentration (REF)	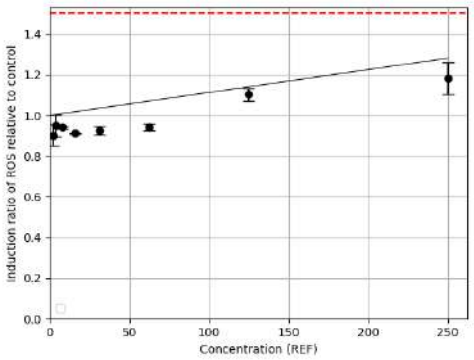 induction ratio of ROS relative to control Concentration (REF)
19	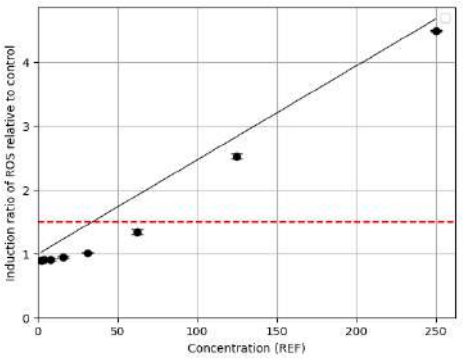 induction ratio of ROS relative to control Concentration (REF)	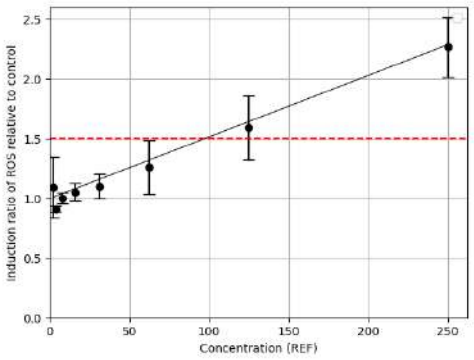 induction ratio of ROS relative to control Concentration (REF)
20	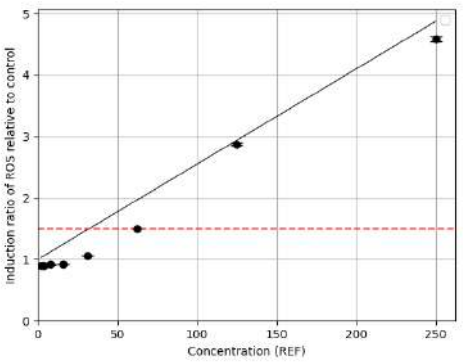 induction ratio of ROS relative to control Concentration (REF)	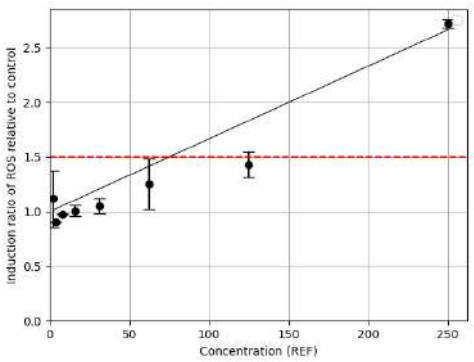 induction ratio of ROS relative to control Concentration (REF)

21	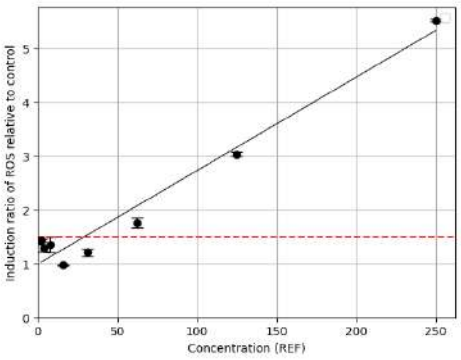	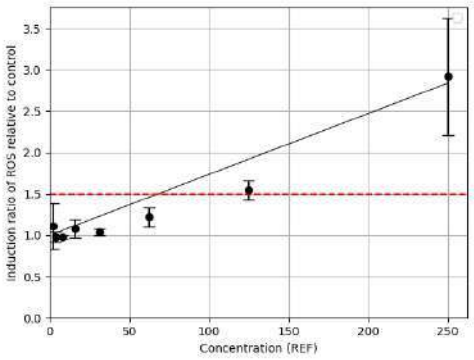
22	Not analyzed due to sample exhaustion	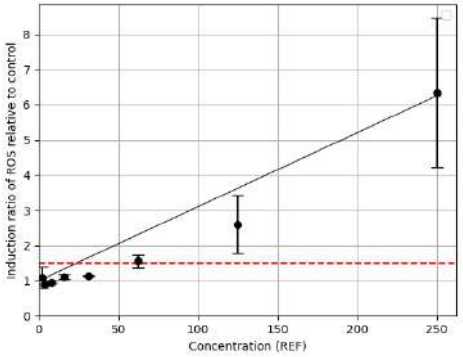
23	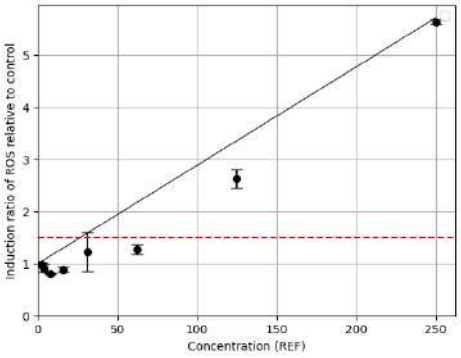	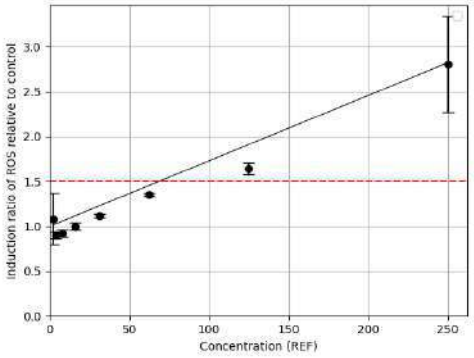
24	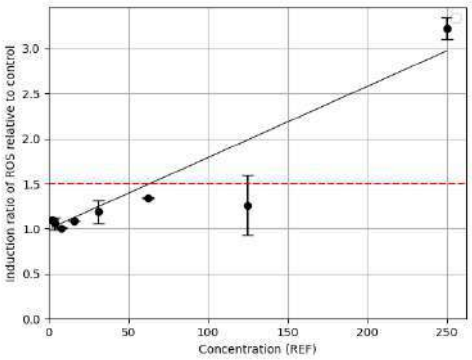	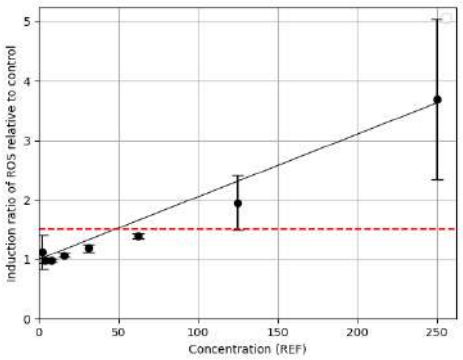

25	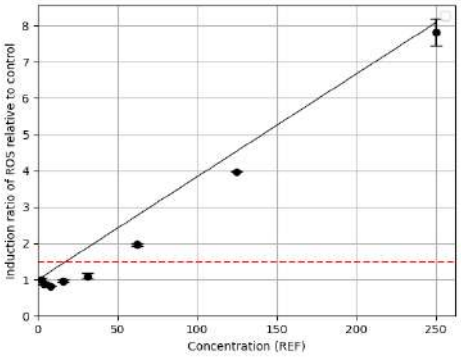	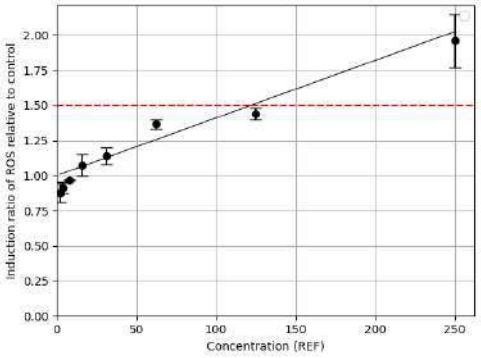
26	Not analyzed due to sample exhaustion	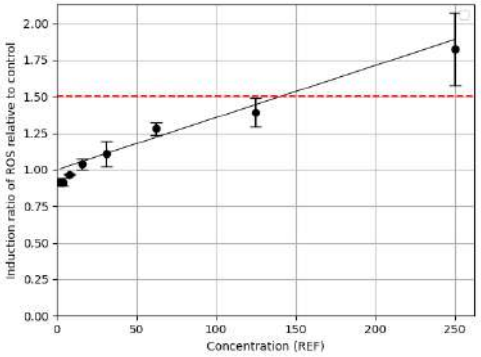
27	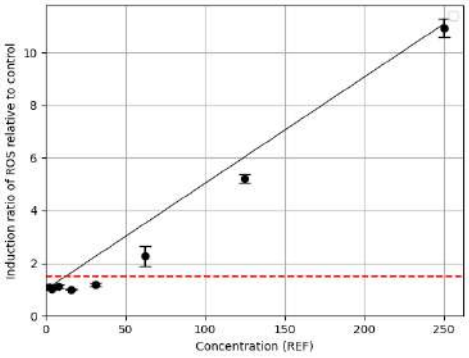	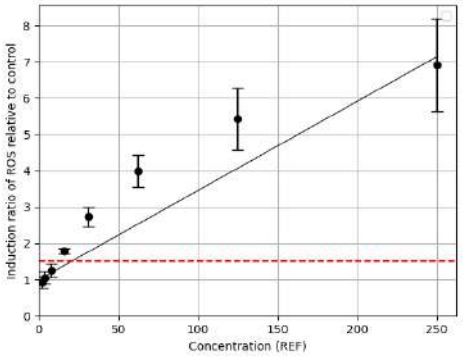
28	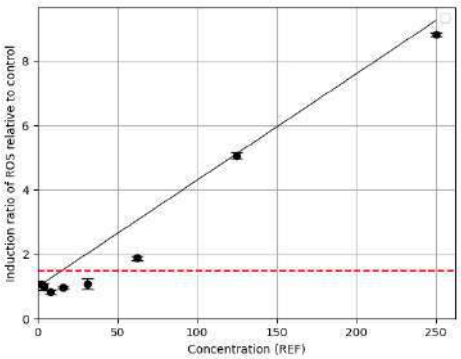	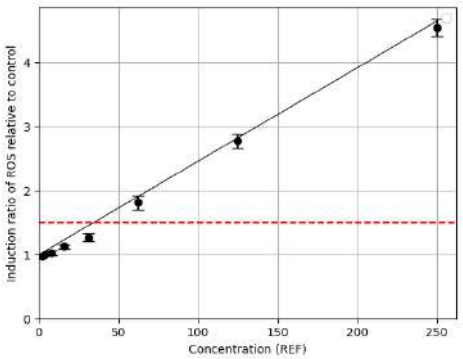

29	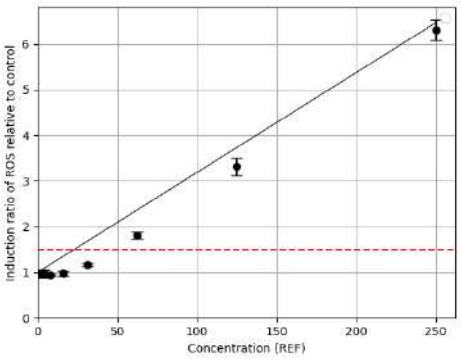	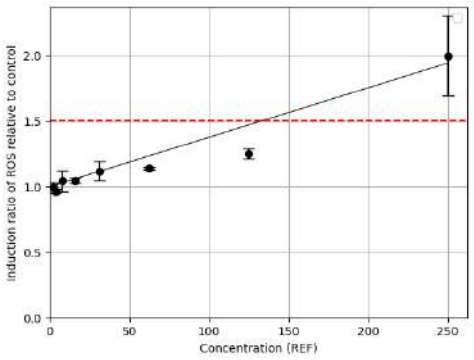
30	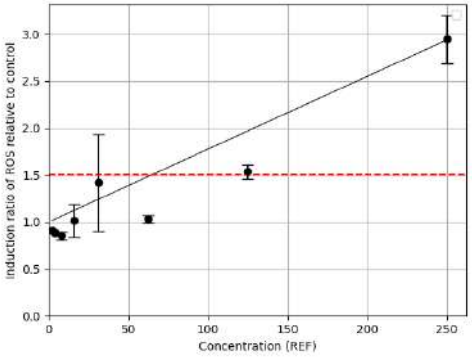	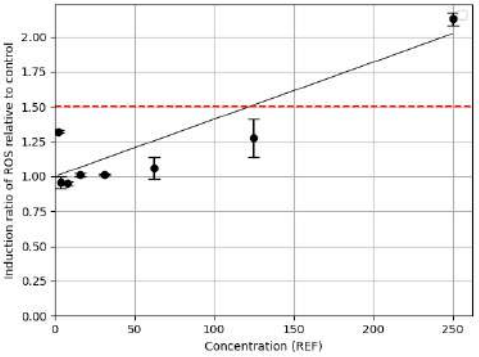
31	Not analyzed due to sample exhaustion	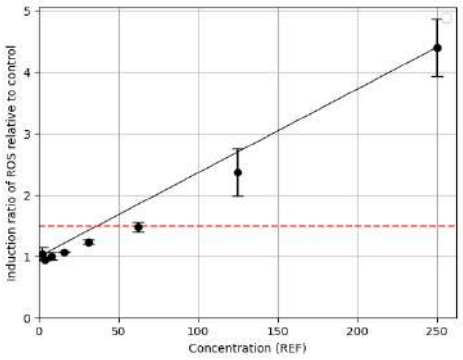
32	Not analyzed due to sample exhaustion	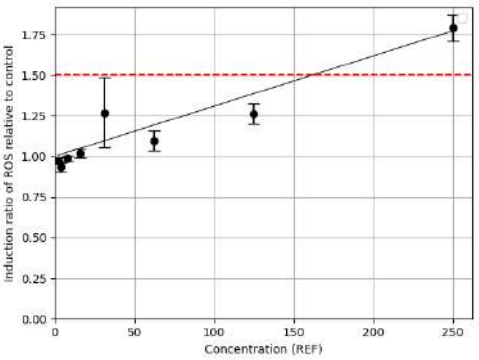

33	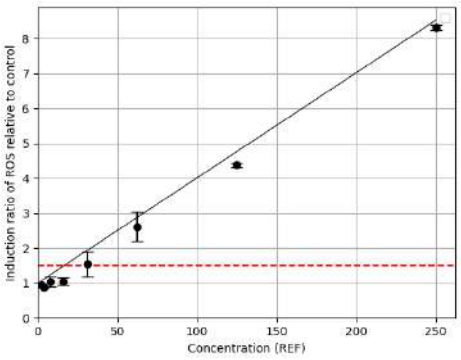 Induction ratio of ROS relative to control Concentration (REF)	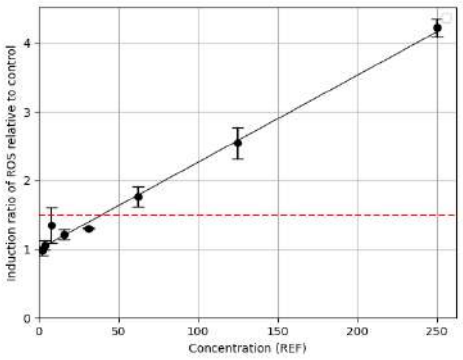 Induction ratio of ROS relative to control Concentration (REF)
34	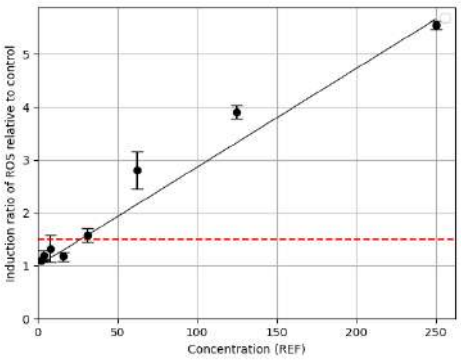 Induction ratio of ROS relative to control Concentration (REF)	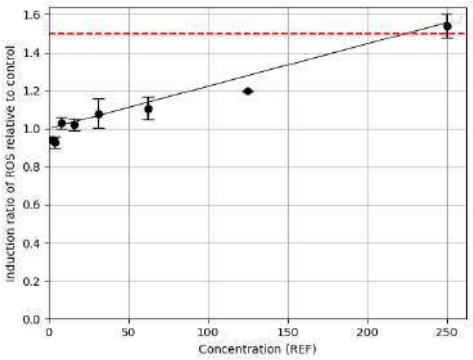 Induction ratio of ROS relative to control Concentration (REF)
35	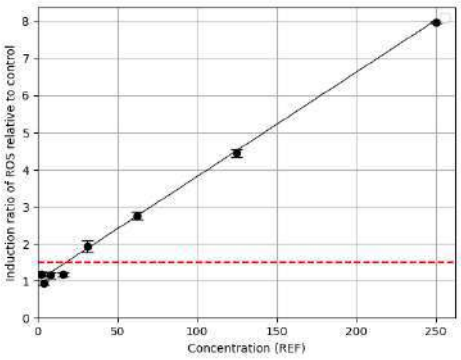 Induction ratio of ROS relative to control Concentration (REF)	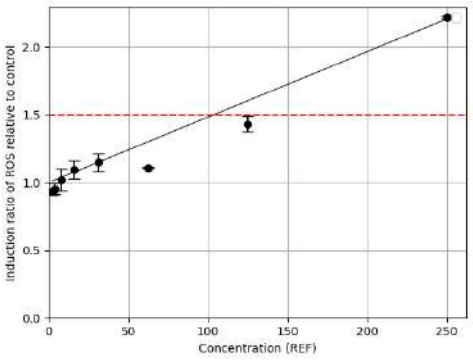 Induction ratio of ROS relative to control Concentration (REF)
36	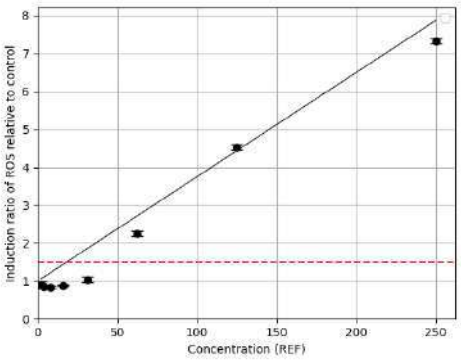 Induction ratio of ROS relative to control Concentration (REF)	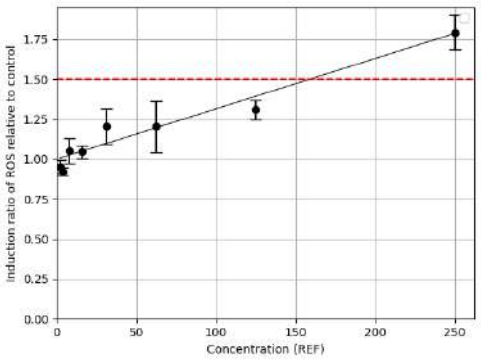 Induction ratio of ROS relative to control Concentration (REF)

Concentration-effect curves of ROS induced by seawater extracts in the Indo-Pacific humpback dolphin skin fibroblast cell line.

Sites	Wet season	Dry season
1	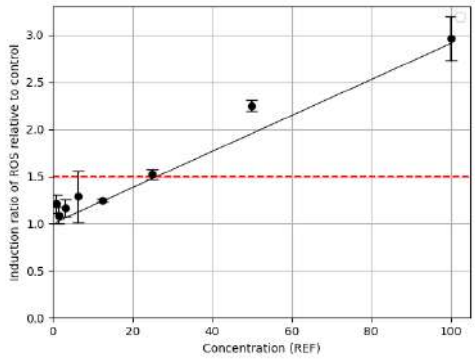	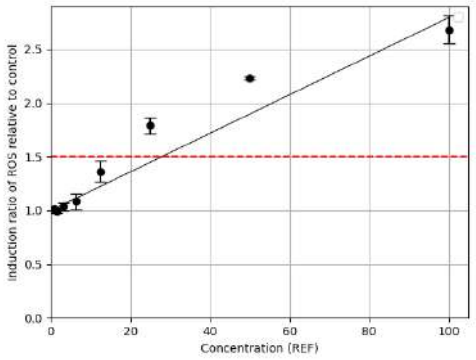
2	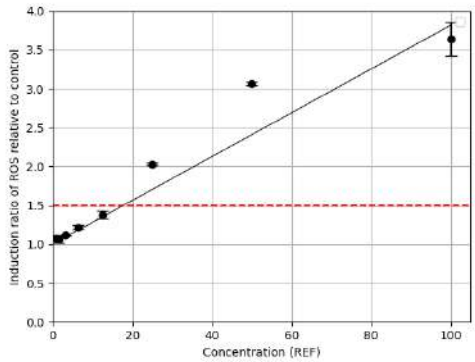	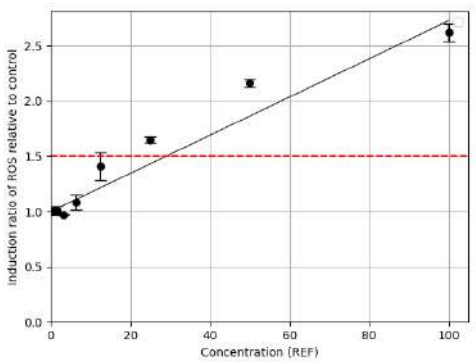
3	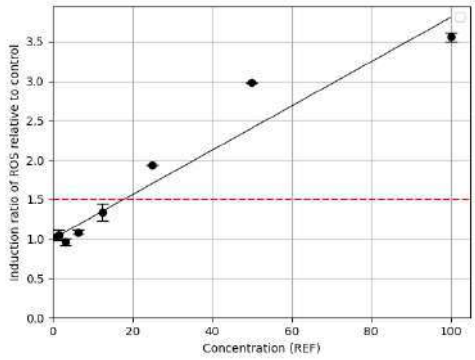	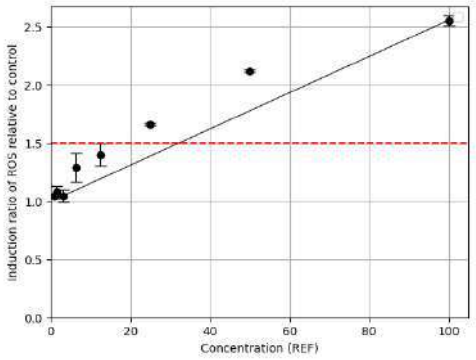

4	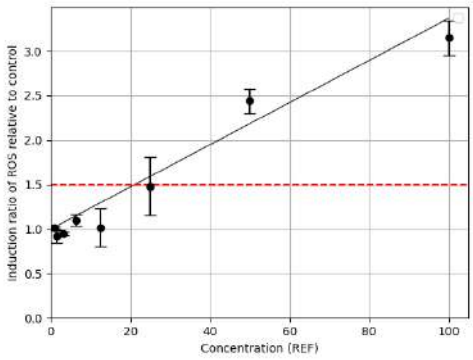 induction ratio of ROS relative to control Concentration (REF)	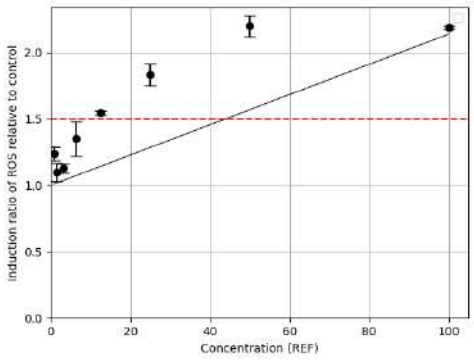 induction ratio of ROS relative to control Concentration (REF)
5	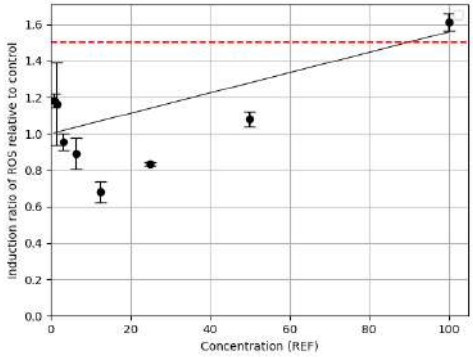 induction ratio of ROS relative to control Concentration (REF)	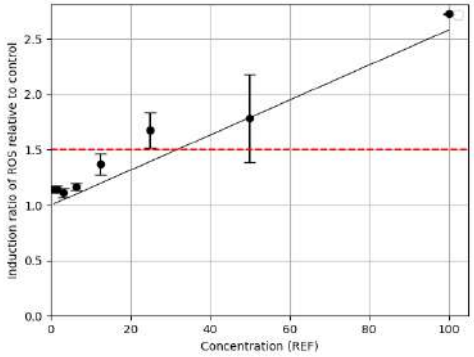 induction ratio of ROS relative to control Concentration (REF)
6	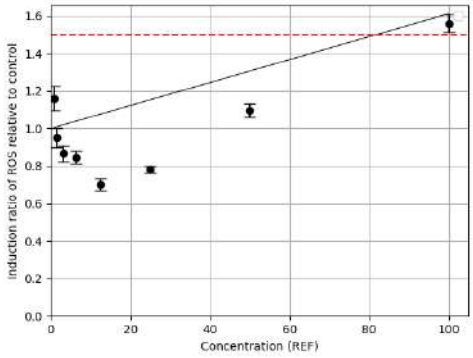 induction ratio of ROS relative to control Concentration (REF)	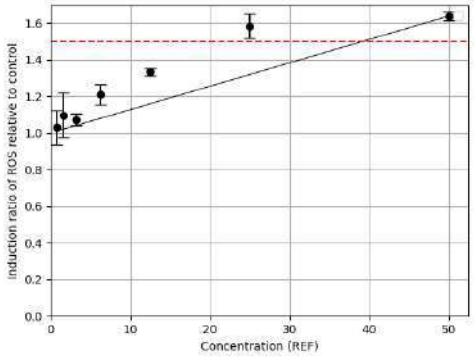 induction ratio of ROS relative to control Concentration (REF)
7	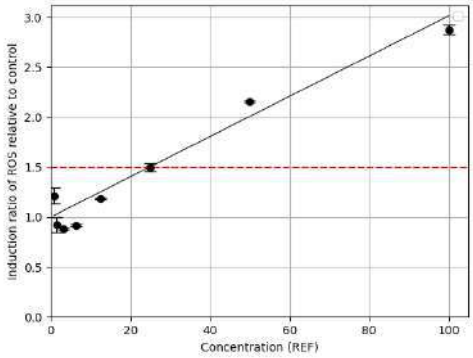 induction ratio of ROS relative to control Concentration (REF)	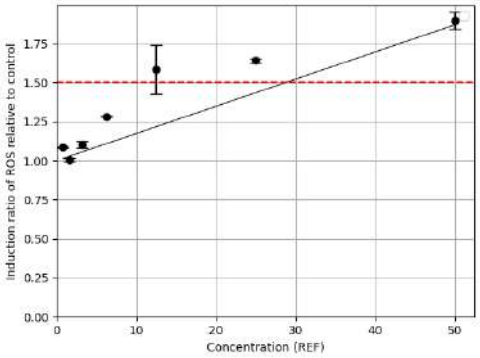 induction ratio of ROS relative to control Concentration (REF)

8	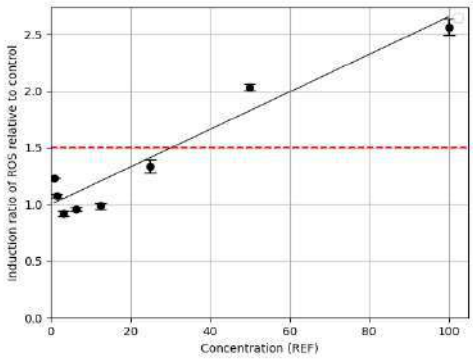 induction ratio of ROS relative to control Concentration (REF)	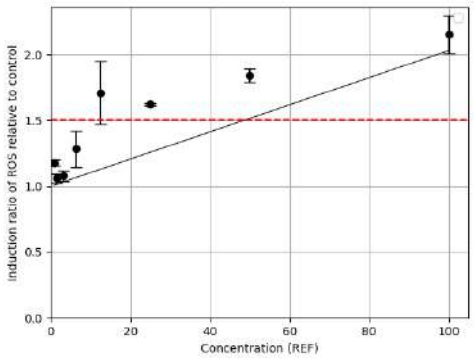 induction ratio of ROS relative to control Concentration (REF)
9	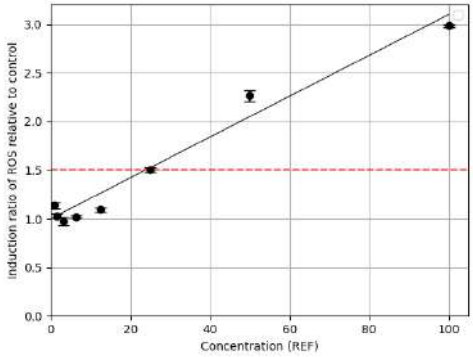 induction ratio of ROS relative to control Concentration (REF)	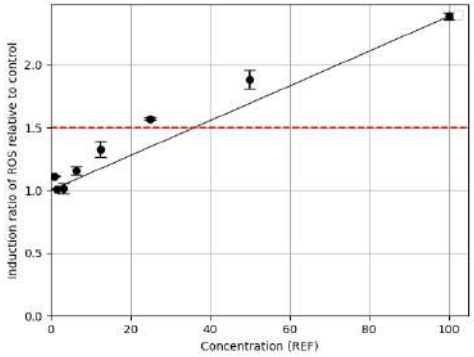 induction ratio of ROS relative to control Concentration (REF)
10	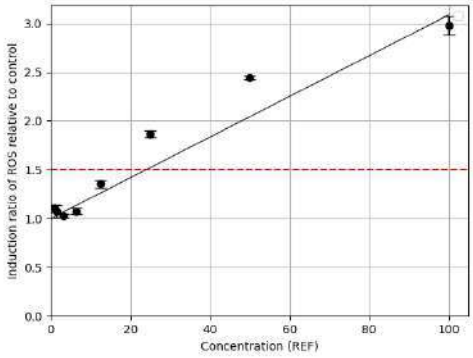 induction ratio of ROS relative to control Concentration (REF)	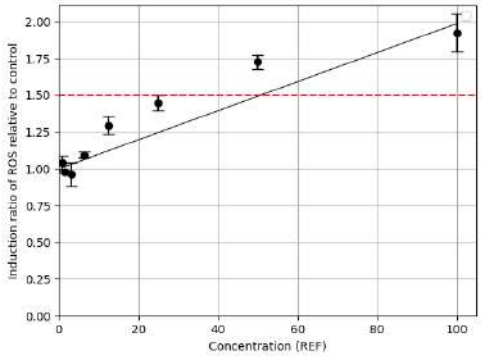 induction ratio of ROS relative to control Concentration (REF)
11	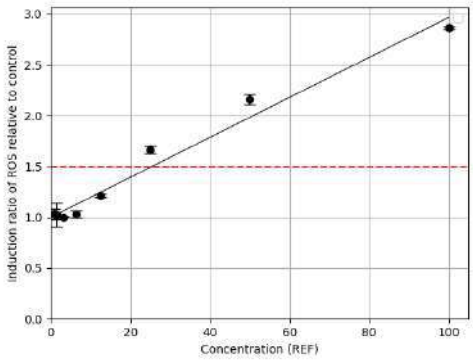 induction ratio of ROS relative to control Concentration (REF)	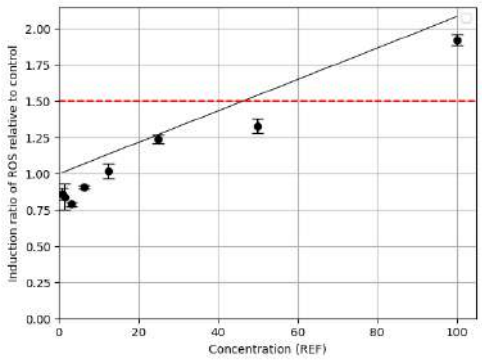 induction ratio of ROS relative to control Concentration (REF)

12	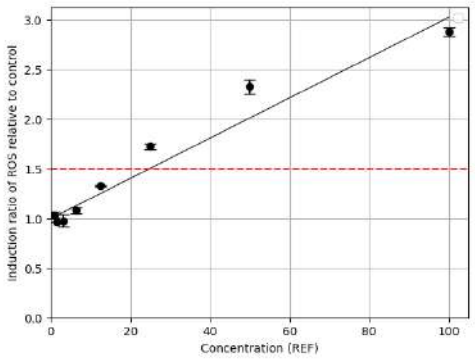 Induction ratio of ROS relative to control Concentration (REF)	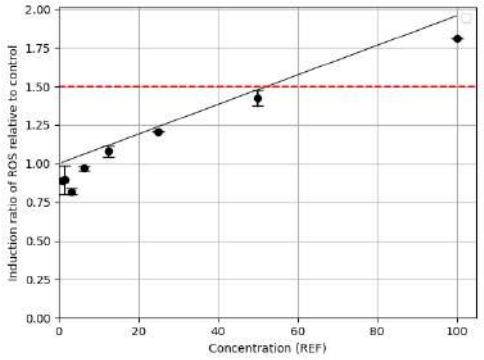 Induction ratio of ROS relative to control Concentration (REF)
13	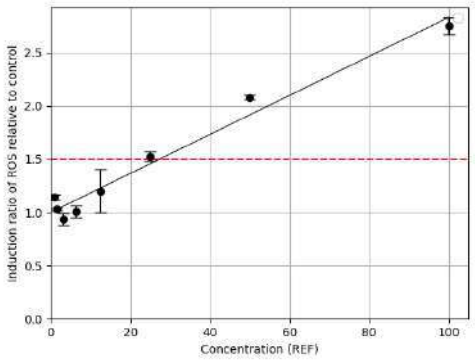 Induction ratio of ROS relative to control Concentration (REF)	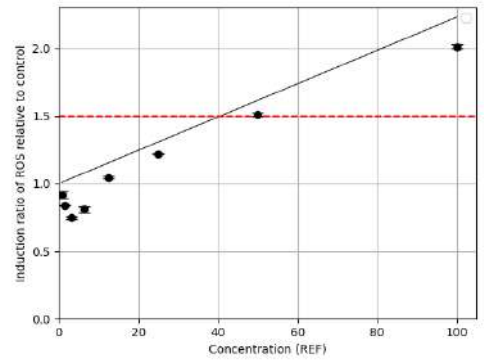 Induction ratio of ROS relative to control Concentration (REF)
14	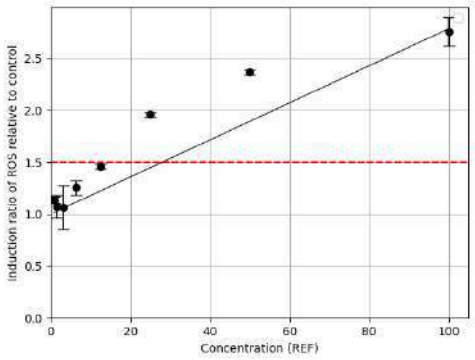 Induction ratio of ROS relative to control Concentration (REF)	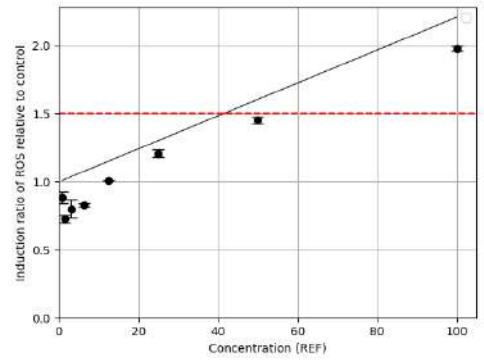 Induction ratio of ROS relative to control Concentration (REF)
15	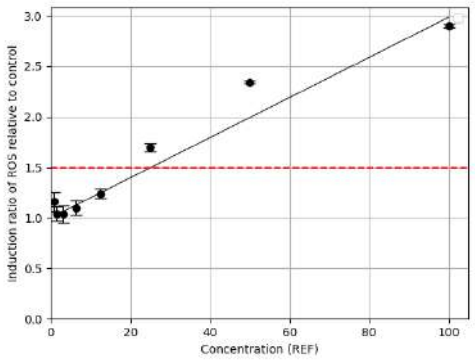 Induction ratio of ROS relative to control Concentration (REF)	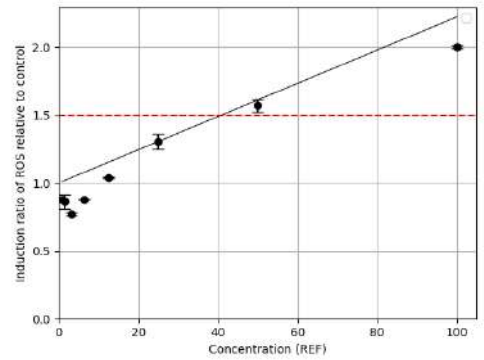 Induction ratio of ROS relative to control Concentration (REF)

16	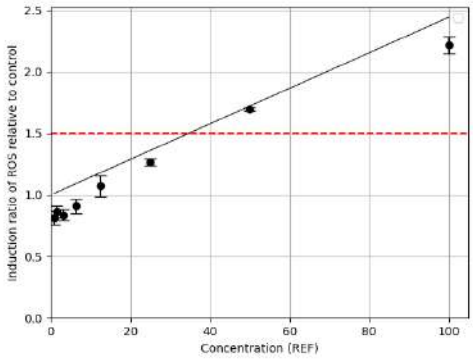 induction ratio of ROS relative to control Concentration (REF)	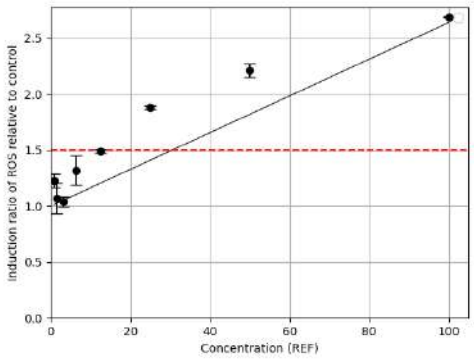 induction ratio of ROS relative to control Concentration (REF)
17	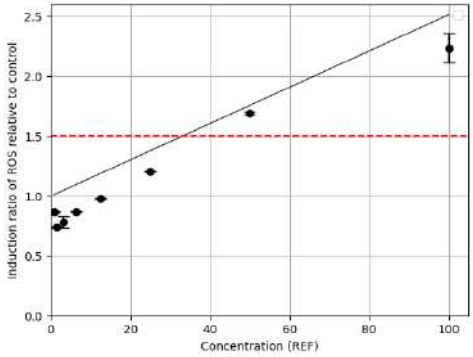 induction ratio of ROS relative to control Concentration (REF)	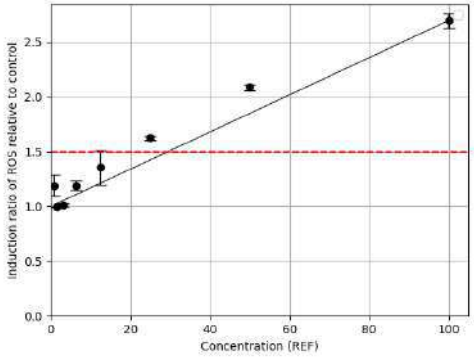 induction ratio of ROS relative to control Concentration (REF)
18	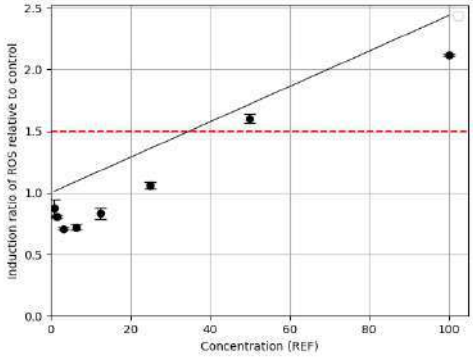 induction ratio of ROS relative to control Concentration (REF)	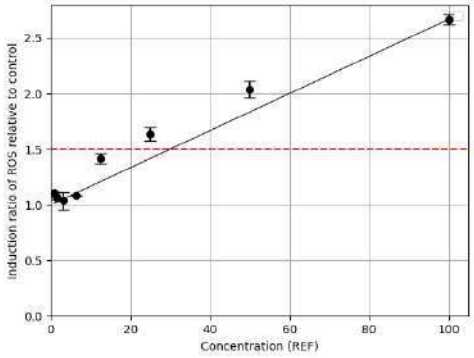 induction ratio of ROS relative to control Concentration (REF)
19	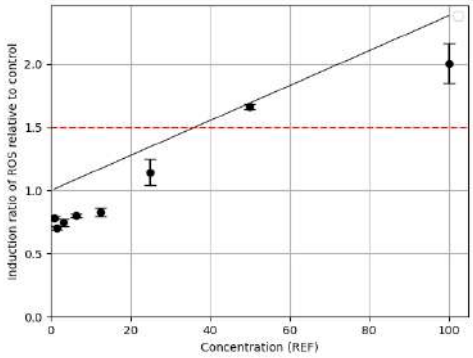 induction ratio of ROS relative to control Concentration (REF)	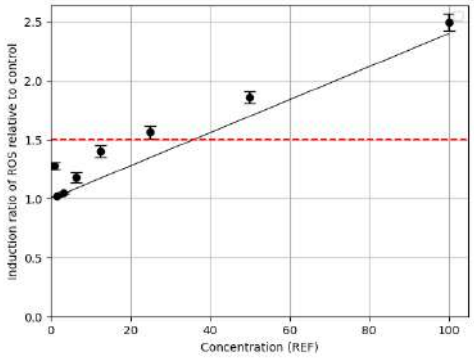 induction ratio of ROS relative to control Concentration (REF)

20	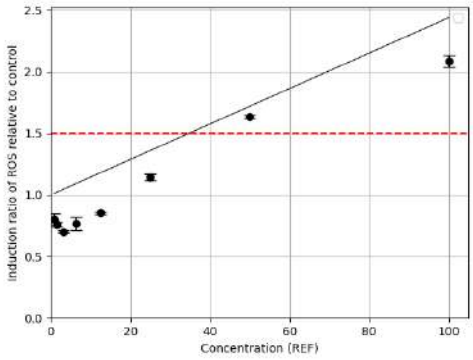 induction ratio of ROS relative to control Concentration (REF)	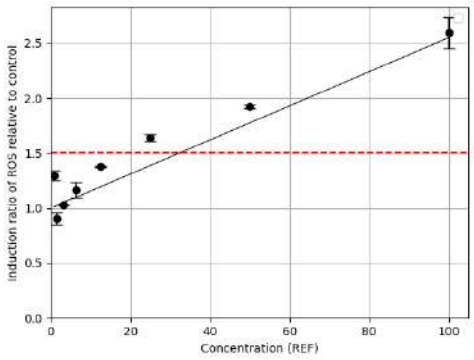 induction ratio of ROS relative to control Concentration (REF)
21	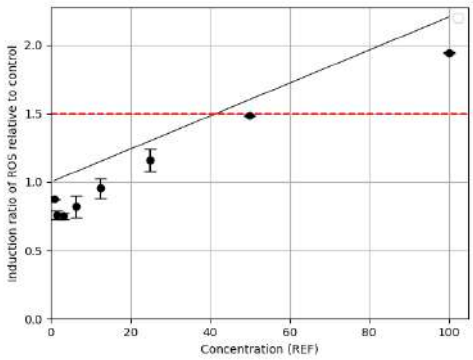 induction ratio of ROS relative to control Concentration (REF)	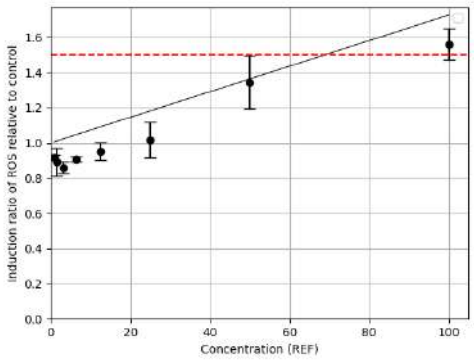 induction ratio of ROS relative to control Concentration (REF)
22	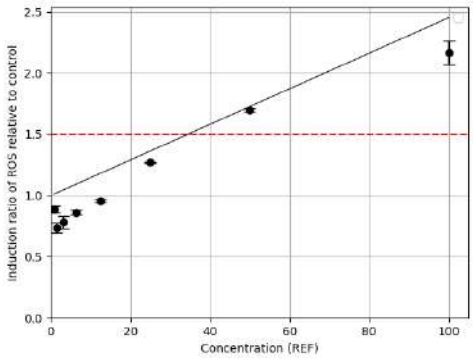 induction ratio of ROS relative to control Concentration (REF)	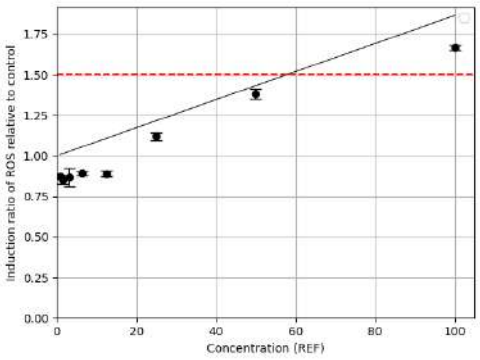 induction ratio of ROS relative to control Concentration (REF)
23	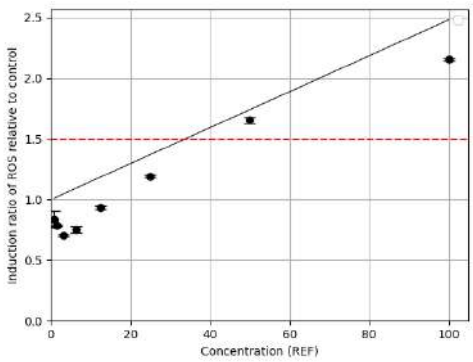 induction ratio of ROS relative to control Concentration (REF)	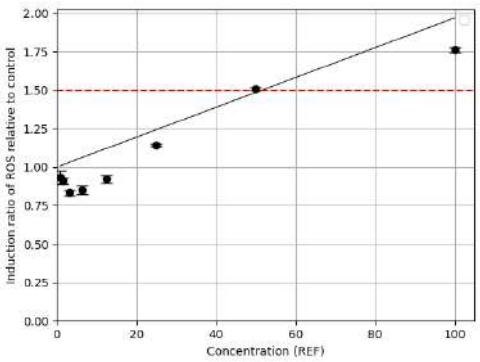 induction ratio of ROS relative to control Concentration (REF)

24	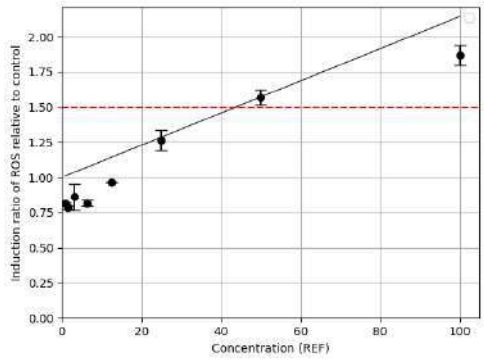 induction ratio of ROS relative to control Concentration (REF)	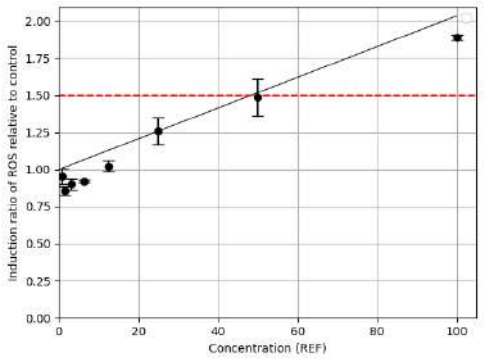 induction ratio of ROS relative to control Concentration (REF)
25	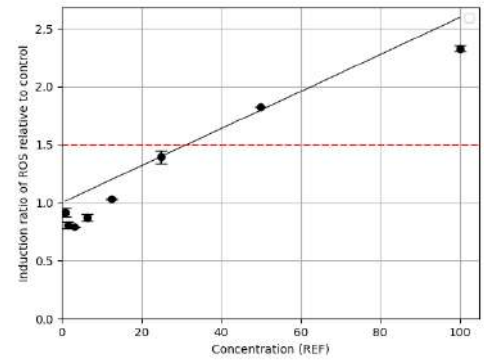 induction ratio of ROS relative to control Concentration (REF)	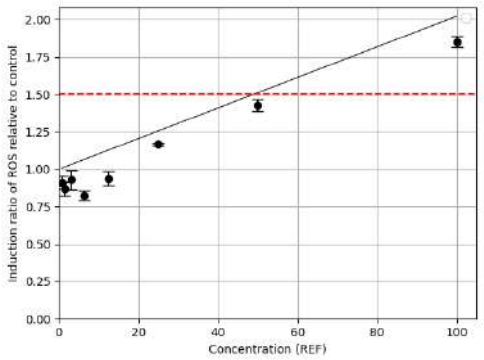 induction ratio of ROS relative to control Concentration (REF)
26	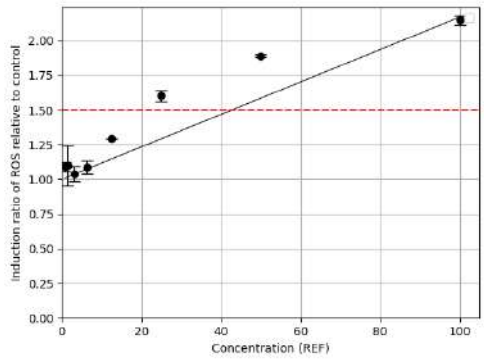 induction ratio of ROS relative to control Concentration (REF)	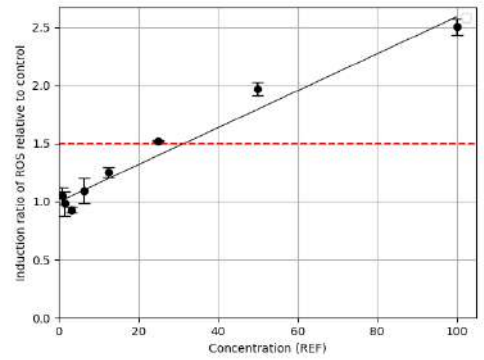 induction ratio of ROS relative to control Concentration (REF)
27	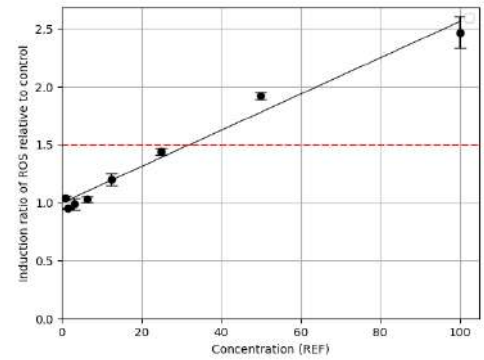 induction ratio of ROS relative to control Concentration (REF)	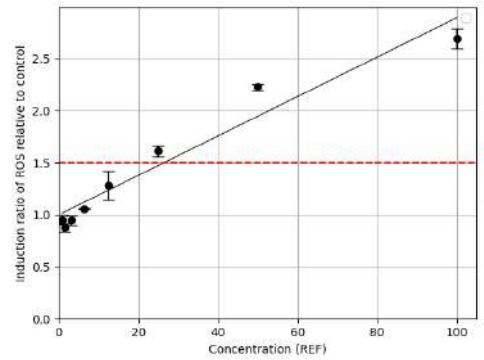 induction ratio of ROS relative to control Concentration (REF)

28	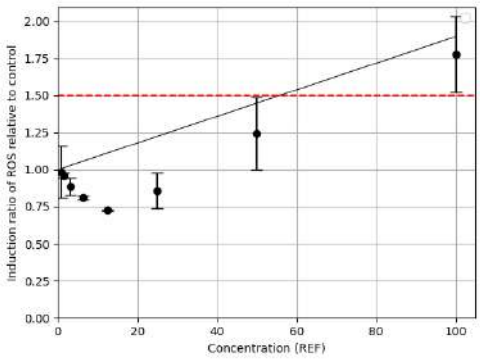 induction ratio of ROS relative to control Concentration (REF)	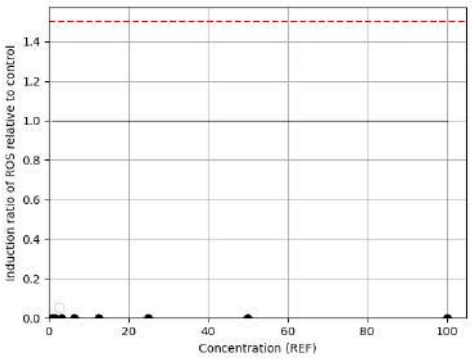 induction ratio of ROS relative to control Concentration (REF)
29	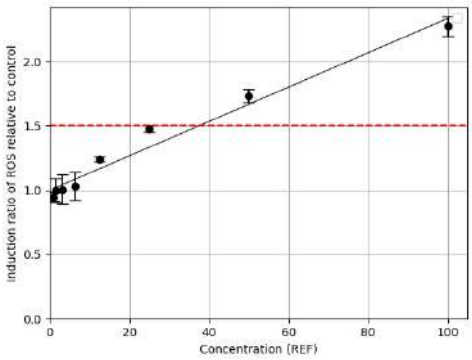 induction ratio of ROS relative to control Concentration (REF)	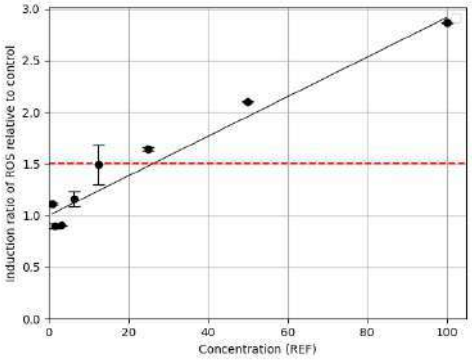 induction ratio of ROS relative to control Concentration (REF)
30	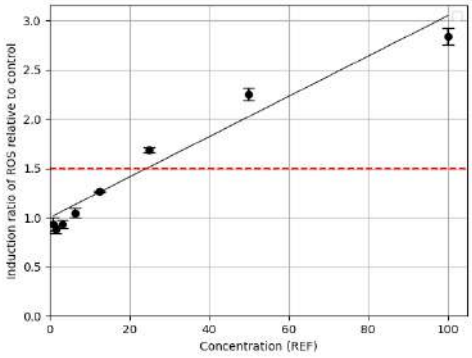 induction ratio of ROS relative to control Concentration (REF)	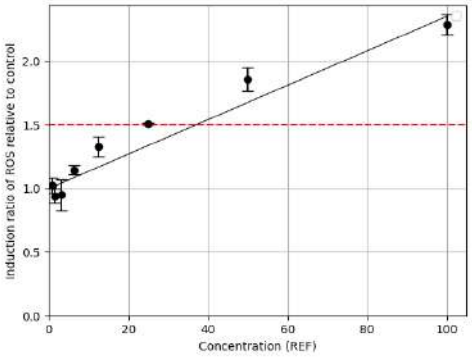 induction ratio of ROS relative to control Concentration (REF)
31	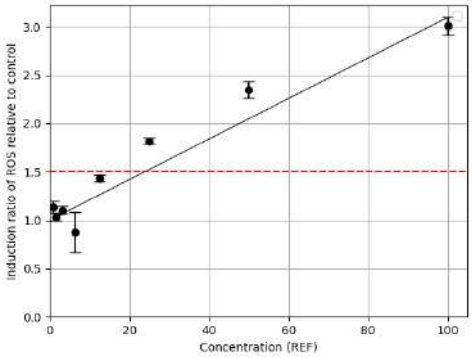 induction ratio of ROS relative to control Concentration (REF)	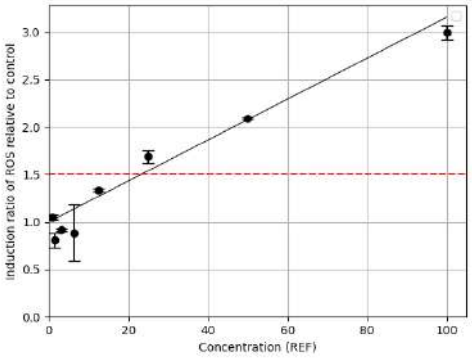 induction ratio of ROS relative to control Concentration (REF)

32	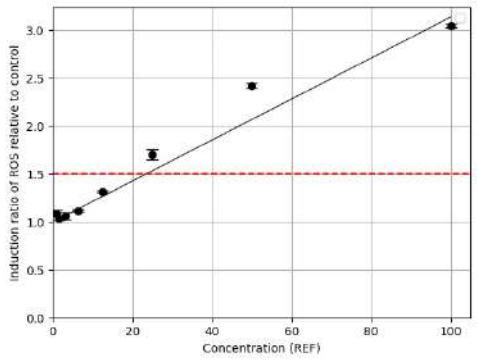 induction ratio of ROS relative to control Concentration (REF)	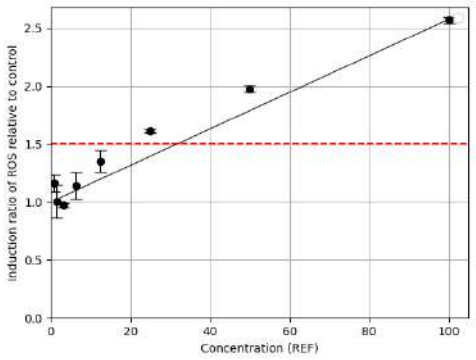 induction ratio of ROS relative to control Concentration (REF)
33	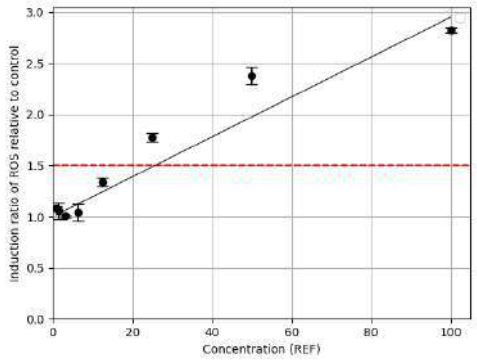 induction ratio of ROS relative to control Concentration (REF)	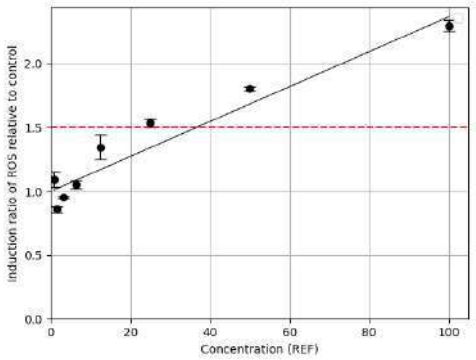 induction ratio of ROS relative to control Concentration (REF)
34	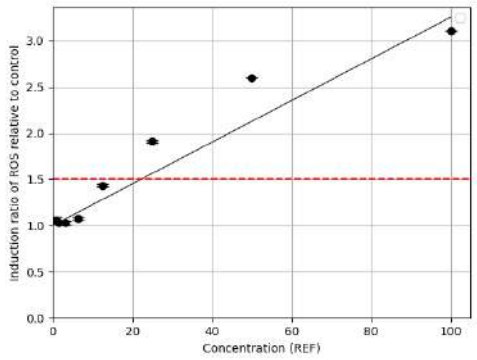 induction ratio of ROS relative to control Concentration (REF)	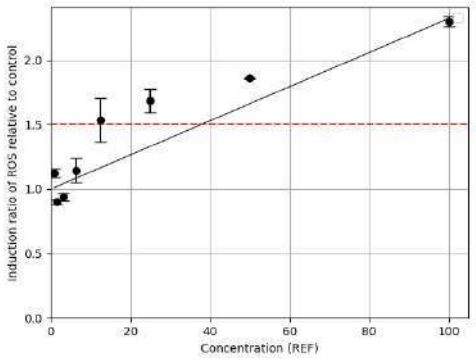 induction ratio of ROS relative to control Concentration (REF)
35	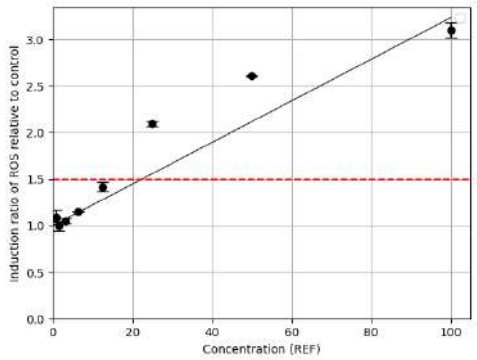 induction ratio of ROS relative to control Concentration (REF)	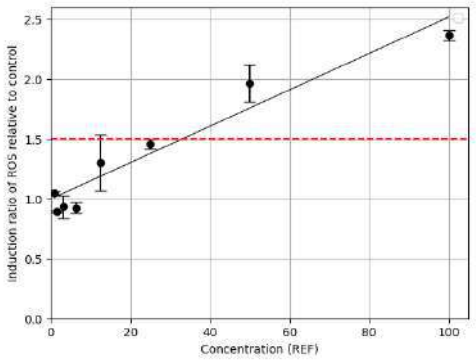 induction ratio of ROS relative to control Concentration (REF)

36	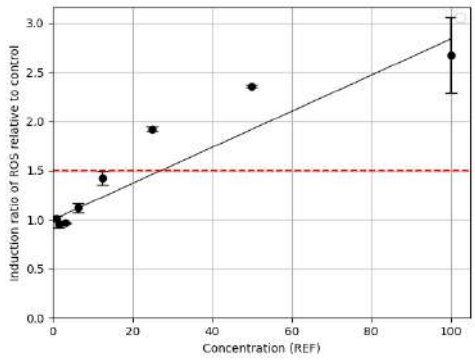	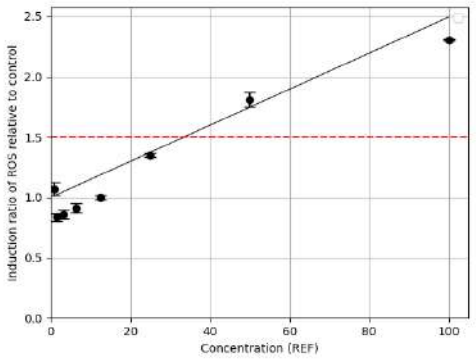

Experimentally determined versus modeled concentration-effect curves for mixtures of active algal toxins (PTX-2, OA, GYM, and DTX-1), PFAS (PFOS, 6:2 Cl-PFESA, and 8:2 Cl-PFESA), UV filters (EHS, BP-4, and HMS), and antibiotics (AMOX and ETM) present at the measured concentration compositions in seawater extracts. Sites 1, 9, 17, 26, and 35 were selected to represent the northern, eastern, southern, central, and western waters of Hong Kong, respectively, for FPT and CWDT. IPQ = Index of Prediction Quality (see eqs 4 and 5 in the Chapter 3 for details). IPQ values between 1 and -1 indicate good agreement between the model and experimental results.

Sites	FPT	IPQ	CWDT	IPQ
1 Wet season	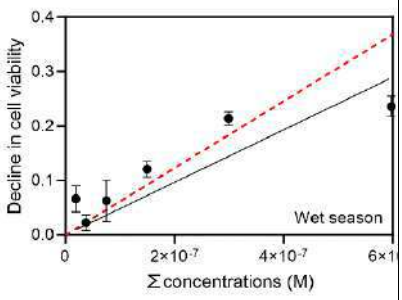	2.70	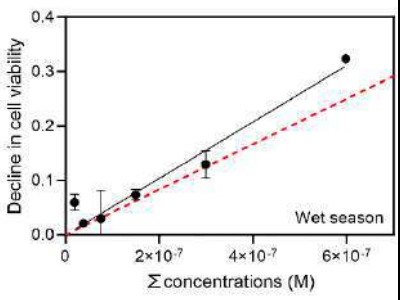	-0.58
9 Wet season	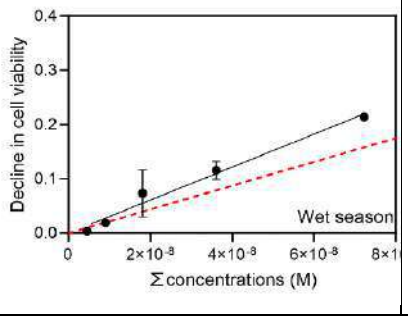	-0.93	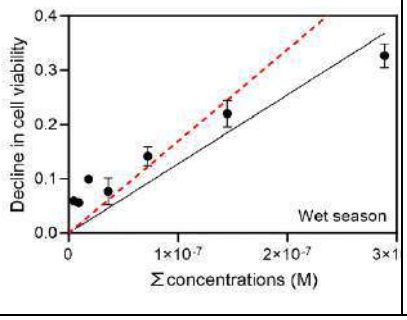	0.26

Sites	FPT	IPQ	CWDT	IPQ
17 Wet season	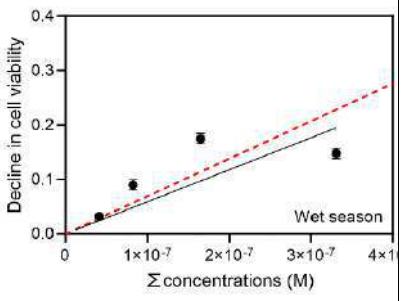	-0.98	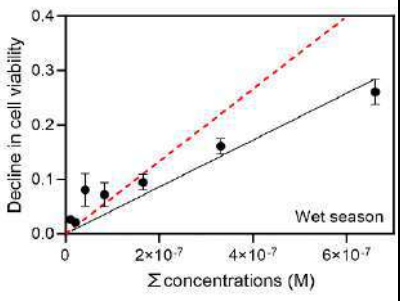	-0.12
26 Wet season	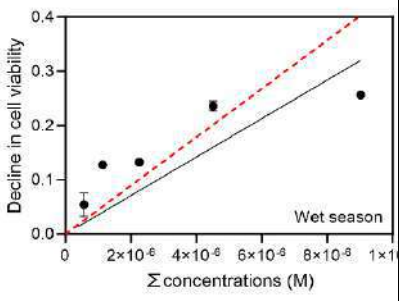	-0.93	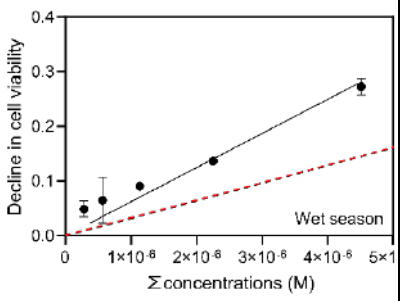	0.80
35 Wet season	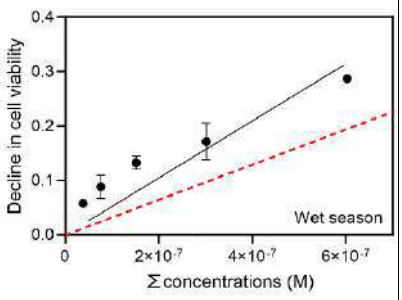	-0.90	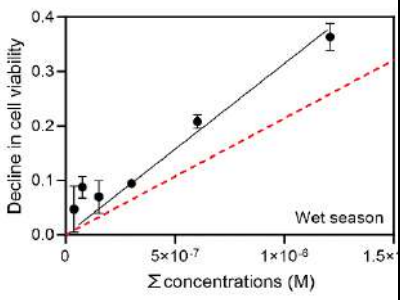	-0.85
1 Dry season	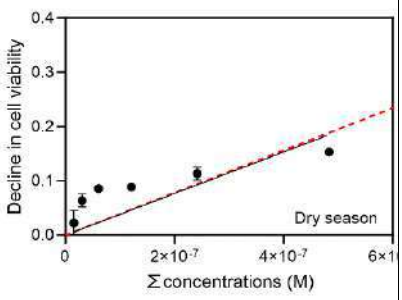	-0.79	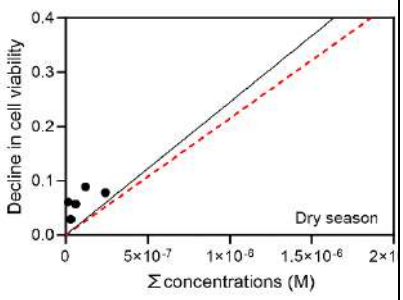	-0.21
9 Dry season	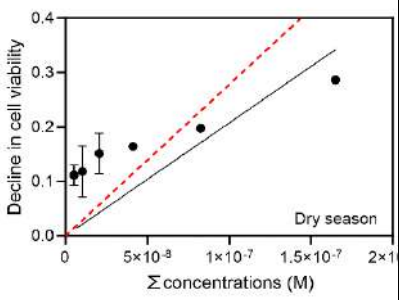	-0.95	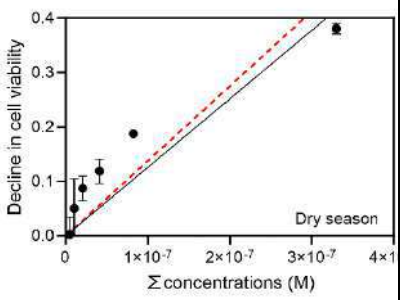	0.53

Sites	FPT	IPQ	CWDT	IPQ
17 Dry season	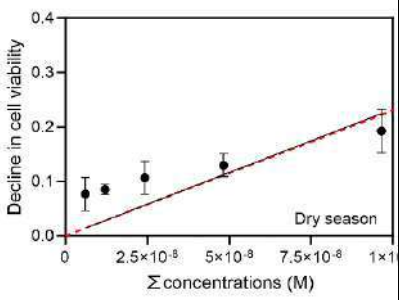	-0.94	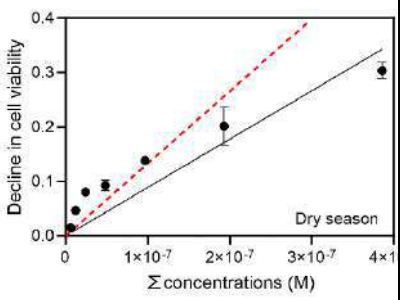	-0.40
26 Dry season	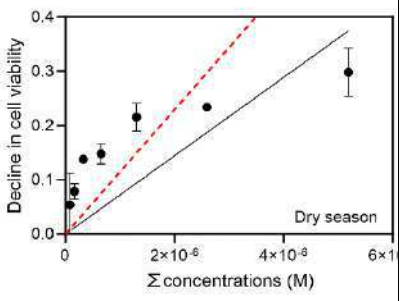	-0.86	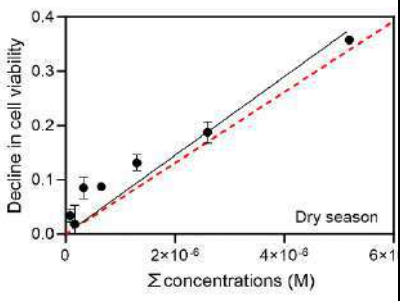	-0.03
35 Dry season	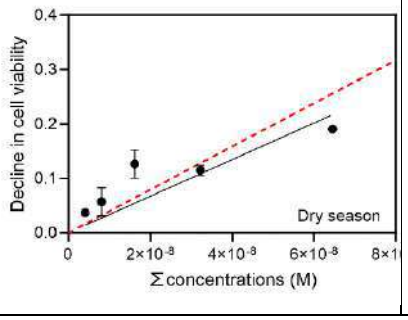	-0.85	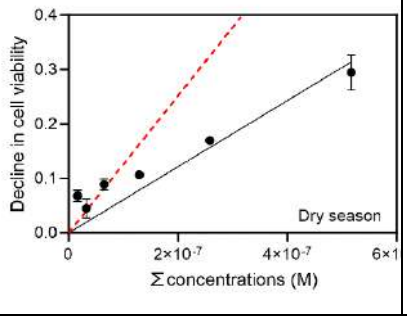	-0.74

Appendix II

PFBA

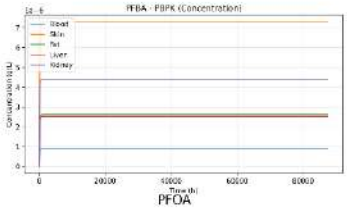

PFPeA

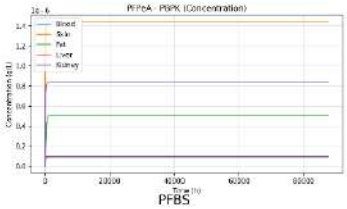

PFOA

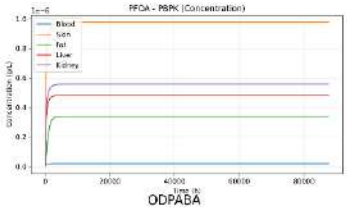

PFBS

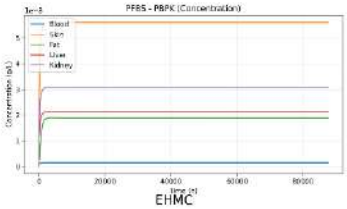

ODPABA

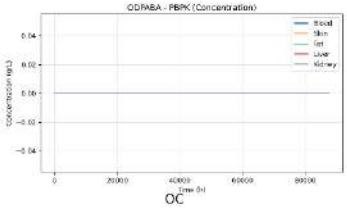

EHMC

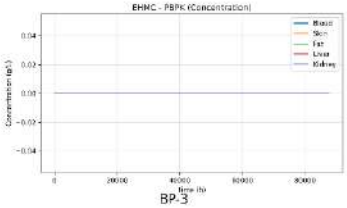

OC

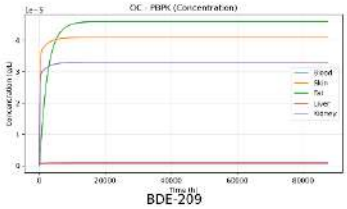

BP-3

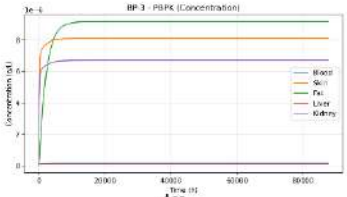

BDE-209

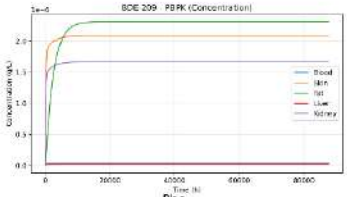

Ace

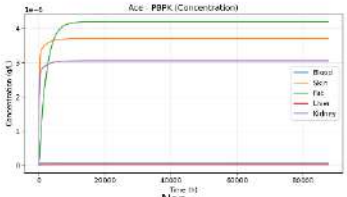

Phe

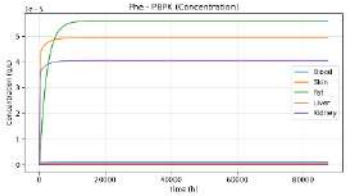

Nap

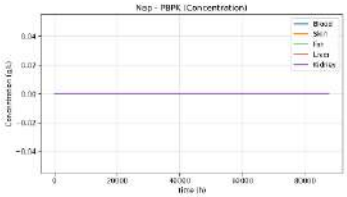

4-MBC

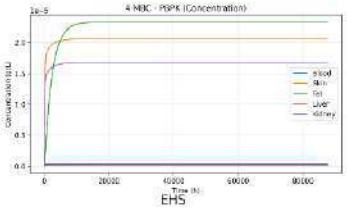

HMS

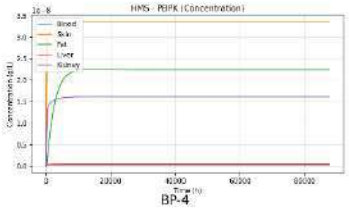

EHS

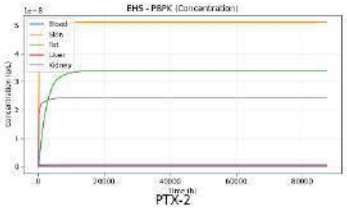

BP-4

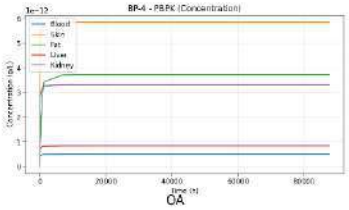

PTX-2

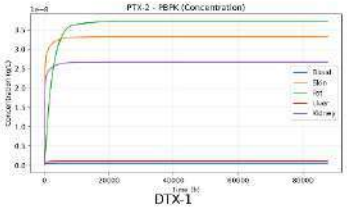

OA

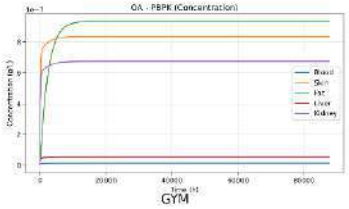

DTX-1

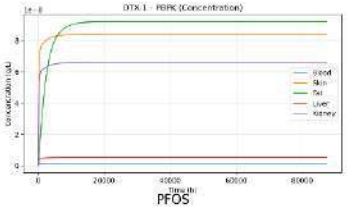

GYM

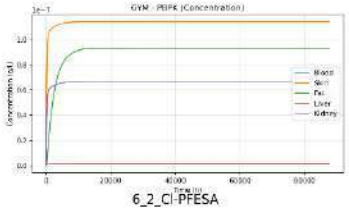

PFOS

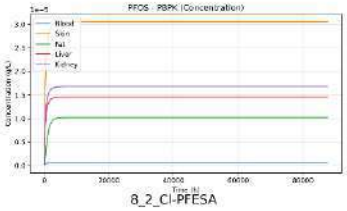

6_2_Cl-PFESA

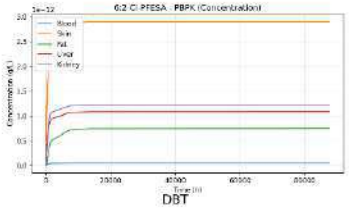

8_2_Cl-PFESA

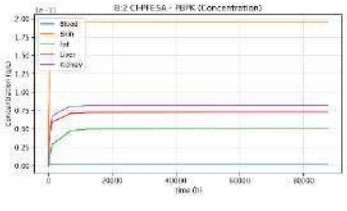

DBT

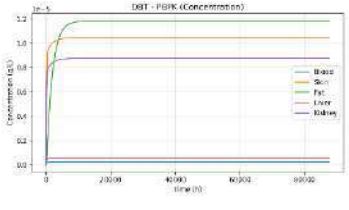

Appendix III

Python code for PBTK model establishment.

```
import numpy as np
import pandas as pd
import matplotlib.pyplot as plt
from scipy.integrate import odeint
import os, re, json

# =========================
# 1) Read dataset
# =========================
# Compounds, P_skb, P_fab, P_skw, P_liver, P_kidney, Kp, C_water,
CL_liver [, phi] [, C_diet]
excel_file = "Data.xlsx"
df = pd.read_excel(excel_file)

# =========================
# 2) Parameters
# =========================
# Q (L/h)
Q_bsk, Q_fat = 10.31, 1.01
Q_liver, Q_kidney = 5.05, 3.84

# V (L)
V_sk, V_a, V_fat = 11.2, 26.78, 33.04
V_liver, V_kidney = 5.03, 2.03

# Clearance
Q_gfr = 31.36           # L/h
f_ub_plasma = 0.1       # 0-1
phi_default = 0.0       # 0-1

# Sin-water
A_ex = 2.8e4            # cm^2
Cf = 1000.0             # cm^3/L
```

```
# Diet pathway
BW = 200.0              # kg
AE = 0.9                # assimilation efficiency (0-1)

# Time frame
t_eval = np.linspace(0, 87600, 800)  # h (0~10 yrs)
y0 = [0.0, 0.0, 0.0, 0.0, 0.0]

# outputs
save_folder = "Results"
os.makedirs(save_folder, exist_ok=True)

#
SAFE_P_MIN = 1e-3
EPS_CLIP   = 1e-15
EPS_AUC    = 1e-18

# ========================
# 3) SA
# ========================
SA_PARAMS = [
    'Q_bsk','Q_fat','Q_liver','Q_kidney',
    'V_a','V_sk','V_fat','V_liver','V_kidney',
    'P_skb','P_fab','P_skw','P_liver','P_kidney',

'Kp','A_ex','Cf','C_water','CL_liver','Q_gfr','f_ub_plasma','p
hi',

    'C_diet','BW','AE'
]
SA_EXCLUDE = ['Q_gfr', 'f_ub_plasma', 'A_ex', 'Cf', 'BW', 'AE']

def _safe(name: str) -> str:
    return re.sub(r'[\\/*?:"<>| ]', '_', str(name))

def _unique_sheet_name(base: str, used: set) -> str:
    base = base[:31] if len(base) > 31 else base
```

```
    name = base or "Sheet"
    i = 1
    while name in used:
        suffix = f"_{i}"
        name = (base[:31 - len(suffix)] + suffix) if len(base)
+ len(suffix) > 31 else (base + suffix)
        i += 1
    used.add(name)
    return name

# ==========================
# 5) ODE
# ==========================
def PBTK_conc_ode(
    y, t,
    Q_bsk, Q_fat, Q_liver, Q_kidney,
    V_a, V_sk, V_fat, V_liver, V_kidney,
    P_skb, P_fab, P_skw, P_liver, P_kidney,
    Kp, A_ex, Cf, C_water,
    C_diet, BW, AE,                人）
    CL_liver, Q_gfr, f_ub_plasma, phi
):
    C_a, C_sk, C_fat, C_liv, C_kid = [float(v) for v in y]

    # skin (g/h) urine (g/h)
    J_derm  = max(Kp, 0.0) * A_ex / Cf * (C_water - C_sk / P_skw)
    J_urine = Q_gfr * (1.0 - phi) * f_ub_plasma * C_a

    # ——R_oral->blood (g/h)
    # DC = 0.123 * BW^0.8 (kg/day); C_diet: ng/g(dry); AE: 0-1
    # kg/day * (ng/g) -> g/day need ×1e-6；then /24 -> g/h
    DC_per_day = 0.123 * (BW ** 0.8)                # kg/day
    R_oral_gph = DC_per_day * max(C_diet, 0.0) * AE / 24.0 * 1e-
6  # g/h

    # (1) Blood
    dC_a_dt = (
        Q_bsk   * (C_sk  / P_skb    - C_a) +
```

```
        Q_fat   * (C_fat / P_fab    - C_a) +
        Q_liver * (C_liv / P_liver  - C_a) +
        Q_kidney* (C_kid / P_kidney - C_a)
        - J_urine
        + R_oral_gph
    ) / V_a

    # (2) Skin
    dC_sk_dt = (Q_bsk * (C_a - C_sk / P_skb) + J_derm) / V_sk

    # (3) Fat
    dC_fat_dt = (Q_fat * (C_a - C_fat / P_fab)) / V_fat

    # (4) Liver
    dC_liver_dt = (Q_liver * (C_a - C_liv / P_liver) - CL_liver
* C_liv) / V_liver

    # (5) Kidney
    dC_kidney_dt = (Q_kidney * (C_a - C_kid / P_kidney)) /
V_kidney

    return   [dC_a_dt,   dC_sk_dt,   dC_fat_dt,   dC_liver_dt,
dC_kidney_dt]

# =========================
# 6) AUC
# =========================
def run_once(params, y0, t_eval):
    sol = odeint(
        PBTK_conc_ode, y0, t_eval,
        args=(
            params['Q_bsk'], params['Q_fat'], params['Q_liver'],
params['Q_kidney'],
            params['V_a'],   params['V_sk'],   params['V_fat'],
params['V_liver'], params['V_kidney'],
            max(params['P_skb'],                  SAFE_P_MIN),
max(params['P_fab'], SAFE_P_MIN),
```

```
            max(params['P_skw'],                    SAFE_P_MIN),
max(params['P_liver'], SAFE_P_MIN),
            max(params['P_kidney'], SAFE_P_MIN),
            max(params['Kp'],       0.0),       params['A_ex'],
params['Cf'], max(params['C_water'], 0.0),
            max(params.get('C_diet', 0.0), 0.0), params['BW'],
params['AE'],
            max(params['CL_liver'], 0.0), params['Q_gfr'],
            np.clip(params['f_ub_plasma'], 0.0, 1.0),
            np.clip(params['phi'], 0.0, 1.0)
        ),
        atol=1e-9, rtol=1e-6, mxstep=10000
    )
    sol = np.where(np.abs(sol) < EPS_CLIP, 0.0, sol)
    C_blood = np.maximum(sol[:,0], 0.0)
    C_skin  = np.maximum(sol[:,1], 0.0)
    auc_bld = float(np.trapezoid(C_blood, t_eval))
    auc_sk  = float(np.trapezoid(C_skin,  t_eval))
    return sol, auc_bld, auc_sk

# =========================
# 7) Parameter assembly
# =========================
def make_param_dict(row):
    return {
        'Q_bsk': Q_bsk, 'Q_fat': Q_fat, 'Q_liver': Q_liver,
'Q_kidney': Q_kidney,
        'V_a': V_a, 'V_sk': V_sk, 'V_fat': V_fat, 'V_liver':
V_liver, 'V_kidney': V_kidney,
        'P_skb': max(float(row['P_skb']), SAFE_P_MIN),
        'P_fab': max(float(row['P_fab']), SAFE_P_MIN),
        'P_skw': max(float(row['P_skw']), SAFE_P_MIN),
        'P_liver': max(float(row['P_liver']), SAFE_P_MIN),
        'P_kidney': max(float(row['P_kidney']), SAFE_P_MIN),
        'Kp': max(float(row['Kp']), 0.0),
        'A_ex': A_ex, 'Cf': Cf,
        'C_water': max(float(row['C_water']), 0.0),
        'CL_liver': max(float(row['CL_liver']), 0.0),
```

```
        'Q_gfr': Q_gfr, 'f_ub_plasma': f_ub_plasma,
        'phi': float(row['phi']) if 'phi' in df.columns else
phi_default,
        'C_diet': float(row['C_diet']) if 'C_diet' in df.columns
and pd.notna(row['C_diet']) else 0.0,
        'BW': BW,
        'AE': AE
    }

# =========================
# 8) SA
# =========================
def                    get_sa_target_params(base_list=SA_PARAMS,
global_exclude=SA_EXCLUDE):
    targets   =   [p   for   p   in   base_list   if   p   not   in
set(global_exclude)]
    if not targets:
        print("[WARN] target parameter list is empty; SA has
been skipped.")
    else:
        print(f"[INFO] global exclude: {global_exclude} -> real
SA parameter umber: {len(targets)}")
    return targets

# =========================
# 9) Local SA
# =========================
def local_sa(params_base, y0, t_eval, target_params, rel=0.05,
metric='AUC_blood'):
    if not target_params:
        return pd.DataFrame(), np.nan

    _, auc_bld0, auc_sk0 = run_once(params_base, y0, t_eval)
    if metric == 'AUC_blood':
        auc0, alt0 = auc_bld0, auc_sk0
    else:
        auc0, alt0 = auc_sk0, auc_bld0
    used_metric = metric
```

```
    if not np.isfinite(auc0) or auc0 < EPS_AUC:
        if alt0 >= EPS_AUC:
            used_metric = 'AUC_skin' if metric=='AUC_blood' else
'AUC_blood'
           auc0 = alt0
            print(f"[INFO]    baseline    {metric}≈0,    revised
{used_metric} to do SA.")
        else:
            print(f"[INFO]     {metric}     all     alternative
indicators≈0, SA has been skipped.")
            return pd.DataFrame(), auc0

    rows = []
    for p in target_params:
        up = params_base.copy()
        if                          p                          in
['P_skb','P_fab','P_skw','P_liver','P_kidney','Kp','C_water','
CL_liver','C_diet']:
            up[p] = max(up[p]*(1+rel), 0.0)
        else:
            up[p] = up[p]*(1+rel)

        _, auc_bld_up, auc_sk_up = run_once(up, y0, t_eval)
        auc_up  =  auc_bld_up  if  used_metric=='AUC_blood'  else
auc_sk_up

        dn = params_base.copy()
        if                          p                          in
['P_skb','P_fab','P_skw','P_liver','P_kidney','Kp','C_water','
CL_liver','C_diet']:
            dn[p] = max(dn[p]*(1-rel), 0.0)
        else:
            dn[p] = dn[p]*(1-rel)

        _, auc_bld_dn, auc_sk_dn = run_once(dn, y0, t_eval)
        auc_dn  =  auc_bld_dn  if  used_metric=='AUC_blood'  else
auc_sk_dn
```

```
        sc_plus  = (auc_up/auc0 - 1.0) * 100.0
        sc_minus = (auc_dn/auc0 - 1.0) * 100.0
        mean_abs = (abs(sc_plus) + abs(sc_minus)) / 2.0
        rows.append({'param': p, 'Sc_plus_%': sc_plus,
                     'Sc_minus_%':    sc_minus,    'MeanAbs_%':
mean_abs,
                     'AUC_orig':      auc0,      'metric_used':
used_metric})

    df_sa     =     pd.DataFrame(rows).sort_values('MeanAbs_%',
ascending=False).reset_index(drop=True)
    return df_sa, auc0

# =========================
# 10) Main cycle
# =========================
final_rows = []
sa_summary_rows = []

sa_all_path             =             os.path.join(save_folder,
"PBTK_sensitivity_all.xlsx")
sheet_used = set()
writer = pd.ExcelWriter(sa_all_path, engine="openpyxl")

SA_TARGETS_GLOBAL = get_sa_target_params()

for _, row in df.iterrows():
    cmp = row['Compounds']
    params = make_param_dict(row)

    if  params['C_water']  <=  0  or  params['Kp']  <=  0  or
params['A_ex'] <= 0:
        print(f"[INFO] '{cmp}' Exposure input may be invalid
(C_water={params['C_water']}, Kp={params['Kp']}).")
    if params.get('C_diet', 0.0) <= 0:
        print(f"[INFO] '{cmp}' C_diet not provided or set to 0
（ng/g, the oral intake component will be 0.")
```

```
    # ── Calculate
    sol, auc_blood, auc_skin = run_once(params, y0, t_eval)
    sol_plot = np.maximum(sol, 0.0)

    if not np.all(np.isfinite(sol_plot)):
        which = np.where(~np.isfinite(sol_plot))
        print(f"[WARN] '{cmp}' non-finite values（inf/NaN）
appeared in the solution, plotting and SA have been skipped.
index：{which}")
        last = np.nan_to_num(sol_plot[-1], nan=0.0, posinf=0.0,
neginf=0.0)
        final_rows.append({
            'Compound': cmp,
            'C_blood_gL':     float(last[0]),     'C_skin_gL':
float(last[1]),
            'C_fat_gL':   float(last[2]),         'C_liver_gL':
float(last[3]),
            'C_kidney_gL': float(last[4]),
            'AUC_blood':     float(auc_blood),     'AUC_skin':
float(auc_skin),
            'phi_used':    params['phi'],    'Kp_used_cm_per_h':
params['Kp'],
            'CL_liver_used_L_per_h': params['CL_liver'],
            'Cwater_used_g_per_L': params['C_water'],
            'Cdiet_used_ng_per_g': params.get('C_diet', 0.0),
            'BW_used_kg': params['BW'], 'AE_used': params['AE'],
            'P_skb': params['P_skb'], 'P_fab': params['P_fab'],
'P_skw': params['P_skw'],
            'P_liver':      params['P_liver'],      'P_kidney':
params['P_kidney'],
            'note': 'non-finite solution; plot & SA skipped'
        })
        continue

    # ── Curve
    C_bld, C_sk, C_fat, C_liv, C_kid = sol_plot.T
```

```
    # ── Concentration plot
    safe = _safe(cmp)
    fig, ax = plt.subplots(figsize=(7.2, 4.2))
    for                arr,                lab                in
[(C_bld,'Blood'),(C_sk,'Skin'),(C_fat,'Fat'),
                      (C_liv,'Liver'),(C_kid,'Kidney')]:
        ax.plot(t_eval, arr, label=lab)
    ax.set(xlabel='Time (h)', ylabel='Concentration (g/L)',
           title=f'{cmp} - PBTK (Concentration)')
    ax.legend(); ax.grid(alpha=0.3)
    try:
        fig.tight_layout()
    except Exception as e:
        print(f"[INFO] tight_layout failure（{cmp}）：{e}")
    fig.savefig(os.path.join(save_folder,  f'{safe}_conc.png'),
dpi=300)
    plt.close(fig)

    # ── Endpoint summary
    final_rows.append({
        'Compound': cmp,
        'C_blood_gL':      float(C_bld[-1]),      'C_skin_gL':
float(C_sk[-1]),
        'C_fat_gL':    float(C_fat[-1]),          'C_liver_gL':
float(C_liv[-1]),
        'C_kidney_gL': float(C_kid[-1]),
        'AUC_blood':       float(auc_blood),       'AUC_skin':
float(auc_skin),
        'phi_used':     params['phi'],     'Kp_used_cm_per_h':
params['Kp'],
        'CL_liver_used_L_per_h': params['CL_liver'],
        'Cwater_used_g_per_L': params['C_water'],
        'Cdiet_used_ng_per_g': params.get('C_diet', 0.0),
        'BW_used_kg': params['BW'], 'AE_used': params['AE'],
        'P_skb':  params['P_skb'],  'P_fab':  params['P_fab'],
'P_skw': params['P_skw'],
        'P_liver':        params['P_liver'],        'P_kidney':
params['P_kidney']
```

```
    })# ========================
# 11) Output
# ========================
out_xlsx                =                os.path.join(save_folder,
'PBTK_concentration_outputs.xlsx')
pd.DataFrame(final_rows).to_excel(out_xlsx, index=False)

sa_summary_xlsx           =           os.path.join(save_folder,
'PBTK_sensitivity_summary.xlsx')
summary_df.to_excel(sa_summary_xlsx, index=False)

config_json = os.path.join(save_folder, 'run_config.json')
with open(config_json, 'w', encoding='utf-8') as f:
    json.dump({
        "excel_file": excel_file,
        "SA_params_base": SA_PARAMS,
        "SA_exclude_global": SA_EXCLUDE,
        "SA_rel_change": 0.05,
        "global_params": {
            "Q_bsk": Q_bsk, "Q_fat": Q_fat, "Q_liver": Q_liver,
"Q_kidney": Q_kidney,
            "V_a": V_a, "V_sk": V_sk, "V_fat": V_fat, "V_liver":
V_liver, "V_kidney": V_kidney,
            "Q_gfr":    Q_gfr,    "f_ub_plasma":    f_ub_plasma,
"phi_default": phi_default,
            "A_ex": A_ex, "Cf": Cf, "BW": BW, "AE": AE
        },
        "t_eval":     [float(t_eval[0]),     float(t_eval[-1]),
len(t_eval)]
    }, f, ensure_ascii=False, indent=2)

print(f"[OK]   Concentration   plots   &   outputs   saved   in:
{save_folder}")
print(f"[OK]    Sensitivity    ALL-in-one    workbook    saved:
{os.path.join(save_folder, 'PBTK_sensitivity_all.xlsx')}")
print(f"[OK] Sensitivity summary saved: {sa_summary_xlsx}")
print(f"[OK] Endpoints table saved: {out_xlsx}")
```